Molecule–Surface–Scattering with Velocity–Controlled Molecular Beams

im Fachbereich Physik
der Freien Universität Berlin
eingereichte Dissertation

angefertigt am
Fritz-Haber-Institut
der Max-Planck-Gesellschaft
und an der
Georg-August-Universität Göttingen

Fabian Grätz

Berlin, 2014

Erstgutachter:	Prof. Dr. Gerard Meijer Fritz-Haber-Institut der Max-Planck-Gesellschaft Freie Universität Berlin
Zweitgutachter:	Prof. Dr. Ludger Wöste Freie Universität Berlin
Disputation:	25. März 2013

Kurzfassung

Diese Dissertation beschreibt die Konzeption und den Aufbau einer neuartigen Apparatur zur Streuung von Molekülen an Oberflächen. Die Apparatur besteht aus einer Kombination aus Stark-Abbremser und einer modernen Oberflächen-Streukammer. Pulse zustandsselektierter Moleküle werden nach vorheriger Trennung vom Trägergas mit variabler Geschwindigkeit und bisher unerreichter Energieauflösung von wohldefinierten Oberflächen gestreut. Ergebnisse für die Streuung von CO($a^3\Pi$) in verschiedenen Vibrationszuständen an Au(111) werden vorgestellt.

Ein Molekülstrahl, in dem die Moleküle schnell aber kalt sind, wird durch gleichzeitige Überschallexpansion von CO und Xe oder Ar erzeugt. Um die Manipulation von CO mittels elektrischer Felder zu ermöglichen, wird es durch einen schmalbandigen Laser in den $a^3\Pi_1$-Zustand angeregt, der sowohl über eine lange Lebenszeit als auch über ein hohes Dipolmoment verfügt. Anschließend wird mit Hilfe eines elektrostatischen Hexapols der metastabile CO-Strahl abgelenkt und auf die Eintrittsöffnung des Stark-Abbremsers fokussiert, wodurch eine vollständige Trennung vom Rest des Molekülstrahls erreicht werden kann. Die Geschwindigkeit des metastabilen CO von anfangs 360 m/s kann in den 131 Stufen des Stark-Abbremser im Bereich von (512 ± 4) m/s bis (50 ± 4) m/s variiert werden. Dies entspricht Kollisionsenergien im Bereich von $(307 \pm 5)\,\mathrm{cm}^{-1}$ bis $(3.0 \pm 0.5)\,\mathrm{cm}^{-1}$. Durch minimale Änderungen am Aufbau lässt sich dieser Bereich auf Geschwindigkeiten von bis zu (1300 ± 25) m/s erweitern, was einer Kollisionsenergie von $(1980 \pm 80)\,\mathrm{cm}^{-1}$ entspricht. Vor dem Streuprozess besteht die Möglichkeit, die Moleküle mittels eines Lasers in ausgewählten Quantenzuständen zu präparieren. Die Streukammer ist so gestaltet, dass sie den variablen Einsatz von Lasern zulässt, was eine Vielzahl von Möglichkeiten für Präparation und Detektion der Moleküle ermöglicht. Sowohl Hexapol als auch Abbremser sind so konzipiert, dass die komplette Apparatur ausheizbar ist. Ultrahochvakuum in der Streukammer wird ferner durch drei differentielle Pumpstufen zwischen der Düse und der Oberfläche erreicht. Dieser Aufbau ermöglicht es, den Molekülstrahl ohne messbaren Druckanstieg in der Streukammer von der Oberfläche zu streuen.

Oberflächen-Streuexperimente an einer Au(111)-Oberfläche wurden mit CO im metastabilen Zustand durchgeführt. Die Kollision führt zur Abregung in den elektronischen Grundzustand und wird von Elektronenemission begleitet, da die Anregungsenergie des metastabilen CO die Austrittsarbeit der Goldoberfläche übersteigt. Für die Effizienz dieses Prozesses konnte ein Wert von 0.13 ± 0.05 emittierten Elektronen pro einfallendem metastabilen Teilchen ermittelt werden. Ein Teil des einfallenden metastabilen CO wurde für diese Messung mittels eines Lasers ionisiert. Dadurch

kann die Effizienz des Prozesses durch den Vergleich der Intensitäten des Signals der ionisierten Moleküle mit der Verminderung des Elektronenemission-Signals gemessen werden.

Indem einfallende Moleküle mittels des Franck-Condon Pumpverfahrens in höheren Vibrationszuständen des CO($a^3\Pi$)-Zustands präpariert wurden, konnte zudem die Effizienz der Elektronenemission in Abhängigkeit vom Vibrationsniveau der einfallenden Moleküle bestimmt werden. Diese ist für metastabiles CO in den Vibrationszuständen $v = 1, 2, 3$ durchschnittlich um den Faktor $1,5$ höher als für den Vibrationsgrundzustand. Abregung von CO in den drei nächsthöheren Vibrationsniveaus, $v = 4, 5, 6$, führt im Mittel sogar zu einer $2,6$-fachen Erhöhung der Elektronenemission im Vergleich zum Vibrationsgrundzustand. Im Bereich von 93 m/s bis 512 m/s wurde kein Einfluss der Geschwindigkeit des metastabilen CO auf die Effizienz der Elektronenemission festgestellt. Dagegen steigt letztere um 27 % an, wenn die Oberfläche von 250 K auf 900 K erhitzt wird. Keines der bisher entwickelten theoretischen Modelle ist bislang dazu in der Lage, diese Resultate quantitativ zu reproduzieren. Daher ist es erstrebenswert, diese Modelle zu erweitern, um insbesondere den Einfluss der Vibration auf die Abregung von metastabilen Molekülen an Metalloberflächen korrekt beschreiben zu können.

Abstract

This thesis describes the design and construction of a novel molecule-surface scattering apparatus. The setup combines a Stark decelerator with a state-of-the-art surface scattering chamber, and allows background-gas free scattering of packets of velocity-controlled polar molecules in selected quantum states from well-defined surfaces with unprecedented energy resolution. Results for scattering of CO($a^3\Pi$) in different vibrational quantum states from a clean Au(111) surface are presented.

CO is co-expanded with Xe or Ar to yield a supersonic molecular beam which produces fast, internally cold molecules. Excitation of CO to the long-lived electronically excited $a^3\Pi_1$ state makes it accessible to manipulation with electric fields due to the state's large dipole moment. The complete removal of both carrier gas and remaining ground-state CO is achieved by focusing and deflecting the metastable CO with a switched electrostatic hexapole state selector. The 131-stage Stark decelerator is used to tune the velocity of a part of the metastable CO pulse, with an initial velocity of 360 m/s, in the range from (512 ± 4) m/s – (50 ± 4) m/s, corresponding to an incident translational energy between (307 ± 5) cm^{-1} and (3.0 ± 0.5) cm^{-1}, respectively. This range can be extended up to (1300 ± 25) m/s, corresponding to an energy of (1980 ± 80) cm^{-1}, by simple modifications to the setup. Prior to collision, the molecules can be laser-prepared in different vibrational and rotational quantum states. State-selective detection of the scattering products makes it possible to determine the quantum state, the scattering angle, and the kinetic energy of the scattered molecules. Therefore, detailed information about the scattering process can be obtained. The design of the machine allows for flexible laser access near the surface, such that a variety of different preparation and detection schemes can be employed. Ultra-high vacuum conditions in the scattering chamber are achieved by baking the entire apparatus, including the decelerator and the hexapole. Because of the carrier gas removal and a total of three differential pumping stages, no pressure rise is detected in the scattering chamber due to the incident molecular beam.

Scattering experiments of CO($a^3\Pi$) on Au(111) have been performed. The scattering process leads to electron emission because the metastable excitation energy exceeds the work function of the surface. The electron emission yield, i.e. the number of electrons emitted per incident metastable particle, has been measured to be 0.13 ± 0.05. A laser ionization-depletion method is used which makes it possible to directly compare the intensity of the metastable CO ionization signal to the intensity decrease of the electron emission signal. It was also shown that vibrationally excited metastable CO leads to a higher electron emission yield. By preparing different vibrational distributions of CO in the $a^3\Pi$ electronic state via Franck-Condon pumping,

the electron emission yield was determined for groups of vibrational levels. The first three vibrationally excited levels have an increased electron emission yield which on average is a factor of 1.5 larger than that of the vibrational ground state. Averaged over the vibrational levels with quantum number $v = 4, 5, 6$, this factor is approximately 2.6. In the range between 93 m/s and 512 m/s, the electron emission was observed to be independent of the velocity of the incident molecules. When the surface temperature is raised from 250 K to 900 K, the intensity of the electron emission signal increases by 27 %. These results are not in agreement with the models currently used to describe the de-excitation of electronically excited molecules at metal surfaces. This demonstrates the need for more theoretical work to incorporate the role of vibration into the description of the de-excitation mechanism.

Contents

Chapter 1

Introduction

At the center of fundamental research has always been the urge to understand two things: what is the matter surrounding us made of, and how does it interact? This thesis deals with a process which, when put in simple terms, happens everywhere around us all the time: molecules collide with a surface. This in itself should be enough to motivate the question: what happens during these collisions? The more precise question to ask is: how much and in which ways do the molecules and the surface exchange energy? As a scientist, of course, the way in which the air around us impacts on the surface of, say, the pages of this thesis, is rather ill-defined when one wants to learn about interactions between air and paper on a microscopic level. In this thesis, an apparatus is described with which collisions of molecules with surfaces can be investigated with an extremely high degree of control over all the scattering parameters.

In order to study in detail how a molecule exchanges energy with a surface upon collision, several steps are necessary. First of all, the complexity of the problem can be much reduced by allowing only one species at a time to hit the surface. This necessarily implies that one has to work under ultra-high vacuum conditions. Otherwise, gas molecules surrounding the surface of interest would continuously scatter from it and potentially stick to it, thus changing the outcome of any experiment. Second, one needs to know what the surface actually looks like. Instead of starting with an arbitrarily chosen material and characterizing it by means of sophisticated spectroscopic methods, it is preferred to use a material known to form a very simple and stable surface, clean it, and then keep it clean. Combining these two aspects by injecting molecules into a vacuum chamber, placing a surface in their path, and detecting the energy and angle of scattered molecules already constitutes a very simple surface scattering experiment.

In practice, however, a much higher degree of control is desired. First of all, molecules will also collide with each other and exchange translational and internal energy. The results of such experiments give averages over many microscopic degrees of freedom. A common approach to circumvent this problem is to choose the parameters of the molecular beam such that a proper supersonic expansion occurs. This technique is well-established and has been used for many decades [1, and references therein]. In the expansion, the internal energy of the molecules is converted into translational kinetic energy, and leads to a directed beam of molecules with velocities ranging from $350\,\mathrm{m/s}$ – $3500\,\mathrm{m/s}$. Redistribution of energy is so efficient that almost no internal energy is left for molecules to vibrate or rotate. Control over these molecules can be

taken one step further. By using one or more lasers tuned to the appropriate wavelength, molecules can be prepared in single vibrational and rotational energy levels, such that they all vibrate and rotate with the same frequencies. All of these methods, which manipulate the internal degrees of freedom of a particle, have matured over many years of experimental application.

The challenge of changing an important degree of freedom, namely the forward velocity at which molecules impact on the surface, has not been tackled much. The aforementioned method of shooting molecules into vacuum creates a beam whose velocity is determined by the mass and heat capacity per particle and the temperature of the molecules. Some coarse velocity control is therefore possible by cooling or heating the gas mixture, or by admixing rare gases of different molar weight to the molecule of interest. A simple method to change the incident velocity *normal* to the surface is to vary the angle of incidence at which the molecular beam hits the surface. Detailed studies have shown that the transfer of momentum normal to the surface usually exceeds the parallel momentum transfer, but the amount of energy transfer usually depends on both the incident energy and the angle of incidence [2–4].

Over the last one and a half decades, the field of *cold molecules* research has fueled the development of new ways to manipulate the velocity of molecular beams. Molecules in a molecular beam are already cold in the sense that they travel at almost the same velocity, meaning that their velocity distribution is narrow. In addition, their internal energy, determined by their quantum state, is low. For many experiments, though, it is advantageous if the molecules are not only cold, but also slow or at rest in the laboratory frame. Several approaches exist to produce a slow beam of neutral molecules. One of the most common and successful techniques is Stark deceleration. It is based on the Stark effect, which is named after Johannes Stark, who received the Nobel prize in 1919 for the discovery that atomic energy levels are split in the presence of an electric field [5–7]. The first Stark decelerator was realized in 1999 by Bethlem *et al.* [8], who slowed down a beam of metastable CO from 225 m/s to 98 m/s using time-dependent electric fields.

Stark deceleration relies on the fact that polar molecules will avoid regions of high electric field strength when they are in certain quantum states. These quantum states correspond to an antiparallel orientation of a classical dipole moment with respect to the electric field. The reason for this is that the energy levels of a molecule in such a quantum state are shifted towards higher energies with increasing field strength. When these molecules approach a pair of electrodes, which create an inhomogeneous electric field, they will gain potential energy at the cost of kinetic energy, and will thus slow down. If the fields are switched off before the molecule leaves the region near the electrodes, the molecules' velocity is reduced. In a Stark decelerator, many of these electrode pairs are arranged in a periodic array, such that the forward velocity of molecules can be reduced step by step. The working principle of the Stark decelerator bears similarities to that of a linear accelerator for charged particles, like the well-known two mile long accelerator at the *Stanford Linear Accelerator Center (SLAC)* [9]. The main difference is that the forces in the Stark decelerator depend on the gradient

of the electric *field strength* and the magnitude of the *electric dipole moment*, whereas the forces in a common particle accelerator are proportional to gradient of the *electric potential* and the *charge* of the particles. Obviously, the Stark deceleration technique is also capable of accelerating neutral polar molecules, but it is the slowing down which makes it so valuable for molecular beam experiments. Using Stark deceleration, it is even possible to bring polar molecules, for example CO [10] and ammonia [11, 12], to standstill in a trap located behind the decelerator.

A variety of other methods has been successfully developed to produce slow beams of neutral particles. Many of them rely on magnetic [13], optical [14], and microwave [15] fields, or use radiative pressure for deceleration [16]. Several techniques exist that are based on effusive beams, either by cooling a reservoir [17], or by filtering out the slow part of a thermal beam of molecules. In addition, more uncommon approaches like shooting molecules out of a rapidly rotating nozzle [18, 19] have been reported.

Samples of cold molecules prepared by one of the mentioned methods are used in a wide range of applications. In spectroscopy, the energy resolution is ultimately limited by the interaction time with the detector, according to the uncertainty relation $\Delta E \Delta t \geq \hbar/2$. Obviously, for a molecular beam passing through a detector of a fixed length, the interaction time will be inversely proportional to the beam's velocity. This enhancement in precision has been successfully demonstrated in an experiment where the resolution of a microwave spectrum obtained from a Stark decelerated beam of $^{15}NH_3$ could be significantly improved compared to a faster beam [20]. Similar experiments were also performed using OH radicals [21]. High-resolution spectroscopy on specific molecular species is of particular interest because it allows tests of fundamental physics. Using cold polar molecules, the time-variation of the electron to proton mass ratio [22, 23] and the finestructure constant [24], or the existence of a nonzero electric dipole moment of the electron [25, 26] can be probed.

Scattering experiments performed with cold molecules also offer astonishing insights into chemical reactions. At low collision energies, collision cross sections are expected to exhibit pronounced resonances, and will be nonzero even in the limit of zero Kelvin [27]. The resonances arise because two colliding particles can orbit each other only with a quantized value of angular momentum, an effect which can only be observed if particles approach each other slowly. Recently, those resonances have been observed for the first time in the scattering of electronically excited He atoms with Ar and H_2 at collision energies below 1 meV, using a setup where two beams of similar forward velocity were merged. State-to-state inelastic scattering cross sections have been measured for collisions of Stark-decelerated OH radicals scattering with different rare gase atoms [28, 29], D_2 [30], and state-selected NO molecules [31]. In the apparatus described in this thesis, the benefits of using Stark decelerated molecular beams in scattering experiments are extended towards collisions of CO with the solid surface of a metal.

The interaction between molecules and solid surfaces is both diverse and important for many aspects of everyday life. Of particular economic and ecologic importance is

the field of heterogeneous catalysis, where the activation barrier of a chemical reaction is lowered by a material in a different phase. Considering that the production of ammonia, an important precursor to many fertilizers, accounts for about 1.4 % of worldwide fossil fuel consumption [32, p. 121], it is obvious that making such chemical reactions more energy efficient on an industrial scale will equate to enormous savings. Both Fritz Haber [33] and Carl Bosch [34] were awarded the Nobel prize for the synthesis of ammonia and its subsequent implementation on an industrial scale. One of the two reactants, H_2, is obtained mainly from steam reforming, where methane (or other hydrocarbons) reacts with water to yield molecular hydrogen and CO. The yield of H_2 is usually increased further by combining steam reforming with the well-known water-gas shift reaction, $CO + H_2O \rightleftharpoons CO_2 + H_2$. Even though exothermic, this reaction proceeds very slowly, so that catalysts based on iron oxide or copper are needed to make use of it efficiently [35]. Carbon monoxide and the water-gas shift reaction also play a major role in the closely related Fischer-Tropsch synthesis [35, 36], where longer hydrocarbon chains are produced from the reaction of CO with H_2. Common catalysts for this process are based on Fe, Ru, Co, and Ni [36].

While these important processes have been realized for the first time in the first half of the last century, the focus in catalysis research has since increasingly shifted towards surface science studies, in which a microscopic understanding of the mechanisms underlying catalysis is sought. Towards this goal, experimental techniques like scanning tunneling microscopy [37] or atomic force microscopy [38] have been developed to study single particles on a surface. To understand the same experiments from a theoretical point of view, the framework of density functional theory (DFT) [39] has been widely employed to model the gas-surface interface by calculating a particle's energy in different orientations and positions on and near a surface.

A complete picture of molecule-surface interactions requires detailed understanding of the different steps involved, as described in reference [40, 41]. An approaching molecule may either bounce off or adsorb, i.e. stick, to the surface. In the latter case, it can potentially dissociate — i.e. split up into smaller components — and react, or gather enough thermal energy to depart again into the gas phase. While the entire process is important, it makes sense to study the single steps individually in different systems. Consider, e.g., a molecule which exhibits rich dynamics once it is adsorbed on the surface, but will always stick to it upon impact. It would be rather dull trying to study the dynamics of the impact, since no change will be observed. In order to obtain insights into the mechanisms of energy exchange happening at the gas-solid interface, it is more fruitful to study systems where adsorption takes place rarely or not at all, since the properties of the rebounding molecule can be probed easily, and the knowledge can then be transfered to adsorption reactions. The energy exchange between molecule and surface can be manifold: The molecule's momentum both perpendicular and parallel to the surface may increase or decrease. It may gain or loose translational energy from or to the surface. Even more importantly, it can exchange internal energy, which was stored inside its vibration or rotation, with degrees of freedom of the solid. Energy is gained or lost from the solid mainly in the form of

phonons, i.e. vibration of the regular array of atoms which constitute the solid.

In some cases, electronic excitation inside the solid is also involved in the energy transfer between molecules and the surface. An electron in the surface can gain energy in a surface scattering event such that it moves faster than other electrons, leaving behind a hole in the original velocity distribution of electrons. This process was believed to be negligible for a simple reason: Since the nuclei of both surface and molecule are much heavier than the electrons, they will move much slower. To a good approximation, one can therefore assume that the electrons adapt instantly to the slowly varying position of the nuclei. This decoupling of electronic and nuclear motion is commonly known as the Born-Oppenheimer approximation (BOA). Typically, only the vibrational and rotational energy spacing of a diatomic molecule is on the same order as the collision energy. Therefore only the nuclear degrees of freedom should matter in the collision with a surface, and electronic excitation or de-excitation should not happen. In recent years, however, increasing evidence has been found which indicates that this picture is incomplete. Many cases of the breakdown of the Born-Oppenheimer approximation relevant for surface scattering are now known [42]. One intriguing example of this occurs in the collision of vibrationally excited nitric oxide with a metal surface. Upon impact, part of the vibrational energy is converted to kinetic energy of an electron within the metal, such that the electron is ejected from the surface into vacuum [43, 44]. Even more surprisingly, this electron emission becomes more likely the slower the molecule approaches the surface [45]. It has been suggested that in the scattering event, vibrationally excited NO is negatively ionized [46, 47], such that electron emission in fact proceeds via this transient anionic state [45].

The situation is different if it is not only electronic degrees of freedom of the surface that are involved, but if the incident particle also is in an electronically excited state. Usually, the first electronically excited state of a molecule is several electron volts higher in energy than the ground state. Upon de-excitation, this energy can be transferred to the surface, and this often leads to ejection of an electron if the work function of the surface is sufficiently low. This process was discovered in 1924 [48] and has been extensively studied since the 1950's [49] for electronically excited atoms. In many cases it involves the exchange of electrons between the atom and the surface. Only a few studies have looked at the de-excitation of electronically excited molecules on surfaces. The collision of electronically excited CO, carrying 6 eV of energy, with a clean gold surface that has a workfunction of 5.3 eV, is a well-known example where electron emission is observed. This is the system which has been studied in detail within the research presented in this thesis. An important aspect is that, due to the exchange of charge and large amount of electronic energy involved, the electron emission process is not easily modeled by the method of DFT mentioned before.

This thesis describes in chapters 3–5 the design and characterization of a novel apparatus for molecule-surface scattering experiments. The apparatus combines a Stark decelerator, which is similar to the one built by Bethlem *et al.* [8], but more advanced in design, with a setup for scattering particles from a surface and detecting the scattered products. After reviewing a few of the properties of CO that are most important

for this work in chapter 2, a description of how the molecular beam is created will be given in chapter 3. Special emphasis is put on a sophisticated method that removes all unwanted species from the molecular beam. Chapter 4 deals with the design and characterization of the decelerator, highlighting the features that are necessary for mating it with the surface scattering part of the setup. This part of the apparatus, where the actual collisions to be studied take place, and which contains all of the important devices for surface diagnostics and manipulation, is introduced in chapter 5. In chapter 6, experiments are presented in which electronically excited CO collides with a well-defined gold surface whose work function is lower than the molecule's excitation energy, and the resulting emission of electrons is monitored. A detailed study is conducted to investigate to what extent additional vibrational excitation influences the ejection of electrons from the surface. In addition, the influence of surface temperature and velocity of incident molecules is investigated. An outlook of how the capabilities of the new apparatus will be used in the future is then given in chapter 7, along with a concise summary of this manuscript.

Chapter 2

Properties of Carbon Monoxide

Carbon monoxide, at standard temperature and pressure, is an odorless, transparent gas which becomes liquid at 81.7 K at a pressure of 1 bar. It occurs naturally in the atmosphere and is a common by-product of combustion processes. Due to its high abundance, it is one of the most important and also most studied diatomic molecules. Because it is a reactant in important processes like the Fischer-Tropsch synthesis and steam reforming, it has been in the focus of heterogeneous catalysis research for many decades. Since it has undesired toxic properties, noble metals like platinum are used in modern cars to catalyze its oxidation to CO_2.

In the electronic ground state, the bond between oxygen and carbon is closest to a triple bond [50, p. 3-93], which is easy to understand from the linear combination of atomic orbital (LCAO) approximation of molecular orbital theory. In the ground state the six electrons from carbon and eight electrons from oxygen occupy the lowest molecular orbitals resulting from the $1s$, $2s$, and $2p$ states of the atoms, i.e. the ground state is a $X^1\Sigma^+$ state with the configuration $(1s\sigma)^2(1s\sigma^\star)^2(2s\sigma)^2(2s\sigma^\star)^2(2p\pi)^4(2p\sigma)^2$. Since oxygen contributes four of the six bonding electrons, it is charged slightly positive despite it being more electronegative than carbon, which causes CO to have a small permanent electric dipole moment of 0.112 D [51].

In recent years, CO has been identified as a possible candidate molecule to measure the variation of fundamental constants, such as the ratio of proton to electron mass, with time. This is feasible for two reasons. CO is one of the few molecules which are observed in relatively high abundance in interstellar clouds, which makes it possible to obtain molecular spectra which represent snapshots from a long time ago (see, e.g. [52]). At the same time, it was demonstrated that molecular beams of CO may be effectively brought to standstill [53], which allows very long observation times. Thus, in principle molecular constants can be measured with very high precision, such that observing a time variation of level shifts on a laboratory timescale may become feasible [22, 23].

The first electronically excited state of CO, $a^3\Pi$, has an orbital configuration of $(1s\sigma)^2(1s\sigma^\star)^2(2s\sigma)^2(2s\sigma^\star)^2(2p\pi)^4(2p\sigma)^1(2p\pi^\star)^1$, and is from now on referred to as $CO^\star$. Its large dipole moment of 1.37 D [54], which points from the oxygen atom to the carbon atom, i.e. now the oxygen atom is negative, allows to manipulate $CO^\star$ in the laboratory by means of electric fields. Conveniently, the $a^3\Pi$ state is metastable, i.e. it has a long lifetime of 2.63 ms [10]. This is sufficiently long to use it in molecular beam experiments, where flight times of molecules are typically on the order of a few milliseconds. Moreover, since CO is available commercially in a bottle, intense

molecular beams of it can be easily realized. The structure of energy levels of CO* and its Stark effect will be briefly reviewed in this chapter, based on references [55–58].

2.1 Energy Levels of Carbon Monoxide

The total Hamiltonian for a diatomic molecule like CO can be split up into different terms accounting for the coupling of according angular momenta, and is given by (see, e.g., reference [59], which treats the Λ-doubling term separately):

$$\hat{H} = \hat{H}_{\mathrm{ev}} + \hat{H}_{\mathrm{rot}} + \hat{H}_{\mathrm{SO}} + \hat{H}_{\mathrm{SS}} + \hat{H}_{\mathrm{SR}} + \hat{H}_{\mathrm{LD}} \,. \tag{2.1}$$

The different terms, in order of appearance, are the electronic-vibrational, rotational, spin-orbit, spin-spin, spin-rotation, and the so-called Λ-doubling Hamiltonian. A detailed description of how the individual terms are calculated from the relations that will be defined in Eq. (2.3) for CO* using tensor algebra is given in reference [57]. Here, only the most important aspects are briefly discussed.

The two main contributions come from the vibronic term $\hat{H}_{\mathrm{ev}}$ and the rotational Hamiltonian $\hat{H}_{\mathrm{rot}}$. Let us first consider the effect of vibration. The eigenvalues of the purely vibrational Hamiltonian can be derived from first principles, in analogy to the quantum mechanical harmonic oscillator. Energies resulting from such a procedure are usually represented as [56]

$$G(v) \equiv \frac{E_{\mathrm{vib}}(v)}{hc} = \omega_e(v+1/2) - \omega_e x_e (v+1/2)^2 \,, \tag{2.2}$$

where $\omega_e = \frac{h\nu_{osc}}{hc}$ is the frequency of the harmonic oscillator converted to energy in wavenumbers, and the term with the constant $\omega_e x_e \ll \omega_e$ represents a correction for anharmonic oscillation. Eigenfunctions of the vibrational Hamiltonian are in first approximation given by the well-known wavefunctions of the harmonic oscillator, $|v\rangle$, which can be found in elementary textbooks of quantum mechanics, e.g. in reference [60]. Unless explicitly needed, the vibrational quantum number v will be omitted from the label of the wavefunction. Typical values of the relevant constants for CO are [61] $\omega_e(X^1\Sigma^+) = 2169.8\,\mathrm{cm}^{-1}$, $\omega_e(a^3\Pi) = 1743.4\,\mathrm{cm}^{-1}$, $\omega_e(e^3\Sigma^-) = 1117.7\,\mathrm{cm}^{-1}$, and $\omega_e(b^3\Sigma^+) = 2199.3\,\mathrm{cm}^{-1}$, while $\omega_e x_e$ is usually in the range of 10–12 cm^{-1}.

In order to calculate the eigenvalues of the rotational Hamiltonian, one first has to determine an appropriate basis set in which to describe its eigenstates. The best choice for a basis depends on how strongly the different angular momenta in a diatomic molecule precess about each other, and determines an order in which these angular momenta can be added to simplify the problem of angular momentum coupling. When calculating the energy levels of CO in the $a^3\Pi$ state, it is appropriate to use Hund's case (a) [62] to express eigenstates of the Hamiltonian. For a molecule like CO, which contains no atoms with nuclear spin for the most abundant isotopomer $^{12}C^{16}O$, the relevant angular momenta are the total electronic angular momentum, **L**; the total electronic spin, **S**; the total angular momentum, **J**; the angular momentum

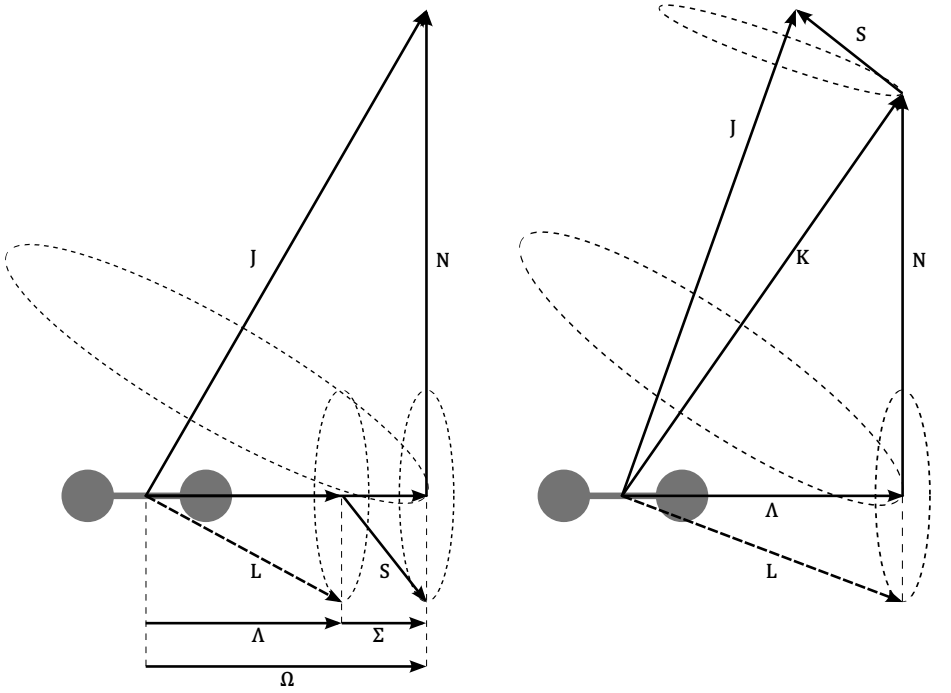

(a) Hund's case (a).

(b) Hund's case (b).

Figure 2.1: Coupling of angular momenta in Hund's cases (a) and (b). See text for details.

of rotation of the nuclear framework, **N**; and the total angular momentum exclusive electron spin, $\mathbf{K} \equiv \mathbf{J} - \mathbf{S}$, following the notation of Herzberg [56].

In Hund's case (a), **L** couples strongly to the internuclear axis, such that its projection onto this axis, $\mathbf{L}_z$, is at all times well-defined. Furthermore, spin-orbit coupling is strong enough to couple the total electronic spin to **L**, such that its projection onto the internuclear axis, $\mathbf{S}_z$, is also well-defined, and addition of both projections yields the projection of J, $\mathbf{L}_z + \mathbf{S}_z = \mathbf{J}_z$, onto the nuclear axis. As the coupling of **L** to the internuclear axis is very strong, the total electronic angular momentum itself is ill-defined in Hund's case (a) [55, chapter 3.2]. For the other angular momenta and their projections, the quantum numbers J, S, Ω, Λ, and Σ can be defined as eigenvalues of

the corresponding operators:

$$\begin{aligned}
\mathbf{J}^2 \left|JS\Omega\Lambda\Sigma M\right\rangle &= J(J+1) \left|JS\Omega\Lambda\Sigma M\right\rangle \\
\mathbf{S}^2 \left|JS\Omega\Lambda\Sigma M\right\rangle &= S(S+1) \left|JS\Omega\Lambda\Sigma M\right\rangle \\
\mathbf{J}_z \left|JS\Omega\Lambda\Sigma M\right\rangle &= \Omega \left|JS\Omega\Lambda\Sigma M\right\rangle \\
\mathbf{L}_z \left|JS\Omega\Lambda\Sigma M\right\rangle &= \Lambda \left|JS\Omega\Lambda\Sigma M\right\rangle \\
\mathbf{S}_z \left|JS\Omega\Lambda\Sigma M\right\rangle &= \Sigma \left|JS\Omega\Lambda\Sigma M\right\rangle \\
\mathbf{J}_Z \left|JS\Omega\Lambda\Sigma M\right\rangle &= M \left|JS\Omega\Lambda\Sigma M\right\rangle \,.
\end{aligned} \tag{2.3}$$

Here, wavefunctions are given in Dirac bra-ket notation and labeled according to their good quantum numbers. In addition to the projections onto the internuclear axis discussed above, the projection of $\mathbf{J}$ onto the *space*-fixed axis Z, $\mathbf{J}_Z$, is also included, which will be important once the molecule is exposed to an external electric field, and whose quantum number is labeled M. The quantum numbers defined in this way will only take on values which conform to the basic couplings of Hund's case (a), i.e. $\Sigma = -S, \ldots, +S$, $M = -J, \ldots, J$, and $\Omega = |\Lambda + \Sigma|$. At the same time, $J = \Omega, \Omega+1, \Omega+2, \ldots$ will by convention only take on positive values. A problem arising from the chosen basis functions is that their parity is not defined, i.e. they are not eigenfunctions of the inversion operator, which reverses direction of the projections $\mathbf{J}_z$, $\mathbf{L}_z$, and $\mathbf{S}_z$. Definite parity functions can be defined by symmetrizing the wavefunction:

$$\left|JS\Omega\Lambda\Sigma M\pm\right\rangle \equiv \frac{1}{\sqrt{2}} \left(\left|JS\Omega\Lambda\Sigma M\right\rangle \pm (-1)^{J-S} \left|JS\Omega - \Lambda - \Sigma M\right\rangle \right) . \tag{2.4}$$

Unless an external field is applied or electronic states are perturbed, states of different parity will be degenerate. Once the degeneracy is lifted, the result will be that every J-level is split in two states with opposite parity.

To calculate its rotational energy levels, a diatomic molecule may to good approximation be treated as a nonrigid rotor, with the moment of inertia I_B along an axis perpendicular to the internuclear axis. Its energy for a given total angular momentum J, in analogy to a classical nonrigid rotor, is given by [56]

$$F(J) \equiv \frac{E_{\text{rot}}(J)}{hc} = B_v J(J+1) - D_v J^2 (J+1)^2 \,. \tag{2.5}$$

Here, $B_v = B_e - \alpha_e(v+1/2)$ is the rotational constant of a rigid rotor corrected for the vibration of the molecule; $B_e \equiv \frac{h}{8\pi^2 c I_B} \approx 1 - 2\,\text{cm}^{-1}$ is the equilibrium rotational constant for the non-vibrating molecule, and the term lead by $\alpha_e \approx 10^{-2}\,\text{cm}^{-1}$ is the vibrational correction factor. Similarly, $D_v = D_e - \beta_e(v+1/2)$ is correcting for the fact that the rotor is nonrigid, i.e. it accounts for centrifugal distortions of the molecule. D_e is on the order of $6 \times 10^{-6}\,\text{cm}^{-1}$. As $\beta_e \ll D_e$, the correction is often neglected and D_e used instead of D_v. The rotational constant about an axis is proportional to the inverse of the corresponding moment of inertia. It is crucial to realize that in fact,

a diatomic molecule is not a nonrigid rotor, but instead a symmetric top, where the moment of inertia, I_A, about the internuclear axis is caused by the electron cloud and therefore is much smaller. In analogy with Eq. (2.5), the energy of rotation may be written as [56, p. 220]

$$\tilde{F}(J) \equiv \frac{\tilde{E}_{\mathrm{rot}}(v)}{hc} \approx B_e \left[J(J+1) - \Omega^2 \right] + A_{\mathrm{rot}} \Omega^2 \,, \tag{2.6}$$

with the rotational constant $A_{\mathrm{rot}} \gg B_e$. Since typically, the lowest values for A_{rot} are on the order of $5 \times 10^5\,\mathrm{cm}^{-1}$, the spacing introduced by A_{rot} is much larger than vibration. Therefore, this part of the rotational Hamiltonian is usually split off and combined with vibration into the electronic-vibrational term $\hat{H}_{\mathrm{ev}}$. It gives rise to the individual electronic states, designated by the term symbol ${}^{2S+1}\Lambda_\Omega$, where $\Lambda = 0, 1, 2 \ldots$ is denoted by the symbol $\Sigma, \Pi, \Delta, \ldots$ by convention.

The spin-orbit component $\hat{H}_{\mathrm{SO}}$ of the Hamiltonian causes states with nonzero Λ and S to split into $2S+1$ states. Since the splitting is proportional to $A_{\mathrm{SO}} \times \Lambda\Omega$, with a value of the spin-orbit constant of $A_{\mathrm{SO}}(a^3\Pi) \approx 41\,\mathrm{cm}^{-1}$ [59], it is larger than the rotational spacing. Thus, an electronic ${}^3\Pi$ state with $\Lambda = \Sigma = 1$ is split up into three spin manifolds, which are commonly labeled either as F_1, F_2, and F_3, or simply by their value of Ω. Each of these Ω manifolds will feature its own ladder of rotational levels.

The spin-spin and spin-rotation Hamiltonians, $\hat{H}_{\mathrm{SS}}$ and $\hat{H}_{\mathrm{SR}}$, only lead to small corrections. For a fixed spin S, the spin-spin interaction between different electrons introduces a level shift of the different Ω manifolds proportional to $C_{\mathrm{SS}} \times 3\Sigma^2$, where the spin-spin constant is $C_{\mathrm{SS}} \approx 1.7 \times 10^{-2}\,\mathrm{cm}^{-1}$. The coupling between electronic spin and nuclear framework rotation has a similar order of magnitude (the associated constant has a value of $1.4 \times 10^{-2}\,\mathrm{cm}^{-1}$) and introduces level shifts which depend on J, S, Σ, and Ω.
More important is the the term $\hat{H}_{\mathrm{LD}}$, which is not strictly speaking a correction of a single electronic state, but rather results from perturbation of a Π state by a different electronic Σ state. The effect is to split levels of different parity, which are otherwise degenerate, by the so-called Λ-doubling. In the case of CO ($a^3\Pi_{\Omega=1}(v=0, J=1)$), the two states of different parity are split by 394 MHz. Values for all constants, except the ones explicitly cited, are from reference [59].

When other states of CO, like the higher-lying ${}^3\Sigma$ states, are concerned, it is more common to use a Hund's case (b) basis set to label the energy levels. In this description, which is summarized here following reference [56], $\mathbf{S}$ does not couple to the internuclear axis at all, while $\mathbf{L}_z$ is well defined. As a result, $\mathbf{L}_z$ and $\mathbf{N}$ couple to the angular momentum, $\mathbf{K} = \mathbf{L}_z + \mathbf{N}$, with associated quantum number K, which subsequently couples with the spin to yield the total angular momentum, $\mathbf{J} = \mathbf{K} + \mathbf{S}$. For Σ states, this scheme represents an obvious choice for the basis set, since the spin can only couple to the internuclear axis by first coupling to $\mathbf{L}$. In principle, vibrational structure does not change, but a few changes arise for rotation. Possible values of the total angular momentum are now $J = K+S, K+S-1, \ldots, |K-S|$, except for $K = 0$

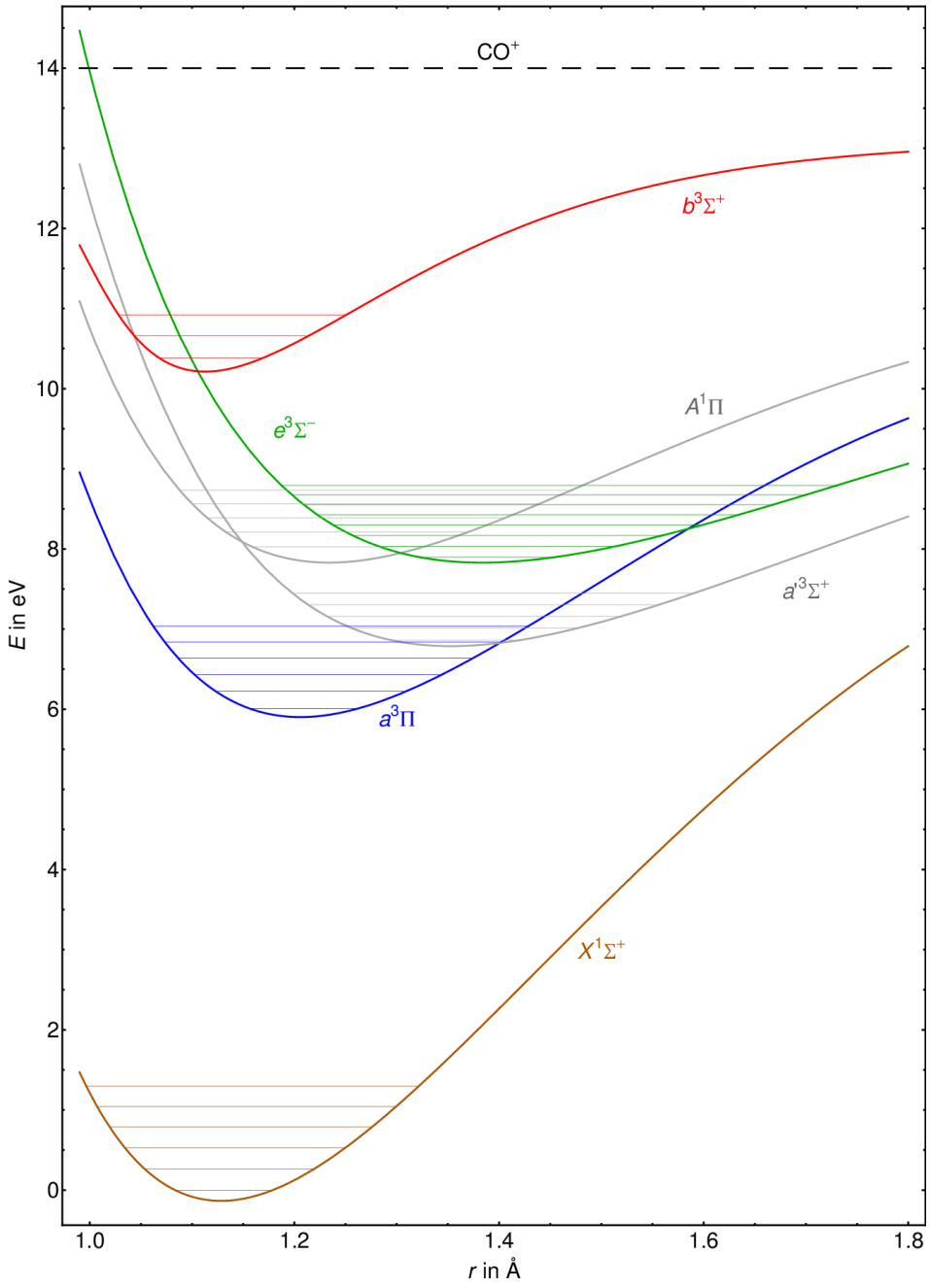

Figure 2.2: Energy diagram of CO. Vibrational levels are calculated using constants from references [61, 63]. Potential curves are calculated using the LEVEL program [64].

where, of course, only $J = S$ occurs. Energy levels will therefore occur in groups of $2S + 1$. The electronic ground state, $X^1\Sigma^+$, will thus only have single rotational levels, whereas in the higher-lying $^3\Sigma^\pm$ states, rotational levels with $K > 0$ come in groups of three, each group being labeled by its respective $K = N$ value. States within a group are often labeled F_1,F_2,and F_3 according to whether J has the value $K + 1$, K, or $K - 1$. The parity of each rotational level depends on K, and is given by $\pm(-1)^K$ within a $\Sigma^\pm$ state. The lowest-lying energy levels of both the $a^3\Pi$ state and the $b^3\Sigma^+$ state are shown in Fig. 6.12 on page 121 of chapter 6. For singlet states, like the $X^1\Sigma^+$ ground state of CO, the choice of Hund's case (a) or (b) is identical since they only differ in the way **S** couples. An overview of all the electronic states of CO relevant to this work is shown in Fig. 2.2.

2.2 Stark Effect of CO*

As it passes through the apparatus described in this thesis, CO* is manipulated by means of large, inhomogeneous electric fields. In this section, the effects of an electric field on the energy levels of CO in its $a^3\Pi_1(v = 0, J = 1)$ state are explained. The Hamilton operator of an external electric field is given by $\hat{H}_{\text{st}} = -\boldsymbol{\mu} \cdot \boldsymbol{\mathcal{E}} = -\mu\mathcal{E}\cos(\alpha)$, where $\boldsymbol{\mu}$ is the vector of the permanent dipole moment which points from negative to positive charge, and α is the angle between the dipole moment and the external electric field. Because the dipole moment is fixed to the internuclear axis of the molecule, whereas the electric field is defined to be fixed to the space-fixed Z-axis in the laboratory frame, the symmetry of $\hat{H}_{\text{st}}$ is exactly the same as in the common case of electromagnetic radiation interacting with a molecule in the dipole approximation. Consequently, the same selection rules have to be obeyed when the coupling between different states is calculated. More specifically, matrix elements of $\hat{H}_{\text{st}}$ are only nonzero for $\Delta J = 0, \pm 1$, $\Delta M = 0$, and $\Delta\Omega = 0$. In addition, only states of different parity are coupled for $\Delta J = 0$, while two states with $\Delta J = \pm 1$ only mix if their parity is the same. Nonzero matrix elements are given by [58, 65, 66]:

$$\langle J, M\Omega\pm|\, \hat{H}_{\text{st}}\, |J, M\Omega\mp\rangle = -\mu\mathcal{E}\frac{M\Omega}{J(J+1)} = \mu_{\text{eff}} \times \mathcal{E}\ , \tag{2.7}$$

$$\langle J, M\Omega\pm|\, \hat{H}_{\text{st}}\, |J+1, M\Omega\pm\rangle = -\frac{\mu\mathcal{E}}{J+1}\sqrt{\frac{((J+1)^2-\Omega^2)\,((J+1)^2-M^2)}{(2J+1)(2J+3)}}\ , \tag{2.8}$$

where $\mu_{\text{eff}} = M\Omega/(J(J+1))$ is the so-called *effective* dipole moment of a state. As a consequence, the first states to couple are the two components of the Λ-doublet, split by the Λ-doubling $E_\Lambda = 394\,\text{MHz}$, which comprise the $J = 1$ state. When the external field strength is small enough such that these matrix elements are much smaller than the spacing between the $J = 1$ and the $J = 2$ level, it is sufficient to use the approximate (2×2) Hamiltonian

$$\hat{H}_{\text{st},\Lambda} = \begin{pmatrix} E_\Lambda/2 & -\mu_{\text{eff}}\mathcal{E} \\ -\mu_{\text{eff}}\mathcal{E} & -E_\Lambda/2 \end{pmatrix}\ . \tag{2.9}$$

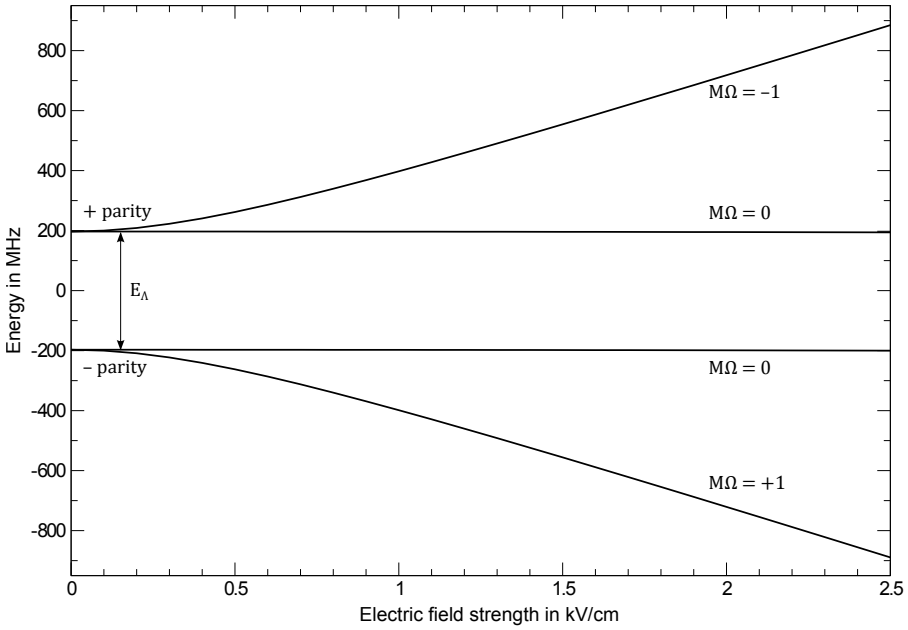

Figure 2.3: Stark effect of CO at low electric field strength. The region where the Stark effect deviates considerably from a linear curve extends over the first 0.75 kV/cm.

The eigenvalues are readily calculated as

$$W_{\mathrm{st},\pm} = \pm\sqrt{(E_\Lambda/2)^2 + (\mu_{\mathrm{eff}}\mathcal{E})^2}\,. \tag{2.10}$$

For very low field strengths, $\mu_{\mathrm{eff}}\mathcal{E}/E_\Lambda \ll 1$ holds, and $W_{\mathrm{st},\pm}$ is approximately quadratic in the electric field strength. For intermediate field strengths, where $\Delta E(J=1, J=2) \gg \mu_{\mathrm{eff}}\mathcal{E}/E_\Lambda \gg 1$, the Stark effect is linear in $\mathcal{E}$.

The Stark effect of CO $a^3\Pi_1(v=0, J=1)$ is shown in Fig. 2.3. Each parity component of the Λ-doublet splits up in two states, one with $M=0$ which is not influenced by the electric field, and one with $M \neq 0$, which decreases with electric field strength for the lower $-$ parity component, and increases for the $+$ parity level. In the latter case, the potential energy of a molecule increases as it is exposed to the external electric field. Since a particle always tries to minimize its energy in an external potential, a molecule in such a quantum state is called *low*-field seeking. In contrast, the potential energy of a molecule in the lower $-$ parity state decreases with increasing field strength. It therefore experiences a force towards higher field strength and is called *high*-field seeking.

When the magnitude of matrix elements in Eq. (2.8) becomes appreciable compared to the rotational spacing, the Stark energy cannot be calculated by a simple analytical formula any more. The reason for this is that $\hat{H}_{\mathrm{st}}$ is block-diagonal with all matrix

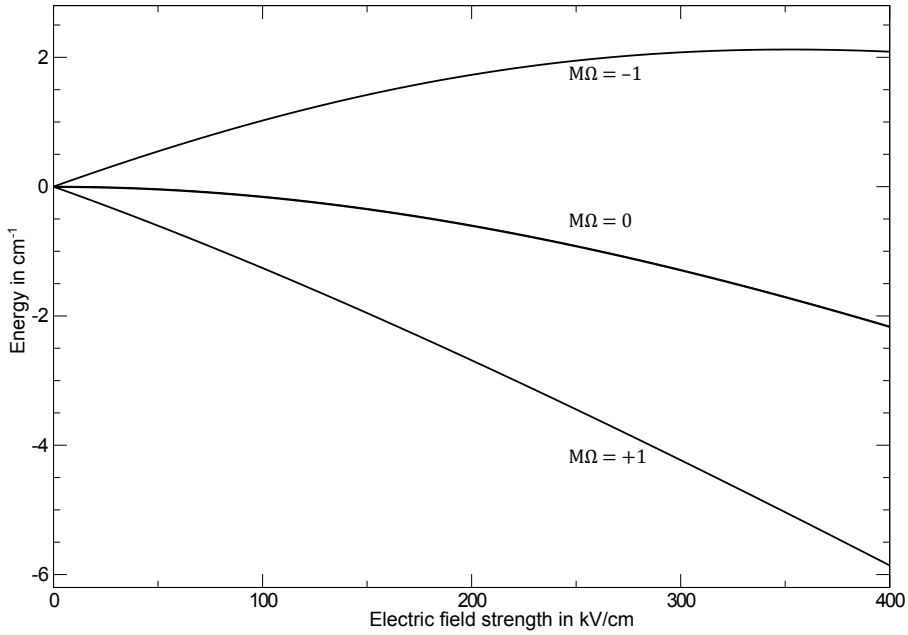

Figure 2.4: Stark effect of CO at high electric field strength. Due to interactions with higher J states, the Stark energy of the low field seeking component starts to decrease again at high electric field strength. It deviates from the linear behavior by more than 10 % at field strengths of about 90 kV/cm.

elements connecting states with J and $J+1$ populated. In principle, calculation of the Stark energy thus requires the eigenvalues for an infinitely large matrix to be found. Practically, one can cut this matrix at a sufficiently large value of J, and solve for the eigenvalues numerically, keeping track of parity such that levels can be sorted in the right order. For the calculations and simulations presented in later chapters, use was made of numerical calculations of the Stark effect of CO performed by Samuel A. Meek [57] and earlier work by Rienk T. Jongma [58]. The Stark effect at higher field strengths is shown in Fig. 2.4. As early as $\mathcal{E} = 100\,\mathrm{kV/cm}$, the Stark energy is seen to reach only 88 % of the value predicted by the linear dependence given in Eq. (2.7), and at 150 kV/cm and 200 kV/cm, this value decreases to 82 % and 75 %, respectively.

Chapter 3

Background-Gas free Molecular Beams

One of the main objectives of the apparatus designed for the project described in this thesis is to produce short, quantum-state pure, energy-tunable pulses of molecules for subsequent surface scattering. This chapter describes the techniques employed and the experimental means involved in obtaining a background-gas free, quantum-state pure beam of metastable CO, while chapter 4 will give details on how the velocity of the beam is varied.

3.1 Supersonic Molecular Beams

As a starting point of any molecular or atomic beam experiment, one has to inject the species of interest into the vacuum chambers of the machine. Various approaches to making a molecular beam exist [67]. For the purpose of this experiment, a slow and intense beam is desired which has a large fraction of its population in the rovibrational ground state. Moreover, both the decelerator and many of the detection schemes are intrinsically operated in a pulsed fashion. Using a pulsed molecular beam has the advantage of reducing the load on the turbomolecular pumps. This effectively allows to use a higher number of molecules per unit of time compared to a continuous beam. The most convenient approach is therefore to generate a supersonic expansion of CO in a heavy carrier gas at a repetition rate of 10 Hz.

As an intense, cold molecular beam is crucial for the success of the experiment, it is beneficial to recapitulate the underlying physical processes. Since it is a research area on its own, however, only the aspects most relevant for the experimentalist will be discussed here; a detailed description can be found in reference [67].

When one mole of an ideal gas at pressure $p_0 \approx 1$ bar from a reservoir at temperature T_0 adiabatically expands through a small orifice into a region of lower pressure $p_1 \approx 0$ bar, it will cool down to the new temperature T_1. In the course of this expansion, which is supersonic if the pressure gradient is sufficiently high, enthalpy is converted to kinetic energy: $-\Delta H = {}^1/_2\, M v^2$, M being the molar mass. The so-called terminal velocity, which is the maximum velocity obtained when converting all enthalpy to kinetic energy, can be shown to be [67, p. 17]

$$v_t = \sqrt{2C_p \frac{T_0}{M}} = \sqrt{2R\left(\frac{\gamma}{\gamma - 1}\right)\frac{T_0}{M}}\,, \tag{3.1}$$

where C_p is the molar heat capacity at constant pressure, R the universal gas constant, and γ denotes the adiabatic coefficient. For an ideal gas with f degrees of freedom, $\gamma = \frac{f+2}{f}$, thus the values relevant for this work are $\gamma(\mathrm{Ar}, \mathrm{Xe}) = 5/3$ and $\gamma(\mathrm{CO}) = 7/5$. Both C_p and γ are assumed to be independent of temperature. When a mixture of two species is co-expanded, Eq. (3.1) becomes

$$v_t = \sqrt{2\bar{C}_p T_0 / \bar{M}}\,, \tag{3.2}$$

where $\bar{M} = \sum_i X_i M_i$ and $\bar{C}_p = \sum_i X_i C_{p,i}$ are the average of molar mass and heat capacity of the constituents, respectively, weighted by their mole fractions X_i. An important consequence of Eq. (3.2) is that the maximum beam velocity will decrease as the nozzle temperature is decreased and the molar mass of the gas used increases.

For the case of ideal gases and perfectly adiabatic expansion, two more important relations may be derived, relating final and initial pressure and number densities n_0, n_1 to final and initial temperature [67, p. 18]:

$$(p_1/p_0) = (T_1/T_0)^{\gamma/(\gamma-1)} \tag{3.3}$$

$$\Rightarrow T_1 = T_0 (p_1/p_0)^{(\gamma-1)/\gamma} \tag{3.4}$$

$$(n_1/n_0) = (T_1/T_0)^{1/(\gamma-1)} \tag{3.5}$$

$$\Rightarrow n_1 = n_0 (p_1/p_0)^{1/\gamma} = p_0/(k_B T_0)(p_1/p_0)^{1/\gamma}\,. \tag{3.6}$$

For the work presented here, two different sets of conditions are employed: A mixture of 20 % CO and 80 % of either Ar or Xe is expanded at an absolute pressure of 1.0 bar into vacuum, from a pulsed valve cooled to 101 K and 260 K, respectively. Results of applying this simple model to typical experimental conditions are shown in table 3.1. Several aspects are noteworthy when interpreting these numbers. Most

	20 %CO, 80 %Ar	20 %CO, 80 %Xe
CO partial stagnation pressure (p_0)	0.2 bar	0.2 bar
stagnation temperature (T_0)	101 K	260 K
terminal velocity (v_t)	357 m/s	328 m/s
final temperature (T_1)	0.5 K	1.3 K
initial density (n_0)	$1.4 \times 10^{19}\,\mathrm{cm}^{-3}$	$5.6 \times 10^{19}\,\mathrm{cm}^{-3}$
final density (n_1)	$2.8 \times 10^{13}\,\mathrm{cm}^{-3}$	$1.1 \times 10^{13}\,\mathrm{cm}^{-3}$

Table 3.1: Calculated key parameters of the molecular beams used in the experiment. A final pressure of $p_1 = 1 \times 10^{-5}$ mbar is assumed in the calculation.

important, both cases listed create beams of about 360 m/s final velocity in the real experiment, which agrees well with the model for the Ar seeded beam, but is somewhat higher than expected for Xe. A more detailed comparison of calculated and experimentally observed terminal velocities in supersonic expansion of CO can be

found in reference [57]. The final longitudinal temperature of the beam, estimated from the width of the velocity distribution determined from time-of-flight profiles, is on the order of 1 K, which agrees well with the model. Values for the final CO density are calculated for a final pressure of $p_1 = 1 \times 10^{-5}$ mbar, which corresponds to the equilibrium pressure determined by a cold cathode gauge in the source chamber. The actual peak pressure directly after the nozzle has opened is most likely higher than the time-averaged pressure displayed by the gauge, resulting in higher densities. Typical values for the density are estimated to be about $1 \times 10^{14}\,\mathrm{cm}^{-3}$, which is somewhat higher than the calculated values. Also, the experimentally determined $CO^{\star}$ signal intensity is higher when using Xe instead of Ar, in contrast to the calculated values. Note that CO might also form clusters with rare gases, an effect which will be more pronounced for heavier seed gases. In addition, the lighter component of a mixture of two gas species will spread out more in the transverse direction, such that the fraction of the beam passing through the skimmer will favor the heavier gas [67]. This effect is also called mass-focusing. Both of these effects have been neglected in the above considerations.

It is important to realize that the final temperature, T_1, calculated in the simple model only describes the *translational* temperature, i.e. it serves as a means to characterize the velocity spread of the beam in the forward direction. As molecules are undergoing a limited number of collisions, cooling of internal degrees of freedom is never perfect, and the efficiency for cooling of different degrees of freedom depends on the cross-section for the corresponding collisions. As a result, translational, rotational, and vibrational temperatures usually obey the relation $T_{\parallel} < T_{rot} < T_{vib}$. Typical values obtained in our group are $T_{rot} \approx 5\,\mathrm{K}$ and $T_{vib} \approx 50\,\mathrm{K}$.

3.1.1 Molecular Beam Production

For the production of cold supersonic beams, a pulsed solenoid valve (*Parker-Hannifin* General valve 99S4-A2-P2-99B08, PCTFE poppet, 0.76 mm orifice with cone) is used which has been modified in the following way: the tension of the main spring can be controlled from outside the vacuum by means of a micrometer which is pressing directly against the back of the main spring, thus controlling the force which acts on the poppet closing the nozzle orifice. This allows operation of the spring under optimum conditions for a large temperature range. Moreover, the body of the valve is embedded in a copper block which is equipped with inlet and outlet for cooling or heating of the valve. For typical experiments, a mixture of 20 % CO in Ar or Xe at a backing pressure of 1 bar is expanded at a valve temperature of 101 K and 260 K, respectively. The valve is cooled by a flow of dry nitrogen which first passes through a copper coil immersed in liquid nitrogen, thus reaching temperatures just above 77 K, and subsequently passes an in-line electrical resistance heater before reaching the nozzle. The temperature of the nozzle front plate is measured by a type K thermocouple and fed to the input of a PID controller (*Eurotherm* 2408), whose output is used to control the power of the in-line heater. The CO/rare gas supply system can be evacuated by a small diaphragm pump (*Pfeiffer* MVP 015-2, 0.25 l/s).

The nozzle can be mounted in one of two special flanges, which can be accurately attached to the source chamber by means of two alignment pins, thus simplifying the nozzle alignment. While one flange is used to center the valve relative to the source chamber, the second flange mounts the nozzle offset from the center at an angle of 3.5°.

As molecules in the expansion travel faster than the local speed of sound, it is important to realize that they undergo basically no collisions in late stages of the expansion. By introducing obstacles, such as walls equipped with orifices for differential pumping, into the beam, particles will scatter off the wall and subsequently may collide with molecules about to pass through the orifice. This unwanted effect can be reduced by shaping the orifices to reduce backscattering into the beam, most commonly realized by means of a so-called skimmer. It has the shape of a curved cone with the tip cut off such that the sharp edges extend nearly parallel to the beam direction, minimizing the obstruction of the molecular beam. As will be shown in section 4.4.4 (p.70), the intensity of the beam may suffer significant losses even when a rounded orifice is inserted into a previously skimmed beam as far as 180 mm downstream of the nozzle.

Being operated at a repetition rate of 10 Hz, the nozzle produces pulses of rotationally and vibrationally cold CO with a duration of approximately 100 µs. A skimmer (*Beam Dynamics, Inc.* Model 2, Nickel), located 30 mm downstream from the nozzle, cuts out the central part of the molecular beam, and permits it to pass into the hexapole section of the setup. Two skimmers of 2.0 mm and 1.5 mm diameter have been mounted and aligned on two different supports, one of which centers its skimmer relative to the source and hexapole chamber, while the other one centers the skimmer on an axis tilted by 3.5 °, thus centering it with respect to the tilted nozzle setup.

3.2 Focusing Neutral Polar Molecules with Electric Fields

When a molecule possessing a permanent electric dipole moment is subject to an external electric field, $\boldsymbol{\mathcal{E}}(\mathbf{r})$, its energy levels are shifted by the Stark energy, $W(\mathcal{E})$, with respect to the field free situation. As a result, there will be a force

$$\begin{aligned}\mathbf{F}(\mathbf{r}) &= -\nabla W(\mathcal{E}(\mathbf{r})) \\ &= \mu_{\text{eff}} \nabla |\boldsymbol{\mathcal{E}}(\mathbf{r})| \,, \end{aligned} \tag{3.7}$$

acting on the molecule. Here, $\mathcal{E} \equiv |\boldsymbol{\mathcal{E}}(\mathbf{r})|$ is the absolute value of the electric field strength, and $\mu_{\text{eff}} \equiv -\mathrm{d}W/\mathrm{d}\mathcal{E}$ is the effective electric dipole moment introduced earlier in section 2.2. If $\boldsymbol{\mathcal{E}}(\mathbf{r})$ is uniform, the resulting force will be zero, but a torque will align the molecule with respect to the electric field. For an inhomogeneous electric field, however, the molecule will experience a force towards a region either of high or of low electric field strength, depending on whether it is in a high-field seeking ($\mu_{\text{eff}} > 0$) or low-field seeking ($\mu_{\text{eff}} < 0$) quantum state. The classical analogue to a high-field seeking (low-field-seeking) state is an electric dipole which is oriented parallel (anti-parallel) to the electric field, which is energetically favorable (unfavorable).

The following sections will give an overview of how one can exploit the forces acting on molecules in inhomogeneous electric fields to manipulate the motion of molecules using both static and time-dependent electric fields.

Electrostatic and magnetostatic fields have been used to manipulate the trajectories of both charged and neutral particles for a long time. For neutral species, Stern and Gerlach first demonstrated the use of an inhomogeneous magnetic field to split up a beam of neutral silver atoms into its spin components [68, 69]. In particular, state-selected beams of neutral dipolar molecules have been successfully produced using electrostatic quadrupole [70–72] and hexapole [73, 74] focusing devices, some of them combined with beam stops on the main axis to block the unfocused part of the beam. In general, the electric potential, Φ, of an ideal two-dimensional multipole of order $2n$ is given in planar spherical coordinates r and φ by [75]:

$$\begin{aligned}
&\Phi(r,\varphi) = \Phi_0 \left(\frac{r}{r_0}\right)^n \cos n\varphi \\
\Rightarrow\ &\boldsymbol{\mathcal{E}}(r,\varphi) = (\mathcal{E}_r, \mathcal{E}_\varphi) = -\nabla\Phi = \frac{\Phi_0 n}{r_0}\left(\frac{r}{r_0}\right)^{n-1}(-\cos n\varphi, \sin n\varphi) \\
\Rightarrow\ &\mathcal{E}(r,\varphi) = |\boldsymbol{\mathcal{E}}(r,\varphi)| = \Phi_0 \frac{n\, r^{n-1}}{r_0^n} \propto r^{n-1}\,,
\end{aligned} \tag{3.8}$$

with Φ_0 and r_0 being defined via the boundary condition $\Phi(r = r_0, \varphi) = \Phi_0 \cos n\varphi$. A linear restoring force towards the center axis of the multipole device is desired for perfect focusing. The potential of a particle in the focusing device should therefore be proportional to r^2. For a molecule whose Stark effect is linear, $W(\mathcal{E}) \propto \mathcal{E}$, this means that one should use $n = 3$, i.e. a hexapole focuser. Eq. (3.8) then becomes:

$$\begin{aligned}
\Rightarrow\ &\boldsymbol{\mathcal{E}}(r,\varphi) = \frac{3\Phi_0}{r_0^3} r^2 (-\cos 3\varphi, \sin 3\varphi) \\
\Rightarrow\ &\mathcal{E}(r,\varphi) = \frac{3\,\Phi_0}{r_0^3} r^2 \propto r^2\,.
\end{aligned} \tag{3.9}$$

The exact electric potential in Eq. (3.8) can be created by 6 hyperbolically shaped electrodes [76], but it is more convenient to use cylindrical rods, which will only slightly distort the electric field. No analytic solution for the potential created by 6 rods arranged symmetrically about the origin is known. However, it has been shown [77] that the fields are least distorted compared to the ideal multipole if the rod radius, ρ, is chosen such that it is slightly bigger than half the inner radius, r_0, of the hexapole, namely, $\rho = 0.565 r_0$. For trajectory calculations, the field of the hexapole has been numerically calculated using a finite element program [78] in two dimensions; fringe fields at beginning and end have been neglected. The magnitude of this calculated field strength is depicted in Fig. 3.1.

For efficient spatial focusing of CO by a hexapole, two main issues have to be overcome: First, the population in the metastable state of CO decays exponentially with time. Thus, the hexapole needs to be short to avoid losses due to a long transit time

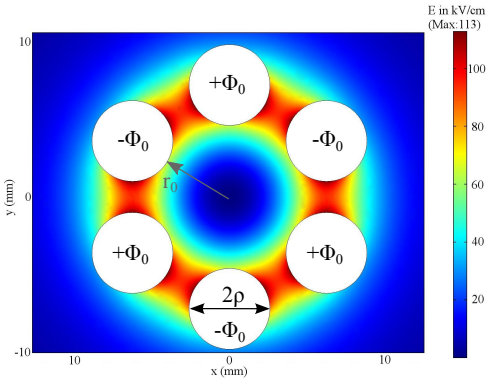

Figure 3.1: Numerically calculated magnitude of the electric field strength in a planar cut through the hexapole for $\Phi_0 = 10\,\mathrm{kV}$, $\rho = 2.6\,\mathrm{mm}$, $r_0 = 4.6\,\mathrm{mm}$.

of the molecules. In addition, the focus obtained for $CO^\star$ is not just an image of the inbound molecules, but instead is blurred. This effect can be understood from the following argument: $CO^\star$ molecules passing close to and roughly parallel to the center axis of the hexapole never sample a region of high electric field strength. Due to the Λ-doubling in the metastable state, the Stark effect at low field strength is quadratic and therefore weak, and the potential is not harmonic. As a result, the central and most intense part of the beam experiences only a very small focusing effect.

In order to counteract these problems, an improved hexapole has been designed which is used in a rather uncommon fashion. The operating voltage is increased as described in the next section, and a focusing and deflection scheme is used which exploits the higher field strength far away from the axis of symmetry. When a molecule in a quantum state with a linear Stark shift enters an ideal electric hexapole field, it will start to perform sinusoidal oscillations in the transverse direction. As a consequence, a hexapole focuser acts on polar molecules of constant velocity in the same way in which an optical lens acts on light: For an extended object located at exactly twice the focal length away, an optical lens will create an image of original size, but flipped about the main optical axis, at equal distance behind the focal plane. Similarly, the image of an object which is further away will be reduced in size and focused to a plane that is closer to and behind the lens. In analogy, the hexapole focuser, whose focal length is adjustable by varying either the voltage applied to the electrodes or the time that the electrodes are switched on, will image the transverse distribution of molecules exiting the nozzle onto a plane behind the device.

For the focusing of molecules, the hexapole is arranged collinear with the molecular beam axis. Deflection of molecules by a certain angle in addition to focusing can be achieved by mounting the nozzle offset with respect to the main symmetry axis of the hexapole, such that molecules enter the hexapole preferentially on one side and are deflected towards the center. As the free aperture of the hexapole is limited in size, an offset alone will cause many molecules emerging from the nozzle to crash into

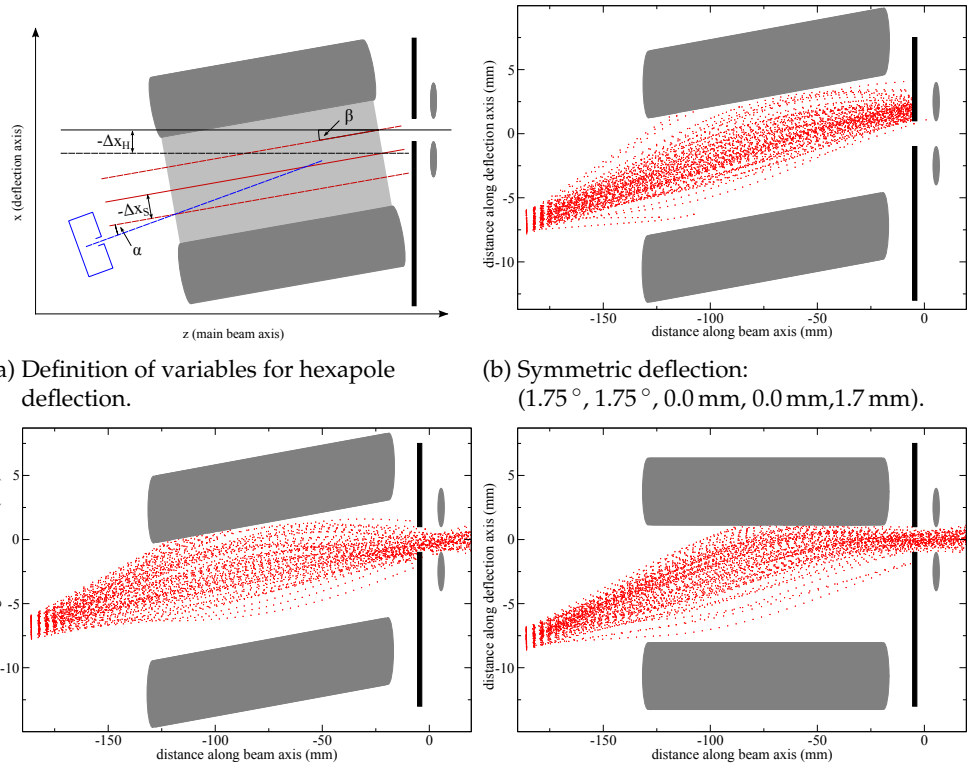

(a) Definition of variables for hexapole deflection.

(b) Symmetric deflection: (1.75 °, 1.75 °, 0.0 mm, 0.0 mm,1.7 mm).

(c) Symmetric offset deflection: (1.75 °, 1.75 °, 1.5 mm, 1.5 mm,2.2 mm).

(d) Optimized deflection: (3.5 °, 0 °, -0.75 mm, -3.45 mm,2.6 mm).

Figure 3.2: Different options for hexapole deflection with their corresponding $(\alpha, \beta, \Delta x_S, \Delta x_H, \Delta x_S + (\ell/2)\tan\alpha)$ values. In all cases, the hexapole focuser is switched on such that molecules traveling at 360 m/s experience the electric field for the entire length of 110 mm.

the electrodes. This can be counteracted by additionally rotating the nozzle about the center of the hexapole such that molecules will enter the hexapole closer to its main axis. Note that a mere rotation about the center point of the hexapole does not lead to any significant deflection. This is because for an idealized thin lens, the center beam, i.e. the straight line connecting the original object with the center of the lens, will always pass through the focused image as well. A molecule leaving the nozzle directed at the center of the hexapole will thus not be deflected to a good approximation. A small change of direction will, however, occur because the hexapole is in fact not thin but has a significant length.

If Λ-doubling is neglected, there are thus three effects which determine the efficiency of deflection: First, the amount of offset of the nozzle from the hexapole axis determines the deflection neglecting molecules crashing into electrodes. Second, the angle of rotation of the nozzle about the center of the hexapole determines how many molecules will avoid hitting the electrodes. Third, a rotation will also decrease the overall deflection because the hexapole deviates from a thin lens due to its length. Molecules injected by a rotated nozzle will thus experience a reduced force in the desired direction of deflection.

Once the length, ℓ, inner radius, r_0, and rod voltage, Φ_0, of the hexapole are fixed, four parameters are sufficient to completely describe the deflection device: The angle, α, by which the nozzle is rotated in the (x, z) plane about the hexapole center, the angle, β, by which the hexapole main axis is rotated in the (x, z) plane about the downstream beamline, the offset, Δx_S, at which the molecular beam *enters* the hexapole, and the offset, Δx_h, of the hexapole main axis with respect to the downstream beam line at the *exit* of the hexapole. Here, the z-axis is collinear with the beamline axis downstream the hexapole. See Fig. 3.2a for details. Note that by defining Δx_H relative to the entrance of the hexapole instead of its center point, the actual offset which determines the amount of deflection is given by $\Delta x_S + (\ell/2)\tan(\alpha)$.

From trajectory simulations performed for a straight beamline, the optimum length of the hexapole for focusing molecules into the entrance of the decelerator has been determined to be $\ell = 110\,\text{mm}$. Further simulations have been performed for selected candidate geometries, determining both the deflection and the fraction of molecules which manage to pass both through an aperture of 2 mm diameter and between the first decelerator electrodes.

Trajectories resulting from an intuitive, symmetric approach of deflecting molecules while minimizing collisions with the electrodes are shown in Fig. 3.2b. The molecular beam enters the hexapole at the center under an angle of $\alpha = 1.75°$. While this is sufficient for most molecules to avoid the electrodes, the desired deflection of 3.5° is not achieved. This is because the nozzle offset of $(\ell/2)\tan\alpha + \Delta x_S = 1.7\,\text{mm}$ is too small, and in addition molecules sample a large part of the near axis region where the Λ-doubling prevents efficient focusing and deflection. Keeping $\alpha = 1.75°$ constant while increasing the offset to an effective value of $(\ell/2)\tan\alpha + \Delta x_S = 2.2\,\text{mm}$ leads to much better results, as is depicted in Fig. 3.2c. The beam is deflected by almost 3.5°, but the combination of large offset and small angle results in many molecules hitting the electrodes. Similar to the case described before, a large fraction of

molecules experiences the near-axis region of low field strength, causing blurring of the focus. This problem can be prevented by shifting the point of entrance further away from the obstructive electrode while increasing the angle α to compensate for the change in the effective offset. A systematic search in the $(\alpha, \delta x_S)$ parameter space yields the best result for which trajectories are shown in Fig. 3.2d. Molecules enter the hexapole at $\Delta x_S = -0.75\,\mathrm{mm}$ under an angle of 3.5°, such that the effective offset is $(\ell/2)\tan\alpha + \Delta x_S = 2.6\,\mathrm{mm}$. A total deflection of 3.5° is obtained. Note that by injecting the molecules at the wrong side of the hexapole axis, they are first deflected opposite to their final direction for a length of $\Delta x_S/\tan(\alpha) = 12.6\,\mathrm{mm}$. This effect is compensated by the larger effective offset and the fact that molecules which are deflected most are not lost at the electrodes. In addition, molecules will pass the region of low field strength faster due to the increased value of α, such that the effect of Λ-doubling is not as pronounced as before. Final values for the position and orientation with respect to the downstream beamline are $\beta = 0°$ and $\Delta x_H = -3.45\,\mathrm{mm}$. This has the added advantage that the hexapole can be mounted parallel to the downstream beamline. As will become clear later (see section 3.3), this allows the collision energy range of the machine to be extended by making the hexapole position adjustable. With these optimized parameters, only 1.5 % of the carrier gas and electronic ground state CO molecules which make it through the skimmer pass on to the next chamber, whereas 63 % of CO* trajectories lead through the aperture according to simulations. For comparison, a straight hexapole ($\Delta x_S = \Delta x_H = 0\,\mathrm{mm}$, $\alpha = \beta = 0°$) is able to focus 79 % of all CO* molecules that make it through the skimmer through the aperture.

Since apparently only the fields on the far side of the hexapole are effective in deflecting the beam, attempts were also made to use a simpler geometry for the electrodes. Most notably, one could replace one half of the hexapole, i.e. three of the six rods, by a grounded plate located in the symmetry plane of the hexapole, such that the electric field in the other half remains unchanged according to the method of images. This fails, however, if the molecules enter in the blocked half of the hexapole as in Fig. 3.2d, whereas shortening the plate to not cover the entry would lead to a huge distortion of the field. A more sophisticated approach would be to only use four of the six hexapole rods, omitting two rods on one side. A thorough search was conducted over many possible geometries of rod positions similar to the original positions of the rods in the hexapole. For each geometry, the electric fields were calculated using the finite element program `Comsol` [78] and loaded into the `libcoldmol` package [79]. Subsequent scanning of the $(\alpha_s, \Delta x_s)$ parameter space shows that no deflection better than with the optimized hexapole geometry could be achieved, mostly due to imperfect focusing. Using a suitable electrode geometry consisting of a charged rod positioned over a grounded round trough, an electrostatic device can be constructed which provides a large electric field strength gradient in one transverse direction. It has been shown to be very efficient for pure deflection of molecular beams of polar molecules [80–82]. Since it provides no focusing effect in the other transverse direction, though, it is ill-suited for coupling the molecular beam into the Stark decelerator.

There is yet another common approach to state selection and carrier gas removal, which has been demonstrated first in magnetic focusing of atoms [83]. An obstacle,

referred to as beam stop, is introduced into a hexapole focuser on the center of the molecular beam axis, blocking the original beam. Giving the advantage of complete carrier gas removal, this procedure unfortunately also removes a significant fraction of the molecules of interest, namely the ones traveling close to the molecular beam axis which are not focused enough to pass around the beam block. Apart from being slightly less efficient, this setup also makes alignment of the beamline more challenging, and is more prone to electric discharges than a simple tilted device. For these reasons, the tilted hexapole setup has been preferred for the design of the apparatus.

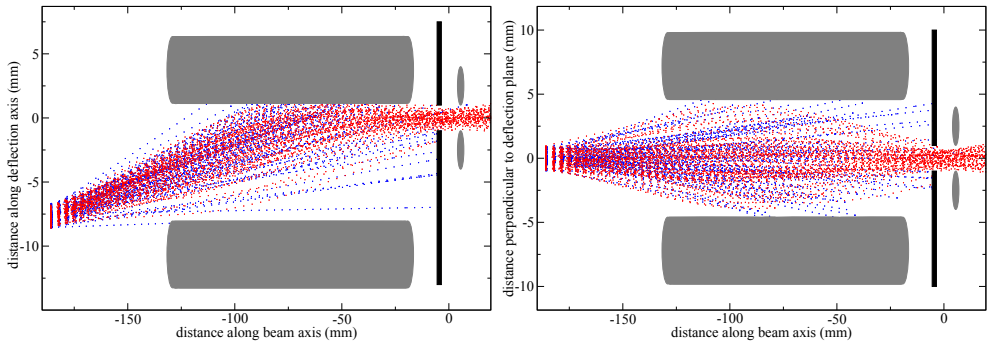

(a) In plane of tilt.

(b) Perpendicular to plane of tilt.

Figure 3.3: Trajectory simulations of hexapole deflection and focusing of $CO^\star$ (red) and carrier gas (blue) removal.

The final results for hexapole deflection in both transverse directions are depicted in Fig. 3.3. In order to estimate the total efficiency, a closer look needs to be taken at the full 6-dimensional overlap of hexapole emittance and decelerator acceptance, i.e. the size of the $CO^\star$ distribution emitted from the hexapole has to be compared to the maximum phase space area which can be stably transported through the decelerator. Phase space distributions resulting from trajectory simulations are depicted in Fig. 3.4. Since the hexapole has only a very limited effect on the (z, v_z)-phase space in beam direction, only the overlap in the (x, v_x)- and the (y, v_y)-phase space is shown. Black dots represent the transverse decelerator acceptance of molecules in front of the decelerator that are guided at 360 m/s in the $s = 3$ mode (see section 4.1 for details). The red dots show the phase space distribution resulting from hexapole deflection for the optimum geometry of Fig. 3.2d, whereas the green dots have been calculated for a hexapole in perfectly linear geometry as a reference. Out of the plane of tilt, the distributions are nearly identical, while in the direction of tilt, a significant region of the phase space is not filled when using the tilted geometry. These are the molecules which hit the hexapole rods. However, hardly any of the missing phase-space population lies inside the ellipse which indicates an upper bound for the decelerator acceptance, and even fewer molecules are lost from the most dense part of the decelerator phase space acceptance. Therefore, no significant performance issues of the tilted

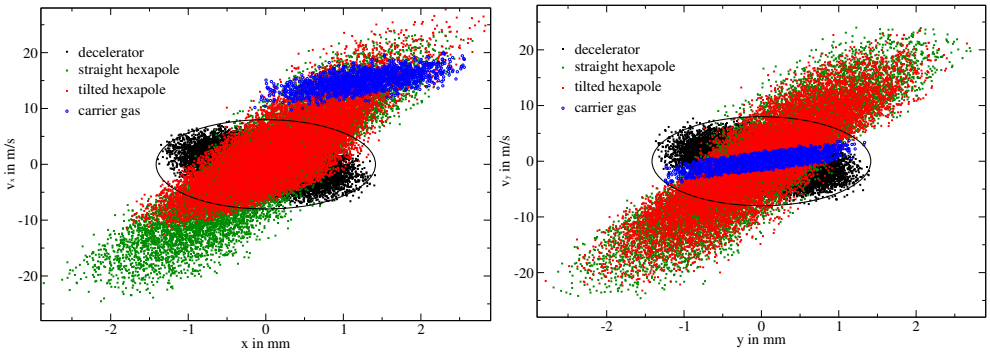

(a) In plane of tilt.

(b) Perpendicular to plane of tilt.

Figure 3.4: Transverse phase space emittance of the hexapole compared to the phase space acceptance of the decelerator.

geometry as compared to a perfectly straight hexapole are expected when being used in combination with the Stark decelerator. The carrier gas and CO in its electronic ground state, represented by the blue dots, miss the entrance of the decelerator in the direction of the tilt.

3.3 A New Hexapole Focuser Design

The molecular beam stage containing the hexapole described theoretically above serves the purpose of optimizing the overlap in the six-dimensional phase space $(\mathbf{r}, \mathbf{v})$ between the incoming molecular beam and the acceptance of the Stark decelerator, and of improving the base pressure by eliminating the background gas.

An obvious way to keep the overall length of the hexapole device as short as possible is to increase its maximum operating voltage. In order to achieve this, the mounting of the hexapole rods was designed to have a maximum insulation path in between opposite voltage parts. The traditional way of attaching the electrodes of a hexapole focuser is to mount electrodes directly to an insulator support, which has pre-fabricated holes to accommodate the rods. Because the maximum voltage which can be applied to the hexapole is limited by surface discharges via the insulator, additional slits and holes are located in the ceramic support. These increase the minimum pathway along the surface between adjacent electrodes, such that higher operating voltages can be achieved. As can be seen in Fig. 3.5a, in the new design hexapole rods of the same polarity are mounted on stainless steel plates, which are mounted to an insulator frame made from MACOR©. In this design, the surface distance between electrodes along the insulator is increased to 75 mm. As a consequence, the device can be safely operated at ± 14 kV, which means that the hexapole can be shorter due to the stronger focusing effect. At a length of 110 mm (115.2 mm taking into account the hemispherical end caps), the hexapole allows for proper focusing and deflection

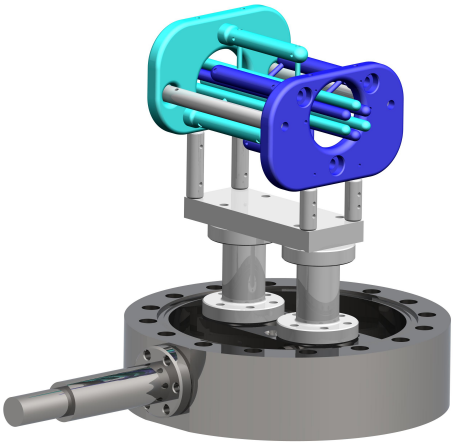

(a) Schematic of hexapole design. Parts shown in blue and cyan are on opposite high voltage, while white parts are made from insulator material.

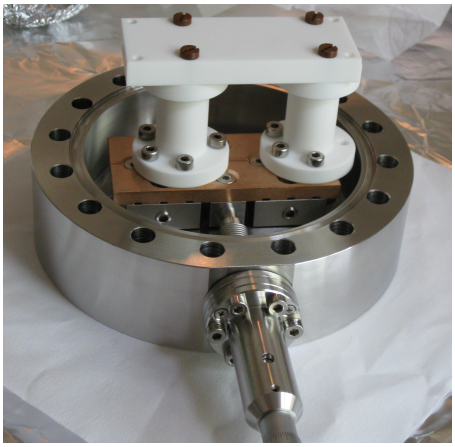

(b) *In-situ* displacement of the hexapole. While the hexapole is not yet mounted in this picture, the micrometer pushing on the mount is clearly visible.

Figure 3.5: Hexapole design details.

of beams of $CO^{\star}$ with velocities of up to 360 m/s.

A similar design for a hexapole has been described in reference [84]. The method of carrier gas removal, however, is different for the device described here: as explained in detail in section 3.2, the molecular beam pulse enters under an angle of $\alpha_s = 3.5\,^{\circ}$ and offset by $\Delta x_S = -0.75$ mm. The hexapole is mounted on two stainless steel UHV compatible translation stages and can be displaced in the tilt direction via a micrometer-actuated linear translation stage, as shown in Fig. 3.5b. This unique feature serves two purposes. First, it allows the *in-situ* optimization of the hexapole position on experimental signal (e.g., in cases where the nozzle is misaligned). Even more importantly, it allows for a useful modification of the experimental setup: by shifting the hexapole such that it is collinear with the main decelerator axis, and subsequently adjusting the skimmer and nozzle mounting, one can make the entire beamline straight. This is important since the hexapole bending limits the maximum initial velocity prior to de- or acceleration to 360 m/s. As a consequence, the final velocity which can still be reached by means of acceleration is limited to 512 m/s (cf. sections 4.1 and 4.3). For faster final velocities, the initial velocity has to be increased by first making the initial beam faster, which is readily done by increasing the valve temperature and seeding in lighter carrier gases. The hexapole, even though not capable of focusing the faster beam perfectly due to its insufficient length, at least will provide some focusing effect which increases the incoupling into the decelerator. As a drawback, this method of high velocity beam production will not reduce the carrier gas background more than the differential pumping alone. This potentially limits measurements at high beam velocities to surface temperatures above the point where the

seed gas will stick. For a detailed discussion of surface contamination by the direct beam, see section 5.1.

To ease the procedure of changing from a straight to a bent beamline, both the skimmer and the nozzle are mounted in a special fashion. The wall between source and hexapole chamber hosts a large orifice, to which two stainless steel supports are custom-fitted. These disc-like supports may be replaced while accurately maintaining their position relative to the hexapole. One of the discs is equipped with a pre-aligned skimmer mounted to its center, while the other one incorporates both the offset and the angle needed to properly fit a second pre-aligned skimmer in the tilted setup. Both discs have their side pointing towards the hexapole highly polished to avoid electric discharges. Similarly, there exist two different mounting flanges for the nozzle, one having a centered bore, the other one modified for the tilted setup. The nozzle itself is mounted and centered to a tube which hosts all the necessary feedthroughs and fits accurately into the supporting flanges, rendering options for large nozzle position adjustments unnecessary. Minor adjustments may be made by means of tipping the nozzle around the O-ring which seals against atmosphere, or by adjusting hexapole timing and position. A schematic view of straight and tilted setup is shown in Fig. 3.6.

High voltage is supplied to the hexapole via two fast high voltage push-pull switches (*Behlke Power Electronics GmbH* HTS-201-06-GSM) capable of switching between 17 kV and ground with a rise time of 200 ns. The switches are backed by capacitors charged by two high voltage power supplies (*Spellman* SL20P1200 / SL20N1200, 20 kV, 1200 W). Switching the high voltage provides a convenient way of adjusting the focal length of the hexapole. Moreover, intense UV light at 206 nm will produce photoelectrons when hitting stainless steel surfaces, potentially giving rise to discharges. Switching on the high voltage only when the laser is not firing circumvents this problem when exciting the CO near the hexapole rods. The voltage is supplied to the hexapole rods via two ceramic high voltage feedthroughs rated to 60 kV DC. A solar blind PMT (*Hamamatsu* R821, 160 nm $-$ 320 nm, gain: 4×10^5) is used to monitor the fluorescence of molecules passing through the skimmer and through the aperture to the decelerator chamber. It can be mounted either directly behind the skimmer or behind the differential pumping wall separating hexapole and decelerator vacuum region.

In order to gain access for both the excitation laser beam and the hexapole close to the differential pumping walls, these walls have been incorporated into the first vacuum chamber. The latter is machined from a solid block of stainless steel, accommodates a center bore of 160 mm diameter, and is divided into two main regions, separated by a wall which itself contains a hole fitted to the skimmer mounting plates (*vide supra*). While the first region constitutes the source chamber, the second region can be separated further into two parts by means of inserting a special disc which is fastened to a groove inside the wall of the chamber. Since this second region comprises the whole hexapole and a small part of the decelerator vacuum region, its walls have been polished for high voltage compliance. The hexapole is placed such that the closest surface-surface distance to the walls on either end is larger than 10 mm.

The entire beamline is aligned by eye using an accurate optical telescope. In general,

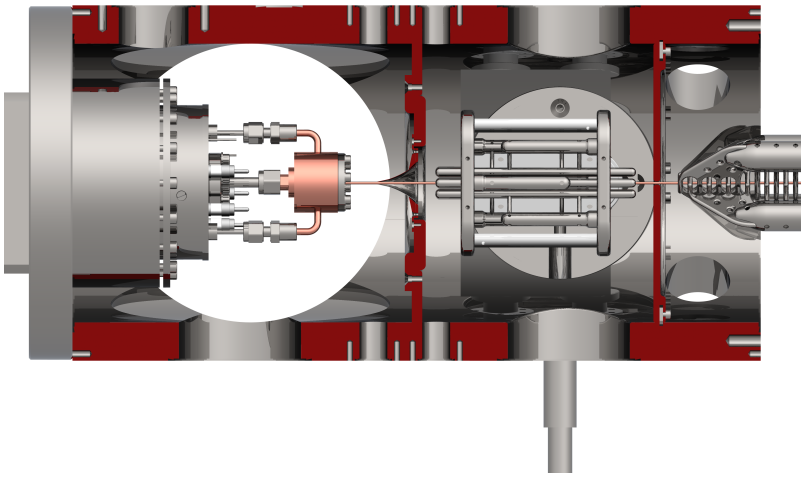

(a) Straight geometry.

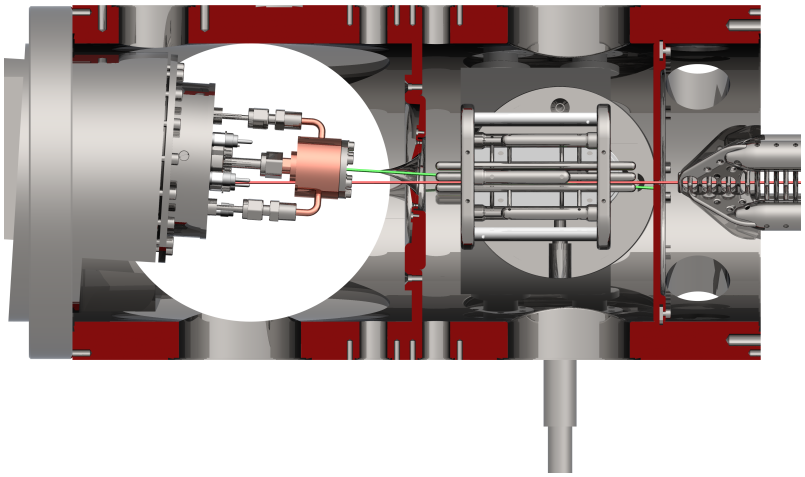

(b) Tilted geometry.

Figure 3.6: Top view of hexapole, skimmer and nozzle position in straight (a) and tilted (b) setup. The vacuum chambers are cut in half.

the process is as simple as mechanically defining two points, usually by mounting small orifices, at the front and rear of the molecular beam machine. Aided by two mirrors, the optical path of the telescope is then aligned to pass through these two points, whereupon the devices can be aligned to be collinear with the optical axis. For hexapole, skimmer, and nozzle alignment, two optical axes have to be defined by two pairs of holes, one pair coinciding with the center-to-center axis of front and rear flange, the other axis tilted by 3.5°. The hexapole can be equipped with end caps containing holes in the appropriate places to ease the alignment. With the aid of the micrometer-actuated translation stages, the accuracy of the hexapole's alignment is estimated to be ± 0.025 mm. The errors in beamline alignment are thus smaller than the inaccuracies in aligning the individual devices, which are usually on the order of ± 0.05 mm. The same two plastic caps containing the orifice for beamline alignment are used to align the hexapole rods with respect to each other. Each fits into the center hole of the metal support plates, and contains six holes which confine the electrodes to their optimum position. Adjustments are made by changing the position of the metal support plates and the angle of electrode mounting until the position of the electrodes matches the holes in the caps.

3.4 Hexapole Focusing and Bending Results

The performance of hexapole focusing and bending was measured in a test setup consisting only of the pulsed valve, the excitation laser, the hexapole focuser itself, and a detector. A supersonic expansion of 20 % CO in Ar with a velocity of about 360 m/s is produced by cooling the pulsed valve down to 101 K. Directly in front of the skimmer, a laser beam with a wavelength of 206 nm, focused to be $\approx$ 2 mm in diameter at its intersection with the molecular beam, excites CO from the electronic ground state ($X^1\Sigma^+(v = 0, J = 1)$) to the metastable $a^3\Pi_1(v = 0, J = 1)$ state. In principle, this transition is spin-forbidden, but since the $a^3\Pi$ state is mixed with the higher-lying $A^1\Pi$ state via spin-orbit-coupling [85], it can be pumped using narrow bandwidth ($\approx$ 150 MHz) laser pulses of about 3 ns duration with a pulse energy of typically 1 mJ (see section 5.3.1). After passing through the hexapole, CO* is detected by a standard MCP detector (*R. M. Jordan Co., Inc.* C-0701, 18 mm active diameter) mounted directly to the first vacuum chamber, 66.5 mm downstream from the end of the hexapole.

The time-of-flight traces of CO* detected by the MCP are recorded with a digital oscilloscope. When the length of the high voltage pulse provided to the hexapole is varied in the linear setup, the focusing behavior shown in Fig. 3.7 is observed. The high voltage is pulsed such that focusing takes place symmetrically about the center of the hexapole for a molecule traveling at 360 m/s. Without any voltage applied to the hexapole rods, the time-of-flight trace exhibits a peak at early arrival times, which corresponds to molecules traveling on axis. Since a molecule with a larger longitudinal velocity can have a higher transverse velocity component and still pass through all the apertures, this free flight peak is expected to favor faster molecules. As the

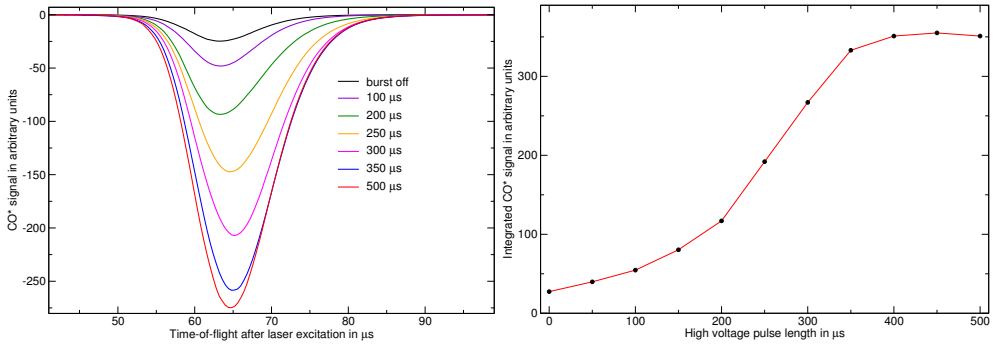

(a) Time-of-flight traces of CO* focused by the hexapole. The focusing length is varied by changing the duration of the high voltage pulse.

(b) Integrated time-of-flight signal for the traces shown on the left.

Figure 3.7: CO* signal behind the hexapole as a function of focusing strength. The setup of nozzle, skimmer, and hexapole is collinear.

voltage is switched on, a contribution arises from slower molecules that are focused through the aperture behind the hexapole. With increasing duration of the high voltage pulse, this slow contribution increases. Note that the apparent shift towards later arrival times with increasing high voltage pulse duration is due to the fact that the sum of the slow and the fast contribution is dominated more and more by the growing slow component. In fact, the focused peak starts to shift towards faster arrival times once the duration of the high voltage pulse is longer than 300 µs. Interestingly, the integrated signal, shown in Fig. 3.7b, increases even when the duration of the high voltage is increased from 350 µs to 400 µs, despite the fact that molecules traveling at 360 m/s take only 305 µs to pass the straight section of the hexapole focuser. This indicates that some focusing takes place at the exit of the hexapole. In the linear setup, the integrated signal increases by a factor of 13 for optimum focusing compared to the free flight.

More crucial for carrier gas separation than the collinear setup is the case where nozzle and skimmer are tilted, and the hexapole is shifted (cf. Fig. 3.6b). With the remaining setup as just described, the focal length is varied in four different ways: The start of the high voltage pulse, t_s, is kept constant while the end timing, t_e, is scanned (Fig. 3.8a), t_e is kept constant while t_s is varied (Fig. 3.8b), and t_e and t_s are both varied symmetrically about the time t_c where molecules with a velocity of 350 m/s reach the center of the focuser (Fig. 3.8c). In addition, the voltage applied to the hexapole is then scanned with optimized timings (Fig. 3.8d). Two surprising effects are observed: At constant start time, the signal decreases after reaching a maximum, even after molecules traveling at 350 m/s have left the hexapole. For a fixed end time, however, the signal continues to rise even for times where the molecules have not yet reached the device. The reason in both cases is most likely the electric

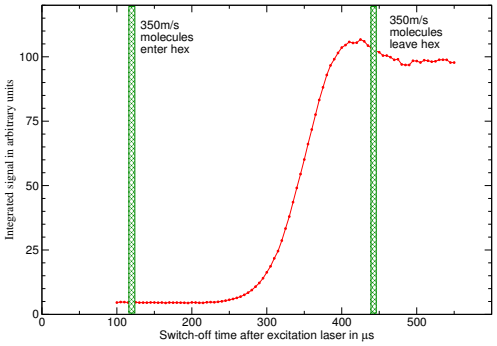

(a) Integrated time-of-flight signal for different switch-off times of the hexapole. High voltage is switched on at 50 µs.

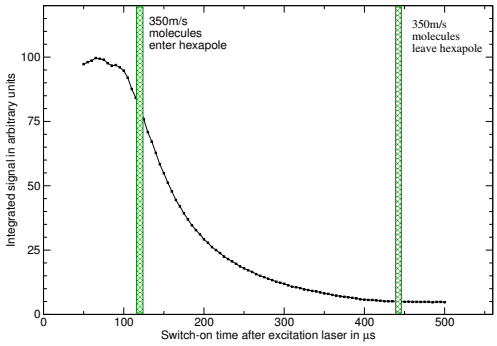

(b) Integrated time-of-flight signal for different switch-on times of the hexapole. High voltage is switched off at 600 µs.

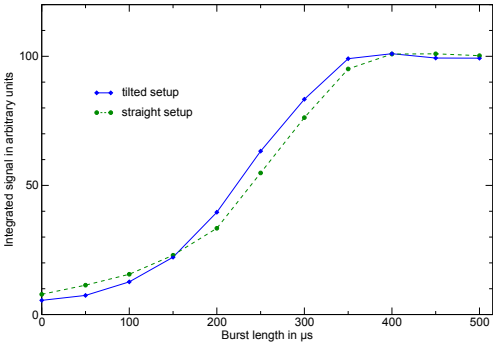

(c) Integrated time-of-flight signal for different burst durations symmetric about the hexapole center. The dashed green curve shows the focusing behavior of the straight hexapole for comparison.

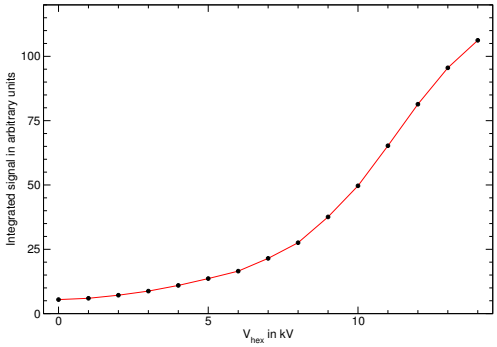

(d) Integrated time-of-flight signal for different voltages applied to the hexapole. High voltage is switched on at 50 µs– 375 µs.

Figure 3.8: $CO^{\star}$ signal behind the hexapole as a function of focusing strength. The duration of the high voltage pulse is varied from the beginning of the hexapole (a), from the end of the hexapole (b), and centered around the middle of the hexapole (c). Start, middle, and end refer to molecules traveling at 350 m/s. Focusing strength is also varied by changing the high voltage for fixed timings (d).

field between the hemispherical end caps of the hexapole and the nearby differential pumping walls. Behind the device, over-focusing occurs when the high voltage is on for too long, even when the molecules are already between the hexapole and the aperture to the next chamber. At the entrance of the hexapole, however, it appears that it is favorable to "capture" the molecules as soon as possible, thus preventing a fraction of them from crashing into the far side rods of the hexapole. When the high voltage

pulse is applied symmetrically, as depicted by the solid blue curve in Fig. 3.8c, both effects approximately cancel each other, resulting in a smooth focusing curve that is similar to the one obtained for the straight setup, reproduced as the dashed green curve.

Two aspects of hexapole focusing and bending become apparent from the data shown in Fig. 3.8. First of all, the best strategy to obtain optimum signal is to switch on the hexapole as early as possible, and carefully optimize the time when it is switched off for the desired velocity. Experimentally, this is realized by triggering the high voltage switch 5 µs after the excitation laser, which is deemed to provide ample security in the case that the laser beam produces photoelectrons by hitting the hexapole rods. Second, in the tilted setup the integrated CO* signal under optimum hexapole operating conditions is a factor of 21 higher than when the hexapole is switched off. The corresponding signal increase for the straight setup is by a factor of 13. It should be noted that these numbers refer to CO* being detected by an MCP whose diameter is sufficiently large to detect all molecules which pass through the aperture into the next chamber. This is different for the final setup in which molecules are detected behind the decelerator. While the gain factor increases for the straight setup as expected for strictly geometrical reasons, the signal without high voltage applied to the hexapole drops to zero in the bent setup. Thus, the molecular beam may be effectively switched off completely by mistiming or stopping the hexapole trigger. The voltage dependence of the signal, shown in Fig. 3.8d, surprisingly shows no effect of over-focusing, instead it rises up to the operating voltage of ± 14 kV without apparent saturation. This can be attributed to two effects. First of all, the effect of low field strength near the axis of the device are less severe, enlarging the signal. In addition, the effect of favorable end effects at the entry are enhanced. When detecting all molecules which are entering the next chamber, the signal is expected to increase further with higher voltage. However, over-focusing is bound to happen eventually, which will decrease the phase space overlap with the decelerator. Since the hexapole proved to be more difficult to condition to high voltage after a series of discharges, attempts to increase the voltage even further have been abandoned.

3.5 Conclusion

A state-selected, background-gas free molecular beam of metastable CO ($a^3\Pi_1, v = 0, J = 1$) is produced by a supersonic expansion of CO in Argon or Xenon, laser excitation of CO to the metastable CO*, and subsequent electric hexapole state selection of CO*. The electric hexapole acts as a lens for molecules in low-field seeking quantum states. Deflection of CO* is achieved by letting the molecular beam enter the hexapole off-center under an angle of 3.5°. In this geometry, only CO molecules in the desired quantum state are focused and deflected through an aperture placed behind the hexapole, while the carrier gas and remaining electronic ground state CO collide with the differential pumping wall. A new design for the hexapole focuser has been implemented which allows it to be operated at higher voltages than usual,

so that the length of the focusing device can be kept short. Using this new device, the CO^* intensity behind the hexapole has been observed to increase by a factor of 21 when the focuser is switched on compared to when the high voltage is off. Because the hexapole is mounted on translation stages, only minor modifications are necessary to change the experimental setup to a straight beamline.

Chapter 4

Tuning the Velocity of Molecules

The first attempts to manipulate the velocity of neutral polar molecules by exploiting their Stark effect were undertaken in the late 1960's [86–88], but struggled with the technical requirements, especially the switching of high voltage. The first successful implementation of a decelerator was then realized by Bethlem *et al.* in 1999 [8], who used a decelerator of shorter length but otherwise identical dimensions to the one constructed for the research project described in this thesis to decelerate CO $(a^3\Pi_{\Omega=1,2}, v = 0)$ in a low-field seeking quantum state. Since that time, many other molecular species in low-field seeking quantum states have been slowed down successfully in similar decelerators, including ND_3 [11], OH [89], H_2CO [90], SO_2 [91], $NH(a^1\Delta)$ [92], OD [93], LiH [94], NO [95], and CaF [96]. Many of these species have also been trapped, some by using advanced reloading schemes involving optical pumping to another state (NH, [97]). Further candidate molecules for which Stark deceleration is feasible [12] are CH, SH, SD, CH_2F_2, CH_3F, HCN, and LiD (only species are given for which a significant velocity change may be reached in at least one quantum state using the decelerator described in this thesis).

A miniaturized version of a Stark-type decelerator has been realized applying waveforms to the planar electrodes of a microchip. $CO^\star$ molecules could be decelerated to standstill in the resulting traveling wells above the surface, and afterwards trapped [57, 98]. Based upon the very same concept of a traveling potential well, macroscopic scale ring decelerators have been employed for manipulating $CO^\star$ [99], YbF [100], and NH_3 [101]. The large Stark effect in highly excited Rydberg states has been exploited to build a so-called Rydberg decelerator which consists of only few stages. Deceleration of Ar atoms [102], as well as deceleration and subsequent trapping of H atoms [103, 104] and H_2 [105, 106] has been achieved.

Molecules in high-field seeking quantum states are more complicated to decelerate than molecules in low-field seeing quantum states. Since a maximum of the electric field strength cannot be created in free space by any electrode configuration (see, e.g., [107]), molecules in high-field seeking quantum states tend to crash into the electrodes. The scheme of decelerating high-field seeking molecules based on alternating gradient focusing has been successfully employed to decelerate OH [108], benzonitrile (C_7H_5N) [109], CaF [96], and YbF [110], as well as to change the velocity of Cs atoms, exploiting their polarizability, in a one-stage prototype setup [111].

A number of other deceleration schemes has been used for various neutral atomic and molecular species. Microwave deceleration of ND_3 has been demonstrated, using a microwave Stark decelerator exploiting the AC Stark effect [15]. Short intense

laser pulses offer another means of providing large local electric fields. NO [112] and benzene (C_6H_6) [14] have been decelerated using such an optical Stark decelerator. Following a similar approach as Stark deceleration, but using time-dependent magnetic fields, paramagnetic species can be decelerated using a so-called Zeeman decelerator (note that this is not the same as a Zeeman slower commonly used for loading magneto-optical traps.) So far, it has been applied to H and D atoms, Ne, Ar, O_2, and CH_3 radicals [113]. An overview of these methods, and also other methods to obtain samples of cold molecules which are not listed above, is given in references [13, 114].

4.1 Key Concepts in Stark Deceleration

As has been explained in section 3.2, inhomogeneous electric fields are needed to exert a net force on a dipolar molecule. Perhaps the easiest way of creating such fields, which is also well-suited to set up a periodic array, is to use two rod-shaped, parallel electrodes charged to high voltage of opposite polarity. Consider the geometry depicted in Fig. 4.1, where the two infinitely long cylindrical electrodes of radius R, centered at $\mathbf{r} = (\pm d, y, 0)$, are extending parallel to the y-axis, such that their surface distance is $2(d - R)$. Obviously, these electrodes will create an electric field along the z-axis which is highest between the electrodes, while along the x-axis, the electric field strength has its maxima at the electrode surfaces. A Stark decelerator consists

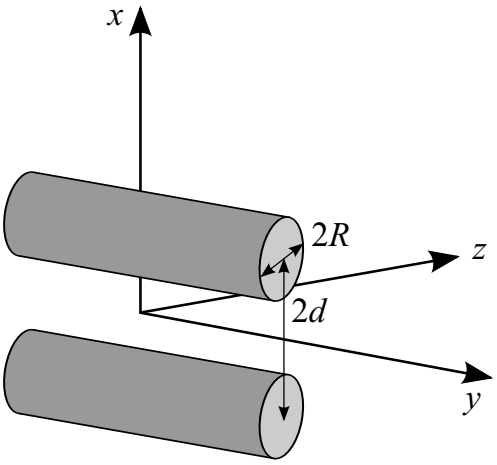

Figure 4.1: Electrode geometry for creating an inhomogeneous electric field along the x- and z-axis. Electrodes of radius R are centered at $(x, z) = (\pm d, 0)$ and extend infinitely along y.

of a periodic array of these pairs of rods along an axis defined as the z-axis, where adjacent pairs have a center-to-center distance of L. All even pairs are rotated by 90° about the z-axis compared to the odd ones. High voltage is applied such that either

all even pairs are charged and odd pairs grounded, or vice versa. In such an array, a low-field seeking molecule will experience repeating Stark energy maxima along the z-axis, which makes the electrode shape ideally suited for manipulating the velocity of low-field seeking molecules. An array of n electrode pairs gives rise to $n-1$ electric field stages, i.e. the electric fields between a charged and an uncharged electrode pair which can be used to manipulate the motion of low-field seeking molecules. For just one pair of electrodes, the electric potential can be calculated analytically exploiting the method of images using two line charges [115, 116, problem 3.11], and is given by:

$$\Phi(x,z) = \frac{V_0}{2\cosh(d/R)} \ln\left(\frac{(x+\sqrt{d^2-R^2})^2+z^2}{(x-\sqrt{d^2-R^2})^2+z^2}\right), \tag{4.1}$$

where electrodes are at potential $\pm V_0$. The electric field may be readily obtained from computation of $\boldsymbol{\mathcal{E}} = -\nabla\Phi$, yielding as the result for the absolute value of the field strength:

$$\mathcal{E}(x,z) = \frac{2V_0}{\operatorname{arccosh}(d/R)} \times \sqrt{\frac{d^2-R^2}{d^4-2d^2\left(R^2+x^2-z^2\right)+R^4+2R^2\left(x^2-z^2\right)+\left(x^2+z^2\right)^2}}\,. \tag{4.2}$$

Of particular interest are the cases where either $x=0$ or $z=0$. The field along the x-axis is a useful measure of the maximum field strength in the decelerator:

$$\mathcal{E}_{x-\text{axis}}(x,z=0) = \frac{2V_0\sqrt{d^2-R^2}}{(d^2-R^2-x^2)\operatorname{arcosh}(d/R)}, \tag{4.3}$$

and leads to the maximum overall (for $z=0$, $x=\pm(d-R)$) and maximum z-axis (for $x=z=0$) values of the electric field strength;

$$\mathcal{E}_{\text{max,z-axis}} = \frac{2V_0}{\sqrt{d^2-R^2}\operatorname{arcosh}(d/R)} \tag{4.4}$$

$$\mathcal{E}_{\text{max,electrodes}} = \frac{V_0(d+R)/R}{\sqrt{d^2-R^2}\operatorname{arcosh}(d/R)}\,. \tag{4.5}$$

Note that the ratio of the maximum field strength at the electrodes to the maximum field strength along the z-axis is thus $(d+R)/(2R)$. In the decelerator described in section 4.3, this ratio is equal to $4/3$.

The field along the z-axis is useful for calculating the movement of a molecule traveling along the main molecular beam machine axis, since any transverse forces on such a molecule will cancel out, and is given by:

$$\mathcal{E}_{z-\text{axis}}(x=0,z) = \frac{2V_0\sqrt{d^2-R^2}}{(d^2-R^2+z^2)\operatorname{arcosh}(d/R)}\,. \tag{4.6}$$

Note that the electric potential in Eq. (4.1) was calculated neglecting the influence of any neighboring electrode pairs. This will not have any significant effect on the maximum field strength values calculated above. However, the formula (4.6) will need to be corrected for sufficiently large z values. This necessitates numerical calculation of the electric potential with a finite elements program. Despite representing only an approximation, the equations derived above are still useful to benchmark numerically calculated fields. The field of two charged rods, surrounded by two pairs of grounded rods, has been calculated and exported on an 0.01 mm grid using the program `COMSOL` [78].

In sections 4.1.1 and 4.1.2, we will now explore how molecules are effected by these electric fields as they travel through the device, closely following the detailed description given in references [117–122].

4.1.1 Longitudinal Motion

In order to describe the longitudinal motion of a molecule traveling along the z-axis, the straightforward approach is to first numerically obtain the potential energy of a molecule on the z-axis, i.e. the Stark energy $W(\mathcal{E}(z))$. This is done either by correcting Eq. (4.6) for high z values, or numerically computing the electric field strength and fitting it with analytical functions, thereafter combining it with the Stark effect of CO* given in section 2.2. The resulting equation of motion, $F(z) = -\partial W/\partial z = m\ddot{z}$, can then also be solved numerically. However, a more beneficial approach, which provides far more insight into the dynamics of deceleration and acceleration, is based on expanding the exact potential in terms of a Fourier series and finding an approximate but analytical solution to the equation of motion. The validity of this method should be obvious from the fact that the array of electrodes exhibits a periodicity of $2L$. Due to this periodicity, it is advisable to describe the motion of a molecule in a decelerator in terms of its reduced position, $\frac{z\pi}{L}$, which has a periodicity of 2π. The origin is now chosen with respect to the electric potential such that electrodes at $\frac{z\pi}{L} = \pi/2$ are grounded, whereas electrodes at $\frac{z\pi}{L} = -\pi/2$ and $\frac{z\pi}{L} = 3\pi/2$ are charged. Note that as a consequence, the reduced position jumps by π every time the decelerator is switched. The general Fourier series of the potential energy $U(\frac{z\pi}{L}) \equiv W_{\mathrm{st}}(\mathcal{E}(\frac{z\pi}{L}))$, taking the charged electrode position $\frac{z\pi}{L} = -\pi/2$ as the center point, is then given by

$$U\left(\frac{z\pi}{L}\right) = \frac{a_0}{2} + \sum_{n=1}^{\infty}\left[a_n \cos\left(n\frac{z\pi}{L} + \frac{n\pi}{2}\right) + b_n \sin\left(n\frac{z\pi}{L} + \frac{n\pi}{2}\right)\right] \tag{4.7}$$

$$= \sum_{n=1}^{\infty} a_n \cos\left(n\frac{z\pi}{L} + \frac{n\pi}{2}\right) \tag{4.8}$$

$$= -a_1 \sin\frac{z\pi}{L} - a_2 \cos 2\frac{z\pi}{L} + a_3 \sin 3\frac{z\pi}{L} + \ldots - \ldots - \ldots + \ldots + \ldots, \tag{4.9}$$

where in the second line, the symmetry of the electric field about any charged pair of electrodes was exploited, thus $b_n \equiv 0\,\forall n$, and a_0 was chosen to be zero since only differences in energy are relevant. The coefficients a_n are determined by $a_n =$

$\frac{1}{\pi}\int_{-\pi/2}^{3\pi/2} U(\frac{z\pi}{L})\cos\left(n\frac{z\pi}{L}+\frac{n\pi}{2}\right)\mathrm{d}(\frac{z\pi}{L})$. Alternatively, a fit of the function (4.7) up to $n = 6$ is also sufficient. For a geometry given by $L = 5.5\,\mathrm{mm}$, $d = 2.5\,\mathrm{mm}$ and $R = 1.5\,\mathrm{mm}$, a voltage of $\pm 14\,\mathrm{kV}$ applied to every second electrode pair, and the Stark effect of CO $(a^3\Pi_{\Omega=1}, v = 0, J = 0, M\Omega = -1)$ from section 2.2, one obtains the numerical values (in cm^{-1}):

$$a_1 = 0.5617,\ a_2 = 0.1177,\ a_3 = 0.03386, \tag{4.10}$$

$$a_4 = 0.008849,\ a_5 = 0.001863,\ a_6 = 0.0005440. \tag{4.11}$$

The resulting potential energy along the beam axis is sketched for configuration A with odd and configuration B with even electrodes on high voltage in Fig. 4.2a. To explore the motion of a molecule in this potential, its reduced position with respect to the potential directly after switching between electric field configurations will be denoted by the so-called phase angle, ϕ. Note that ϕ is not continuous in the sense that it is only defined at one specific time per switching period.

Consider now a molecule which travels exactly the distance L within each switching cycle, i.e. its phase angle remains constant. The phase angle and velocity of this so-called *synchronous* molecule are denoted by ϕ_0 and v_0, respectively. Of course, this concept of a synchronous molecule requires the decelerator to be switched between configurations correctly. Since the synchronous molecule moves exactly by $\Delta z\pi/L = \pi$, the difference in its potential energy after one switching cycle will be

$$\Delta U(\phi_0) = U(\phi_0+\pi) - U(\phi_0) = 2\sum_{n\,\mathrm{odd}}^{\infty}(-1)^{(n-1)/2}a_n \sin n\phi_0 \approx 2a_1\sin\phi_0\ , \tag{4.12}$$

corresponding to a constant kinetic energy change per stage of $\Delta E_{\mathrm{kin}} = -\Delta U(\phi_0)$. For $\phi_0 = 0$, the synchronous molecule will lose and gain exactly the same amount of kinetic energy, thus no net change in velocity occurs. Hence, this mode of operation is referred to as *guiding*. If $\phi_0 < 0$, the molecule will gain kinetic energy, while for $\phi_0 > 0$, the molecule will be decelerated. Maximum deceleration is obtained for $\phi_0 = 90°$, i.e. when the fields are switched every time the synchronous molecule is right between the charged electrodes. Operation of the decelerator for $\phi_0 > 0$ is schematically depicted in Fig. 4.2b. By switching the electric fields in an appropriate way, this array of electrode pairs can thus be used to decelerate or accelerate molecules. Furthermore, it should be obvious from Fig. 4.2b that a molecule with similar velocity as the synchronous molecule, but slightly lagging (leading) it in position, will experience an extra acceleration (deceleration) within each switching cycle which brings it closer to the synchronous molecule. Hence, there exists a group of molecules which will stay close to the synchronous molecule throughout the entire deceleration process. A more quantitative treatment of this concept, known as *phase stability*, will be given now.

In order to construct an equation of motion for a molecule subjected to the electric fields of a Stark decelerator, one has to describe its motion in terms of continuous variables, whereas the phase angle ϕ is only defined at discrete times, as is the kinetic energy change. In a first step, one can approximate the continuous force acting on the

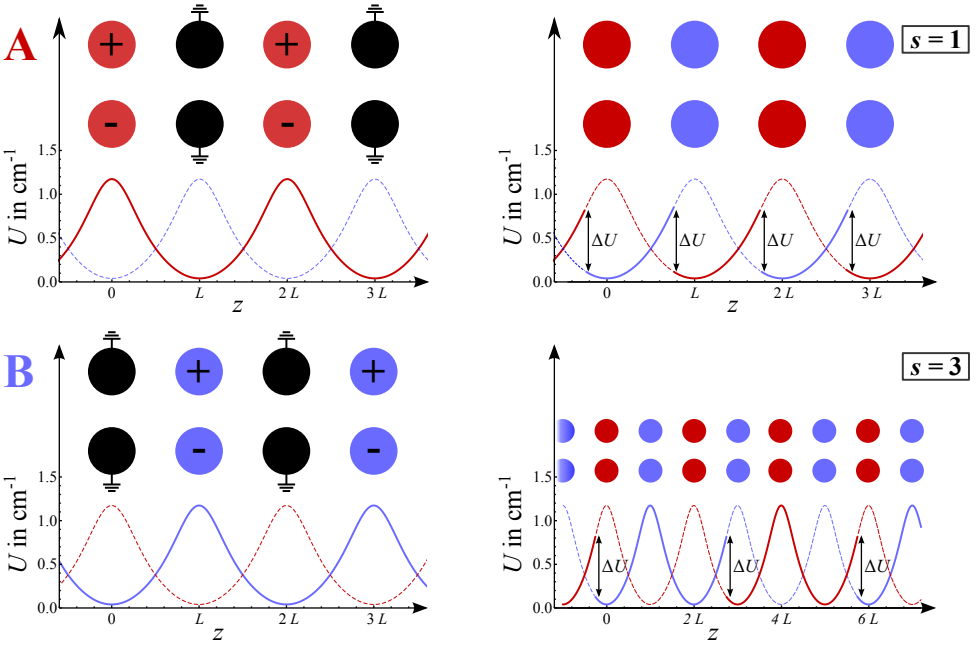

(a) Potential energy (solid curves) along the molecular beam axis for configuration A, where all odd electrode pairs are charged and even pairs grounded, and the opposite configuration B. Electrodes shown as black circles are grounded. Dotted lines indicate the potentials after the configuration is switched.

(b) Operation of the decelerator at a constant phase angle of $\phi_0 = 47°$ in $s = 1$ (top) and $s = 3$ (bottom) mode. For the definition of the parameter s, see Eq. (4.34) on page 49. The potential energy of $CO^\star$ is given by the solid lines. Voltages are switched between configurations every time the synchronous molecule reaches the same potential energy. Electrodes depicted in dark red (light blue) are charged while the molecule travels along the solid dark red (light blue) path, the others are grounded.

Figure 4.2: Schematic of decelerator switching.

synchronous molecule by the *average* force acting within one electric field stage [123]:

$$F(\phi_0) \approx \overline{F}(\phi_0) = -\frac{\Delta U(\phi_0)}{L} = -\frac{2}{L}\sum_{n\,\mathrm{odd}}^{\infty}(-1)^{(n-1)/2}a_n \sin(n\phi_0)\ . \tag{4.13}$$

This approximation is valid as long as the velocity change per stage is small compared to the velocity of the synchronous molecule. Similarly, the relative phase, $\Delta\phi = \phi - \phi_0$, and relative velocity $\Delta v = v - v_0$, even though defined in terms of variables that are well-defined only at switching time, can now be generalized to be continuous in time. The reason behind this is that the motion of a molecule with position and velocity reasonably close to the synchronous molecule is well-described by its average change in position and velocity over one stage. Let us now consider a molecule traveling on axis with velocity v_0, which at the beginning of a switching cycle has a phase $\phi = \phi_0 + \Delta\phi$. For reasonably small $\Delta\phi$, the force acting on this molecule can be approximated using Eq. (4.13):

$$F(\phi_0 + \Delta\phi) \approx -\frac{\Delta U(\phi_0 + \Delta\phi)}{L} = -\frac{2}{L}\sum_{n\,\mathrm{odd}}^{\infty}(-1)^{(n-1)/2}a_n \sin\left(n(\phi_0 + \Delta\phi)\right)\ . \tag{4.14}$$

The force acting on that molecule relative to the synchronous molecule for a fixed phase angle ϕ_0 is then given by:

$$F_{\phi_0}(\Delta\phi) = -\frac{2}{L}\sum_{n\,\mathrm{odd}}^{\infty}(-1)^{(n-1)/2}a_n \left[\sin\left(n(\phi + \Delta\phi)\right) - \sin(n\phi_0)\right] \tag{4.15}$$

$$\approx -\frac{2a_1}{L}\left(\sin(\phi_0 + \Delta\phi) - \sin\phi_0\right)\ , \tag{4.16}$$

such that the equation of motion for a molecule *relative to the synchronous molecule* becomes [123]:

$$\frac{mL}{\pi}\frac{\mathrm{d}^2\Delta\phi}{\mathrm{d}t^2} = -\frac{2}{L}\sum_{n\,\mathrm{odd}}^{\infty}(-1)^{(n-1)/2}a_n \left[\sin\left(n(\phi_0 + \Delta\phi)\right) - \sin(n\phi_0)\right] \tag{4.17}$$

$$\approx -\frac{2a_1}{L}\left[\sin(\phi_0 + \Delta\phi) - \sin(\phi_0)\right]\ .$$

This equation can be solved either numerically or even analytically [124], but deep insights into the dynamics and stability of a Stark decelerator can be gained already by studying the structure of this differential equation. Since it describes the motion relative to the synchronous molecule, ϕ_0 is only a parameter and thus constant in time, and its time derivatives are zero. Thus, Eq. (4.17) is in fact identical to the differential equation of a biased pendulum, i.e. a pendulum on which a constant torque acts such that its stable equilibrium position is at an angle of ϕ_0. In the case of $\phi_0 = 0$, Eq. (4.17) becomes that of an unbiased pendulum, i.e. a harmonic oscillator.

An exhaustive treatment of how the concepts of a biased pendulum may be exploited in describing a Stark decelerator may be found in references [121, 125]; here,

only some important aspects from this work will be reviewed. First, note that the expression

$$V_{\phi_0}(\Delta\phi) = -\frac{2}{\pi}\sum_{n\,\mathrm{odd}}^{\infty}(-1)^{(n-1)/2}a_n\left[\frac{1}{n}\cos\left(n(\phi_0+\Delta\phi)\right)+(\phi_0+\Delta\phi)\sin(n\phi_0)\right] \quad (4.18)$$

$$\approx -\frac{2a_1}{\pi}\left[\cos(\phi_0+\Delta\phi)+(\phi_0+\Delta\phi)\sin\phi_0\right]\,, \quad (4.19)$$

represents a potential for the effective force given by Eq. (4.15), which can be easily verified by the differentiation $F(\Delta\phi) = -\frac{\mathrm{d}V_{\phi_0}(\Delta\phi(z))}{\mathrm{d}z} = -\frac{\pi}{L}\frac{\mathrm{d}V_{\phi_0}(\Delta\phi)}{\mathrm{d}(\Delta\phi)}$. In the following description of the motion of a molecule with respect to the synchronous molecule, it is convenient to use the variable $\phi = \phi_0 + \Delta\phi$, i.e. the origin of the molecule's position is shifted by $-\phi_0$. Note that ϕ is now defined as a continuous variable in time, and the following equations are still only valid for the motion with respect to the synchronous molecule. For the sake of simplicity, the same variable ϕ will be used which was defined previously only for discrete points in time.

In terms of stability of longitudinal motion, much can be learned from plotting the so-called longitudinal phase space, i.e. the curves $v(\phi)$ for different total energies and fixed phase angles ϕ_0. Note that v and ϕ are related via $v = {}^{dz}/_{dt} = L/\pi \cdot {}^{d\phi}/_{dt}$. These curves are easily obtained from the total energy conservation and the known expressions for kinetic and potential energy:

$$E_{\mathrm{tot}} = E_{\mathrm{kin}} + V_{\phi_0} \quad (4.20)$$

$$= \frac{1}{2}mv^2 - \frac{2a_1}{\pi}\left(\cos\phi + \phi\sin\phi_0\right) \quad (4.21)$$

$$\Rightarrow v(\phi, E_{\mathrm{tot}}) = \pm\sqrt{\frac{2}{m}\left(\frac{2a_1}{\pi}(\cos\phi+\phi\sin\phi_0)+E_{\mathrm{tot}}\right)}\,. \quad (4.22)$$

The total energy, E_{tot}, may be obtained from the position and velocity at any point in time. An important criterion in classifying the motion of a molecule inside the potential of Eq. (4.18) is the height $V_{\max} = V_{\phi_0}(\phi_{\max})$ at the position $\phi_{\max}$ of the local maxima of V_{ϕ_0}. If the total energy of a molecule is less than $V_{\max}$, the molecule will be confined in a potential well and perform oscillations around the synchronous molecule. If, on the other hand, E_{tot} exceeds $V_{\max}$, the molecule will leave the potential well and depart from the synchronous molecule. The position of the maximum thus corresponds to the instable tipping point of a pendulum. Values for $\phi_{\max}$ and the $v(\phi)$ curves corresponding to the maximum total energy which can be still confined

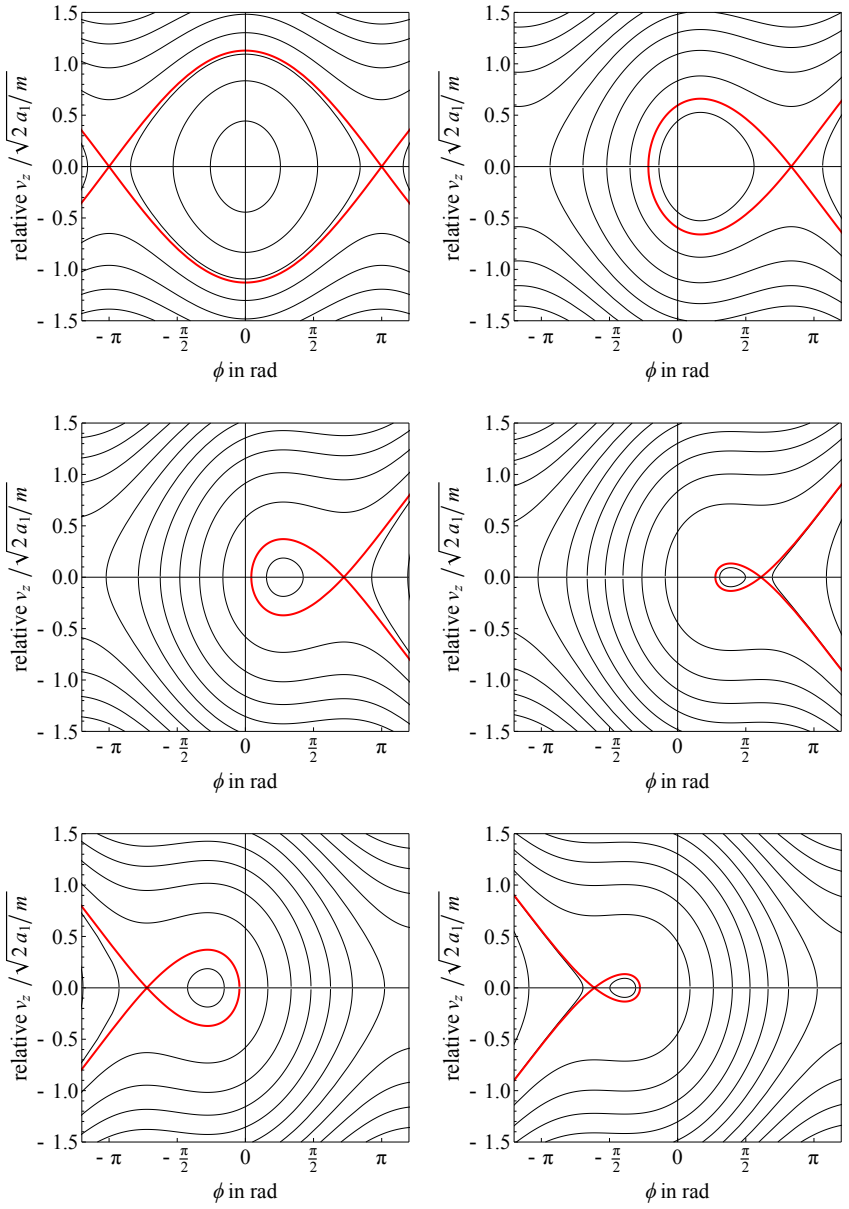

Figure 4.3: (v, ϕ) phase space of longitudinal motion for phase angles, ϕ_0, of (left to right, top to bottom) 0°, 30°, 50°, 70°, -50°, -70°. Separatrices are indicated in red. The energy difference between trajectories is $0.5a_1$ in all cases.

are given by [121, 126]:

$$\phi_0 \geq 0 : \phi_{\max} = \pi - \phi_0 \tag{4.23}$$

$$\Rightarrow v_{\max} = \pm\sqrt{\frac{4a_1}{m\pi}(\cos\phi + \cos\phi_0 + (\phi - \pi + \phi_0)\sin\phi_0)} \tag{4.24}$$

$$\phi_0 < 0 : \phi_{\max} = -\pi - \phi_0 \tag{4.25}$$

$$\Rightarrow v_{\max} = \pm\sqrt{\frac{4a_1}{m\pi}(\cos\phi + \cos\phi_0 + (\phi + \pi + \phi_0)\sin\phi_0)}\,. \tag{4.26}$$

In Fig. 4.3, the trajectories resulting from Eq. (4.22) are plotted for different values of ϕ_0, with the trajectory obtained from equations (4.23)–(4.26) highlighted in red. This trajectory splits the phase space into three different parts: a high-velocity part, where molecules travel faster than the synchronous one, overtaking it eventually; a low-velocity section, in which molecules will start trailing behind; and then an area in which a molecule is confined and which it will never be able to leave. Due to the characteristic of splitting up the phase space, this trajectory is called the *separatrix*, and the area bound by it is said to be *phase-stable*, meaning the phase of the molecule oscillates within certain bounds. This concept is crucial in understanding the working principle of a Stark decelerator: In contrast to a normal molecular beam, where molecules will spread out, they are stably confined within a certain $(\mathbf{v}, \mathbf{r})$ space, and can in principle be transported through the entire array of electrode pairs. Deceleration or acceleration occurs in a fashion that may be approximated as a traveling well potential. Note, however, that the stronger the deceleration/acceleration, the smaller the region of confinement in phase space is, as can be clearly seen from Figs. 4.3 and 4.4.

For many applications, it is advantageous to know the number of oscillations that a phase-stable molecule undergoes around the synchronous molecule within a certain time, or number of stages. This quantity can be calculated from the longitudinal oscillation frequency, which may be approximated from Eq. (4.17): For molecules close to the synchronous molecule, $\Delta\phi$ is small, and one can approximate

$$\sin(\phi_0 + \Delta\phi) = \sin\phi_0\cos\Delta\phi + \cos\phi_0\sin\Delta\phi \approx \sin\phi_0 + \Delta\phi\cos\phi_0\,, \tag{4.27}$$

such that the equation of motion becomes [12]:

$$\frac{\mathrm{d}^2\Delta\phi}{\mathrm{d}t^2} \approx -\frac{2a_1\pi\cos\phi_0}{mL^2}\Delta\phi\,. \tag{4.28}$$

Thus, the longitudinal frequency and period of oscillation for small angles is given by:

$$\frac{\omega_{\text{analytic},z}}{2\pi} = \sqrt{\frac{a_1\cos\phi_0}{2\pi mL^2}} = 1.12\,\text{kHz} \times \sqrt{\cos\phi_0} \tag{4.29}$$

$$\tau_{\text{analytic}} = \frac{2\pi}{\omega_{\text{analytic},z}} = \sqrt{\frac{2\pi mL^2}{a_1\cos\phi_0}} = 0.890\,\text{ms}/\sqrt{\cos\phi_0}\,, \tag{4.30}$$

where again the numerical values are for typical conditions of $V = \pm 14.0\,\mathrm{kV}$ and CO*. Under these conditions, in a beam being guided at 360 m/s, the molecules perform roughly 2.2 oscillations around the synchronous molecule within the 131 electric field stages of the decelerator. In addition, for $\phi_0 = 0$ the exact longitudinal frequency for a given turning point ϕ_{max} can be obtained easily from the known solutions for the period of a pendulum [127]:

$$\frac{\omega_z(\phi_{\mathrm{max}})}{2\pi} = \frac{\omega_{\mathrm{analytic},z}}{2\pi} \times \frac{2\pi}{4\mathcal{K}(\sin\phi_{\mathrm{max}}/2)}\,, \tag{4.31}$$

where $\mathcal{K}$ is the complete elliptical integral of the first kind. A more detailed analysis of longitudinal frequencies, however, shows that the influence of higher terms in the equation of motion may not be neglected. By numerical integration of the equation of motion and solving for $v(2\pi/2\omega) = 0$, the longitudinal frequencies shown in Fig. 4.6 (see p. 52) are obtained. Terms up to $n = 5$ needed to be taken into account to properly reflect the nearly flat region around $\phi_{\mathrm{max}} = 0$. In this manner, values of

$$\omega_{\mathrm{num},z}/2\pi \approx 1.03\,\mathrm{kHz} \tag{4.32}$$

$$\tau_{\mathrm{num},z} = 2\pi/\omega_{\mathrm{num},z} \approx 0.971\,\mathrm{ms} \tag{4.33}$$

are obtained for the central region extending 1 mm in both directions of the synchronous molecule. For phase angles other than $\phi_0 = 0$, the longitudinal frequency may be calculated by an identical procedure.

Worthwhile as the treatment above may be in understanding the existence of stable areas in phase space, it is important to note that significant deviations in the size of those areas are observed once higher n terms are taken into account in the differential Eq. (4.17). Fig. 4.4a shows this effect for the case of CO*. Including the $n = 3$ term and subsequent numerical integration leads to separatrices which, for higher phase angles, increase in size and become increasingly round. Further adding the $n = 5$ term to the analysis, however, leads to no distinguishable effect.

So far, only molecules which travel a distance of one stage per switching cycle have been considered. Phase stability may, however, also occur for faster molecules. Consider a molecule which travels at a velocity $v = 3v_{\mathrm{sw}}$, where $v_{\mathrm{sw}} \equiv L/\Delta t_{\mathrm{switch}}$ is the velocity of switching the electric fields between configurations and corresponds to the velocity of a synchronous molecule which travels exactly the distance L per switching cycle. This molecule will then traverse a distance of $3L$ per switching cycle, and its kinetic energy will thus change in every cycle as if it was traveling at v_{sw}. However, due to its faster speed, it will only lose or gain a third of the kinetic energy *per electric field stage* compared to a molecule traveling at v_{sw}. In fact, the same argument holds true for any molecule with velocity v_s for which $s \equiv v_s/v_{\mathrm{sw}}$ is an odd integer, due to the periodicity of the potential of $2L$ and the fact that switching between configurations introduces a shift in position of L. For even integer values of s, in contrast, the position with respect to the potential will change every time the fields are switched. Because a molecule with velocity v_s travels a distance sL within one switching period, its equation of motion is obtained by replacing L by sL in the expression of the

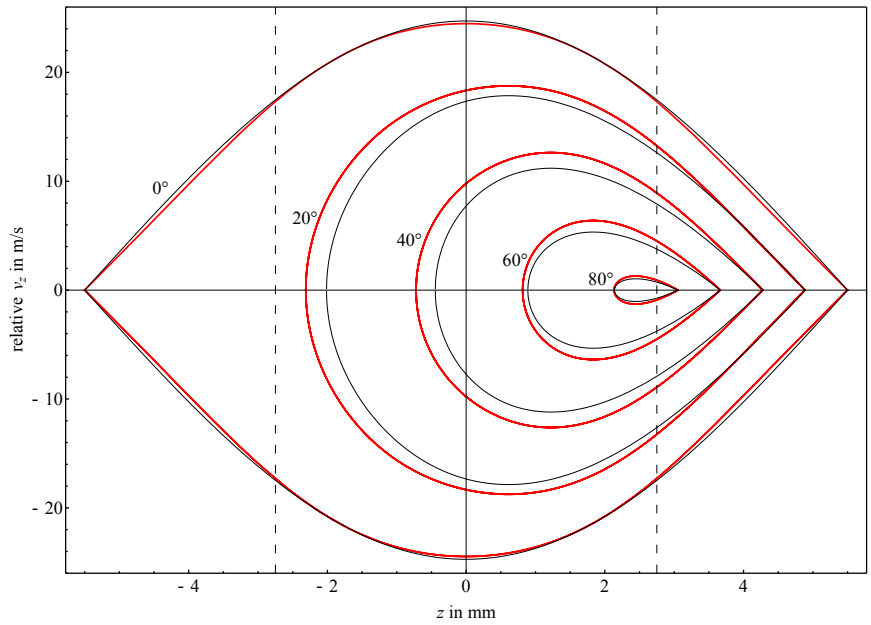

(a) Comparison of analytic solution (thin black lines) with numerical calculation up to n=3 (thick red lines).

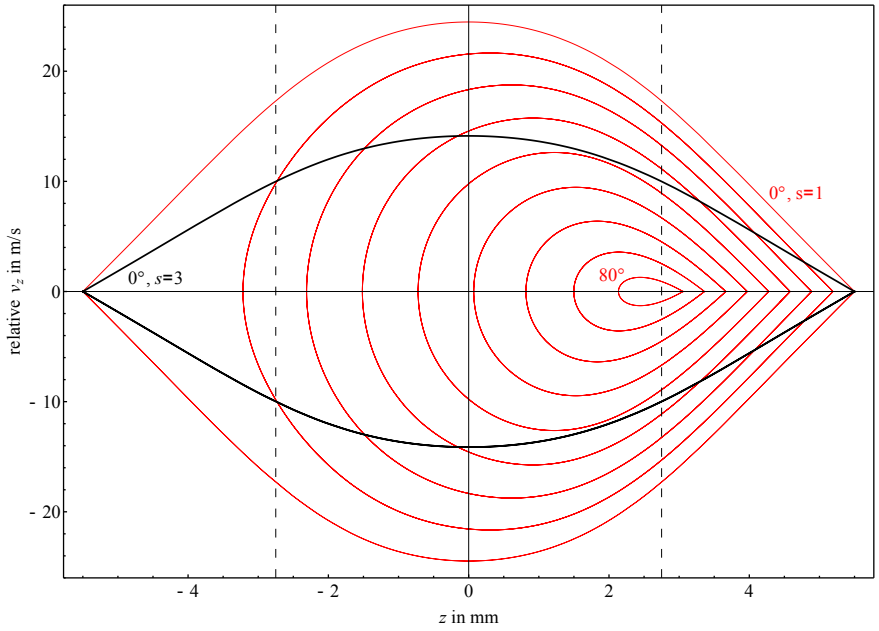

(b) Separatrices for $s = 1$ up to 80° in steps of 10°. The thick black line denotes the separatrix for $\phi_0 = 0°, s = 3$. For the definition of the parameter s, see Eq. (4.34) on page 49.

Figure 4.4: Phase stable area inside the separatrix for different values of ϕ_0 between 0° and 80°. Positions of electrodes are indicated by dashed vertical lines.

force [128]:

$$\frac{mL}{\pi}\frac{\mathrm{d}^2\Delta\phi}{\mathrm{d}t^2} = -\frac{2}{sL}\sum_{n\,\mathrm{odd}}^{\infty}(-1)^{(n+1)/2}a_n\left[\sin(n(\phi_0+\Delta\phi)) - \sin(n\phi_0)\right]$$
$$\approx -\frac{2a_1}{sL}\left[\sin(\phi_0+\Delta\phi) - \sin\phi_0\right]\ . \tag{4.34}$$

Comparing this expression to Eq. (4.17), it is readily seen that the curves of constant energy in phase space, and thus the separatrix, contain an extra factor of $1/\sqrt{s}$, i.e. their size in velocity space is smaller. The same is true for the longitudinal frequency of oscillation in equations (4.29) and (4.31).

From the above treatment it should be clear that there are at least two options for guiding and decelerating a molecular beam of $CO^\star$ at a given initial velocity v_{CO}: Either by switching the decelerator corresponding to the velocity $v_{sw} = v_{CO}$, or by choosing the slower velocity $v_{sw} = v_{CO}/3$. The former is called the $s = 1$ mode of operation, whereas the latter is known as the $s = 3$ mode. The separatrix for $s = 3$ guiding is also shown in Fig. 4.4, and the schematic of switching compared to the $s = 1$ mode is depicted in the lower panel of Fig. 4.2b. A thorough theoretical analysis of the full equation of motion shows that there exist more phase-stable areas in the (v_z, z) phase space than just for odd values of s. In fact, first order resonances may be identified for any $s = {}^{l}/_{n}$ where n and l are odd, and weaker second-order resonances where either one or both of n and l are even [121, 128]. Both of these correspond to phase-stable regions. For the present work, only $s = 1$ and $s = 3$ are of any practical interest, but it should be emphasized that all the structure present in the experimental time of flight profiles in chapter 4.4 is not due to noise, but may in fact be explained by the inherent dynamics of the decelerator.

Of course, the description of the decelerator so far involves only one of three dimensions, or two of six coordinates. In the next section, it will be investigated what restrictions the transverse movement of the molecules through the apparatus imposes on this simple model.

4.1.2 Transverse Motion

The dynamics involved in a Stark decelerator have been explored and described in detail before [12, 123], especially regarding the stability of trajectories when longitudinal and transverse motion are treated together in a full six-dimensional approach [120]. It has been found that under certain circumstances, it is preferable to use the $s = 3$ mode of operation instead of the more intuitive $s = 1$ [122, 129]. No full description of transverse motion and its coupling to the longitudinal motion will be given in this section, instead only the aspects important for understanding the decelerator and the distribution of molecules which will finally hit the surface will be reviewed, based on the references mentioned above.

When comparing the one-dimensional model with trajectory simulations which numerically integrate the full equation of motion for a large variety of initial conditions,

rich dynamics are revealed. As can be seen in Fig. 4.5, the one-dimensional model correctly predicts the general outline of the phase stable regions, but inside these areas, instable regions are observed. These appear as a distinctive ring, called the halo, which is seen up to values of $\phi_0 \approx 60°$, and a central hole which is only present at low phase angles. Moreover, the phase space acceptance is larger than predicted for low phase angles, starting at about 60°. Since the plain longitudinal model clearly misses these features, an explanation has to be sought in the coupling of transverse and longitudinal motion.

To gain an insight into the transverse motion of a molecule in the Stark decelerator, it is again useful to approximate the time-dependent forces acting on a molecule as it travels through the array of electrodes by a force which is averaged over switching cycles. For the sake of simplicity, the following treatment will be limited to the case $\phi_0 = 0°$, but qualitatively, the same arguments hold for different values of ϕ_0. Unlike the case of longitudinal motion, one has to include two switching cycles in the average, since every odd pair is rotated by 90°, making the transverse force unequal in alternating stages. As before, this approach is justified if the longitudinal velocity is high enough that the molecule will change its transverse position only slightly within one stage. Considering a molecule with velocity $v_z \approx v_0$, which moves approximately a distance of $2L$ per two switching cycles, this average force is then given by [12]

$$\overline{F}_{x,y}(\phi) \approx \frac{1}{2L} \int_{\phi L/\pi}^{(\phi+2\pi)L/\pi} F_{x,y}(z')dz' \ , \tag{4.35}$$

where again, the phase angle ϕ is the reduced position at the time of switching. Since in the above approximation, the average force is equal for both transverse directions x and y, only y is used below for simplicity. Furthermore, the electric field in the transverse direction, as given in Eq. (4.2), is of the general type $\mathcal{E}(y) \propto -1/(y^2 - y_0^2) \approx 1/y_0^2 + y^2/y_0^4$ for small values of y, where y_0 is a constant. Combined with a nearly linear Stark shift of CO*, one obtains a transverse potential which may be reasonably well approximated as being harmonic, i.e.$\propto y^2$. Thus, to good approximation the equation of motion for molecules in the transverse direction becomes:

$$\frac{d^2y(t)}{dt^2} = -\omega_y^2(\phi)y \ . \tag{4.36}$$

It is important to note that the transverse frequency, ω_y, depends on the phase angle of the molecule, and therefore, for all non-synchronous molecules, on time. Due to the symmetry of the electric potential, $\omega_z(\phi)$ is symmetric about $\phi = 0$. The transverse frequency of a molecule will follow the longitudinal motion of the molecules at twice their frequency, because within every half-period of longitudinal oscillation, ω_y has the same value at $+\phi$ and at $-\phi$. Hence, we may expand the squared frequency of the molecule as a Fourier series with a periodicity of $2\pi/2\omega_z$ and write the equation of motion as [120]

$$\ddot{y}(t) = y \sum_{n=0}^{\infty} \omega_{y,n}^2 \cos(n2\omega_z t) \ . \tag{4.37}$$

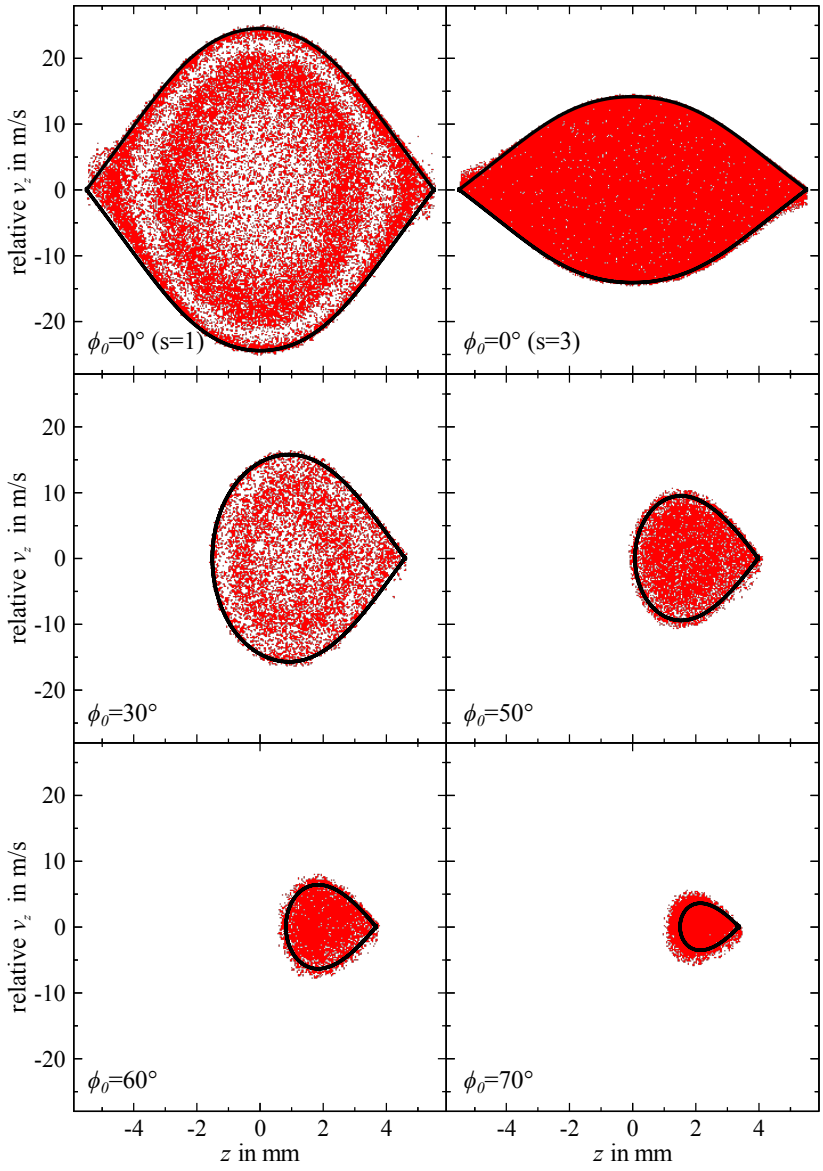

Figure 4.5: Longitudinal phase-space acceptance for different synchronous phase angles, ϕ_0, obtained from trajectory simulations. The $s = 1$ mode of operation is used unless indicated otherwise. Red dots are positions in the (v_z, z) phase space of molecules which will reach the end of the device, at the time the decelerator is switched on the first time. For comparison, separatrices of the 1-D longitudinal model are shown as black lines. In the 3-D model, unstable regions are found even in the area predicted to be phase-stable by the 1-D theory.

This differential equation is called *Hill's equation* [130], and is well-known if one neglects all terms of second and higher order. In this specific case, it becomes the *Matthieu* differential equation, which is commonly used to describe the motion of ions in a Paul trap [131, 132].

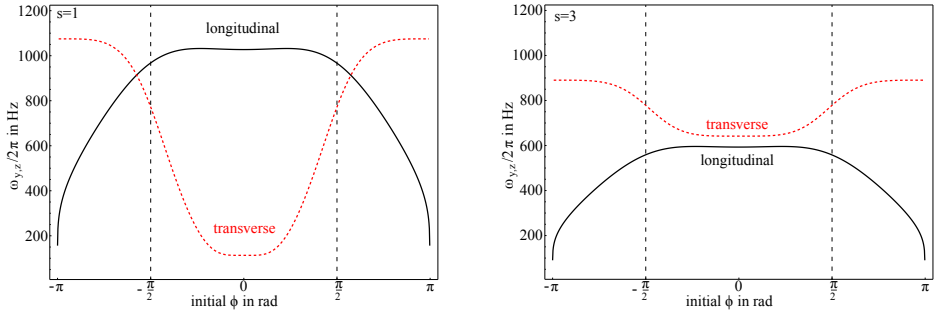

(a) $s = 1$ mode (b) $s = 3$ mode

Figure 4.6: Comparison of longitudinal (black, solid) and transverse (red, dashed) oscillation frequencies $\omega_z/2\pi$ and $\omega_y/2\pi$ as a function of initial reduced position ϕ relative to the synchronous molecule for the guiding operation mode ($\phi_0 = 0$). The positions of the electrodes are indicated by dashed vertical lines.

Hill's equation exhibits regions of stability in the $\omega_{y,n}$ parameter space [133, p. 93], meaning that for certain ranges of $\omega_{y,n}$ values, stable solutions exist, equivalent to oscillating behavior of $y(t)$ in a stable phase-space region. Parameter values outside the stable region will lead to trajectories which oscillate with exponentially growing amplitude, resulting in loss from the decelerator. In fact, it has been shown that for the case of guiding, the missing ring in the longitudinal acceptance of a Stark decelerator may be associated with the unstable regions resulting from the Matthieu equation for transverse motion [120].

Rather than solving Hill's equation directly, a more intuitive understanding of losses in the decelerator may be obtained from a close inspection of the natural longitudinal and transverse frequencies of oscillation. These are depicted in Figs. 4.6a and 4.6b for the $s = 1$ and $s = 3$ mode, respectively. The longitudinal frequency, ω_z, is readily obtained from a numerical solution of Eq. (4.17). The transverse frequency, $\omega_y(\phi)$, can be retrieved by fitting the effective transverse potential to the Ansatz $U_{\text{eff},\phi}(y) = \frac{m}{2}\omega_y^2(\phi)\, y^2$ within 1 mm off axis. The effective potential itself is obtained by averaging of the transverse potential over two switching cycles.

The most important feature in the $s = 1$ case shown in Fig. 4.6a is the crossing close to $\phi = \pm 3\pi/4$, which is fairly close to the region where the empty halo appears in the phase space. Molecules with an initial reduced position near this crossing will be transversely driven with a frequency close to their resonance frequency. Driving this oscillation leads to parametric amplification, in which the amplitude of the trans-

verse oscillation grows exponentially until the molecules crash into the electrodes. For the Stark decelerator, this is equivalent to a zone of instable trajectories in the region where ω_z and ω_y are equal or almost equal.

The empty hole in the center of the phase space acceptance, which is clearly visible in the trajectory simulations shown in Fig. 4.5 for small phase angles in the $s = 1$ mode, is due to a different loss mechanism. Since the synchronous molecule is always closer to the grounded pair of electrodes than the charged ones, the transverse focusing forces are very weak. This leads to a high probability for molecules to be lost in the transverse directions, despite the fact that longitudinally they would seem to be the most stable ones. As this loss mechanism is slow, the boundary of this region is rather diffuse, in contrast to the outer ring which is rather well-defined.

For high phase-angles, the stable area in the trajectory simulations eventually starts to surpass the bounding separatrix. To understand why this is the case, consider a molecule with velocity $v = v_0$ and position $\phi = \phi_0$ identical to the synchronous molecule, but traveling about 1 mm off the molecular beam axis. As it approaches the electrodes, it will experience an electric field strength which is higher than on the axis, and will hence penetrate less deep into the electric field stage. This means that when the electrodes are switched, the longitudinal position of the off-axis molecules is further away from the electrodes. Thus, the molecules may be considered to have a lower phase angle. One can therefore think of the decelerator operating at an *effective* phase angle $\phi_{0,eff} < \phi_0$, which represents an average over the transverse distribution. As their phase angle increases, molecules spend more time close to the electrodes. Thus, the effective phase angle will be close to the nominal value at low values of ϕ_0, and only deviate significantly at higher values. This is exactly what is observed in Fig. 4.5: For $\phi_0 \geq 60°$, phase space acceptance is increased due to the higher value of the effective phase angle. In principle, this means that deceleration is possible even for $\phi_0 = 90°$, which indeed has been observed [120]. Deceleration at $\phi_0 = 90°$ and acceleration at $\phi_0 = -90°$ are also observed in the experiments that are shown in Fig. 4.14 and Fig. 4.16 in sections 4.4.2 and 4.4.3, respectively. For convenience, time sequences are nonetheless labeled by their nominal phase angle ϕ_0, since it provides a more intuitive representation of the switching times.

In stark contrast to the situation for $s = 1$, trajectory simulations in Fig. 4.5 for guiding in $s = 3$ mode show no signature of instable areas. Consulting Fig. 4.6b reveals the reason for absence of the unstable halo: No crossing of longitudinal and transverse frequencies is observed in the case of $s = 3$ guiding, so no parametric amplification of either motion takes place. Moreover, since only every third stage is being switched, molecules initially around $\phi = 0$ pass through one pair of charged electrodes. This improves the transverse confinement, at the cost of a small loss in longitudinal acceptance. Even though the total number of molecules will be similar for $s = 1$ and $s = 3$ for guiding, the $s = 3$ mode is preferred because it offers a better longitudinal velocity resolution and also yields a more pronounced and homogeneous peak shape due to the uniform filling of the phase space. In this mode, however, only every third stage is effectively used for kinetic energy manipulation. Since the lifetime of $CO^\star$ of 2.63 ms is on the order of time of flight through the apparatus, it would be unfavorable to

construct a decelerator meant to be operated in this mode for deceleration. Instead, all experiments involving deceleration and acceleration described in this thesis are conducted in the $s = 1$ mode unless stated otherwise.

It should be noted that there are two other loss mechanism, the first of which imposes a severe restriction on deceleration: If molecules move slowly enough, the assumptions used to construct the effective transverse potential become invalid, and a pronounced coupling of longitudinal and transverse motion leads to the loss of most molecules. The onset of this effect is observed at velocities as high as 100 m/s, and no molecules are observed behind the decelerator for velocities smaller than 30 m/s. This intrinsic problem may be overcome either by using specially designed electrodes for the last stages of the decelerator, or by constructing a so-called ring decelerator [99] which was mentioned in the introduction to this chapter. The other loss mechanism is related to so-called non-adiabatic transitions. As the molecule travels through the decelerator, it may pass regions of very low electric field strength. The change of Stark energy with time, either due to the molecule's motion or the switching of the electric fields, may induce transitions to non-low-field seeking states, as described in reference [134].

$\phi_0(^\circ)$	v_f(m/s)	Δv_f(m/s)	$E_{\text{coll}}(\text{cm}^{-1})$	$\Delta E_{\text{coll}}(\text{cm}^{-1})$
−90	512	4	307	4.8
−50	470	11	259	12.1
−30	430	16	216	16.1
0	360	14	152	11.9
30	272	16	87	10.2
40	235	14	65	7.4
50	193	11	44	5.0
60	145	8	25	2.7
70	87	6	8.9	1.2
75	50	4	3.0	0.5

Table 4.1: Final velocity, v_f, and collision energy, E_{coll}, for different phase angles at an initial velocity of 360 m/s. Energy and velocity width refer to half the width of the full phase-stable area. Values for $\phi_0 = 0$ are given for the $s = 3$ mode.

In addition, the mere rotation of the vector of electric field strength by 90° at the time of switching may be too fast for the molecule to follow adiabatically [135]. For CO*, these losses have been observed in deceleration experiments on a chip [98], but not yet in a Stark decelerator. To minimize regions of small electric fields, the switches can be operated not between high voltage and ground, but between high voltage and $V_{bias} \leq 300$ V. No effect of applying a bias voltage has been observed, indicating that non-adiabatic transitions do not play a major role for Stark deceleration of CO*.

From the full-fledged three-dimensional trajectory simulations as shown in Fig. 4.5, it is straightforward to determine the final velocity as well as the velocity spread. The

velocity spread, Δv_f, for a given final velocity, v_f, is highly relevant in scattering experiments, since it determines the energy resolution with which the scattering process can be probed. An overview of final velocities and the associated velocity width can be found in table 4.1 for commonly used phase angles and an initial longitudinal velocity of 360 m/s. Values for the collision energy, E_{coll}, i.e. the kinetic energy corresponding to the z-component of the final velocity, and the energy width, ΔE_{coll}, are given in addition. Note that all values for Δv_f and ΔE_{coll} correspond to half the width of the full phase-stable area.

4.2 Simulation of the Molecular Beam Machine

The analytical concepts developed in the previous section are well suited to obtain an intuitive understanding of the motion of molecules in the decelerator. In order to predict the final phase-space distribution of molecules, it is nonetheless advisable to use a full three-dimensional numerical simulation of the machine, results of which have already been presented. Simulations are performed using the `libcoldmol` particle trajectory calculation framework [79], which was extended to incorporate a variable-size Stark decelerator and a freely rotatable hexapole focuser. Electric fields and electric field gradients are calculated employing the program `COMSOL` [78] and tabulated as separate files, as is the Stark effect of CO $a^3\Pi_1(v = 1, J = 1, M\Omega = -1)$, which is computed as described in reference [57]. The equation of motion, $\mathbf{F}(\mathbf{r}) = m\, \mathrm{d}^2\mathbf{r}/\mathrm{d}t^2 = -\nabla W(\mathcal{E}(\mathbf{r}))$ can then be rewritten as

$$\frac{\mathrm{d}^2\mathbf{r}}{\mathrm{d}t^2} = -\frac{1}{m}\frac{\mathrm{d}W}{\mathrm{d}\mathcal{E}} \times \nabla\mathcal{E}(\mathbf{r})\,, \tag{4.38}$$

where the values of $\nabla\mathcal{E}(\mathbf{r})$ and $\frac{\mathrm{d}W}{\mathrm{d}\mathcal{E}}$ are easily interpolated from the tabulated gradient and Stark energy. The task of calculating the trajectory is therefore reduced to looking up numbers in large arrays, cubic interpolation between them, and numerical integration of equations of the type $\mathrm{d}^2\mathbf{r}/\mathrm{d}t^2 = const$. Of course, switching of the electric fields has to be accounted for correctly. Numerical integration is performed using a standard Runge-Kutta implementation from the *GNU scientific library* [136]. The `libcoldmol` program allows the user to define the initial phase space distribution of molecules in terms of typical molecular beam parameters (spatial and velocity position and width), skimmer position, supply a burst file identical to the ones used for running the experiment (see section 5.4), and specify details for the time and position where molecules are detected. In addition, time sequences are easily generated by solving Eq. (4.38) along the beam axis for z and v_z only. The user merely has to provide the synchronous phase angle and the starting position. In addition, the machine is freely scalable, meaning that number of decelerator stages can be changed, voltage on both hexapole and decelerator can be adjusted, and hexapole position may be chosen as preferred, by adjusting a simple input file provided for simulation. Fig. 4.7 shows a simulation for typical experimental conditions and operation of the decelerator in $s = 3$ mode at $\phi_0 = 0°$. The simulation is useful to understand the origin of

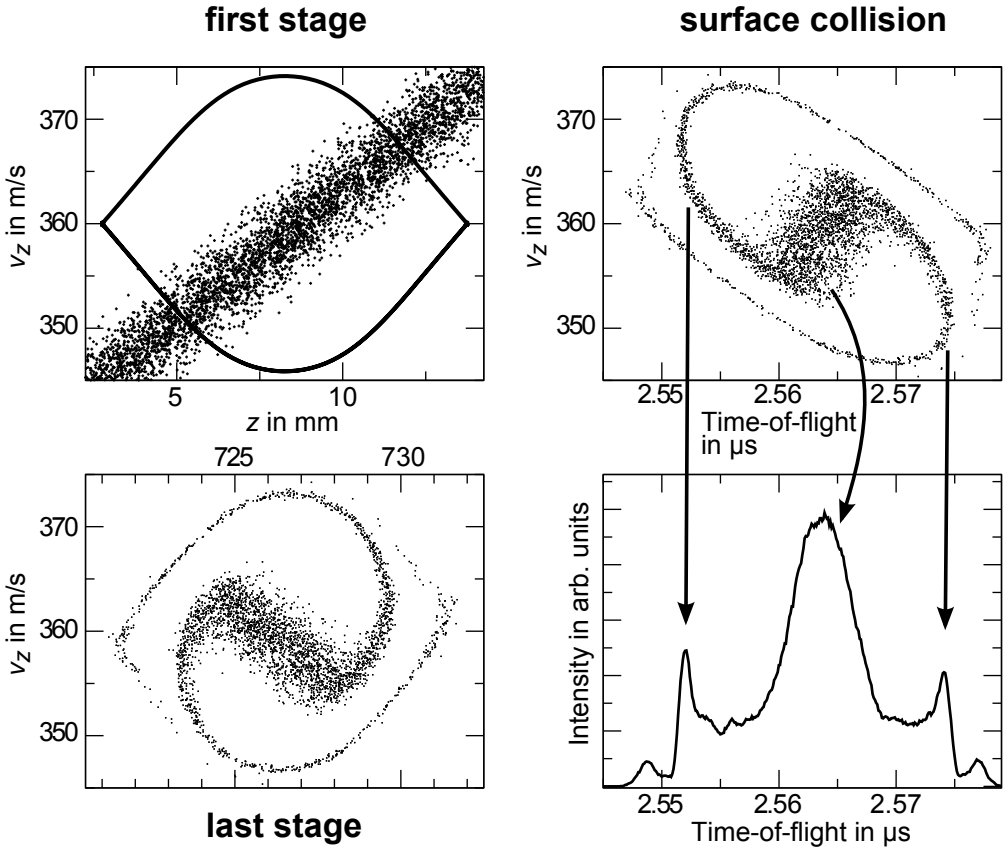

Figure 4.7: Simulation of the time evolution of the CO* distribution for a typical experiment. A narrow slice is coupled into the decelerator acceptance in the first stage (upper left). In the decelerator, the molecules start to rotate in the (v_z, z) phase space. Due to the different oscillation frequencies, a characteristic spiral structure is observed after the last stage (lower left). This spiral structure gives rise to a distinct peak shape in the time-of-flight intensity profile, which in the case of $s = 3$ guiding consists of a main peak and two pronounced side peaks (right side).

the different peaks in the observed time-of-flight profile, which are due to the rotation in phase space of the packet of $CO^{\star}$ molecules in the region bound by the separatrix throughout the decelerator.

4.3 A Bakeable Stark Decelerator

Combining a Stark decelerator with a molecule-surface scattering setup imposes certain restrictions on the design of the apparatus. As will be discussed in the next chapter, the vacuum requirements in the scattering chamber necessitate the heating of the machine to temperatures of about 100 °C. In addition, it would be advantageous to bring the front and rear end of the decelerator as close as possible to the hexapole and surface, respectively. For these reasons, the Stark decelerator described in this section is slightly different in design than previous decelerators of the same type.

The Stark decelerator constructed for the research described in this thesis consists of 132 electrode pairs, giving rise to 131 electric field stages. All electrodes are cylindrical with a hemispherical end cap. Electrodes in a pair are oriented parallel to each other, and every odd pair is rotated by 90° with respect to the even pairs, resulting in the pattern shown in Fig. 4.8a. The other dimensions of the decelerator are identical to those of the first Stark decelerator prototype [8]: Electrodes are 3 mm in diameter, the gap between electrodes in a pair is 2 mm wide, and the center-to-center distance between adjacent electrode pairs is 5.5 mm. The length of electrodes is chosen such that the hemispherical end caps start at a distance of 4 mm away from the center axis, which has been determined by simulations to be sufficient not to disturb the electric fields in the gap region. All electrodes pointing in the same direction are mounted to a stainless steel rod, which is connected via two rod-shaped ceramic insulators to a stainless steel support frame. The rods are oriented such as to make the resulting square-pattern of the electrodes form an angle of 45° with respect to the laboratory frame.

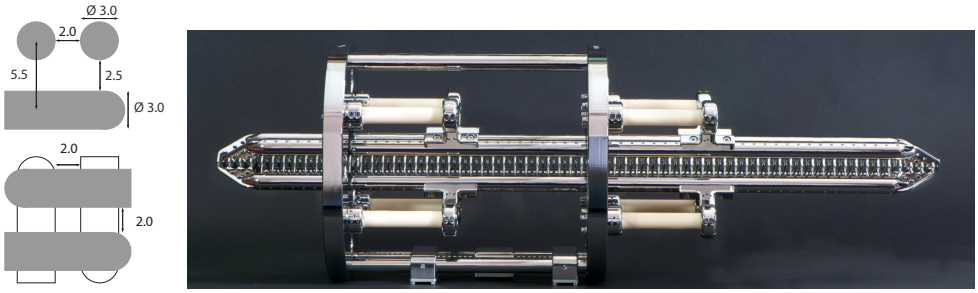

(a) Dimensions in mm.

(b) The fully assembled and aligned decelerator. Note the direction of ceramic insulators. Picture by Georg Heyne, FHI Berlin.

Figure 4.8: The decelerator constructed for the research project.

When taking a closer look at the decelerator, shown in Fig. 4.8b, readers familiar with previous Stark decelerator designs will notice immediately two main features: The decelerator rods are mounted in such a way that all ceramic insulators are pointing in the same direction, and the decelerator is equipped with special end pieces, comprising the first and last four electrodes of each rod. The effect of these end pieces is to reduce the space needed to accommodate the decelerator on either end, since the last electrode needs no additional space for mounting. This design aspect is rather important because it shortens the most critical distances, i.e. at the entrance and exit of the decelerator, where incoupling from the hexapole and close proximity to the surface have highest priority in order not to lose any molecules. While a similar design of decelerator end pieces had been introduced before [129], the new end pieces are considerable simpler in shape, thus reducing the effort and time for machining significantly.

The aforementioned positioning of ceramic insulators is required because the decelerator chamber is subject to baking at temperatures of about 100 °C. Due to the different coefficients of thermal expansion, i.e roughly (all values for $20 - 100\,^{\circ}\mathrm{C}$) $7 - 8 \times 10^{-6}\,\mathrm{K}^{-1}$ for Al_2O_3 [137, p. 446] opposed to $\approx 16 \times 10^{-6}\,\mathrm{K}^{-1}$ for stainless steel 1.4301 (ANSI 304) [138], ceramics and stainless steel parts have to be connected such that no mechanical stress arises at elevated temperatures. Having the ceramic insulators point towards either end of the decelerator would result in a different length of stainless steel parts of the decelerator rods opposed to the decelerator frame. In contrast, distances between mounting points spanned by steel parts are identical in the design of the decelerator shown in Fig. 4.8b.

An aspect which cannot be disregarded in the design of a bakeable Stark decelerator is the fastening of ceramics to stainless steel parts. It is normally realized by clamping of the ceramic by a slitted stainless steel ring, and fixing the ring with small stainless steel bolts. During first bakeout tests, however, it was observed that this connection becomes loose, the result of which is that the decelerator rods are pulled downwards by gravity, severely misaligning the decelerator. Even though the mismatch of diameters between stainless steel clamp and ceramic rod will only be on the order of 12 µm at 100 °C, this failure in effective clamping was reproduced in a simplified test setup at temperatures as low as 90 °C. To overcome this problem, one has to introduce either a material with an even higher coefficient of linear expansion, or use spring-loaded parts in the assembly which will maintain the clamping force during bakeout. As the former seems rather error-prone, possibly breaking the ceramics if coefficients of thermal expansion are not perfectly matched over the whole temperature range, threaded ball spring plungers have been added to the clamping rings. Two M8-threaded ball-spring plungers had to be used, the ball itself needing a flat contact area at the tip.

For testing purposes, the setup shown in Fig. 4.9a was constructed, employing double the weight of one decelerator rod clamped to a single ceramic. By varying size and number of different kinds of spring-loaded plungers, the clamping was successfully modified to withstand temperatures of up to 160 °C, failing only at 170 °C while simultaneously being exposed to severe mechanical shock and vibration. The safety

margin of a factor of ≈ 7, resulting from the over-dimensioning of the test setup, is considered safe enough to bake the modified decelerator up to 100 °C. Modifications to the decelerator are marked in Fig. 4.9b. In order to avoid large temperature gradients during bakeout, the decelerator frame is mounted on Vespel polyimide feet, thermally insulating it from the surrounding vacuum chamber, except for a thin copper wire needed for grounding it via a ceramic current feedthrough. The temperature of the decelerator frame can be monitored by two thermocouple junctions placed on either side.

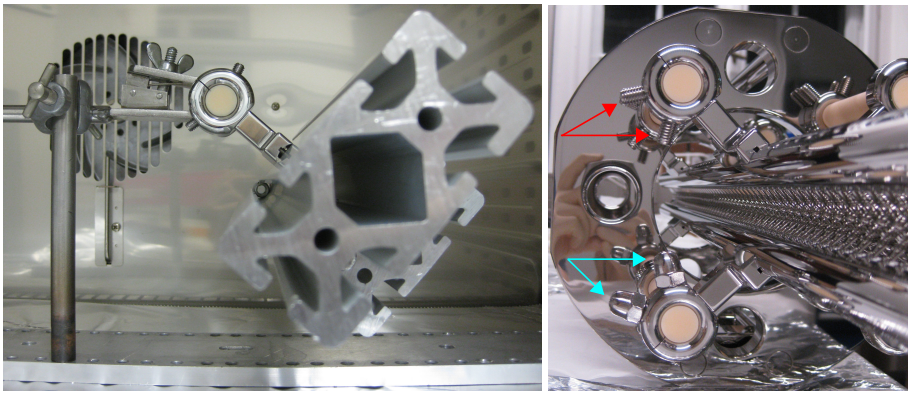

(a) Test setup used in the process of making the decelerator bakeable.

(b) Modified decelerator. Ball-spring plungers and protective caps are marked by red (turquoise) arrows.

Figure 4.9: Modification of the decelerator for bakeout.

The 232 electrodes needed to equip the four rods are hand-selected after visual inspection from a selection of 280 custom-made electrodes. Small deficiencies in the polish are compensated for by an arrangement which places all bruises on one side, and then aligning the corresponding rod such that the well-polished side points towards the other high voltage electrodes. For exact alignment of the decelerator electrodes, only the four mounting rods need to be adjusted, probing the surface-to-surface distance between electrodes with a variety of differently sized gapping tools. First, the beam-axis direction was adjusted recursively with the goal of minimizing the average deviations, then the transversal alignment was conducted. Possibly due to mechanical inaccuracies in the placement of electrode mounting holes, the overall accuracy of both the beam-direction and the transversal gap is only ± 0.075 mm, which is estimated from the worst misalignments being on the order of 0.15 mm.

Alignment of the decelerator with respect to the rest of the beamline is achieved by means of the same optical telescope technique as described in section 3.3. For ease of positioning, the decelerator frame is mounted on four height-adjustable, fine threaded feet, whereas micrometers mounted horizontally to the vacuum

(a) Special end pieces.

(b) Close-up of a single end piece.

Figure 4.10: Details of the decelerator design.

chamber allow horizontal adjustments. Since alignment along the beam axis is far less critical, a simple gapping tool is used to set the decelerator to a distance of 6.5 mm $\pm$ 0.5 mm from both the front and the rear wall of the chamber.

Electrical contact of the decelerator rods is achieved by attaching thin wires made from spring steel to the end of four high voltage ceramic feedthroughs (60 kV DC rated), enabling good electrical conductivity while at the same time limiting heat transfer to the rods. The decelerator is supplied with high voltage via four high voltage push-pull switches identical to the ones used for the hexapole (*Behlke Power Electronics GmbH* HTS-201-06-GSM). All of the switches are dipolar such that the polarity of the high voltage can easily be switched. Moreover, all switches may be chosen to pull the voltage not to ground when off, but instead to a small bias voltage, which may be applied by connecting a low-voltage power supply to the opposite polarity input. The voltage on the decelerator can be controlled independently from the voltage on the hexapole by means of its own two capacitor charging power supplies, with typical operating voltage in the range of $14 - 16.5$ kV.

In an effort to increase the maximum operating voltage of the decelerator, extensive tests have been performed using molybdenum electrodes. Since molybdenum has a very high melting point of 2622 °C [50, p. 12-206], it is also expected to be a suitable material in high voltage applications. In test setups, it was indeed possible to achieve DC high voltages of $\pm$23.0 kV and $\pm$11.0 kV between two hand-polished, rod-shaped molybdenum electrodes (3 mm in diameter, 1 mm and 0.3 mm surface-to surface distances), which corresponds to maximum field strengths of about 510 $^{\mathrm{kV}}/_{\mathrm{cm}}$ and 760 $^{\mathrm{kV}}/_{\mathrm{cm}}$, respectively. However, similar values could be established for stainless steel electrodes, which indicates that the limiting factor for discharging is not just the electrode material, but also the surface finish is extremely important. Since molybdenum is known to be very hard and not easily machinable, it is much more complicated

to polish than common stainless steel (1.4301/ANSI 304). Taking into account that its coefficient of linear thermal expansion, $\alpha_{Mb} = 4.8 \times 10^{-6}\,\mathrm{K}^{-1}$ [50, p. 12-206], is also extraordinarily low for a metal, it is very hard to incorporate it into a bakeable setup, unless one replaces all metal parts of the decelerator by molybdenum. Considering the cost of material, machining, and additional time this would take, a minor gain in operating voltage does not appear to justify the construction of a normal-size Stark decelerator from molybdenum. Note that a miniature wire Stark decelerator made up from tantalum wires mounted on molybdenum supports has been built [139], which is similar to the one introduced in reference [140]. However, due to the much larger scale, this is not realistic for a full size Stark decelerator.

Prior to its first operation and after each exposure to air, both hexapole and decelerator need to undergo a treatment known as *conditioning*. For this process, a DC high voltage is applied to opposing electrodes, and the current between power supply and electrode is being monitored by a digital multimeter with 10 nA resolution. A large ($R \approx 100\,\mathrm{M\Omega}$) resistor, in series with the power supply, protects the setup. At the same time, the pressure in the vacuum chambers is monitored, so that any coincidence of a pressure rise with an electric current can be attributed to an electric breakdown between electrodes. The voltage is then increased in small steps, typically starting at $\pm 8\,\mathrm{kV}$ at a rate of $\pm 1\,\mathrm{kV}/5\,\mathrm{min}$, until the first small discharges can be detected, whereupon the voltage is kept constant until no further discharges can be seen.

The reasoning behind this procedure is the following: Electric breakdown may be caused by surface roughness and contamination in two ways: At points which are microscopically tip-like or sharp, the local field strength will be very high, leading to field emission of electrons. Similarly, contaminant particles on the surface may assemble charge and consequently be repelled from the surface, being accelerated on the oppositely charged electrode. Upon impact, this causes local heating and melting of the surface, potentially leading to the release of more particles from the surface. If a breakdown becomes big enough, it will eventually destroy the high voltage electrode, sometimes even leading to a macroscopic impact crater and characteristic color of the surface, which is readily seen with the naked eye. Small discharges, however, have a "healing" effect, since they locally smooth the surface by melting, thus removing any pointed spots which could potentially cause a fatal destructive discharge at higher voltages. Since the detailed exploration of these effects is a vast field of research on its own, no extensive references will be given, instead the interested reader may find references [141, 142] useful for getting an insight into the topic.

Because of the $100\,\mathrm{M\Omega}$ resistors needed to limit the breakdown current, the conditioning procedure is performed using DC current. In general, the breakdown voltage of any dielectric, including vacuum, decreases with increasing frequency of the applied voltage. In order to account for this lower breakdown voltage, the conditioning is performed to a 10 % higher voltage than is subsequently used in pulsed operation. Still, the magnitude of electric field strength achieved seems too low compared to theoretical predictions. It has been empirically determined that for polished stainless steel electrodes of various geometries, the maximum breakdown voltage is given

by [141]:

$$V_b = \alpha^{-1} E_b d = \alpha^{-1} d \times 580\,\mathrm{kV/cm}\; S_{eff}^{-0.25}\,, \tag{4.39}$$

where $\alpha = E_{avg}/E_{max}$ is a shape factor, S_{eff} in cm^2 is the area exposed to 90 % of E_{max}, V_b is the breakdown voltage across electrodes, and d is the gap width. Using Eq. (4.2), the electric field strength along the electrode circumference, $\mathcal{E}_{rod}(z)$, can be calculated by the substitution $x(z) = d - \sqrt{R^2 - z^2}$. Solving the equation $\mathcal{E}_{rod}(z) = \mathcal{E}_{rod}(z = 0)$ for z yields an angle of 44° along the circumference exposed to 90 % of $\mathcal{E}_{max}$. From this value, assuming an overlap of 8 mm for the electrodes, and using a ratio of $\alpha = 1.21$, the theoretical breakdown voltage can be calculated to be ±43 kV at a maximum field strength at the electrodes of 1050 kV/cm, which is more than twice as high as ever observed in any known Stark decelerator. This is most likely due to the fact that high voltage breakdown is a statistical process — common Stark decelerators sample about 100 electrode pairs, of which only the least well polished is detected as causing an electric breakdown.

4.4 Stark Deceleration of $CO^\star$

In the process of characterizing the performance of the Stark decelerator, a test setup was used which already incorporated the final scattering chamber, but none of the equipment needed to conduct surface scattering experiments. The decelerator is aligned collinear with the main beam axis (i.e., with the axis connecting the two circular apertures which delimit the decelerator vacuum region), starting 6.5 mm surface-to-surface distance behind the wall separating it from the hexapole. The same commercial MCP detector used previously (*R. M. Jordan Co., Inc.* C-0701, 18 mm active diameter) was mounted to an "inverse" full nipple which extends deep enough into the surface chamber from its rear to position the detector surface 46 mm downstream from the center of the last decelerator electrode.

4.4.1 Coupling Molecules into the Decelerator

In order to obtain the maximum number of CO molecules after deceleration or guiding, it is not *a priori* clear whether excitation of CO to the metastable state is best done directly in front of or behind the skimmer. The reasoning behind the first option is straightforward: As the density will be higher close to the nozzle, more CO molecules can be excited at the same fluence and beam size of the laser. Some quenching, i.e. de-excitation due to collisions with carrier gas, may however occur directly after laser excitation, since the supersonic expansion is not fully completed in front of the skimmer. Moreover, some of the molecules excited in front of the skimmer will not make it through the aperture behind the hexapole for geometrical reasons (cf. section 3.2), while excitation behind the skimmer is likely to catch only molecules on favorable trajectories. The overall excitation efficiency was compared by optimizing the position and focus size of the beam for each excitation position separately. Unfortunately, the results were inconclusive due to large signal intensity drifts unrelated to

the laser excitation. The signal intensity of CO* behind the decelerator is of comparable magnitude in both cases, but it remains unclear whether excitation in front of or behind the skimmer should be preferred. Unless mentioned otherwise, experiments are performed with excitation of CO behind the skimmer.

For optimizing the performance of a Stark decelerator, only a few parameters exist which can be varied. Once the initial velocity is fixed, as in this case at 360 m/s, the time difference between laser excitation and first switching of the decelerator, also known as *burst delay* or *incoupling time*, is most important. Since the position of laser excitation is known only approximately, the burst delay has to be optimized to correspond to the correct distance to the position where the decelerator is first switched on. Due to the periodicity of $2L = 11$ mm of the array of electrodes, a time scan of the burst delay will exhibit a periodicity of 30.6 µs for the case of guiding at 360 m/s. For deceleration (acceleration), the first switching of the decelerator takes place later (earlier) than for guiding, thus the burst delay has to be changed accordingly. In the setup described here, all burst files have been defined relative to a fixed laser excitation position. The time of free flight to the position where the decelerator is switched on is thus encoded in the burst file, and no correction is needed regardless of the phase angle ϕ_0.

Optimization can easily be achieved by recording the CO* intensity in a time gate centered at the expected arrival time while varying the burst delay. Alternatively, one can determine the correct burst delay by plotting the time-of-flight traces for different burst delays in a contour plot, as shown in the upper right panel of Fig. 4.11. The intense area in the center of the plot corresponds to incoupling into the correct stage, while the regions on the upper left and lower right correspond to incoupling of molecules two stage too late and two stages too early, respectively. Note that due to the CO excitation by a short laser pulse, only a longitudinal slice is coupled into the longitudinal decelerator acceptance, as indicated by the red area in the lower right panel of Fig. 4.11. As a result, the intense region in the contour color plot is not homogeneously filled, and the time-of-flight profiles depicted in the lower left panel of Fig. 4.11 exhibit two pronounced side peaks (compare Fig. 4.7 in section 4.2). As long as the burst delay is shifted by less than ± 15 µs, the arrival time of the guided peak remains the same, but the peak itself will become asymmetric, as can be clearly seen in the green and black time-of-flight traces depicted in the lower left panel. The maximum of the time-integrated signal shown on the upper left of Fig. 4.11 only matches the best incoupling time if the integration gate is perfectly adjusted. In addition, an irregular laser excitation profile containing different "hot spots" will cause an asymmetric filling of the phase space acceptance, complicating the task of determining the correct burst delay from the integrated signal of the burst delay time scan alone. Centering the burst delay on the intense region, however, provides a robust method for correct incoupling. Instead of adjusting the burst delay, it is also possible to scan the excitation laser position along the beam axis until a symmetric peak structure is observed in the time-of-flight profile. Apart from the time shift needed for deceleration and acceleration, which is encoded in the burst file, the burst delay optimized in this way does not have to be corrected when $\phi_0 \neq 0$ is used. This indicates that the method

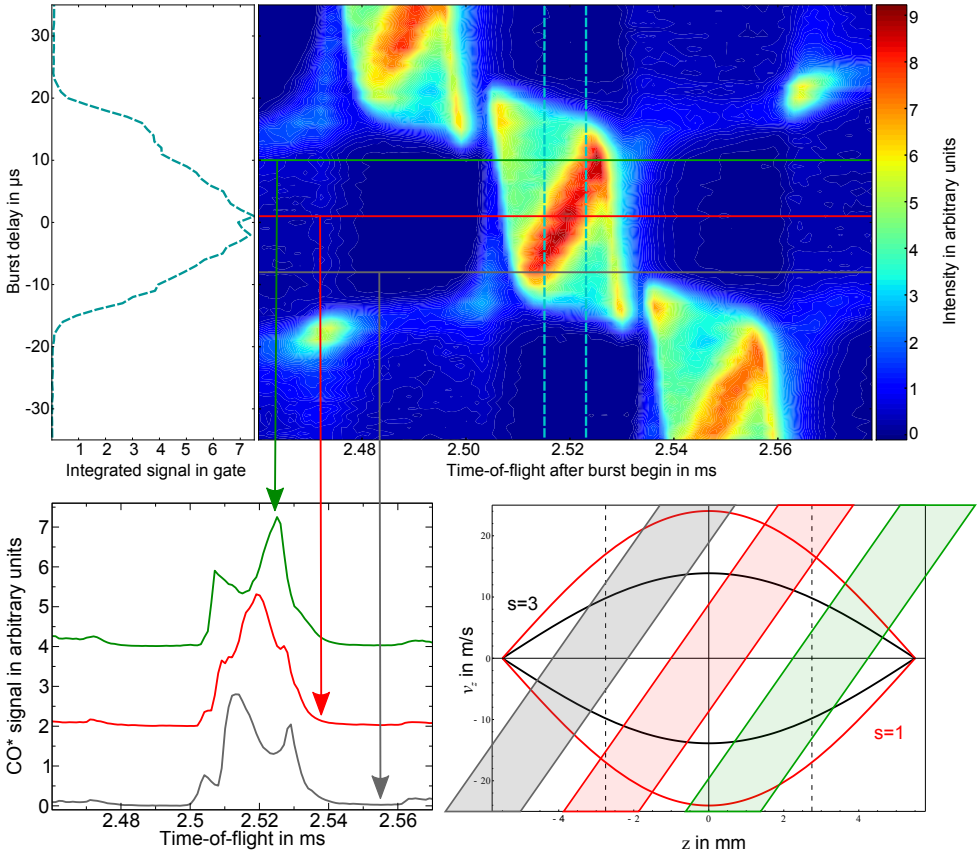

Figure 4.11: Scan of the incoupling time into the Stark decelerator. CO* intensity (color coded) versus burst delay and arrival time at the detector is shown on the upper right side. The panel on the upper left shows the CO* signal integrated over the time gate indicated by dashed vertical lines. Individual time-of-flight traces and schematic of the longitudinal phase space for early (green), late (black), and optimum (red) incoupling are shown on the lower left and right, respectively. All data is for $s = 3$ guiding at 360 m/s, using a preamplifier which limits time resolution.

described above provides a very sensitive way of optimization.

4.4.2 Optimizing the Stark Decelerator

Upon initial alignment of the decelerator, it was noted that with increasing phase angle, the experimental decelerated signal drops much faster than predicted by simulations. An example of this is shown in Fig. 4.12; the slowest final velocity where

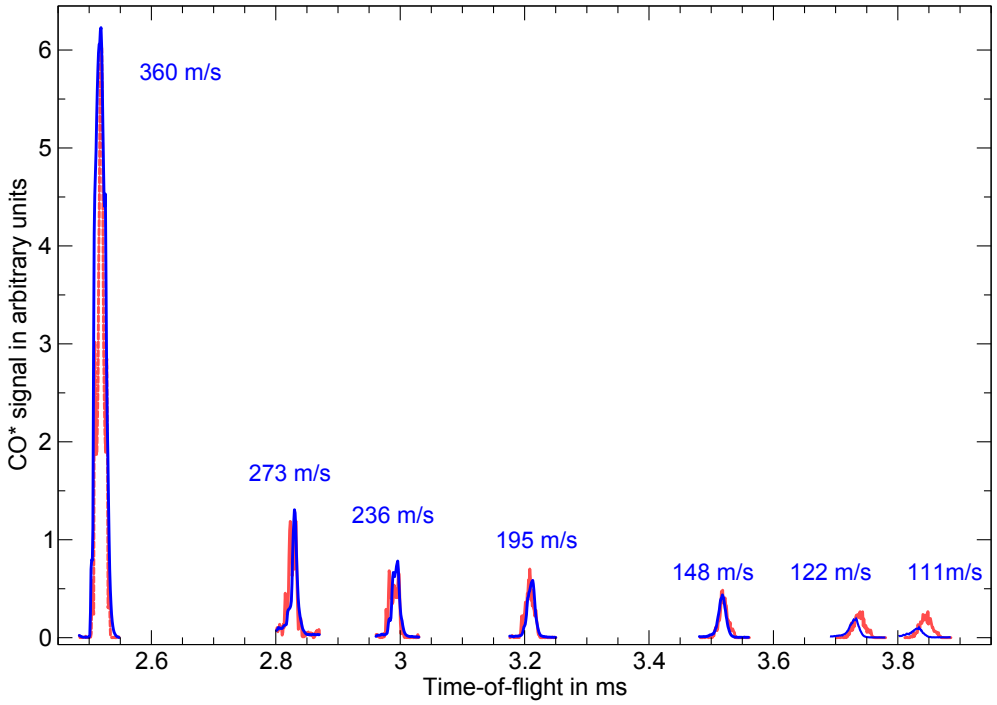

Figure 4.12: Experimental (solid blue lines) and simulated (light red lines) time-of-flight profiles for deceleration at a voltage of ± 14 kV, with the decelerator in its original alignment. The experimental signal at higher phase angles drops compared to simulations.

signal is still observed is at 111 m/s. This behavior is attributed to longitudinal misalignment of the decelerator (see section 4.3, p. 59). The disturbed periodicity of the electrode array is likely to cause an instable region at the theoretical separatrix, thus shifting the real separatrix inward, which effectively increases the phase angle.

For a more thorough characterization, the decelerator is mapped out in the following way: Time sequences of high voltage switching calculated for ± 14 kV are used to scan the final velocity of the beam, and the signal of the decelerated or accelerated peak is recorded as a function of final velocity and actual voltage applied to the decelerator. When varying the voltage, the final velocity remains unchanged, since it is

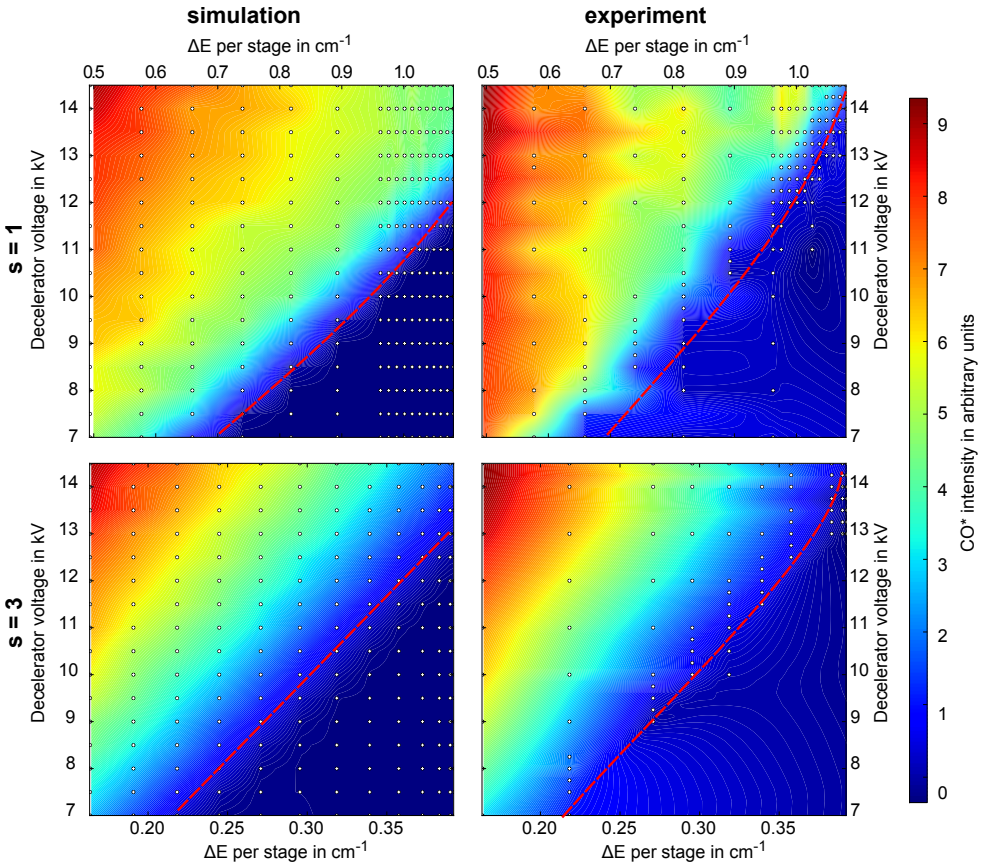

Figure 4.13: Contour color plot of integrated CO* intensity in decelerated peak as a function of energy removed per stage, as determined by the time sequence, and voltage applied to the decelerator. The black and white dots indicate actual data points used for creating the contour plot. A label of 14 kV corresponds to a voltage of $\pm$14 kV applied to opposing rods. Lines of equal signal are nearly linear in the simulations (left), while the signal breaks down at high ΔE for experimental data (right). Dotted red lines are a guide to the eye of the position where the signal disappears, i.e. where phase stable deceleration stops. The effect is present for deceleration in both $s = 1$ and $s = 3$ mode. All data is corrected for different decay of CO* due to different arrival times at the detector.

enforced by the time sequence. Hence, the molecules travel up the potential energy hill to the same height as before, which will be at a different position, thus changing the phase angle of the operation. Results of this two-dimensional scan are summarized in Fig.4.13, where the color-coded integrated intensity of the decelerated peak

is plotted as a function of energy removed per stage, ΔE, and high voltage applied to the decelerator electrodes.

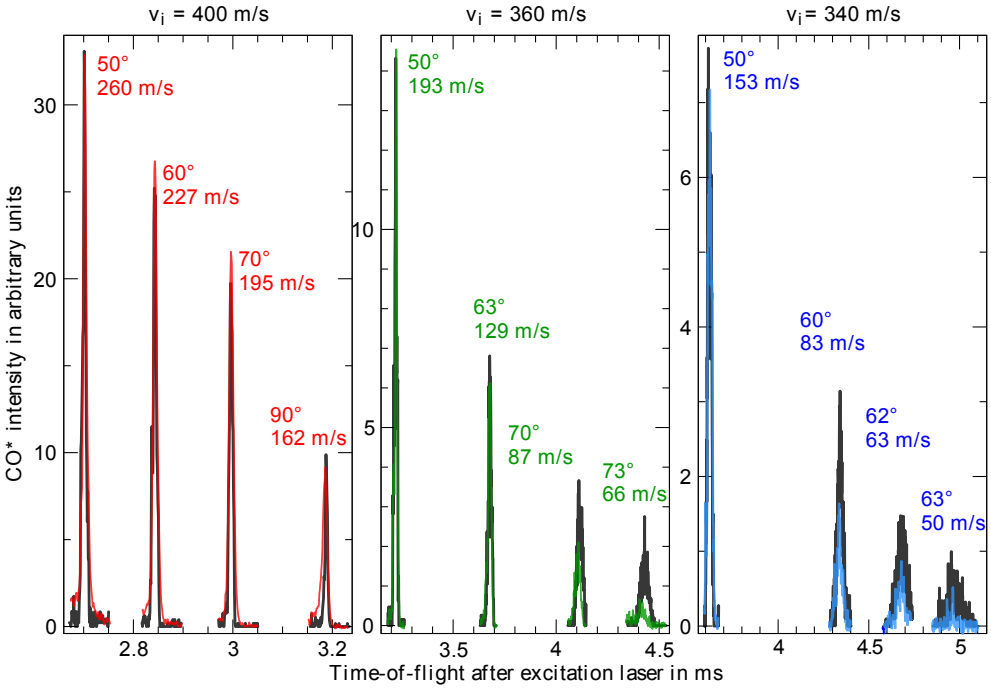

Figure 4.14: Experimental time-of-flight traces for deceleration at an operating voltage of $\pm 16\,\mathrm{kV}$ compared to simulations (black) for $\pm 14\,\mathrm{kV}$. Excellent agreement is seen for an initial velocity of $400\,\mathrm{m/s}$ (left, red traces), but for lower initial velocities of $360\,\mathrm{m/s}$ (center, green) and $340\,\mathrm{m/s}$, deviations are seen for velocities below $100\,\mathrm{m/s}$.

Of special importance is the curve representing zero signal, approximated by the dotted red line, since for every voltage, it indicates the time sequence which corresponds to an effective phase angle of 90°, meaning that no phase-stable area exists for stronger deceleration. These curves are nearly linear, as expected for an almost linear stark shift. When comparing experimental data (right) to simulations (left), it becomes apparent that these curves of zero signal exhibit both a steeper slope and deviate from a straight line at high ΔE. If the only effect of misalignment was a constant decrease of phase-space acceptance, then the curves would merely be shifted, but not tilted. It appears that molecules traveling at a slower speed are influenced more severely by the misalignment than faster ones. This is in agreement with the observation that the increase in slope is more pronounced for deceleration in the $s = 1$ mode (upper row) when compared to the $s = 3$ mode (lower row). Even though this experiment still does not provide a clear indication of the problem, it becomes obvious

that the latter may be mitigated by increasing the operating voltage of the decelerator. Indeed, this is confirmed by experiments performed while switching the decelerator

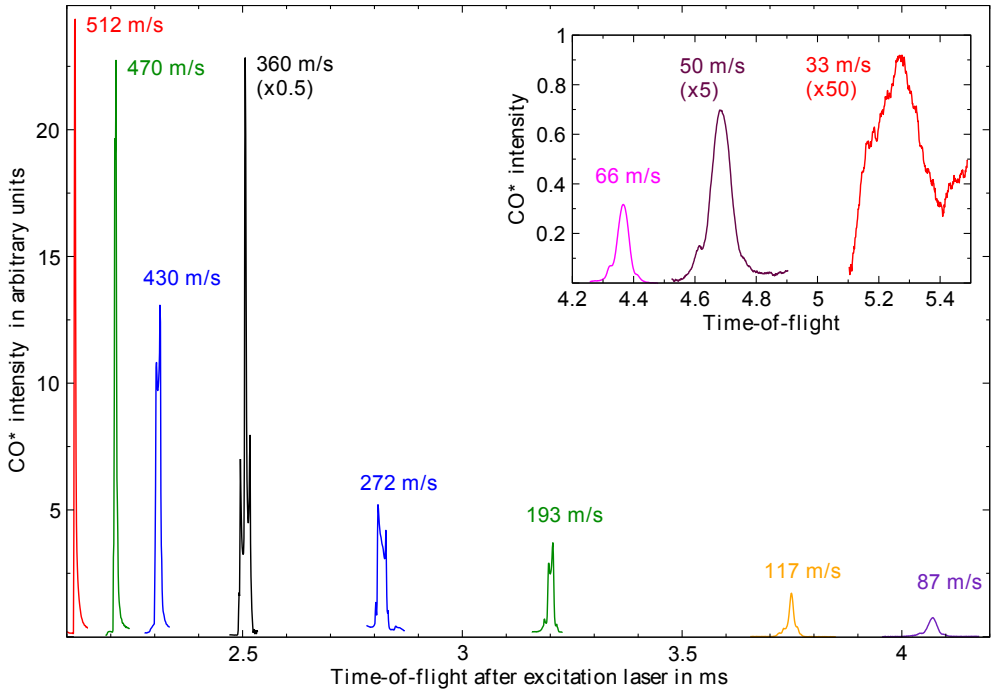

Figure 4.15: Decelerated and accelerated $CO^{\star}$ time-of-flight traces for different final velocities. All data is taken with the re-aligned decelerator operated at a voltage of $\pm 16.5\,\mathrm{kV}$ and initial velocities of $360\,\mathrm{m/s}$. $CO^{\star}$ is detected by collecting electrons ejected upon collision with a Au(111) surface with an MCP. Better time resolution is achieved by using less pre-amplification than in previously shown time-of-flight traces. The inset shows a zoomed version for the lowest velocities, its signal scale is the same as for the main plot.

at $\pm 16\,\mathrm{kV}$. The time-of-flight traces depicted in Fig. 4.14 show quantitative agreement with simulations for $\pm 14\,\mathrm{kV}$ except for low velocities. When comparing, e.g., the last two traces for $v_i = 360\,\mathrm{m/s}$ with the two center traces of $v_i = 340\,\mathrm{m/s}$, it is evident from the parameters used that the signal drop is now exclusively a function of final velocity rather than phase angle.

In the course of the second bakeout, the mechanical framework of the decelerator failed to withstand the elevated temperatures. During the complete realignment of the decelerator, one of the four rods supporting the electrodes was turned around such that rear and front end were interchanged. As a result, the longitudinal alignment of electrodes was observed to be slightly more accurate than before. In addition,

the transverse gap was aligned to a value slightly smaller than before. This realignment enhanced the overall performance of the decelerator, as can be seen from the time-of-flight traces in Fig. 4.15: Final CO* velocities up to 512 m/s and down to 33 m/s are easily accessible when the decelerator is switched at ±16.5 kV and burst files calculated for ±14 kV are used. The main reason for this is believed to be due to an improved decelerator alignment.

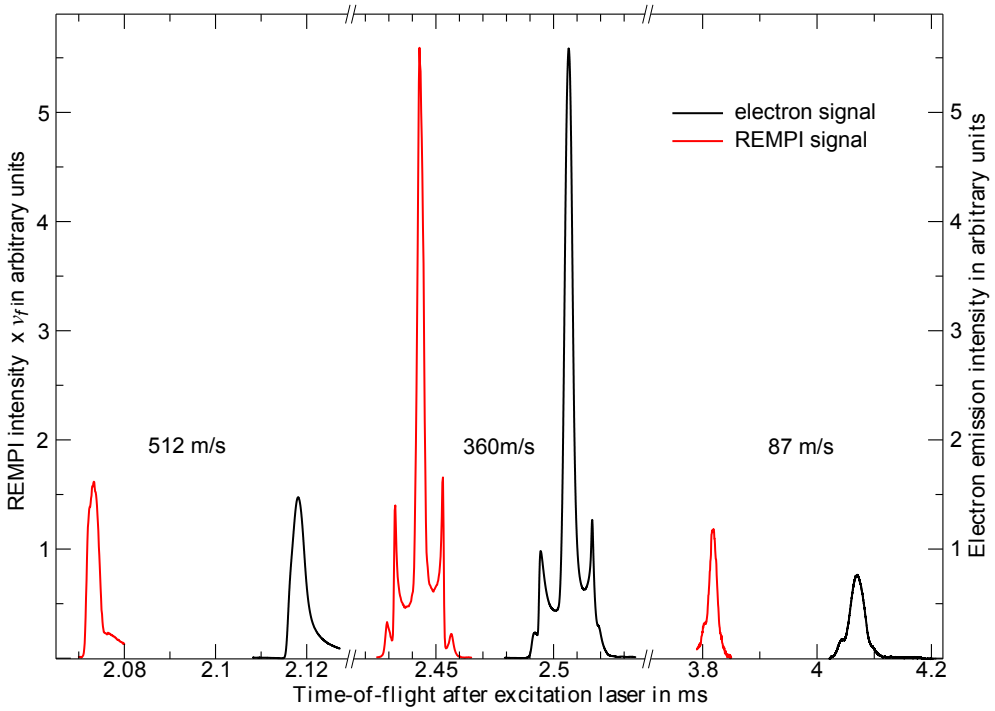

Figure 4.16: REMPI detection of decelerated and accelerated CO* signal 22 mm in front of the surface for different final velocities v_f. For comparison, time-of-flight traces of the electron emission from the surface are shown. All data is taken in the tilted setup at an operating voltage of ±16.5 kV and initial velocities of 360 m/s. The REMPI signal, which is obtained by scanning the time delay between excitation laser and detection laser, has to be multiplied by the final velocity (see text for details).

4.4.3 REMPI Detection of Decelerated Molecules

Metastable CO leaving the decelerator can be detected in two convenient ways: Either by measuring the emission of electrons upon impact on a surface with work function lower than 6.0 eV, or by resonance-enhanced multiphoton ionization (REMPI) of

$CO(a^3\Pi, v = 0, J = 1)$. A convenient $(1 + 1)$ REMPI scheme exists where the first step is resonant with the $b^3\Sigma^+(v = 0) \leftarrow a^3\Pi(v = 0)$ transition at 283 nm wavelength. Absorption of the second photon is sufficient for ionization, whereupon CO^+ can be detected using a multichannel plate (MCP). Refer to section 5.3 for details. For testing the REMPI detection, the ionization laser at 283 nm and a pulse energy of 3 mJ is overlapped with the molecular beam 22 mm away from the surface, using a 750 mm focal length lens set up to produce a focus about 50 mm behind the intersection with the molecular beam. Voltages on the MCP grids are optimized to provide maximum collection efficiency for both electrons and CO^+. By scanning the timing of the REMPI laser with respect to the 206 nm excitation laser, the time-of-flight shown in Fig. 4.16 is obtained. Comparison with the signal of electrons emitted from the $CO^\star$/Au(111) system shows a slight change in peak shape, which is due to the velocity distribution in the molecular beam. Note that REMPI is sensitive to density, while detection of $CO^\star$ using a gold surface measures the flux, i.e. molecules per time per area. Hence, the REMPI signal has to be multiplied by the velocity of the molecules along the main beam axis when the REMPI laser is scanned in time over the molecular beam pulse. This may be pictured more clearly when considering a pulse of uniform density and fixed length in space which is detected by a laser at a fixed sampling rate: The integrated signal is proportional to the time it takes the beam to pass the detection point, i.e. proportional to its inverse velocity, as has been pointed out before [117, p. 73].

4.4.4 Deceleration in the Linear Setup

When operating the machine in the linear setup, care has to be be taken regarding the molecular beam quality. As the aperture behind the hexapole used in the tilted setup is only 2 mm in diameter, but unlike the skimmer has a rounded edge of 3 mm curve diameter, molecules which miss the hole can be reflected back into the beam. In the tilted setup, the major part of the beam misses the aperture completely, and carrier gas impacting close to the aperture will mainly be reflected away from the incoming molecules. For the linear setup, however, the region around the aperture will be exposed to the highest carrier gas flux. Comparing the PMT fluorescence signal of $CO^\star$ between tilted and linear setup, as shown in Fig. 4.17a, provides evidence that the slow part of the molecular beam is indeed heavily disturbed when the disc containing the aperture is in the beamline. In fact, a shift of the beam towards higher mean velocities is observed, and the decelerated signal rises by a factor of 2.8 when the disc containing the aperture is removed. This can be circumvented by using an aperture which is limited by a near 90° edge on the hexapole side, and in addition is wider than just 2 mm. Mounting of a skimmer is not a feasible option, since space is constrained between hexapole and decelerator, and the sharp edges of the skimmer hole are expected to cause discharges when mounted near the high voltage electrodes. All data shown previously in this chapter is taken in the tilted setup, unless mentioned otherwise.

Time-of-flight traces shown in Fig. 4.17 show that the signal intensity between tilted and straight setup is comparable: for the tilted setup, the integrated $CO^\star$ signal (red)

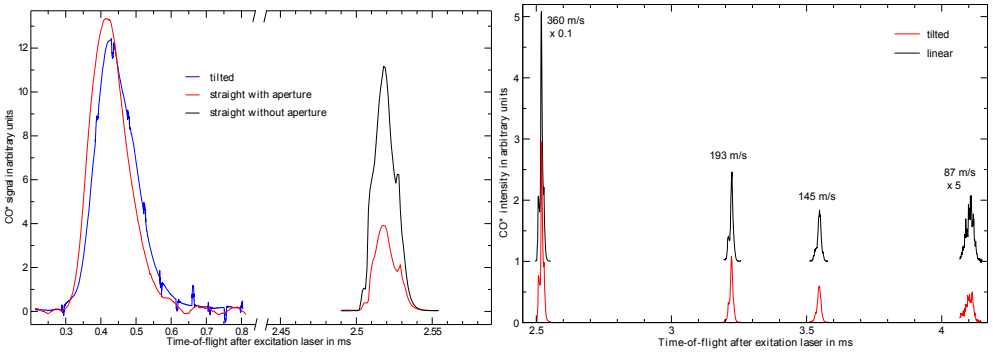

(a) Effect of the differential pumping aperture. Time-of-flight traces on the left show that a shift towards higher velocities occurs in the PMT signal detecting CO* in the decelerator chamber when changing from the tilted (red) to the linear (blue) setup. The guided signal intensity in the linear setup rises by a factor of 2.8 when removing the differential pumping wall, as shown on the right.

(b) Comparison of deceleration in linear (black) and tilted (red) experimental setup. Curves for the linear setup are offset for clarity. The integrated CO* intensity of the tilted time-of-flight traces is about 70 % of the ones recorded in the straight setup.

Figure 4.17: Characterization of CO* deceleration in the linear setup.

decreases to 0.70 ± 0.12 of the linear setup (black). It should be noted, however, that excitation laser power was slightly lower, and the nozzle not operating optimally during the measurements with the tilted setup. Hence, the actual drop in signal is estimated to be by a factor of 0.8 ± 0.2, which is in excellent agreement with the value of 0.7 predicted by simulations in section 3.2 (see p. 25).

4.5 Conclusion

Stark deceleration is a technique to produce a sample of slow, cold polar molecules using pulsed electric fields. A slice of the initial spatial and velocity distribution of a molecular beam pulse can be decelerated or accelerated in a phase-stable way as the molecules are transported through the Stark decelerator. In this chapter, the design, the assembly, and the characterization of a Stark decelerator that is fully bakeable up to 100 °C is described. It is equipped with special end pieces that allow the distance to adjacent parts of the beamline to be minimized. With this Stark decelerator, the velocity of low-field seeking CO* can be tuned in the range from 512 m/s to 33 m/s.

Chapter 5

The Surface Scattering Setup

At the heart of the constructed machine lies the scattering chamber, where the actual collision experiment takes place. Molecules leaving the decelerator are prepared in the desired quantum state, impinge on the surface, and scattering products are detected. In the upper level of the vacuum chamber, the surface is prepared for experiments and its condition is diagnosed. This chapter describes in detail all aspects of the setup which are needed to conduct molecule scattering experiments on a clean surface.

An illustration of the machine, with all the important components highlighted, can be seen in Fig. 5.1.

5.1 Vacuum Considerations

An important aspect in conducting molecule-surface scattering experiments is the condition of the surface under investigation. In the most simple case, one wants a surface clean of any of the adsorbates commonly present in vacuum systems, especially water. More complicated studies involve surfaces decorated with adsorbates, which are likely to be removed upon impact of leftover residual gas. While in the first case it is possible to heat the surface to free it from water molecules, this is obviously not an option for low temperature studies or in the latter case of sensitive surface decoration. Moreover, certain adsorbates cannot be removed from the surface by mere heating, which will start to collect contaminants immediately after cleaning. The more general approach to guarantee surface purity is thus to reduce the residual gas left in the chamber, i.e. provide a better vacuum. In general, a pressure on the order of 10^{-10} mbar is sufficient to ensure a clean surface for a time scale of several hours. This can be seen from the following argument: The impingement rate,I, per unit area of a gas of molecular mass, m, number density, n, temperature, T, and pressure, p, is given by [143]:

$$I = \frac{n\bar{v}}{4} = \frac{1}{4}\frac{p}{k_B T}\sqrt{\frac{8k_B T}{\pi m}} = \frac{p}{\sqrt{2\pi m k_B T}}\,, \tag{5.1}$$

where $\bar{v} = \sqrt{\frac{8k_B T}{\pi m}}$ is the mean speed of particles in an ideal gas following a Maxwell-Boltzmann velocity distribution. Since typical sizes of small molecules are between

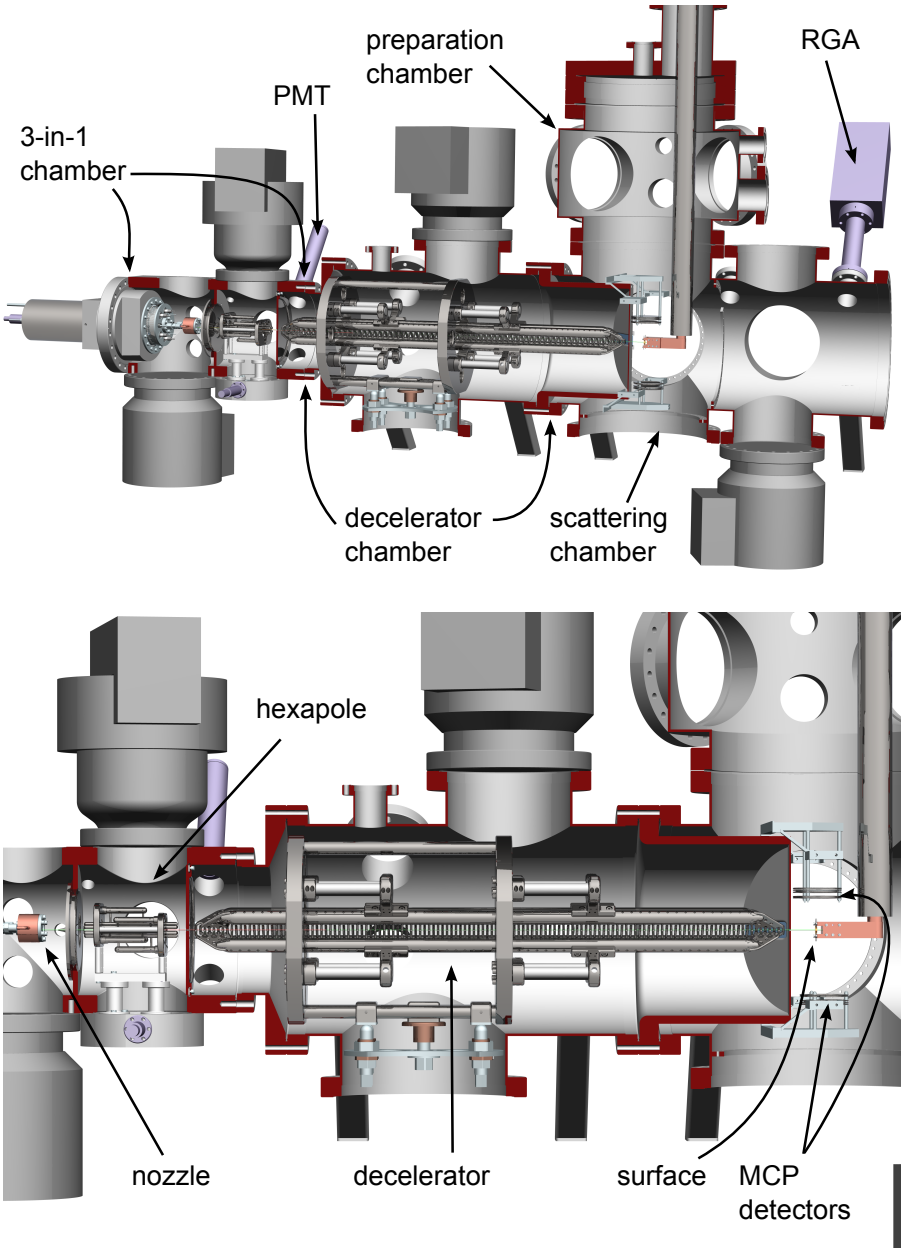

Figure 5.1: Illustration of the experimental setup. The most important elements, from left to right, are nozzle, hexapole focuser, Stark decelerator, and surface. MCP detectors are mounted above and below the gold surface.

$3 - 4$ Å (e.g. for N_2, 3.7 Å [50]), it takes approximately 10^{19} molecules per square meter to cover a surface with one monolayer of adsorbates. Assuming the worst case of a sticking coefficient of 1, i.e. that every molecule hitting the surface sticks to it permanently, dividing this number by the impingement rate of Eq. (5.1) gives a lower limit for the time in seconds that it takes to form a monolayer of adsorbates on a clean surface. It should be noted that a sticking coefficient close to unity is realistic even for inert surfaces such as Au(111), at least for cryogenic temperatures. For example, H_2O on Au(111) is reported to have a sticking coefficient of ≥ 0.95 at 85 K, nearly independent of coverage [144]. For $m = 28$ amu, $T = 295$ K and a pressure of 10^{-6} mbar, it takes about 2.5 s for a monolayer to build up, while the corresponding time for 10^{-10} mbar is already about 7 hours. Since the Au(111) surface is expected to have a sticking coefficient of less than one for many gaseous species, this time is expected to be even larger. In table 5.1, a summary of impingements rates and monolayer formation times is given for different pressures and two typical residual gases in a vacuum chamber, along with values for the two carrier gases employed in the molecular beam setup.

p	impingement rate ($s^{-1}m^{-2}$)				monolayer formation time			
(mbar)	H_2O	N_2	Ar	Xe	H_2O	N_2	Ar	Xe
10^{-8}	4×10^{16}	3×10^{16}	2×10^{16}	1×10^{16}	6 min	4 min	6 min	8 min
10^{-10}	4×10^{14}	3×10^{14}	2×10^{14}	1×10^{14}	10 h	7 h	11 h	14 h

Table 5.1: Typical values of parameters relevant for surface purity for four different species. Sticking coefficients are assumed to be one, and particle radii of $r_{N_2} = 1.85$ Å [50], $r_{H_2O} = 1.37$ Å, $r_{Ar} = 1.64$ Å, and $r_{Xe} = 1.96$ Å [145] are used to estimate the number of atoms or molecules in a monolayer.

In order to establish a vacuum in the 10^{-10} mbar range, two general limitations have to be overcome. First, desorption of molecules, especially water, from the walls of the vacuum chambers usually limits the pressure to the 10^{-9} mbar range. This necessitates a procedure known as *bakeout*: Vacuum chambers are heated to temperatures of 100 °C or above while the turbomolecular pumps (TMP) are running. Rising the temperature causes an initial increase in pressure, because molecules desorb more easily from the surfaces. As many of the desorbed molecules are effectively removed by the TMPs, the final pressure after cooling down to room temperature will be lower, typically in the order of 1×10^{-10} mbar. High temperature limits the choice of materials to be inserted into vacuum considerably, since different coefficients of thermal expansion may cause mechanical stress and eventually failure. Other materials tend to become elastic and deform at elevated temperatures, or start outgassing due to a low vapor pressure, causing contamination. Moreover, since a large temperature difference may cause significant mechanical stress, the heating rate has to be slow and the temperature be controlled carefully both while heating up and while cooling

down.

The second issue to be considered is that the ultrahigh vacuum region of the scattering chamber has to be mated to a molecular beam experiment, which generally operates in the 10^{-5} mbar–10^{-7} mbar regime. In the case described here, the pressure, which is typically 1×10^{-5} mbar in the source chamber, has to be reduced sequentially by differential pumping, i.e. by connecting adjoining vacuum regions only by small orifices. For two given vacuum regions a and b, with $p_a \gg p_b$, where b is equipped with a vacuum pump of pumping speed q_b, and connected to region a by an orifice of area A_{ab}, the equilibrium pressure in b is given by $p_b = {}^{Q_{ab}}/_{q_b}$, where Q_{ab} is the volumetric throughput of gas in mbar $\times$ l $\times$ s^{-1}. Combining the definition of conduction, $Q_{ab} = C_{ab} \times (p_a - p_b) \approx C_{ab} \times p_a$, with the expression for the conduction through a small orifice in the molecular flow regime, $C_{ab} = {}^{\bar{v}A_{ab}}/_4$, yields [146, pp 32-37]:

$$p_b = p_a \frac{C_{ab}}{q_b} + p_{\text{direct}} = p_a \frac{\bar{v} A_{ab}}{4 q_b} + p_{\text{direct}} \,, \tag{5.2}$$

where p_{direct} is the pressure increase due to the pulsed molecular beam directly passing through the aperture, and $\bar{v}$ is again the mean speed of gas molecules assuming a Maxwell-Boltzmann distribution. For the two carrier gases used in this experiment, Ar and Xe, the mean velocities at room temperature are $\bar{v}_{\text{Ar}} = 395\,\text{m/s}$ and $\bar{v}_{\text{Xe}} = 340\,\text{m/s}$, respectively. As described below, the vacuum setup consists of four regions: source, hexapole, decelerator, and scattering chamber, which are connected by 2.0 mm diameter circular orifices. Inserting these values into Eq. (5.2), using the corresponding pumping speeds for Argon (320 l/s for the hexapole region, 665 l/s for other chambers) reduced by 5 % to account for protective meshes, and neglecting the term p_{direct}, one finds as the lower limit for the vacuum regions:

$$\begin{aligned} \tilde{p}_{\text{source}} &\simeq 1 \times 10^{-5}\,\text{mbar}\,, \quad \tilde{p}_{\text{hexapole}} \simeq 1 \times 10^{-8}\,\text{mbar}\,, \\ \tilde{p}_{\text{decelerator}} &\simeq 5 \times 10^{-12}\,\text{mbar}\,, \quad \tilde{p}_{\text{surface}} \simeq 2 \times 10^{-15}\,\text{mbar}\,. \end{aligned} \tag{5.3}$$

When neglecting the pressure increase due to the direct beam, the differential pumping is therefore sufficient to maintain a pressure in the surface chamber of $p \simeq 1 \times 10^{-10}$ mbar or better.

The contribution of the molecular beam to the final pressure can be approximated from geometric considerations as follows: The pulse is assumed to have a duration of typically $\Delta t = 200\,\mu\text{s}$, and have a Gaussian velocity distribution in both transverse directions with a velocity spread $v_\perp$ equal to 10 % of the longitudinal beam velocity $v_\parallel$. The number of molecules that is transversely located inside a disc of radius r after traveling for a distance l is then given by

$$N_{\text{direct}} = n_0 \times V_{eff} \times \left[\frac{\int_0^{v_{\max}} \exp\left(\frac{-2v^2}{v_\perp \sqrt{\ln 2}}\right) \mathrm{d}v}{\int_0^{\infty} \exp\left(\frac{-2v^2}{v_\perp \sqrt{\ln 2}}\right) \mathrm{d}v} \right]^2 \,, \tag{5.4}$$

where n_0 is the initial density $\approx 30\,\mathrm{mm}$ in front of the first skimmer, $V_{eff} = r_{\mathrm{skimmer}}^2 \pi \times \Delta t \times v_{\parallel}$ is the effective volume from which molecules pass through the first skimmer, and $v_{\mathrm{max}} = v_{\parallel} \times r/l$ is the maximum transverse velocity still being transmitted. Using the ideal gas equation as an approximation, the direct pressure contribution can then be calculated for known pumping speed, q, chamber volume, V, and repetition rate, f, of the experiment from the equilibrium pressure increase, Δp, as

$$p_{\mathrm{direct}} = \Delta p \times \frac{V}{q} \times f = \frac{N_{\mathrm{direct}}}{V} k_B T \times \frac{V}{q} \times f = \frac{N k_B T}{q} \times f \,. \tag{5.5}$$

Using values for Argon at room temperature, a longitudinal velocity of $360\,\mathrm{m/s}$, a typical value for n_0 of $2.8 \times 10^{13}\,\mathrm{cm}^{-3}$ (cf. section 3.1), and distances of the orifices from the nozzle of 30 mm, 161.5 mm, and 896.5 mm, the following values for the equilibrium pressure are obtained using Eq. (5.2):

$$\begin{aligned} p_{\mathrm{source}} &\simeq 1 \times 10^{-5}\,\mathrm{mbar}, \quad & p_{\mathrm{hexapole}} &\simeq 5 \times 10^{-7}\,\mathrm{mbar}, \\ p_{\mathrm{decelerator}} &\simeq 1 \times 10^{-8}\,\mathrm{mbar}, \quad & p_{\mathrm{surface}} &\simeq 4 \times 10^{-10}\,\mathrm{mbar}\,. \end{aligned} \tag{5.6}$$

Obviously, these values give a more realistic picture of the optimum achievable pressure in the surface and decelerator part of the vacuum setup when the beam is running than Eq. (5.3).

It is clear that the direct beam will contribute significantly to the base pressure in the scattering part of the machine, which might make performing experiments with a clean sample complicated or even impossible. Especially, note that the surface is exposed directly to the beam, aggravating the problem of monolayer buildup. According to Eq. (5.4), about 5×10^9 molecules per pulse will hit the surface directly. For Argon as a carrier gas, with a size of about 2.74 Å, this corresponds to a potential monolayer building up over the course of 33 minutes. For that reason, countermeasures have to be taken: For measurements at low incident kinetic energies, where Argon, Krypton, or Xenon have to be used as a seed gas, the main part of the molecular beam is contained to the second region of the vacuum setup. This is achieved by mounting the nozzle and first skimmer such that there is no direct line of sight between source and surface chamber, as is described in detail in chapter 3.3. For experiments where high incident kinetic energy in needed, however, the beamline remains linear, and CO can be either seeded in lighter carrier gases or even used in pure form without seed gas. This reduces the issue of surface contamination, since lighter rare gases are expected to have smaller sticking coefficients to Au(111) [147]. No sticking of CO to the Au(111) surface under ultrahigh vacuum conditions has been reported prior to design of the apparatus described here. Trapping and subsequent desorption of CO on Au(111), however, has been reported [148]. Note that some sticking of CO on Au(111) at $T_S \approx 45\,\mathrm{K}$ has meanwhile been observed using the TPD setup mentioned in section 5.2.2. For partial CO pressures higher than 0.7 mbar, sticking has been reported already at room temperature [149].

An import question arises with respect to the vacuum setup given that the system under investigation involves carbon monoxide. Many sources report the outgassing

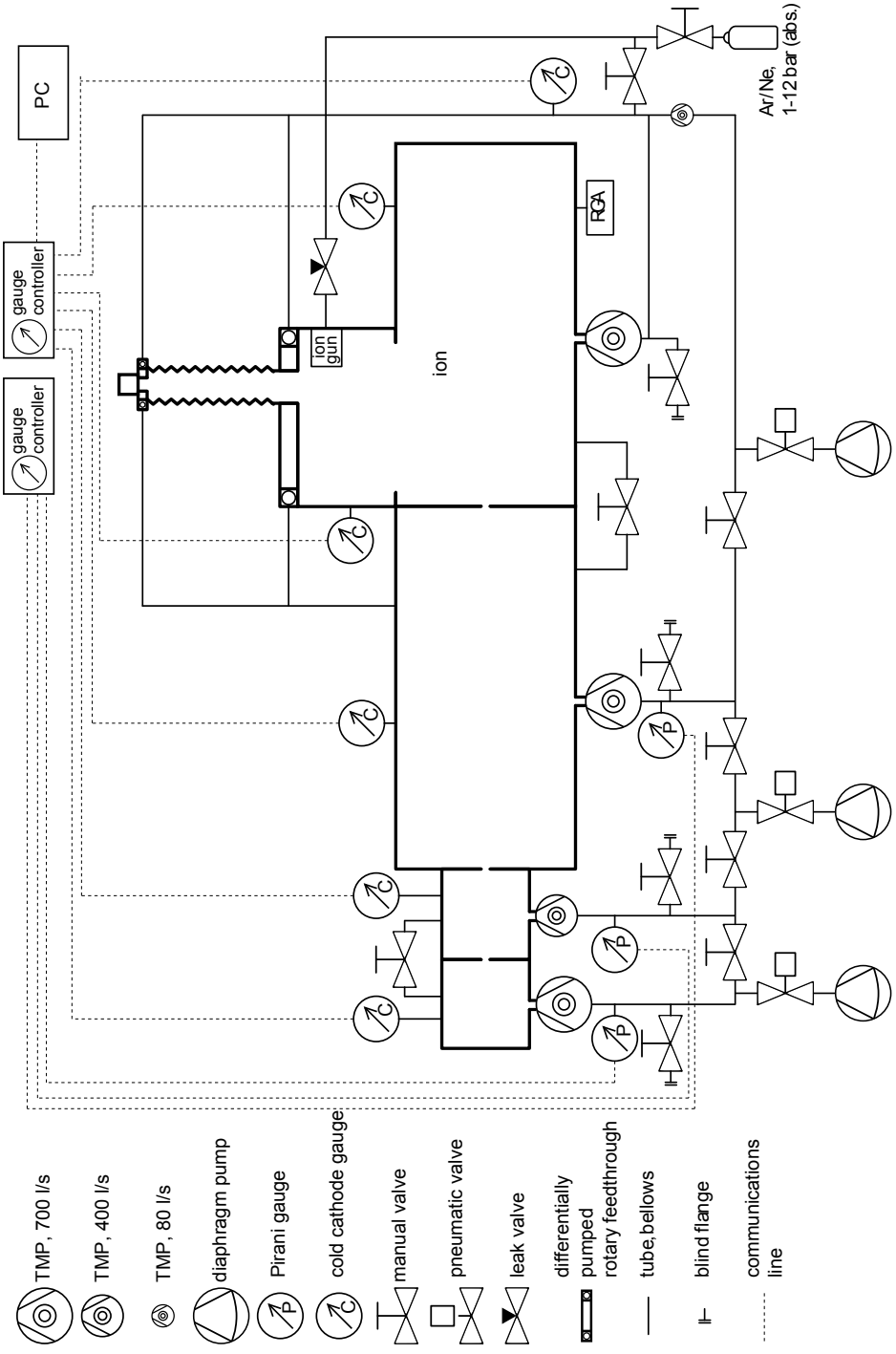

Figure 5.2: Schematic setup of the vacuum system.

of CO from the stainless steel walls of vacuum chambers, to the extent that it appears to be common knowledge in vacuum science and is stated without giving further evidence (see, e.g., [146, pp 238,453]). The presence of a high CO content in the residual gas of the surface chamber can limit the lower detection limit of CO due to a constant background. A thorough survey of literature concerned with the outgassing of steel in ultrahigh vacuum reveals, however, that the CO content in the residual gas can be attributed exclusively to the operation of hot filaments (see, e.g., references [150–155]). For detection of scattering products at low particle densities, it is therefore advisable to use only cold cathode gauges in the scattering chamber, and limit the use of any other hot filament (Auger spectrometer, ion gun, heating wires, residual gas analyzer, etc) as much as possible.

A schematic view of the vacuum system can be seen in Fig. (5.2). The machine is split up into four vacuum regions: The source chamber, pumped by a 685 l/s (all pumping speeds are given for N_2) turbomolecular pump (*Pfeiffer* HighPace 700), the hexapole chamber (*Pfeiffer* HighPace 400, 355 l/s), the decelerator chamber (*Pfeiffer* HighPace 700, 685 l/s), and the scattering and preparation chamber (*Pfeiffer* HighPace 700, 685 l/s). Source and hexapole chamber are connected by a skimmer (*Beam Dynamics, Inc.* Molecular Beam Skimmer Model 2, Nickel) of 2.0 mm orifice diameter (1.5 mm for some setups, see section 3.3), while the other vacuum regions are connected by 2.0 mm diameter circular holes. The outlets of all turbomolecular pumps (TMP), except the one used for the scattering/preparation chamber, are connected to the fore-vacuum line directly, which is evacuated by three oil-free diaphragm pumps (*Pfeiffer* MVP 70, 65 l/min) to a pressure of typically 0.6 mbar. The best final pressure which can be achieved by a TMP backed by a diaphragm pump is on the order of 10^{-10} mbar, due to the limited compression (i.e. ratio of inlet pressure to outlet pressure) of typically 10^{10}. For that reason, the outlet of the scattering chamber TMP is connected to a smaller TMP (*Pfeiffer* HighPace 80, 38 l/s), which creates a vacuum of typically 2×10^{-5} mbar and whose outlet is connected to the main fore-vacuum line. The same TMP is also used to evacuate a gas line used to feed Argon or Neon to a leak valve for surface sputtering (see section 5.2.2), as well as for pumping out the first (i.e., rough vacuum) stage of two differentially pumped rotary feedthroughs. The second (i.e., high vacuum) stage of these differentially pumped rotary feedthroughs is connected directly to the decelerator chamber to provide a backing pressure that is sufficiently low. Monitoring of the fore-vacuum is achieved by three Pirani gauges (*Pfeiffer* TPR 280) mounted near the outlet of the TMP's. Vacuum in the UHV chambers and the small TMP vacuum is measured by bakeable cold cathode gauges that have a lower limit of 2×10^{-9} mbar (*Pfeiffer* IKR 060) for the source, hexapole, decelerator, and preparation chamber, and 1×10^{-11} mbar (*Pfeiffer* IKR 070) for the scattering chamber. No Bayard-Alpert type gauges have been installed in order to reduce the number of charged particles which might cause discharges near high voltage parts, and to minimize the amount of CO being produced in the scattering chamber. All pressure readings are displayed using two control units (*Pfeiffer* Maxi Gauge TPG 256 A), and logged in 15 minute intervals by a personal computer. In addition, a residual

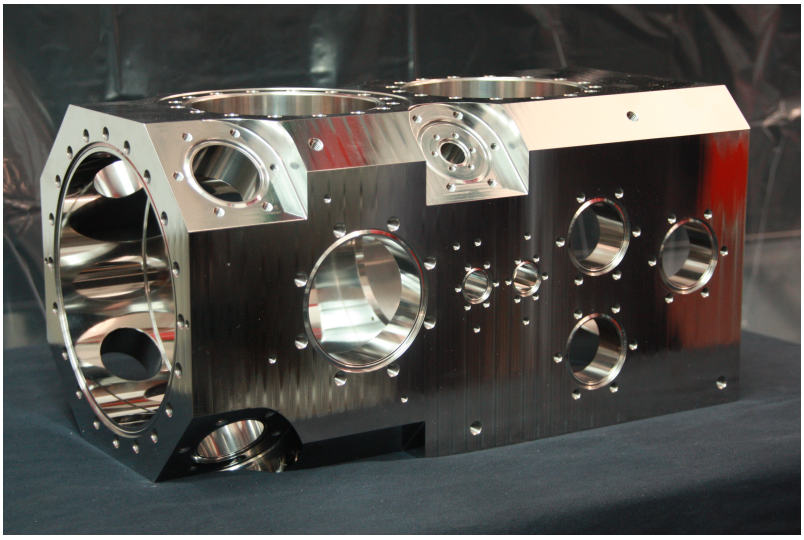

(a) The so-called cube chamber comprises source, hexapole and part of the decelerator manifold in a compact 3-in-1-design with two removable differential pumping walls. The groove for mounting the second wall is visible on the left side.

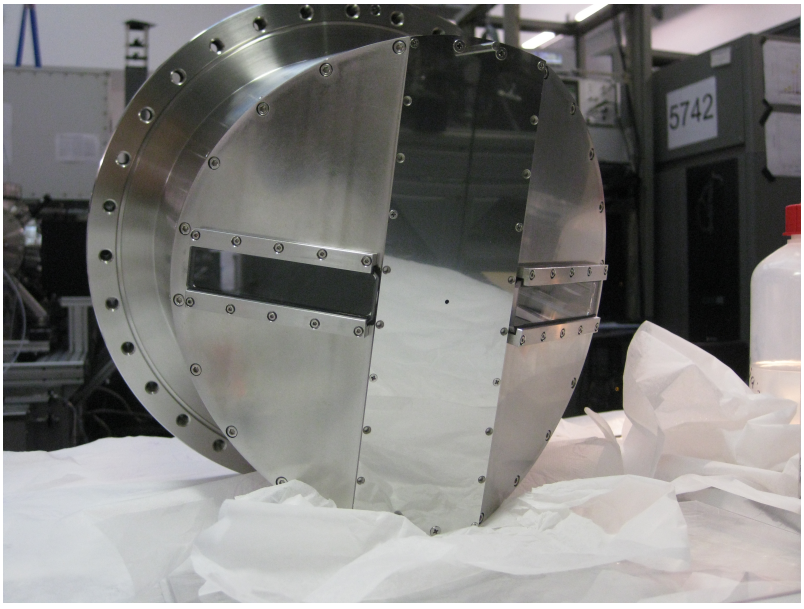

(b) Cap which extends into the scattering chamber and separates it from the decelerator manifold. The two windows are mounted at Brewster's angle and provide laser access through the viewports of the scattering chamber. The inside is highly polished to avoid discharges.

Figure 5.3: Specially designed parts to separate vacuum chamber breaks from vacuum manifold breaks.

gas analyzer (*SRS* RGA 200) is used in the scattering chamber to monitor the composition of the background gas.

The maximum bakeout temperature of the system is limited to 130 °C due to the seals of the differentially pumped rotary feedthroughs. In addition, small amounts of Viton fluoroelastomer are used to safely mount (but not seal) windows in the walls between decelerator and surface chamber. These should not be baked at temperatures above 150 °C. Viton O-rings lubricated with low vapor pressure, high temperature grease are also used as a vacuum seal in the source chamber. In order to allow for some error on the temperature reading, the bakeout temperature is restricted to typically 110 °C in the scattering/preparation chamber, down to 90 °C in the hexapole and source chambers. The temperature of the decelerator, which is monitored independently from the chamber it is mounted in, is limited to 100 °C to avoid damage during bakeout (cf. section 4.3, p. 58).

The most common way of incorporating differential pumping walls into a vacuum system is to place them at the positions where different vacuum chambers are joined. A drawback of this concept is that the CF mating flanges of vacuum chambers will block access from outside close to the differential pumping walls. However, these are usually the locations where direct access is most important: the excitation laser needs to be intersected with the molecular beam close to the skimmer, and the PMT detector can collect fluorescence from metastable molecules most efficiently in the gap between hexapole and decelerator. Most important, however, is the space between decelerator and surface. Here, access is needed for two laser beams, one of which should be able to cross the molecular beam *inside* the decelerator. For these reasons, the positions of vacuum *chamber* breaks and vacuum *region* breaks are designed to be different throughout the entire apparatus. In fact, the first vacuum chamber comprises a total of three vacuum regions. Source and hexapole chamber are partially separated by a wall which is an integral part of the chamber, and whose opening fits the skimmer mounting plate. Behind the hexapole, a small groove is machined along the inner circumference of the chamber. It is used to fasten a solid disc inside the chamber such that no clearance remains, effectively establishing a second "wall" suitable for differential pumping in the high and ultrahigh vacuum. A picture of this chamber can be seen in Fig. 5.3a, whereas a schematic cut is shown in Fig. 3.6. Laser access at the point where decelerator and surface region meet is achieved by means of a special end cap to the decelerator region, shown in Fig. 5.3b. It extends far into the surface chamber and features two long UV fused silica windows mounted at Brewster's angle, allowing full laser access to the last six decelerator stages. The surface chamber features 100 mm diameter viewports, such that the laser beam has to pass through a total of four windows. To minimize the risk of discharges, the inside of the end cap is highly polished, and all edges near the windows are rounded. Incorporating these two specially designed pieces into the vacuum setup allows access to the molecular beam where it is most useful.

5.2 Surface Control

In order to perform experiments on a clean surface in the low collision energy regime, certain requirements have to be met. First of all, the apparatus has to be equipped with the appropriate preparative and diagnostic tools to clean the surface and ensure its purity. To make proper use of these tools, the surface position has to be flexible and accurate enough to easily reach all this equipment, and also to allow for different setups for the actual experiment itself. In addition, the surface temperature needs to be controlled and measured accurately. To fulfill these goals, the approach described in the following section was taken.

5.2.1 Surface Mounting and Positioning

Directly atop the scattering chamber of the apparatus is an additional chamber for surface preparation. All instruments for diagnostics and cleaning are mounted onto this chamber, which provides free ports for easy access to the sample mount when the machine is vented. A so-called dog-leg sample mount is attached to the end of a 3-axis manipulator (*VG Scienta* Omniax MXZ800 and MT211B6S), which provides translation in all three dimensions to the surface. With a maximum travel of 800 mm in the vertical direction, the manipulator easily allows for the 400 mm translation needed. In both horizontal directions the manipulator provides a total of 50 mm of travel. In the central position the surface is 30 mm downstream of the aperture between decelerator and scattering chamber and centered on the molecular beam. In order to gain access to

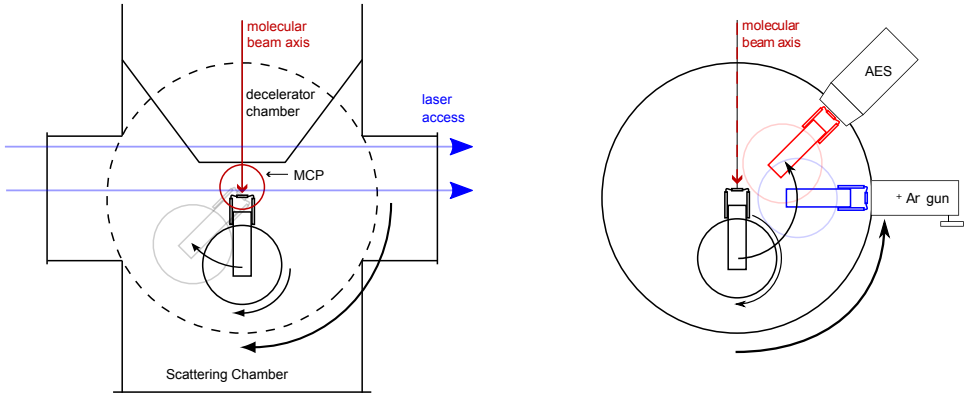

(a) Scattering chamber. The angle of incidence can be varied by rotation of the big DPRF.

(b) Preparation chamber. All instruments are accessible by rotating the small DPRF by 180°and proper positioning of the big DPRF.

Figure 5.4: Sample movement in scattering and preparation chamber.

all instrumentation, rotation is realized by means of two differentially pumped rotary feedthroughs (DPRF). The first one (*VG Sciencta* ZRP100H, DN 100CF) is mounted on top of the z-axis manipulator, whereas the bigger one (*Thermionics* RNN-1000/MS, 13.25"CF) is attached directly on top of the preparation chamber. The dimensions of the dog-leg are such that the sample is centered on the big DPRF. By mounting the whole (x, y, z, φ)-manipulation setup off-center on the big rotation stage, the incidence angle of the beam is easily varied by rotating the big DPRF. At the same time, it has the advantage of making vertical laser access possible if a window is mounted on top of the center of the big DPRF, which is impossible to achieve with a single DPRF setup. This geometry, granting laser access from two different dimensions, allows a great variety in experimental configurations. Fig. 5.4b shows a schematic sketch displaying the surface positioning in the two chambers.

The surface itself, which is constituted by the front face of a gold single crystal (*Monocrystals Co.*, 99.99+ % Au, two sides electropolished, (111) orientation) of 10 mm diameter and 2 mm thickness, is mounted via two tungsten wires to two small copper blocks. These two blocks are connected to a bigger support in such a way that electric insulation is provided by 15.75 mm diameter and 1 mm thick polished sapphire (crystalline Al_2O_3) disks. Apart from its favorable dielectric properties, sapphire also

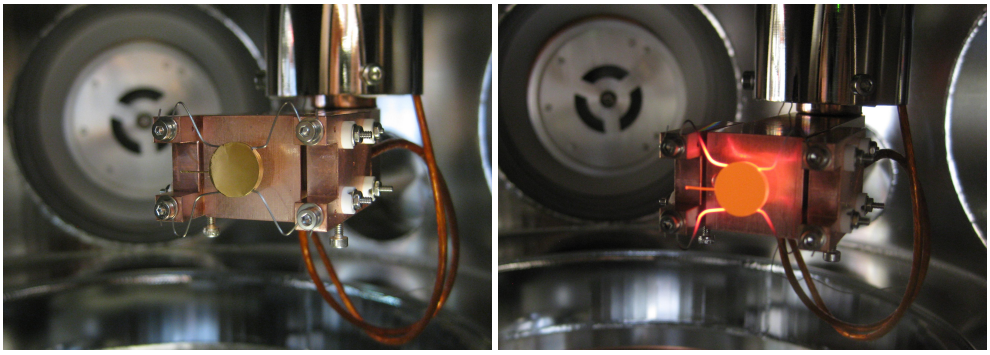

(a) Crystal sample mount. (b) Au(111) heated to 900 °C

Figure 5.5: The Au(111) surface attached to its sample mount. The thermocouple junction is attached at the wire on the left, the W wires used for attaching the crystal to the support are also used for resistive heating. At the rear of the mount, Kapton insulated wires can be seen sticking out of the radiation shield. Small copper blocks on either side of the dog leg are electrically insulated via sapphire spacers.

provides the added advantage of having an extraordinarily high thermal conductivity at cryogenic temperatures, while at ambient temperatures, it is only about twice as high as that of stainless steel, and decreases further with rising temperature. A picture of the Au(111) crystal attached to the sample mount is shown in Fig. 5.5

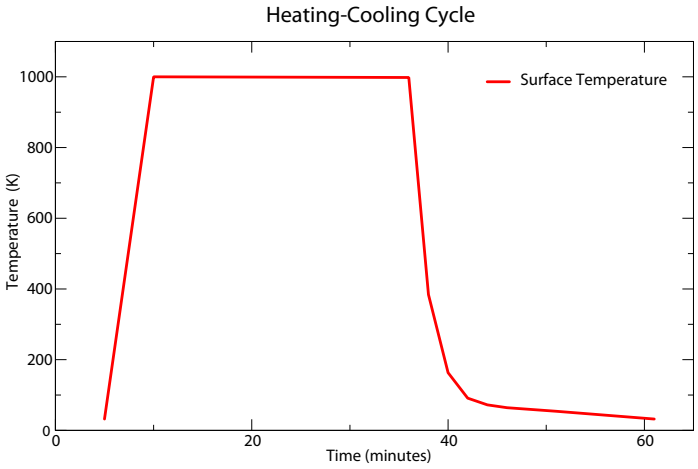

Figure 5.6: Heating-cooling cycle of the Au(111) surface. The temperature was controlled manually.

The temperature of the gold crystal is measured by inserting the junction of an E-type thermocouple into a 0.4 mm diameter hole drilled into the side of the crystal and fixing it with a matching piece of gold wire. Using an E-type thermocouple instead of K-type offers the advantage of having a large thermocouple voltage gradient at low temperatures, while it is reasonably accurate at high temperatures. The thermocouple voltage is converted to temperature using either a temperature meter (*Omega Engineering, Inc* CNi16D54-C24) or by reading the output of a Data Acquisition card (*National Instruments* 9213) using LabView. Both cooling and heating of the surface is used to regulate its temperature. Cooling is provided by a closed cycle Helium cryostat (*Advanced Research Systems, Inc.* CS204B, 50 Hz/200 V operation) operated with the aid of a 3.8 kVA transformer (*Bremer Transformatoren GmbH/FHI ELAB* #4795, transforms 230 V/17.1 A to 200 V/19 A). Heat transfer is achieved by connecting the surface mount via a 1397 mm long solid copper rod to the second stage of the cryostat, while a nickel-plated copper tube connected to the first stage of the cooler provides shielding from blackbody radiation. Resistive heating of the surface is achieved by feeding the output of a high-current power supply (*TDK-Lambda Germany GmbH* GEN 8-180/LN, 180 A, 8 V) via two Kapton-coated wires (rated to 25 A at 2 kV DC) into the two small copper blocks connected to the surface. This produces a large current in the two high resistance tungsten wires, causing the wires and the crystal attached to them to heat up. The setup allows both fast heat-up and fast cool-down times. As the cooling curve in Fig. 5.6 shows, surface temperatures down to 28 K and up to the melting point of gold are easily achieved within five minutes.

5.2.2 Surface Preparation

Among surface diagnostic tools, Auger electron spectrometers (AES), X-ray photoelectron spectrometers (XPS) and low-energy electron diffraction (LEED) are most commonly used to diagnose the condition of a surface. While AES is sensitive to the atomic species which make up the first few layers of a solid, XPS provides a means do determine the electronic band structure. LEED, on the contrary, can be used to study the structure of the surface, i.e. it is useful in determining the arrangement of atoms which make up a surface. Since the Au(111) surface is a very stable crystal face and

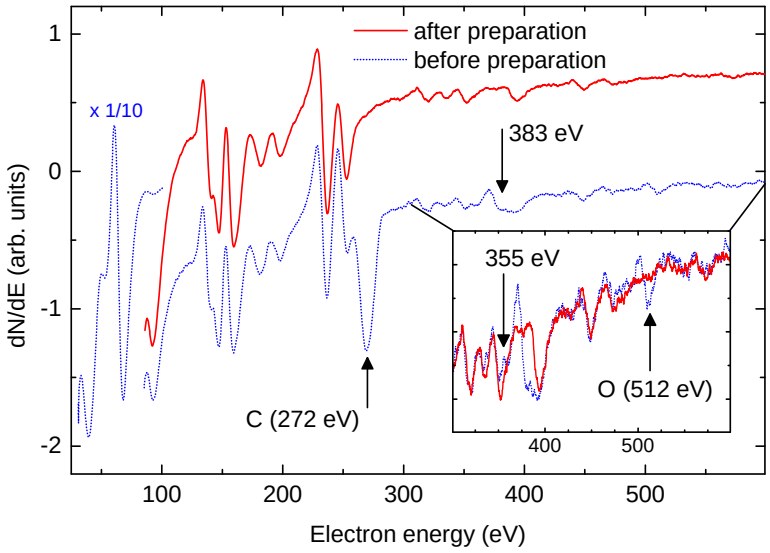

Figure 5.7: AES spectrum of Au(111) prior to (solid red) and after (dashed blue) the cleaning procedure. Curves are shifted for clarity. The inset shows a closeup of a region sensitive to features caused by contaminants, with curves unshifted. The arrows indicate impurities. All curves were acquired using a lock-in amplifier.

known to reconstruct quite easily at elevated temperatures, use of a LEED is deemed unnecessary. In fact, due to the unreactive nature of gold, only small amounts of impurities are expected to occur, which leads to the natural choice of AES as the preferred surface diagnostic tool. The preparation chamber is therefore equipped with a commercial AES (*STAIB INSTRUMENTS, Inc.* ESA-150), which has a working distance of 33 mm, an energy resolution of 1 eV to 10 eV, and can be operated either in combination with a lock-in amplifier or in pulse counting mode.

Most metal surfaces which are reasonably unreactive may be obtained in a pure state by rare gas or hydrogen ion sputtering and subsequent curing of craters caused by the bombardment by heating to elevated temperatures [156]. The procedure used

in this setup is similar to the one described in reference [157]. The surface is positioned in front of an ion gun (*STAIB INSTRUMENTS, Inc.* IG-5-C), grounded, and the number of ions which charges up the surface is monitored by measuring the current I_S between the surface and ground using a digital voltmeter (DVM). For sputtering at ambient temperatures, Ar is employed as the bombarding species, using ion kinetic energies of 3 keV to create surface currents of $I_S \approx 11\,\mu A$ for 20 minutes. For cryogenic temperatures, Argon is replaced by Neon ($I_S \approx 18\,\mu A$) in order to reduce sticking to cold surfaces of the neutralized particles. In both cases, the surface is then annealed at 900 K for 20 minutes. The result of the cleaning process is shown in Fig. 5.7, where the first derivative of the Auger electron signal with respect to energy is plotted versus energy. All the peaks of the spectrum, except for those indicated by arrows, can be assigned to pure gold by comparison with tabulated spectra [158]. The peaks near 372 eV and 512 eV can be unambiguously attributed to carbon and oxygen impurities, respectively. There are also two other peaks in the spectrum where impurities appear to be present: Directly to the left of the gold peak at 397 eV, a broad feature around 382 eV can be clearly distinguished, which is preceded by a sharp dip around 377 eV. The other feature is more subtle and barely visible as a small dip at 355 eV. This may well be explained by the presence of nitrogen, which has its primary peak at 381 eV, accompanied by smaller peaks at 367 eV and 357 eV. Another possible, but unlikely assignment is cadmium, which shows a characteristic signature at 376 eV and 382 eV, along with possible trace amounts of silver, whose peaks at 351 eV and 356 eV coincide with the position of gold peaks, but at different intensities. Whatever the nature of these impurities is, they are completely removed by the cleaning cycle described above. It should be noted that carbon impurities in particular remain on the surface if the crystal is only heated without precedent sputtering.

In addition to the instruments mentioned before, a gas manifold featuring leak valves for dosing the surface with adsorbates is installed on the preparation chamber. In combination with the RGA, mounted to the same chamber and equipped with a small inlet orifice, it comprises a setup for temperature-programmed desorption (TPD) experiments.

5.3 Preparation and Detection of Scattering Processes

For quantum-state specific molecule-surface scattering experiments, it is necessary both to manipulate the incoming quantum state and to detect the scattered quantum state with vibrational, and – if desired – rotational resolution. For the apparatus described here, an effective three step procedure is employed, which can be summarized as a pump-prepare-probe or pump-dump-probe scheme. In the case of CO, the first step for preparing a specific quantum state is conveniently the same as is needed for the manipulation with electric fields: CO in the $X^1\Sigma$ electronic ground state is pumped to the $a^3\Pi_1(v = 0, J = 1)$ metastable state directly in front of the hexapole. Apart from having a large permanent dipole moment this state offers the advantage that it can easily be used in a second step to prepare either ground-state CO in dif-

ferent ro-vibrational states by using a second laser for dumping the molecules back down, or to excite higher levels of CO, e.g. populate higher vibrational levels of the $a^3\Pi_1$ state via Franck-Condon pumping or stimulated emission pumping [159]. The third step consists of detecting specific quantum states of the molecules, preferentially by laser ionization. This happens either after collision with the surface, or, as will be demonstrated in chapter 6, in front of the surface in order to burn a hole into the incoming molecular packet.

5.3.1 Laser Systems

For the experiments described in this thesis, five different laser systems are used: two producing light pulses of 206 nm wavelength for pumping CO to the first electronically excited state, two others for (1+1) REMPI detection of the metastable state via different vibrational levels of the $b^3\Sigma^+$ state, which produce light pulses at 283 nm and between 266 nm and 297 nm wavelength, and a fifth one for excitation of CO from the $a^3\Pi$ state to the $e^3\Sigma^-$ state at a wavelength of 445 nm.

The $a^3\Pi_1(v' = 0) \leftarrow X^1\Sigma^+(v'' = 0)$ transition at 206 nm is spin forbidden and only accessible due to a small amount of singlet character in the upper state due to perturbation by the $A^1\Pi$ state. Therefore, it is beneficial to use a narrow-band laser system to increase the power per bandwidth. The 206 nm laser system initially used, which is sketched in Fig. 5.8a, has been described in detail before [57]. While the final output of the excitation laser system is pulsed, its key component operates in continuous wave (cw) mode: a ring dye laser (RDL, *Radiant Dyes*). It is pumped with a power of 5 W by the second harmonic of a Nd:YVO_4 laser (*Coherent* Verdi) at 532 nm and is operated on the dye sulforhodamine B, with its optical elements tuned to lase at a fluorescence wavelength of 619 nm. The 300 mW cw output of the RDL is used to seed a pulsed dye amplifier (PDA, *Lambda Physik* LPD3000) whose dye cuvettes containing DCM are pumped by an injection seeded Nd:YAG (*Spectra Physics* Quanta Ray PRO-230) laser. The result is a pulsed beam of 80 mJ pulse energy. A KDP crystal is then used to double the frequency to 309 nm. Since the polarization of the frequency doubled light is rotated by 90° in this process, it has to be rotated back by introducing a $\lambda/2$-plate into the beam which corresponds to a $\lambda/4$-plate for the original 619 nm light. The two wavelengths are then mixed in a second crystal to yield the third harmonic of the initial frequency, 48474.642 cm^{-1} (about 206 nm). In this way, 1 mJ energy pulses with a bandwidth of 150 MHz and 3 ns duration can be generated on a daily basis.

After moving the setup to Göttingen, a different approach was used to generate the narrow bandwidth pulsed laser radiation needed for efficient CO excitation, which does not rely on dye lasers. An optical parametric oscillator (OPO) setup, described in detail in reference [160] and depicted schematically in Fig. 5.8b, is pumped by the second harmonic of an injection-seeded Nd:YAG laser (*Spectra Physics* Quanta Ray Lab 170-10, Model 6350) and seeded by a external cavity diode laser (*Toptica Photonics, Inc.* DL-Pro 895) with a wavelength of 917 nm. In the two KTP crystals of the OPO cavity, one photon of the 532 nm pump beam is split up into two photons called

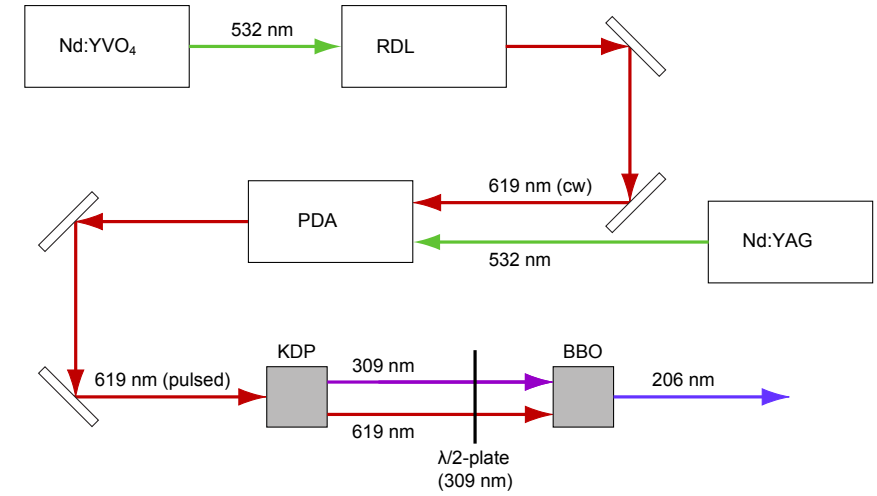

(a) RDL-based setup for 206 nm generation.

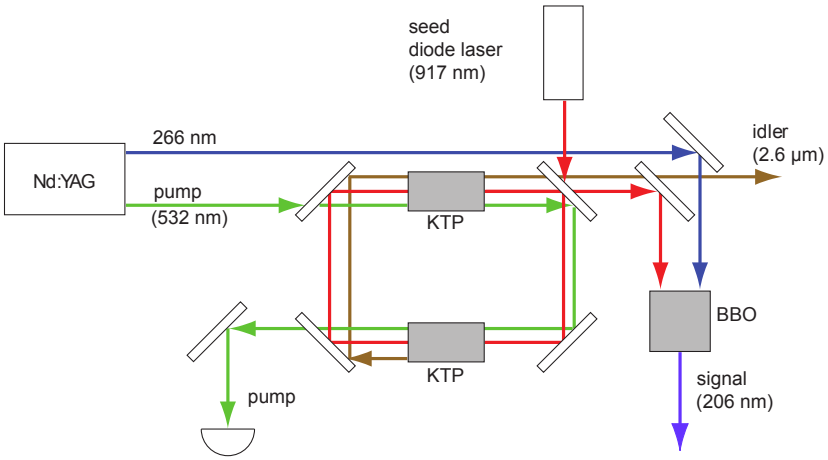

(b) OPO system used to generate 206 nm.

Figure 5.8: Laser systems for narrow band 206 nm generation.

signal and idler, obeying the relation $\nu_{\text{pump}} = \nu_{\text{signal}} + \nu_{\text{idler}}$ with $\nu_{\text{signal}} \geq \nu_{\text{idler}}$. When seeding the cavity, the signal frequency will follow the frequency of the seed laser, such that effectively the seeder frequency is being parametrically amplified. For proper seeding and frequency scanning, active stabilization of the cavity length to be a multiple of the seeder wavelength is needed. For this purpose, the cavity length is scanned via a piezo crystal mounted on the rear of one of the cavity mirrors before the YAG laser is fired, and the IR output of the cavity is being monitored. As the cavity becomes resonant with the seed laser, transmission reaches a minimum, corresponding to a well-defined piezo voltage. While the YAG laser is firing, the cavity is stabilized to resonance by maintaining the piezo at the previously determined voltage. The narrow-band pulsed output of the OPO is then mixed with the simultaneously generated, delayed fourth harmonic output of the Nd:YAG laser at 266 nm in a BBO crystal, where sum frequency generation takes place, yielding pulses of up to 3 mJ energy, 6 ns duration, and less than 0.01 cm^{-1} bandwidth.

Two of the laser systems used for detection and excitation of $\text{CO}^{\star}$ are standard Nd:YAG (Two *Continuum* Powerlite 8000, one formerly a *Spectra Physics* Quanta Ray INDI-40-10) pumped pulsed dye lasers (PDL) (*Quanta Ray* PDL-2, *Sirah Lasertechnik GmbH* Cobra Stretch DA-24). The PDL-2 system, pumped with 532 nm and operated on Rhodamin 6G, generates pulsed light at 566 nm, which is then frequency doubled in a KDP crystal to yield 3.5 mJ pulse energies at 283 nm, with a bandwidth of 0.4 cm^{-1}. The Cobra Stretch PDL system yields 15 mJ pulse energies at 445 nm with 0.08 cm^{-1} bandwidth when operated on Coumarin 450 and being pumped with 355 nm. The third laser system used is a commercial Nd:YAG (*Continuum* Powerlite 9010, SI-2000 Injection seeder) pumped OPO system (*Continuum* Sunlite Ex OPO FX-1) which allows easy frequency tuning in the desired range between 266 nm and 297 nm. Output pulses of 3 mJ are obtained, with a bandwidth of less than 0.3 cm^{-1}.

5.3.2 Detection of CO

Detection of the $a^3\Pi_1(v = 0, J = 1)$ state of CO may proceed via different methods. Since it decays to different vibrational levels of the ground state with a lifetime of 2.63 ms [10], the resulting fluorescence may be detected with a photomultiplier tube (PMT). This method provides low sensitivity, since only a small fraction of the molecules decays within the observable area. The main advantage of this detection method lies in the fact that no molecules in the metastable state are lost due to the detection, since the spontaneous fluorescence occurs anyway as the molecules pass by the PMT detector. For that reason, it is employed for monitoring the number of metastable molecules in the beam passing through the aperture behind the skimmer. A head-on, 15 mm active diameter solar blind PMT (*Hamamatsu Photonics* R821, 3.6×10^5 gain, 160 nm-320 nm) is mounted just outside the chamber, 150 mm away from the beam axis and 23.3 mm downstream of the aperture between hexapole and decelerator. In the given experimental setup, assuming a velocity of 360 m/s, an upper limit of 1×10^{-5} for the detection efficiency of this method can be estimated from simple geometric considerations.

A more efficient way to detect $CO^\star$ is to exploit the fact that it carries 6.0 eV of internal energy. Upon collision with a surface whose work function is lower than this, electrons are emitted from the molecule-surface system. In the simplest case, one can insert an MCP detector into the molecular beam, since the work function of its glass substrate is sufficiently low, and detect the emitted electrons with the MCP itself. Although rather convenient, the efficiency of this method is estimated to be only 7×10^{-4} [58]. It has been employed during the characterization of the machine before the gold surface was available. As an alternative, a clean noble metal surface can be used as a detector, combined with an MCP to extract and detect the emitted electrons. A heated gold surface has been used previously [57, 117] for $CO^\star$ detection, with an estimated detection efficiency of 1×10^{-2}. An advantage of this approach over pulsed laser-based detection techniques is that it is a continuous method, meaning the whole time-of-flight trace of $CO^\star$ may be recorded at once, while a pulsed detection laser has to be scanned in time to yield the same information. On the downside, no quantum state selectivity is achieved. Since the first system under investigation is $CO^\star$ on Au(111), this is the method of choice as long as quantum state selectivity is not important. As will be shown in chapter 6, the detection efficiency of a contaminant-free gold surface is in fact one order of magnitude higher than expected. The most convenient approach of quantum-state selective laser-based detection of $CO^\star$ is a resonant-enhanced multiphoton ionization (REMPI) scheme proceeding via the $b^3\Sigma^+$ state, where the ions are detected using an MCP. Because only two photons of the same color at an easily accessible wavelength of 283 nm are needed and the transition moments are favorable, the ionization is easily saturated when using a focused laser beam with pulse energy on the order of 1-2 mJ. In principle, unity detection efficiency may be obtained applying this technique.

In order to avoid large distortion of the extraction field when using the gold surface-based and (1+1) REMPI detection schemes simultaneously, electrons and ions are extracted by charged plates placed far above and below the surface, respectively. Both MCP stacks are mounted behind grids of 91 % transmission which are spot-welded onto the plates. Each MCP stack consists of two MCPs (*tectra GmbH Physikalische Instrumente* MCP 050, 40 mm active diameter, detection grade) which are arranged such as to have their channels tilted in opposite direction (known as chevron type). Two different voltage dividers split up the output of high voltage power supplies (*iseg Spezialelektronik GmbH* EHQ 105) to create the same voltage across both plates of a stack, charging up the first plate to attract the charged particles. Two further power supplies of the same kind are used for charging of the meshes. While for detection of CO^+, the first plate can be charged negatively, allowing the signal anode to be kept at ground for convenience, the electron detector has to start with a positive potential, resulting in the signal anode being biased to up to +3000 V. For that reason, the pulsed signal is decoupled from the constant high voltage using a 68 nF capacitor before being fed into the oscilloscope. While a first version of the detectors contained only rings to support the meshes, replacing those by larger rectangular plates proved beneficial in terms of reducing stray light and increasing electric field homogeneity. The detection geometry and `SIMION` [161] trajectory simulations demonstrating the perfect

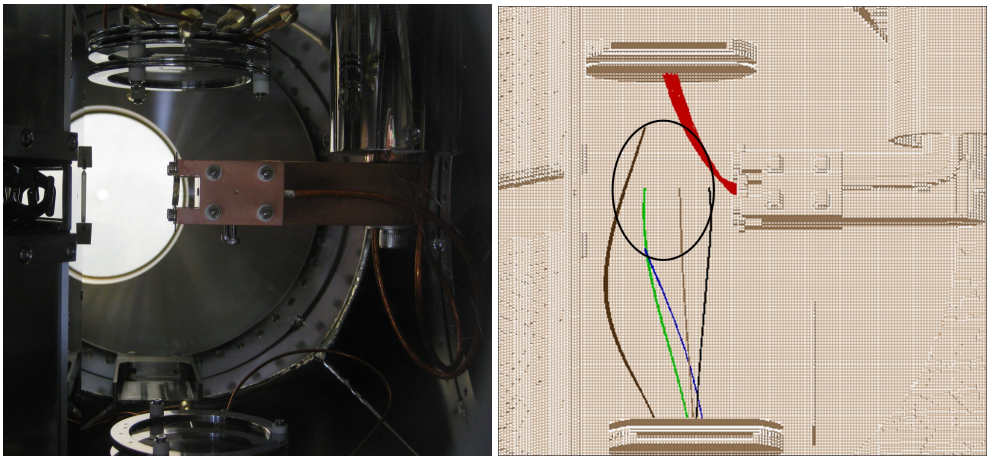

(a) Picture of the surface behind the decelerator. Detectors can be seen above and at the very bottom. Ions are extracted downwards, electrons upwards.

(b) Simulation of particle collection. CO^+ ions are extracted within a large volume indicated by the circle, and also all the electrons from the surface.

Figure 5.9: Detectors for ions and electrons.

collection efficiency are shown in Fig. 5.9. The chosen geometry has the advantage of allowing collection of ions from a large volume such that detection is insensitive to the exact ionization laser position.

In future experiments, CO in its electronic ground state will need to be detected. Several REMPI schemes have been suggested and demonstrated for this purpose, including schemes proceeding via the $B^1\Sigma^+$, $C^1\Sigma^+$, and $E^1\Pi$ state. The (2+1) REMPI detection via the $E^1\Pi$ state at 215 nm is estimated to have a detection limit of $2 - 3 \times 10^6$ [162, 163] molecules per state and cm^3, provides rotational resolution in all branches except the Q–branch [162], and produces not only CO^+, but also $C^+ + O$ [163]. Proceeding via the $C^1\Sigma^+$ state by (2+1) REMPI at 218 nm is about three times more sensitive than via the E state, but rotational resolution cannot be obtained [162]. Employing the same scheme, but via the $B^1\Sigma^+$ state at 230 nm, is estimated to be the most sensitive method (3×10^5 [162] molecules per state and cm^3, or 1×10^{-10} mbar partial CO pressure with CO populating a room temperature distribution of ro-vibrational states [155]). Even though it does not provide full rotational resolution, the rotational distribution may still be estimated when the wavelength is accurately calibrated against the rotationally resolved but weak O- and S-branches. This makes (2+1) REMPI via the $B^1\Sigma^+$ state the most powerful scheme for CO $X^1\Sigma^+$ detection. If, however, full rotational resolution is needed, a (1+1) REMPI scheme, still via the B-state, may be chosen, which also has a very high sensitivity (4×10^5 molecules per state and cm^3 [164]), but requires the rather inconvenient wavelength of 115 nm. A limitation which both of these procedures share is that detection is lim-

ited to $X^1\Sigma(v \leq 2)$, since the B state is known to predissociate for $v \geq 2$ and the Franck-Condon factors of the transition are nearly diagonal. If detection of higher vibrational states is needed, detection schemes proceeding via the $A^1\Pi$ state have to be considered.

5.4 Data Acquisition and Control of the Experiment

Molecular beam experiments require carefully chosen timing of all of the instruments involved in the setup, typically on a microsecond timescale. Therefore, an essential ingredient in controlling a setup such as the one described in this thesis is a computer-controlled delay generator, which sends trigger pulses to the individual components at the proper time, corresponding to the arrival time of molecules at the desired position. For these purposes, the experimental setup incorporates three 4-channel delay generators (*FHI ELAB* DG3008) with 10 ns resolution in a rack-mountable cPCI housing. All 12 channels have a second output, which on one of the delay generators provides an inverted pulse. In order to provide a sequence of multiple triggers needed to pulse the high voltage of the decelerator, there are two special delay generators, capable of delivering trigger pulse trains called *bursts* instead of single pulses, thus referred to as burst units (*FHI ELAB* BU1708). As the hardware is almost identical to the DG3008, they also provide four double output channels each. Controlling these five delay generators using the software `KouDA` allows the beginning and end of every DG3008 channel to be controlled individually via a simple graphical user interface. In contrast, the two BU1708 units are controlled by loading so-called burst files into their memory. A burst file contains one or more burst sequences, each one of which, in principle, comprises a specific experimental setup. Each of these burst sequences consists of a chronological list of timings in nanoseconds and the associated channels which are switched on. Channels are encoded in the following way: Each channel is assigned a value equal to its channel number in binary system, i.e. channels 1, 2, 3, and 4 have values, 1, 2, 4, and 8, respectively. To obtain the identifier for a specific combination of channels being switched on, their values need to be added. The result is then written in hexadecimal representation, i.e. `0x00` corresponds to all outputs off, channels of burst unit 1 only are decoded via the last digit (`0x01`–`0x0f`), and channels of burst unit 2 are decoded via the last but one digit (`0x10`–`0xf0`). Using the hexadecimal representation has a neat advantage: Since each burst unit has exactly 16 possible configurations of channels being on or off, each digit of the channel code represents exactly one burst unit. As the examples given in table 5.2 demonstrate, the code is easily obtained by calculating the code for each unit individually as if it was the only one, and then using the resulting number in the range (`0`–`f`) as the last digit for the first unit, and as last but one digit for the second unit.

This triggering concept is ideally suited for providing the 130 trigger pulses to each decelerator switch, since each channel can be switched on and off multiple times in a burst sequence. Because the primary use of the burst units is to trigger the decelerator, succeeding timings need to differ by at least 1010 ns — this serves as a means of

# of channel	channel values	binary code	burst file code
1	1	00000001	0x01
2	2	00000010	0x02
3	4	00000100	0x04
4	8	00001000	0x08
5	16	00010000	0x10
6	32	00100000	0x20
7	64	01000000	0x40
8	128	10000000	0x80
none	0	00000000	0x00
all	255	11111111	0xff
1,2,3,4	$1+2+4+8=$ 15	00001111	0x0f
5,6,7,8	$16+32+64+128=240$	11110000	0xf0
2,4	$2+8=$ 10	00001010	0x0a
3,4	$4+8=$ 12	00001100	0x0c
5,7	$16+64=$ 80	01010000	0x50
3,4,5,7	$12+80=$ 92	01011100	0x5c
1,3,4	$1+4+8=$ 13	00001101	0x0d
5,7,8	$16+64+128=208$	11010000	0xd0
1,3,4,5,7,8	$13+208=221$	11011101	0xdd

Table 5.2: Examples of burst unit channel encoding for burst files.

protection for the circuits of the high voltage switches. Another advantage of burst units is their ability to scan over multiple experimental trigger schemes. In contrast to the DG3008, which can only be scanned over one channel during a scan, burst files may contain any number of burst sequences as described above, without limitation on the combination of channels used. Connecting other devices to the burst units in addition to the decelerator makes it possible to encode a specific experimental configuration in a burst sequence. Burst sequences can be loaded one after the other for signal recording in an automated scan. This in principle allows scanning of two or more timings at once, effectively doing a multidimensional parameter scan. A simple example with only three sequences is depicted in Fig. 5.10. Sequences are introduced by the sequence number in square brackets, comments are preceded by the pound (#) sign. Providing even more functionality, the scan can be automatically repeated with a randomized order of burst segments, such that scanning multiple times at low averages can be used to eliminate the effect of long term signal drifts on the scan. The setup can also be toggled between several distinct configurations which only differ by timing of the devices. This feature is in fact used to toggle between different detection setups as described in chapter 6. In addition to the afore mentioned delay generators, the 206 nm laser system is triggered by a commercial delay generator

```
[1]             # sequence 1
     1000  0x01 # channel  1
   100000  0x03 # channels 1,2
   110000  0x01 # channel  1
   200000  0x05 # channels 1,3
   210000  0x01 # channel  1
   500000  0xf1 # channels 1,8
   510000  0xf1 # channel  1
   800000  0x00 # all off

[2]             # sequence 2
     1000  0x01 # channel  1
   300000  0x03 # channels 1,2
   310000  0x01 # channel  1
   400000  0x05 # channels 1,3
   410000  0x01 # channel  1
   500000  0xf1 # channels 1,8
   510000  0xf1 # channel  1
   800000  0x00 # all off

[3]             # sequence 3
     1000  0x01 # channel  1
   100000  0x03 # channels 1,2
   110000  0x01 # channel  1
   600000  0x05 # channels 1,3
   610000  0x01 # channel  1
   800000  0x00 # all off
   900000  0xf0 # channels 1,8
   910000  0x00 # all off
```

Figure 5.10: An example of a simple burst file used for scanning multiple trigger signals. Channel 1 stays on for 800 µs in sequence 1, while three trigger pulses of 10 µs duration are send on channels 2, 3, and 8. In sequence 2, the two channels 2 and 3 are triggered later, whereas in sequence 3, channels 3 and 8 are shifted in time.

(*Stanford Research Systems, Inc.* DG535) such that it may be operated as a self-sufficient system. This additional delay generator also provides the main trigger for the whole molecular beam experiment.

Data is acquired by means of a dual channel digital oscilloscope (*Agilent* Aqciris DC 438 U 1066A-002) with 100 MHz bandwidth and 200 MSamples/s, such that signals with a rise time of down to 3.5 ns may be recorded with a time binning of down to 5 ns via `KouDA`, the same software that is used for controlling the delay generators. The

software itself consists of two parts, the first being a real-time system running on the cPCI control computer, which directly accesses all the devices and is able to perform real-time averaging of the signals as well as single event counting. The second part runs on a standard personal computer and provides the user interface and access to all features of the oscilloscope and delay generators. Communication takes place via a fast Ethernet connection, such that the maximum transfer rate is limited by that of the PCI bus of theoretically 133 MB/s.

5.5 Conclusion

The surface scattering chamber of the apparatus described in this thesis features a 3-axis manipulator combined with two rotation stages for flexible positioning of the surface, two detectors for positive and negative particles, and provides space for flexible laser access. The surface temperature can be computer-controlled between 25 K and the melting point of gold. Surface cleaning by ion bombardment and high temperature annealing has been demonstrated to work by Auger electron spectroscopy.

A pressure on the order of 1×10^{-10} mbar in the surface chamber is achieved by means of baking the apparatus at temperatures of 100 °C. Under these conditions, the surface is expected to stay sufficiently clean of contaminations for a time of several hours. No pressure rise is observed when the molecular beam enters the scattering chamber, which indicates that the separation of $CO^\star$ from electronic ground state CO and the carrier gas in the preceding hexapole is successful.

$CO^\star$ can be detected in the source chamber by ionizing it in a (1+1) REMPI process using a pulsed laser with a wavelength of 283 nm and detecting the resulting CO^+ ions with an MCP. A second MCP is used to detect electrons emitted in the $CO^\star$-Au(111) collision.

Chapter 6

$CO^{\star}$-Au(111) Scattering

It is a well-established fact that upon collision in the gas phase, atoms in highly excited metastable states can ionize atoms whose ionization potential, E_{IP}, is lower than the excitation energy, $E^{\star}$, of the metastable [165]. This process is accompanied by emission of electrons, and is now commonly referred to as Penning ionization. An equivalent process may take place at metal surfaces: when the internal energy of the metastable particle exceeds the work function of the metal, the metastable may quench and cause emission of an electron in the process. This effect was first discovered by Webb, who observed that pulsing an electric current through mercury vapor at a well-defined voltage resulted in a photoelectric current at a low work-function surface, which could not be explained by mere radiation. He correctly attributed it to mercury atoms being excited to a metastable state and their subsequent de-excitation at the metal surfaces of the photo-electrodes of his apparatus [48]. A detailed analysis of the processes involved in the relaxation of ions and metastables at metal surfaces was given as early as 1954 by Hagstrum [49]. The kinetic energy spectrum of the emitted electrons proves to be very sensitive to the density of electronic states at the surface. This underlying effect is exploited in the related spectroscopic techniques of *ion neutralization spectroscopy* (INS) [166] and *metastable quenching spectroscopy* (MQS) [167], also known as *metastable atom electron spectroscopy* (MAES) or *metastable impact spectroscopy* (MIES). This chapter describes experiments performed not with metastable atoms but metastable CO, and addresses the issues involved in applying the well-understood models for atom excitation to molecules. Major parts of this chapter are based on references [168] and [169].

6.1 Molecule-Surface Scattering

6.1.1 Metastable Atom–Surface Scattering—A Brief Review

In order to understand the mechanisms underlying the de-excitation of metastable particles and ions at metal surfaces, a brief review will be given here, loosely following references [170, 171]. Key concepts of electron emission during de-excitation of ions and metastable atoms were first introduced by Hagstrum [49, 172, 173], who proposed two main pathways for this process. If the energy difference between ionization potential, E_{IP}, and metastable energy level, $E^{\star}$, of the incoming metastable is less than the work function, Φ, of the metal, the electron in the metastable level of the atom can tunnel to an unoccupied level of the metal surface. This step is called

resonant ionization (RI) and depicted in Fig. 6.1a. The ion produced in this manner can then be neutralized in a process known as Auger neutralization (AN), where an electron from the conduction band of the metal tunnels into the ground state of the ion, and a higher-lying electron from the conduction band is emitted in an Auger process. This process is only possible if the energy released in the recombination from the ionic state to the ground state is larger than 2Φ.

The other possible mechanism is most likely to occur when $E_{\mathrm{IP}} - E^{\star} \geq \Phi$, i.e. when the metastable level is lower in energy with respect to the vacuum level than the Fermi level of the metal. In this case, no resonant ionization of the molecule is possible because all of the electronic states in the conduction band of the metal are occupied. Instead, an electron from the conduction band of the metal can tunnel into the ground state of the molecule, which at the same time releases the excited electron from the metastable state in an Auger process. The mechanism is therefore called Auger de-excitation (AD). This process is only energetically possible if

$$E^{\star} \geq \epsilon_{\mathrm{cb}} - \epsilon_c + \Phi\,, \tag{6.1}$$

where ϵ_c is the energy of the exchanged electron relative to the conduction band which has a width of ϵ_{cb}. By this definition, $\epsilon_{\mathrm{c}} - \epsilon_{\mathrm{cb}}$ is the energy of the electron with respect to the Fermi level, which is negative for an electron below the Fermi level. Eq. (6.1) implies that for electron emission to occur, the exchanged electron has to be closer in energy to the vacuum level than the metastable state is to the molecule's ground state.

A schematic view of this mechanism is illustrated in Fig. 6.1b. When the excited states have different spin multiplicity, as in the common case of a triplet metastable state and a singlet ground state, this electron exchange between surface and molecule is the only possible AD process. If, however, the spins of metastable and ground state have an antiparallel orientation, de-excitation may also occur directly from the metastable state to the ground state, which will lead to electron emission from the metal's conduction band if the released energy is sufficient. This process, which does not involve electron exchange between the surface and the metastable particle, is commonly called the direct mechanism.

Ionic species will in general de-excite via AN. In the case that a metastable level of the corresponding neutral atom lies energetically below the Fermi level of the metal surface, the ion can also undergo resonant neutralization (RN), which can be thought of as the reverse process of RI. In the resonant neutralization step, an electron from the conduction band of the metal neutralizes the ion by tunneling to the metastable atom level. The metastable created like this will then de-excite via the AD mechanism.

When a particle approaches a metal surface, its energy levels will in general shift with respect to the ionization potential due to interactions with the surface. Therefore, energy levels have to be replaced by effective energy levels, $E_{\mathrm{eff}}(d)$, which depend on the surface distance, d. This is especially true for ionic species. Placing a charged particle near a metal surface generates an electric field which can be calculated by the method of images [115, p. 121]. Due to the apparent image charge, the ion experiences an attractive force towards the surface, leading to a stabilization in energy by the

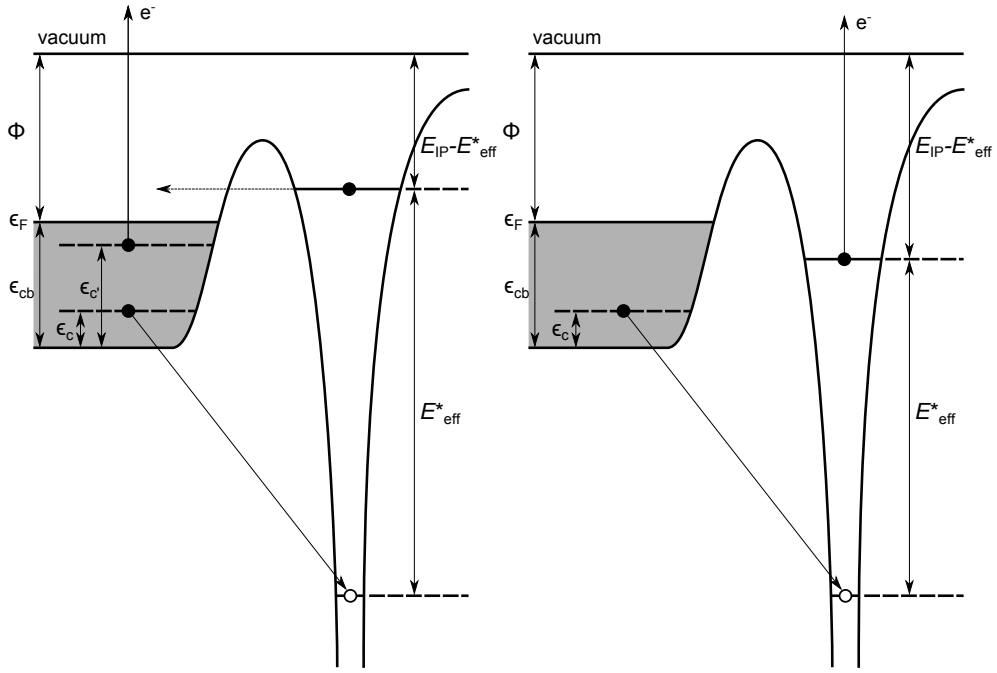

(a) RI+AN (b) AD

Figure 6.1: Mechanisms for metastable de-excitation.

amount

$$E_{\text{img}} = -\frac{3.597}{d-s}\,\text{eVÅ}\,. \tag{6.2}$$

Here, d is the distance of the charge to the position of the jellium edge of the surface, and s accounts for the fact that the electron density involved in creating the image charge potential partly extends into the vacuum region. The parameter s is usually estimated to be 0.5–0.6 Å [171, 174]. This classical approximation is only valid for $d \gtrsim 2\,\text{Å}$; for shorter distances, the energy shift tends towards a constant value due to quantum mechanical effects [174]. The charge–image charge interaction reaches considerable magnitudes close to the surface. For $d = 5\,\text{Å}$, Eq. (6.2) yields $E_{\text{img}} = 0.8\,\text{eV}$, while at 3 Å it already reaches 1.5 eV. Other interaction terms, e.g. due to a permanent dipole, or even a Van-der-Waals like interaction due to the polarizability of the metastable species, have a much smaller contribution at typical distances. As an example, consider the permanent dipole – image dipole interaction, which is given by [115]:

$$E_{\text{dip}} = -\frac{1}{4\pi\epsilon_0}\frac{\mu^2}{2\,(2(s-d))^3}\,, \tag{6.3}$$

with the dipole moment, μ, and the same parameter s as in Eq. (6.2) assumed to be

valid. For a typical value of $\mu = 1.37\,\mathrm{D}$, which is the dipole moment of CO*, this stabilization contributes less than 6 meV even at surface distances as low as 3 Å. Since this is at least two orders of magnitude lower than E_{img}, and less than the uncertainty of many of the energy levels involved, it safely can be neglected.

For all of the de-excitation mechanisms mentioned, the corresponding transition rate in general depends on the overlap of the wavefunctions of the electrons involved, i.e. on the matrix elements [49, 171]:

$$R_{\mathrm{RI}} \propto \langle \Psi_v(1) \,|\, \Psi_m(1) \rangle \tag{6.4}$$

$$R_{\mathrm{AN}} \propto \left\langle \Psi_f(1) \right| \langle \Psi_g(2) | \, \frac{e^2}{r_{12}} \, |\Psi_c(1)\rangle \, |\Psi_{c'}(2)\rangle \tag{6.5}$$

$$R_{\mathrm{AD}} \propto \left\langle \Psi_f(2) \right| \langle \Psi_g(1) | \, \frac{e^2}{r_{12}} \, |\Psi_m(2)\rangle \, |\Psi_c(1)\rangle \ , \tag{6.6}$$

where $\left|\Psi_f(n)\right\rangle$ is the wavefunction of the emitted electron n, $|\Psi_g(n)\rangle$ and $|\Psi_m(n)\rangle$ the wavefunctions of electron n in the ground and metastable state of the atom, respectively, $|\Psi_c(n)\rangle$ and $|\Psi_{c'}(n)\rangle$ refer to electrons n in the conduction band of the metal, and $|\Psi_v(n)\rangle$ denotes the wavefunction of an electron in a formerly vacant state above the Fermi level of the metal. The term e^2/r_{12}, with elementary charge e and distance r_{12} between electrons 1 and 2, accounts for the fact that it is Coulomb interaction between electrons which drives the process.

Some tendencies are immediately apparent from these transition rates: Since the wavefunction of an atom is usually more spatially extended in the metastable state than in the ground state, the overlap with a vacant surface state, $\langle \Psi_v(1) \,|\, \Psi_m(1) \rangle$, will in general be larger than the overlap, $\langle \Psi_g(1) \,|\, \Psi_c(1) \rangle$, between the atomic ground state orbital and the wavefunction of an electron in the conduction band of the metal for a fixed surface distance d. This means that if RI is energetically possible, it will be the dominant mechanism, because on its inbound trip, the metastable will first encounter a region where only RI is possible, but not AD. In all cases of electron emission in which the electron is ejected from the metal, the escape probability of the electron, which depends on its kinetic energy, has to be taken into account. As it is not relevant for the processes considered in this work, it will not be discussed here; details may be found, e.g., in reference [49, p. 345].

When studying the relaxation of metastable particles on metal surfaces, two important ways of characterizing the process are to measure the kinetic energy distribution of emitted electrons and the electron emission yield, γ. The latter is defined as the number of electrons emitted per metastable particle which collides with the surface. In principle, both the energy distribution of the emitted electrons and the value of γ can be obtained by integration from the transition rates. Calculation of the above matrix elements, however, is cumbersome and requires the knowledge or the approximation of all the wavefunctions involved. A common approximation for the case of AD is to use a simple tunneling model to describe the electron transfer to the ground state level of the metastable species, and neglect the overlap between wavefunctions of emitted electron and metastable state. In this simplified model, the transition rate

as a function of distance and energy of the tunneling electron becomes proportional to the tunneling transmission coefficient [175]:

$$R_{\mathrm{AD}}(\epsilon, d) \propto \mathcal{D}(\epsilon)\frac{1}{d}T(\epsilon, d)\ . \tag{6.7}$$

Here, $\mathcal{D}(\epsilon)$ is the electronic density of states (DOS) inside the conduction band, and the term $1/d$ accounts for the fact that it is Coulomb's interaction which drives the electron exchange. The transmission coefficient, $T(\epsilon_{\mathrm{c}}, d)$, for a bound electron inside the metal with binding energy, ϵ_{c}, relative to the bottom of the conduction band is in the most simple case calculated for a rectangular barrier of thickness equal to the surface distance d and a height of $V_0 = \epsilon_{\mathrm{cb}} + \Phi$, where ϵ_{cb} is the width of the conduction band (see, e.g. reference [176]):

$$T(\epsilon_{\mathrm{c}}, d) = \frac{4\epsilon_{\mathrm{c}}(V_0 - \epsilon_{\mathrm{c}})}{4\epsilon_{\mathrm{c}}(V_0 - \epsilon_{\mathrm{c}}) + V_0^2 \sinh^2\left(d/\hbar\sqrt{2m_e(V_0 - \epsilon_{\mathrm{c}})}\right)} \tag{6.8}$$

$$\approx 16\frac{\epsilon_{\mathrm{c}}}{V_0}\left(1 - \frac{\epsilon_{\mathrm{c}}}{V_0}\right)\exp\left(-2d/\hbar\sqrt{2m_e(V_0 - \epsilon_{\mathrm{c}})}\right)\ . \tag{6.9}$$

Here, the approximation in Eq. (6.9) is only valid for $d/\hbar\ \sqrt{2m_e(V_0 - \epsilon_{\mathrm{c}})} \gg 1$. Note that all energies are measured with respect to the conduction band in this equation. Using this model, keeping only the exponential term of Eq. (6.9), Woratschek *et al.* [175] were able to demonstrate that AD takes place at surface distances of 3–5 Å. For comparison, it was shown that RI will already take place at distances larger than 5 Å if it is energetically allowed [177].

Another ionization mechanism has been shown to be involved in the singlet-triplet conversion of He(2^1S) to He(2^3S)(see, e.g., references [178, 179]): as the metastable Helium approaches the surfaces, the electron affinity of the occupied singlet state eventually crosses the Fermi level of the surface, whereupon the metastable atom resonantly captures an electron from the conduction band and forms an anion. Subsequently, the anion either decays to the neutral ground state directly, emitting an electron, or it decays to the metastable triplet state by transferring one electron to the surface.

6.1.2 Extension to Metastable Molecule-Surface Scattering

In principle, all of the mechanisms and arguments given in the previous section remain valid when the metastable particle colliding with the surface is a molecule instead of an atom or atomic ion. A few important aspects, however, need to be considered when dealing with molecules. First of all, the excitation energies of the lowest metastable state are commonly lower, and the the ionization potential of the metastable level, $E^\star_{\mathrm{IP}}$, higher than for rare gas atoms. The $A^3\Sigma_u^+$ state of N_2, e.g., carries an internal energy of $E^\star = 6.17\,\mathrm{eV}$ and requires 9.41 eV for ionization. The higher-lying $N_2(a^1\Pi_g)$ state has values of $E^\star = 8.55\,\mathrm{eV}$ and $E^\star_{\mathrm{IP}} = 7.03\,\mathrm{eV}$, while

for CO*, $E^\star = 6.0\,\mathrm{eV}$ and $E^\star_{\mathrm{IP}} = 8.0\,\mathrm{eV}$ are the relevant energies (all values from references [61, 180]). As a consequence, the metastable level will be below the Fermi level of most metal surfaces like Au(111), as shown in the energy diagrams of Fig. 6.1. This means that the RI+AN process, which is dominant in most of the cases where metastable atoms scatter from clean metal surfaces, will be irrelevant. Even when the image charge stabilization of Eq. (6.2) is taken into account, the energy levels will not cross at reasonable surface distances. In the case of CO ($a^3\Pi$), RI is energetically feasible only when the molecule is 1.9 Å or closer to the surface. As the inbound molecule will reach this point only after having passed the region of 3–5 Å in front of the surface where AD is known to take place (see section 6.1.1), RI is not expected to contribute significantly to electron emission.

A more universal feature of molecules is their vibrational structure, which is obviously not captured by the models developed for metastable and ionic atomic species. At excitation energies, $E^\star$, which are only on the order of 1 eV larger than the work function of the surface, the spacing of vibrational energy levels becomes appreciable, since it is typically on the order of 0.2–0.3 eV [61] for the levels involved. Therefore, vibrational excitation of the metastable state increases the excess energy for electron emission considerably. In addition, the molecule can de-excite to different vibrational levels of the electronic ground state. Relaxation to states other than the vibrational ground state of the molecule effectively reduces the energy available for electron emission. The electron emission yield is therefore not necessarily independent of the vibrational level of the metastable state. In the context CO* scattering from Au(111), it therefore useful to define γ_v as the electron emission yield for a metastable molecule in the vibrational level v. An important aspect is that the intra-molecular Auger process of AD happens instantly on the timescale on which the nuclei of the molecule move. Therefore, the transition probabilities to the different lower vibrational levels have to be weighted by the overlap integral of the vibrational wave functions of metastable and electronic ground state, i.e. the Franck-Condon factors [181] (FCF) of the corresponding molecular transition. The FCF between an upper vibrational level, v', and a lower vibrational level, v'', will be denoted by the symbol $q(v'', v')$.

The above considerations have been implemented in a simple model, which was first introduced by Borst [182], who only considered relaxation to the ground vibrational level, and Zubek [183]. In this model, the total electron emission yield for a metastable molecule with vibrational quantum number, v', is given by

$$\gamma_{v'} \approx \sum_{v''} \left(q(v'', v') \times \int_{\epsilon_F - E_{\mathrm{ex}}}^{\infty} f(\epsilon, T_S)\mathcal{D}(\epsilon)\mathrm{d}\epsilon \right) \tag{6.10}$$

$$\approx \sum_{v''} \left(q(v'', v') \times \mathcal{D}_{\mathrm{avg}} \times E_{\mathrm{ex}} \right) \tag{6.11}$$

$$\propto \sum_{v''} \left(q(v'', v') \times E^\star(v'', v') - \Phi \right) . \tag{6.12}$$

Here, $E_{\mathrm{ex}} = E^\star(v'', v') - \Phi$ is the excess energy available for electron emission, $E^\star(v'', v')$ is the energy difference of upper and lower state, and ϵ_F and Φ denote the Fermi level and work function of the surface, respectively. In the approximation in

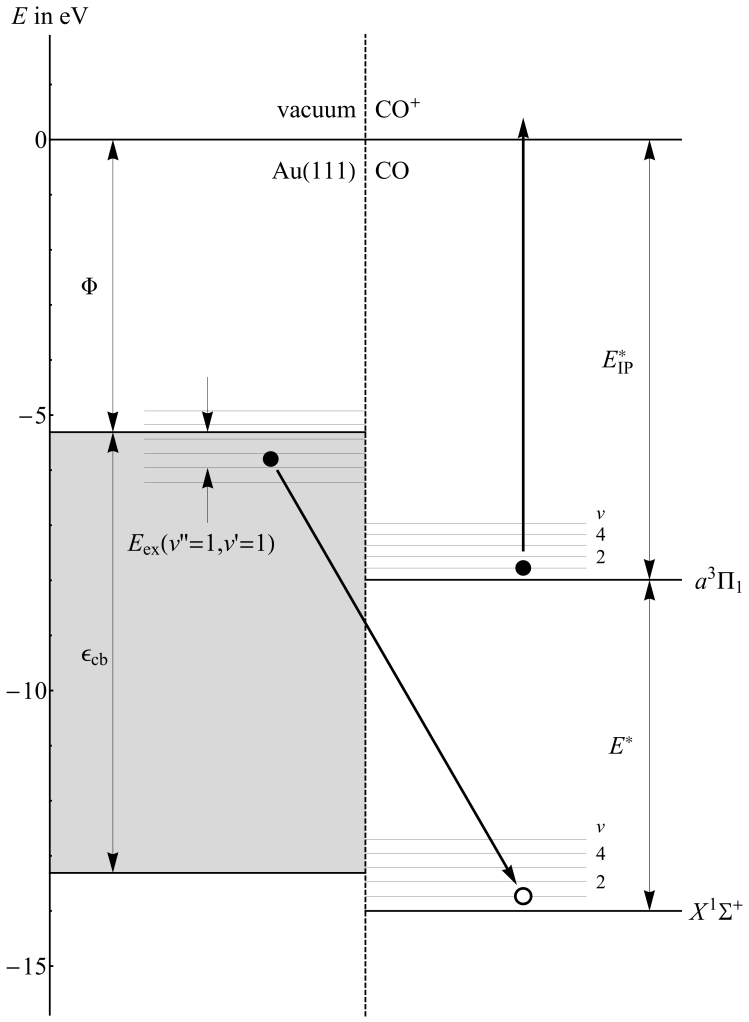

Figure 6.2: Metastable molecule de-excitation at a metal surface. The scheme shows all relevant energies involved in scattering a metastable molecule (right) from a metal surface (left). All energies and term symbols are for CO* on Au(111). When the metastable is excited to $v' = 1$, the excess energy levels depicted as thin lines around the Fermi level of the metal limit the energy range from which an electron can tunnel to the metastable vibrational states. In this case, the electron depicted on the left is just high enough in energy that, when it tunnels to $v'' = 0$ or $v'' = 1$, the electron from the $v' = 1$ level in the metastable state can be emitted. Tunneling to vibrational levels with $v'' \geq 4$ will not lead to electron emission from the $v' = 1$ level for any electron in the conduction band.

the second line, the Fermi function, $f(\epsilon, T_S)$, for a given surface temperature, T_S, is assumed not to deviate significantly from $T_S = 0$, which effectively cuts off the integral at ϵ_F. In addition, the electronic density of states, $\mathcal{D}(\epsilon)$, of the surface is assumed to have the constant value $\mathcal{D}_{avg}$ over the integration range, effectively yielding the same constant pre-factor for any combination of v' and v''. In the case of a Au(111) surface, the assumption of a constant electronic density of states is in good agreement with experimental data for energies down to 2 eV below the Fermi level [184]. The idea behind this model is that, to a very good approximation, the electron yield will rise if there are more electrons energetically available in the conduction band of the metal, i.e. the contribution from any energy interval $d\epsilon$ will be proportional to $\mathcal{D}(\epsilon)d\epsilon$. Note that Zubek proposed the approximation in the last line only, while Eq. (6.10) already comprises a small extension first introduced in the scope of this work. In this chapter, both the approximation and the model including the full integral will be referred to as Zubek's model. The process when a metastable molecule in $v' = 1$ is de-excited to the ground state level $v'' = 1$ is depicted for the case of CO* on Au(111) in Fig. 6.2.

Another possible mechanism for metastable molecule de-excitation at a metal surface bears some similarities to the case of the singlet-triplet conversion observed in metastable He that is described in the previous section. The de-excitation of CO* in this model proceeds by first capturing an electron from the surface to form a transient CO^- anion. In a second step, the anion will autodetach. The ejected electron can either be emitted, if its energy is sufficient, or transfer back to the metal surface. All known states of CO^- are unstable in the sense that they will decay on a time scale of usually less than 10^{-13} s. The existence of these anionic states has mainly been observed as the appearance of Feshbach and shape resonances in electron scattering experiments. A shape resonance can best be pictured in the special case that it is an orbiting resonance. This type of resonance arises when both the kinetic energy of the approaching electron and its angular momentum with respect to the molecule match that of a bound rotational state of the interaction potential, but reaching this bound state is prohibited by a centrifugal barrier. As a result, the electron will start to orbit the molecule for a certain time before it departs again. Feshbach resonances can occur when the kinetic energy of the incoming electron is just below a bound electronic Rydberg state of the molecule. Even though the electrons kinetic energy is insufficient to access the bound state, the influence of the potential is strong enough that a quasi-bound state with a short lifetime exists.

In the case of CO, many electron scattering resonances are known [185]. Several of these resonances have been observed to be involved in the excitation of CO in its electronic ground state to the $a^3\Pi$ state by inelastic scattering of electrons. Those include the $^2\Pi$, $^2\Delta$ and $^2\Sigma^+$ shape resonances at 1.8 eV, 9.2 eV and 10.5 eV, and the $^2\Sigma^+$ Feshbach resonance at 10.04 eV above the electronic ground state, respectively [186–189]. The imprint of the three shape resonances can be observed in the inelastic cross section for excitation of the $a^3\Pi$ state over a range of several electron volts [186, 187]. In contrast, the energy width of the of the $^2\Sigma^+$ resonance has been determined to be only 0.045 eV [190]. The outer electron configurations of the four resonances and of the CO

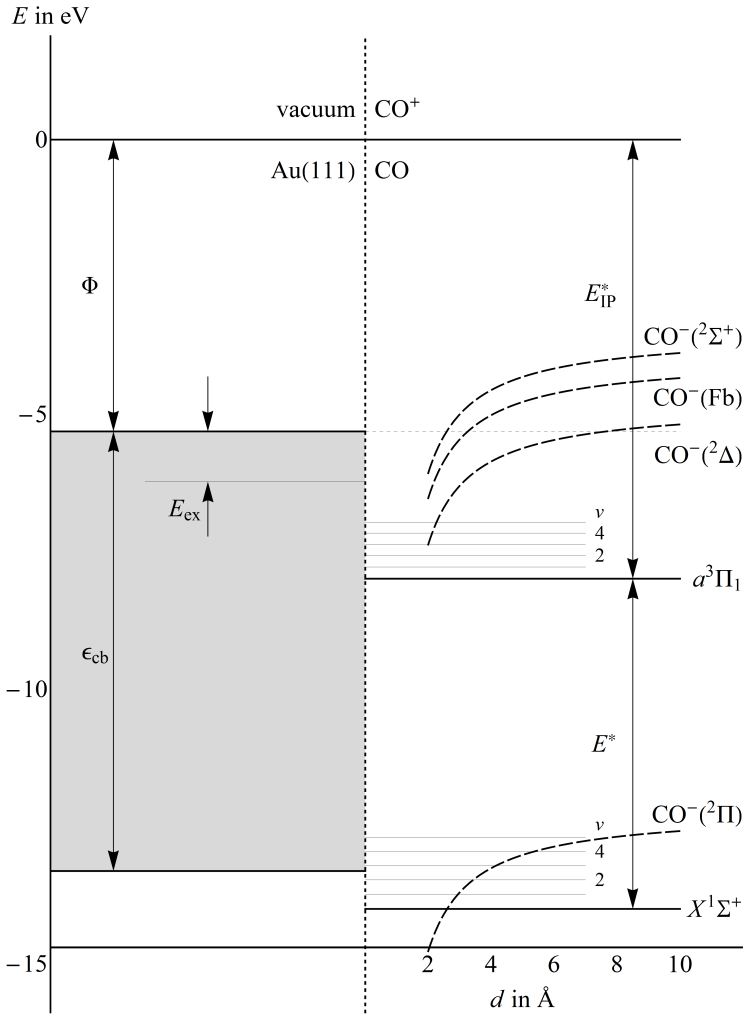

Figure 6.3: Energy levels relevant for de-excitation of CO* at a Au(111) surface via an anionic resonance. The states associated with anionic resonances are depicted as curved dashed lines, where Fb denotes the $^2\Sigma^+$ Feshbach resonance. As soon as the anionic states drop below the Fermi level of the metal due to image charge stabilization, resonant electron transfer from the conduction band of the surface to the molecule is possible. When the ionization step happens at the Fermi level, the tunneling electron has an energy of 2.7 eV with respect to the vibrational ground level of the $a^3\Pi$ state. Upon decay to the electronic ground state of the molecule, the electron will gain the $a^3\Pi$ excitation energy in addition to the initial 2.7 eV with respect to the $a^3\Pi$ state, which is enough to eject the electron if it happens before the resonance level drops below the thin horizontal line indicated on the left.

electronic ground $X^1\Sigma^+$ and $a^3\Pi$ state are given in table 6.1. It is readily seen that

state/ resonance	energy	electron configuration
$X^1\Sigma^+$	0.0 eV	$kl\ 1\pi^4\,5\sigma^2$
$^2\Pi$	1.8 eV	$kl\ 1\pi^4\,5\sigma^2\,2\pi^1$
$a^3\Pi$	6.0 eV	$kl\ 1\pi^4\,5\sigma^1\,2\pi^1$
$^2\Delta$	9.2 eV	$kl\ 1\pi^4\,5\sigma^1\,2\pi^2$
$^2\Sigma^+$	10.5 eV	$kl\ 1\pi^4\,5\sigma^1\,2\pi^2$
$^2\Sigma^+$	10.04 eV	$kl\ 1\pi^4\,5\sigma^1\,3s\sigma^2$

Table 6.1: Electron configuration for selected electronic states and resonances. The inner electron configuration, $1\sigma^2\,2\sigma^2\,3\sigma^2\,4\sigma^2$, is denoted by kl [191].

the de-excitation of CO* ($a^3\Pi$) to its electronic ground state via excitation of the $^2\Pi$ involves two one-electron processes, whereas for the $^2\Delta$ and $^2\Sigma^+$ shape resonances, the de-excitation step is a two-electron process. When the $^2\Sigma^+$ resonance at 10.04 eV is involved, both the excitation and the de-excitation step are two-electron processes. The excitation and de-excitation of the $^2\Sigma^+$ Feshbach resonance appears to be unlikely due to the large number of electrons changing orbitals. However, experiments in which electrons are scattered from electronic ground state CO show a significant enhancement of the CO ($a^3\Pi$) formation when the kinetic energy of the electrons is 10.04 eV [192], indicating a high probability for excitation of the resonance.

To illustrate the role of an anionic resonance in the de-excitation of CO*, consider the case of the $^2\Sigma^+$ resonance at 10.04 eV, which is denoted by "Fb" in Fig. 6.3. At asymptotic surface distances, the $^2\Sigma^+$ resonance is located 1.35 eV in energy above the Fermi level of Au(111). As CO* approaches the surface, image charge stabilization causes the $^2\Sigma^+$ energy to dip below the Fermi level at a surface distance lower than 3.28 Å. At this point, a conduction band electron from the Au(111) surface can be resonantly captured by the approaching CO molecule, leading to the formation of an anion whose electron configuration is that of the $b^3\sigma^+$ state with an additional electron in the $3s\sigma$ orbital. Rapid autodetachment of $CO^-(^2\Sigma^+)$ will follow, in which the most likely de-excitation of the molecule is to the $X^1\Sigma^+$ electronic ground state. An electron which tunnels to the resonance state will be $2.7\,\text{eV} - \epsilon_{cb} + \epsilon_c$ higher in energy than the ground vibrational level of CO*, where again $\epsilon_c - \epsilon_{cb}$ is the energy of the electron with respect to the Fermi level.

When the resonance decays to the electronic ground state, one of the electron from the $3s\sigma$ orbital is ejected, gaining the excitation energy of the $a^3\Pi(v')$ state in addition to its initial energy in the process, while the other electron is transfered back to the 5σ orbital. The final energy of the ejected electron with respect to the $a^3\Pi(v' = 0)$ state will thus be $2.7\,\text{eV} - \epsilon_{cb} + \epsilon_c + E^\star(v'', v') - \Delta E_{img}$. Here, $E^\star(v'', v')$ is the excitation energy of the vibrational level, v', of CO* with respect to the final vibrational level, v'', of the electronic ground state, and $\Delta E_{img} = E_{img}(d_{formation}) - E_{img}(d_{decay})$ is the

energy difference in image charge stabilization between the point of formation and the point of decay of the anion resonance. Since the $a^3\Pi$ state is 2.7 eV lower in energy than the Fermi level, this leads to the condition that electron emission only occurs if

$$E^\star(v'', v') - \Delta E_{\text{img}} > \Phi + \epsilon_{\text{cb}} - \epsilon_{\text{c}} \,. \tag{6.13}$$

For a short-lived anion resonance, ΔE_{img} is small, such that the energetic condition for electron emission when an anionic resonance is involved is approximately the same as for the Auger de-excitation mechanism (see Eq. (6.1)).

Metastable de-excitation via transient anionic states has been reported to play an important role in the de-excitation of metastable N_2 impinging on a clean tungsten surface [193–195]. Other studies suggest that anion resonances are also involved in the de-excitation of CO_2^+ and CO^+ on W(110) [196, 197]. The impact of this model on the electron emission yield will be examined in the discussion of experimental results in section 6.2.3.

6.2 State-Selective Scattering of $CO^\star$ from Au(111)

Low work function surfaces are commonly used to detect ions or metastable particles. The most prominent example are the metal-doped glass plates of any MCP, which are used for detection applications because of their favorable secondary electron yield, γ, i.e. the number of electrons emitted per incident particle. Similarly, the copper beryllium oxide material commonly used in electron multipliers is selected for the very same reason. While secondary electron yields greater than unity are quite common for impact of fast charged particles (see [50, p. 12-125]), detection of metastable particles is usually less sensitive: In principle, the electron yield is limited to less than unity and, on atomically clean metal surfaces, in practice $\gamma \leq 0.3$ often holds (see, e.g., [170, p. 197]). In general, the yield rises with increasing excitation energy, and also depends strongly on the specific surface and metastable species, as well as the surface conditions. Nonetheless, noble metal surfaces have been used as convenient means for detection of metastable particles, in particular atomically clean Ag [198] and amorphous heated gold for the detection of CO* (see, e.g., references [8, 98, 123, 199]). For applications like these, it is of great advantage to calibrate the detector, i.e. determine the electron yield, γ, such that the number of metastable molecules in the beam can be obtained from the signal of electrons emitted. For the experiments with CO in its electronic ground state planned with the apparatus described in this manuscript, using the gold surface as a calibrated metastable detector provides many benefits. Since only a part of the beam will be prepared in the final quantum state, the remaining metastable pulse may be used to monitor the performance of the molecular beam setup up to the surface. Thus, calibrating the metastable signal by determining the electron emission yield will allow an accurate determination of the number of molecules in the desired quantum state which collide with the surface.

6.2.1 Determination of the Absolute Electron Emission Yield

Since the electron emission yield for CO* in its vibrational ground level on Au(111), γ_0, should serve as a reference for future experiments, it needs to be measured for the whole surface temperature and velocity range which can be covered by the machine. This task is greatly simplified by the fact that the *absolute* value of γ_0 needs to be determined only once for a well-defined temperature and velocity. All other data can than be recorded in a *relative* measurement and referenced to the relative value of standard conditions. These standard conditions are chosen for convenience as $v_{CO^\star} = 360\,\mathrm{m/s}$, since it yields the highest signal, and $T_{surf} = 360\,°\mathrm{C}$, since it is high enough in temperature to avoid rapid contamination by background gas, but low enough to allow uncomplicated manual temperature stabilization.

The method chosen to accurately determine the value of γ_0 is an ionization-depletion scheme similar to the one employed by Hotop [200]. The basic idea is to remove part of the metastable beam by laser ionization, measure the resulting dip in the electron emission signal from the surface, and compare it to the number of ions which are produced by the laser, as schematically depicted in Fig. 6.4. A part

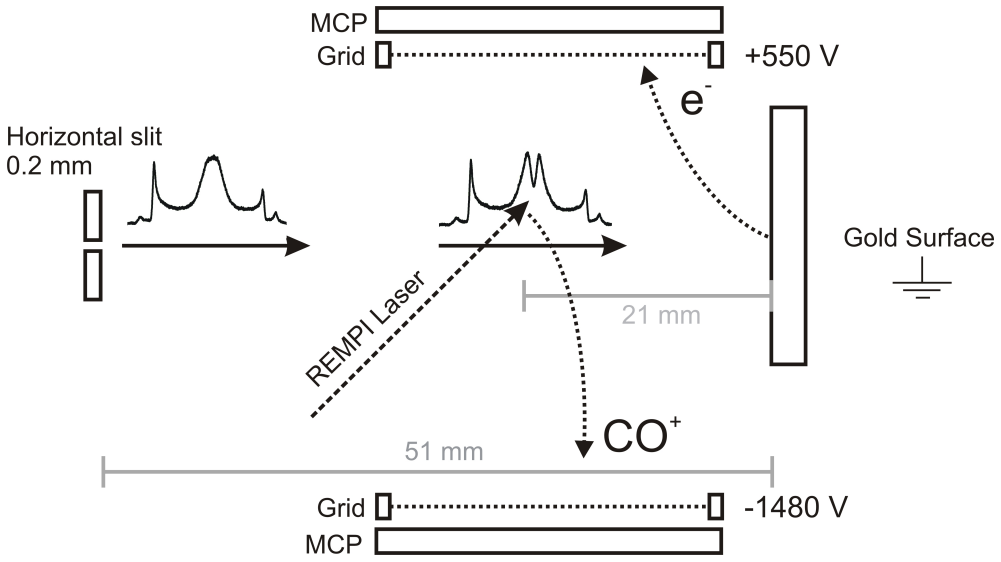

Figure 6.4: Detail of experimental setup near the surface for determination of γ_0 [168]. See text for details.

of the CO* beam can be ionized by a $(1+1)$ REMPI process via the $b^3\Sigma^+(v=0) \leftarrow a^3\Pi_1(v=0)$ transition at 283 nm (see section 5.3.2) 21 mm upstream of the surface. In order to improve the contrast of electron signal with ionization laser switched on compared to electron signal with ionization laser switched off, a 200 µm wide and 8 mm long slit is placed parallel to the laser beam just behind the aperture which separates decelerator and surface chamber, 51 mm upstream the surface. The laser

energy of 2 mJ per pulse is sufficient to saturate the REMPI transition, even though the laser is only gently focused, to a point roughly 10 mm behind the intersection with the molecular beam, by a lens of 750 mm focal length.

In principle, three signal are needed to calculate the value of γ_0: The signals, $\mathcal{D}_d(t)$ and $\mathcal{D}_e(t)$, of electrons originating from the $CO^\star$-surface collision with and without laser ionization, respectively, and the CO^+ signal, $\mathcal{I}(t)$, from laser ionization. Subtraction of one electron signal from the other yields the depletion difference time-of-flight trace, $\mathcal{D}(t) = \mathcal{D}_e(t) - \mathcal{D}_d(t)$, for metastable molecules, which is time-integrated to obtain the integrated depletion, $\bar{\mathcal{D}}$. The ion signal is also time-integrated, obtaining the result $\bar{\mathcal{I}}$, and the value of the electron yield is then given by the expression $\bar{\mathcal{D}}/\bar{\mathcal{I}} \times \exp(t_{\text{arrival}}/\tau)$. Here, the exponential term compensates for the decay of the electron signal due to the finite lifetime τ during the time t_{arrival} which it takes the molecules to arrive at the surface after laser ionization. Note that because $t_{\text{arrival}} \approx 62\,\mu\text{s} \ll \tau = 2.63\,\text{ms}$, this effect is almost negligible, namely, $\exp(t_{\text{arrival}}/\tau) \approx 1.02$.

Experimentally, a few difficulties have to be overcome which necessitate modifications to the above equation: First of all, stray light from the ionization laser reaches the MCP's and causes a background at times when the signals arrive at the surface. In order to unambiguously remove this background, an additional trace is taken with the nozzle of the molecular beam being triggered such that the molecular beam pulse misses the excitation laser in time, and only the stray light is recorded. The background obtained in this manner is then subtracted from the corresponding electron and ion signals.

An interesting aspect of the experiment is the fact that the *total* electron signal exhibits an enhancement when the ionization laser shines into the scattering chamber. At arrival times where no depletion is observed, it appears to be larger than the undepleted signal by a constant factor. To elucidate the reason for this intriguing behavior, the influence of laser frequency and position is investigated. When the REMPI laser is tuned off the molecular resonance, the electron signal is recovered as if no laser was present. In contrast, when the resonant laser pulse is shifted in time by 22 µs such that the $CO^\star$ beam passes directly before or directly after the laser fires, depletion vanishes, but the intensity of the overall signal is still increased by a constant factor. An explanation of the described effect hence has to be sought in the presence of weak, but resonant stray light. It should be emphasized here that the scattering chamber does provide two large (DN 100CF) UV fused silica entry and exit laser windows which are neither mounted at Brewster's angle nor perfectly parallel to each other. As a result, a significant fraction of the laser light will be reflected off the exit viewport and bounce back and forth between the windows, eventually illuminating a large portion of the molecular beam axis with low-intensity light. Since the phenomenon of signal enhancement only occurs on resonance, it is concluded that it is related to a fraction of CO molecules being pumped to the $b^3\Sigma^+$ state. This quantum state has a short lifetime of only 54 ns [201] and will decay back to the $a^3\Pi$ state before the molecules hit the surface, yielding a population distributed according to the Franck-Condon factors (FCF) [181] between the two states. The reasons why molecules in higher vibrational states cause higher electron emission will be discussed in section 6.2.2.

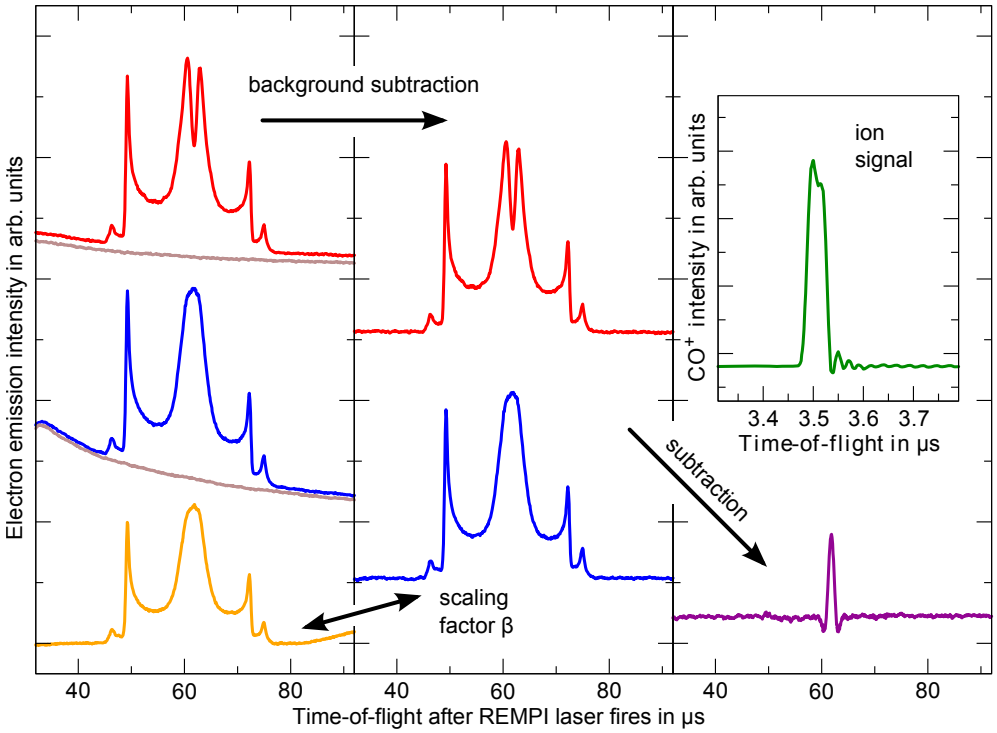

Figure 6.5: Schematic illustration of γ_0 determination from the five experimental time-of-flight traces (left). First, background (light brown) is subtracted to yield $\mathcal{S}(t)$ (blue, center) and $\mathcal{D}_d(t)$ (red, top), and the scaling factor β between stray-light enhanced signal $\mathcal{S}(t)$ and non-enhanced signal $\mathcal{D}_e(t)$ (orange, bottom) is determined (middle). Next, depleted signal is subtracted from the undepleted signal, yielding the actual depletion peak $\mathcal{D}(t)$ (right). Finally, the depleted peak can be compared to the ion peak $\mathcal{I}(t)$ in the upper right inset. Curves are offset for clarity.

Three time-of-flight traces are recorded as a means to account for this enhancement of the signal: One with the ionization laser triggered only after surface collision has taken place to recover the original electron signal $\mathcal{D}_e(t)$, and one, $\mathcal{S}(t)$, with the laser shifted in time by 22 µs relative to the optimum timing, to determine the effect of stray light without depleting the central part of the beam. One additional background trace with the laser shifted and the nozzle mistimed also has to be recorded. After background subtraction, the scaling factor β between the signals is determined such that $\mathcal{S}(t) = \beta \times \mathcal{D}_e(t)$. The depletion difference signal is then calculated as $\mathcal{D}(t) = \beta \times \mathcal{D}_e(t) - \mathcal{D}_d(t)$, and the corrected electron emission yield is given by:

$$\tilde{\gamma_0} = 1/\beta \times \bar{\mathcal{D}}/\bar{\mathcal{I}} \times \exp(t_{\text{arrival}}/\tau) \; . \tag{6.14}$$

Typical values of β are on the order of 1.1. In total, five different experimental configurations have to be probed to properly account for all potential artifacts, which are summed up in the overview of Fig. 6.5. In order to eliminate any drifts in signal, it is advisable to toggle between these five configurations in a random order. This is accomplished by triggering both nozzle and REMPI laser via one of the burst units and toggling between different sequences of a burst file as described in detail in section 5.4.

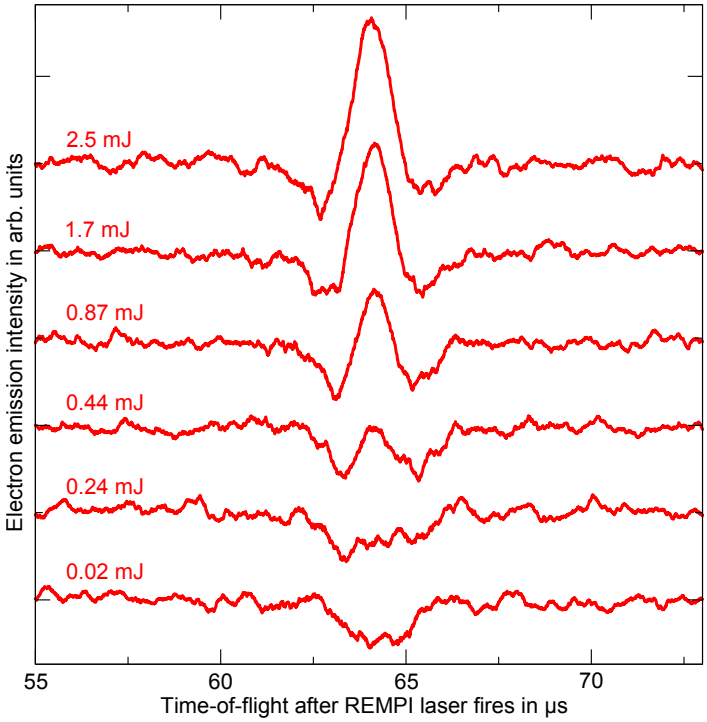

Figure 6.6: Depletion difference time-of-flight traces, $\mathcal{D}(t)$, for different laser pulse energies. Below 0.24 mJ, laser power is not sufficient for ionization, and instead an increase of the electron emission signal (corresponding to a dip in $\mathcal{D}(t)$) is seen which is saturated already at 0.02 mJ. For higher pulse energies, the depletion peak emerges and saturates at 1.7 mJ, but dips are persistently observed on either side of the peak for all energies.

A striking aspect of the depleted peak in Fig. 6.5 are the two negative wings on both sides of the main peak, which correspond to an increase in signal rather than depletion. As opposed to the enhancement of the overall signal mentioned before, this increase is located close in time to the dip due to depleted molecules, which makes it very likely that the wings are caused by the direct laser beam. The time-of-flight trace $\mathcal{D}(t)$ alone does not contain any information about the magnitude of contribution of

signal increase and signal depletion. This makes the factor $\bar{\mathcal{D}}$ in Eq. (6.14) ill-defined: neither is it obvious over what time region $\mathcal{D}(t)$ should be integrated, nor what significance the different areas enclosed between the time-axis and the curve of $\mathcal{D}(t)$ bear. For an accurate determination of γ_0, it is therefore indispensable to conduct a thorough analysis of the two counteracting effects. In a first step, the dependence of laser pulse energy on $\mathcal{D}(t)$ is investigated. The results depicted in Fig. 6.6 clearly support the assumption that the increase in signal is due to laser excitation of CO* to the $b^3\Sigma^+$ state: Since the transition is strong, a dip in $\mathcal{D}(t)$, corresponding to an increase in electron emission signal, is observed to saturate already at very low laser pulse energies of 0.02 mJ. As laser power is increased, resonant ionization of CO* starts to occur above 0.44 mJ and saturates at about 1.7 mJ. For all energies where ionization occurs, the enhancement dip is also clearly observed on either side of the depleted peak. Moreover, the dips are not constant in their arrival time, but rather shift in time as the spatial width of the depletion peak increases. This behavior is strong evidence that molecules in the low intensity wings of the REMPI laser profile are pumped to the $b^3\Sigma^+$ state without being ionized. It supports the aforementioned hypothesis that pumping molecules to this state causes an increase in electron emission.

In an effort to disentangle the contributions of depletion and enhancement, a simple model of the interaction between ionization laser and molecular beam has been developed. It is based on trajectory simulations of molecules in the decelerator using `libcoldmol` [79] (see section 4.2), which for realistic input parameters of the molecular beam yield full six-dimensional final coordinates $(\mathbf{r}(t), \mathbf{v}(t))$ of molecules that reproduce the experimental time-of-flight trace. As can be seen from Fig. 6.7, good agreement between simulation, depicted in light red, and experiment, shown in black, is achieved. Having modeled the distribution of molecules at the exact time that the REMPI laser fires, it is straightforward to implement the experimental findings into a simple model of laser interaction with the molecular beam. This model is schematically illustrated in Fig. 6.8. Knowing that the signal is more or less saturated at the pulse energies used, it is assumed that (1+1) REMPI ionization is saturated within one full width at half maximum (FWHM) of the laser intensity profile $I(r)$, which is taken as Gaussian for the sake of simplicity. For $r > f/2$, where r denotes the distance to the center of the laser focus, and f is the FWHM, ionization is assumed to be proportional to $I(r)$. The reasoning behind this is that the first resonant step of the (1+1) REMPI process is easily saturated, such that the unsaturated ionization signal will depend linearly on the laser intensity. Enhancement happens around the zone of depletion; it is modeled such that it takes place only in a ring of inner radius $f/2$ and an outer radius of $1.75f$, i.e. a zone of width $1.25f$ on either side of the the depletion at high intensity. Only molecules which are not effected by depletion are considered to be enhanced by a constant factor, ε_m. For a molecule in the enhancement region, at a distance r_0 from the laser focus, the signal upon surface collision is computed as $(1 - I(r_0)/I(f/2)) \times \varepsilon_\mathrm{m}$.

The model contains only two free parameters: The FWHM, f, of the REMPI laser at the intersection with the molecular beam, and the strength of the enhancement, ε_m. A thorough search of this two parameter space yields a best agreement with the

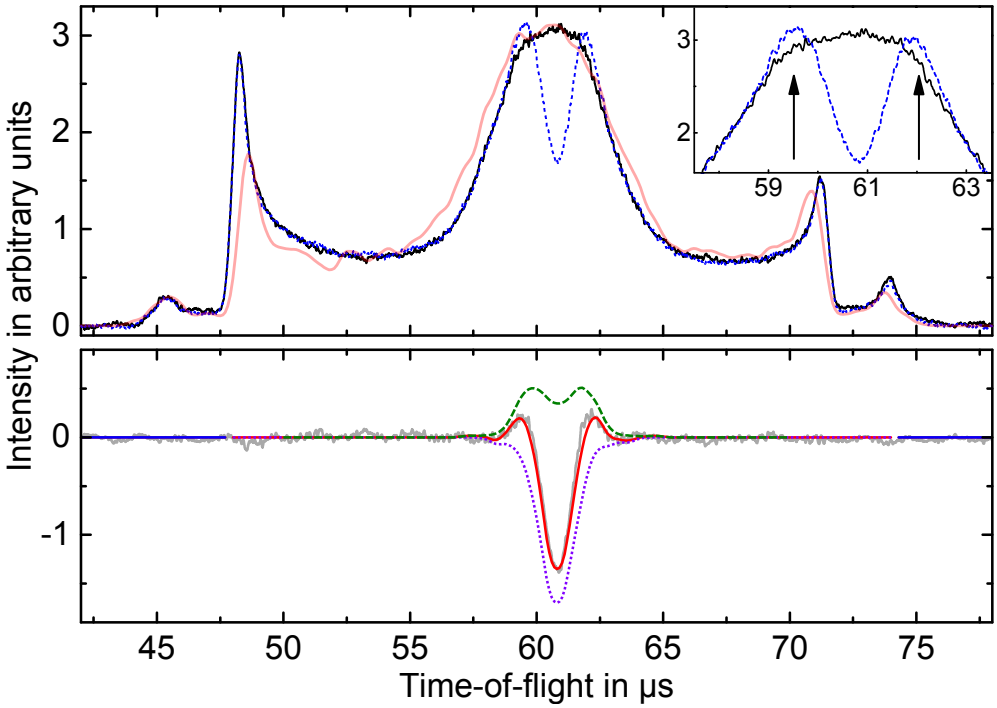

Figure 6.7: Comparison of experimental depleted and undepleted electron emission signal with simulations. The upper panel shows the experimental undepleted time-of-flight trace $\mathcal{D}_e(t)$ (solid black curve) together with a simulation (solid light red curve), and the depleted signal $\mathcal{D}_d(t)$ (dotted blue curve). In the inset on the upper right, the regions of signal enhancement next to the depletion dip are indicated by arrows. In the lower panel, simulation (solid red curve) of the difference depletion signal $\mathcal{D}(t)$ based on a simple model (see text for details) is compared to experimental data (solid gray curve). In addition, contributions of enhancement (dashed green curve) and depletion (dotted purple curve) according to simulations are shown. Figure adapted from reference [168].

experimental data when $f = 410\,\mu\text{m}$ and $\varepsilon_\text{m} = 1.31$. The comparison between experimental data and the model is shown in Fig. 6.7. Two important aspects should be noted about the determination of parameters. First of all, the shape of $\mathcal{D}(t)$ is very sensitive to values of both f and ε_m, such that it is safe to assume that the values given above correspond to a global optimum. It is hence deemed unnecessary to perform a full fit of the model to the data. Second, the choice of the width of the enhancement ring being equal to f is somewhat arbitrary. Indeed, one can find other combinations of ring width and saturation area which also yield satisfying agreement with experimental data, indicating a strong correlation between these two parameters. The

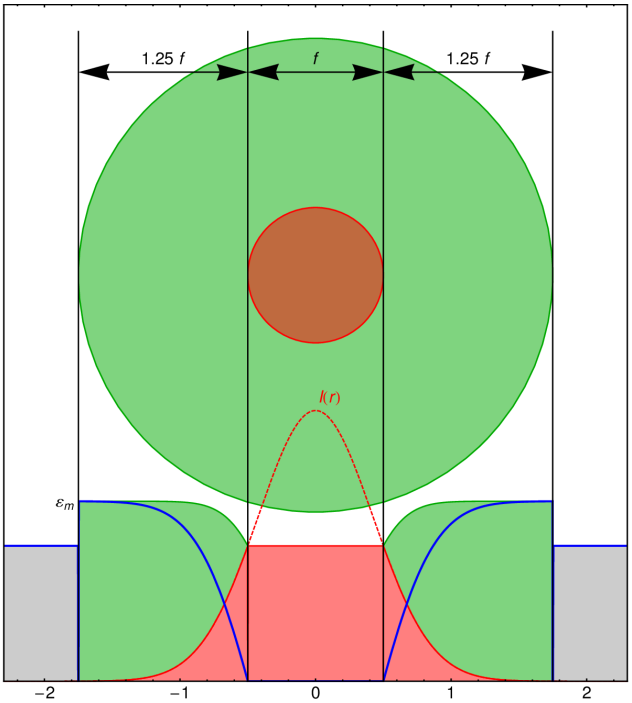

Figure 6.8: Model of depletion (red area) and enhancement (green area) of signal due to the excitation laser. Within one FWHM, f, of the Intensity profile, $I(r)$, ionization is assumed to be saturated. For distances $r \geq f/2$ from the laser focus, depletion decreases $\propto I(r)$, since the first step of the two-photon process is easily saturated. Of the molecules remaining after depletion, those inside a ring of inner radius $f/2$ and outer radius $1.75f$ are enhanced by the factor ε_m. When binning the molecules to the time-of-flight trace, depleted molecules are weighted by zero, whereas enhanced molecules are weighted by the factor ε_m. In the illustration, the computed weighting factor, depicted as the thick blue curve, corresponds to the height of the green shaded area. The horizontal axis of the plot is in units of f.

value of ε_m, however, hardly changes over a reasonable range of ring width to saturation diameter ratios. Also, the peak shape remains very sensitive to ε_m regardless of which combination of ring width and saturation diameter is chosen. Best agreement between the model and the experiment is achieved when the ring width is 25 % larger than the saturation diameter.

In order to understand the peak shapes depicted in Figs. 6.5 and 6.7, it is instructive to study the dynamics of the molecular beam pulse on its way from the decelerator exit to the surface. The left part of Fig. 6.9 shows a snapshot of the (v_z, z) phase space of molecules as they leave the decelerator. The zoomed in view at the top, which ex-

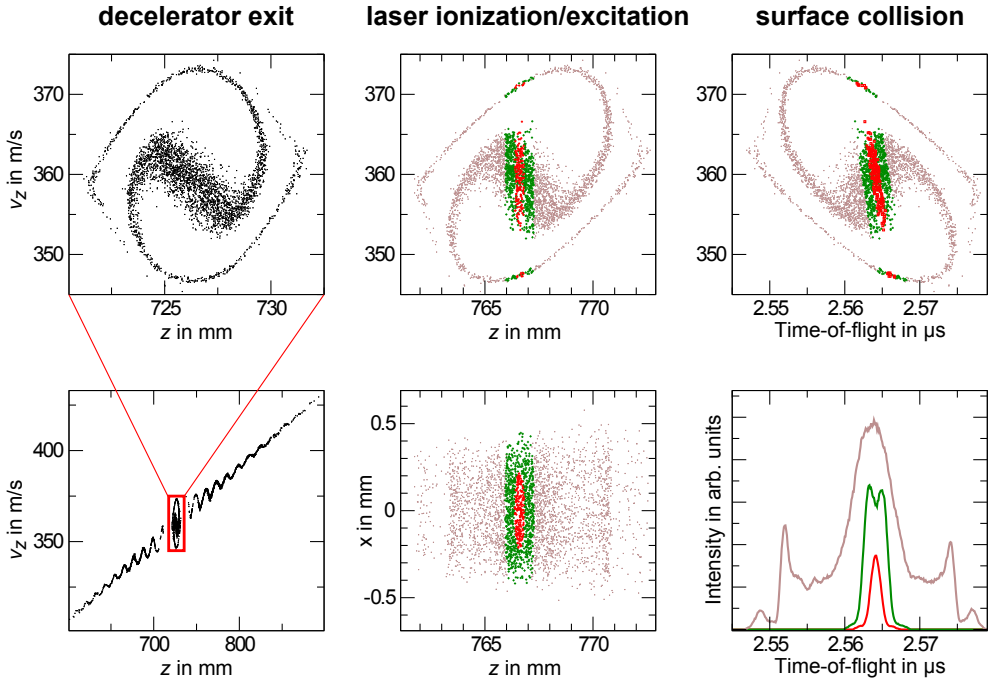

Figure 6.9: Time evolution of the molecular packet after leaving the decelerator. In the (v_z, z) phase space depicted on the left, the part of the distribution responsible for the main peak is almost horizontal, meaning velocity spread is small and spatial spread is big. However, molecules lagging behind have a higher velocity than molecules up front. At the time of laser excitation (middle), the spatial profile of the laser maps onto narrow stripes of depletion (red) and enhancement (green) in the (v_z, z) distribution. By the time the molecules hit the surface (right), faster molecules from the trailing part of the main peak have caught up with slower molecules from the leading part, causing the contributions of enhancement and depletion to overlap. Time-of-flight profiles on the lower right shown in red and green depict the distributions of molecules within a disk of radius $f/2$, and a ring of inner diameter $f/2$ and outer diameter $1.75f$, respectively. Neither scaling of the enhancement nor contributions to depletion outside the saturated region, as described in Fig. 6.8, are included. Note that on the left and in the middle, the situation is depicted for constant time, whereas z is held constant at the surface position on the right side.

hibits a distinct spiral structure, corresponds to molecules in the guided peak. This distribution of molecules can be understood from Fig. 4.6b, which shows that the frequency of rotation of the packet of molecules around the center of the stable phase

space is nearly constant in a large region near the center, but goes to zero towards the outside. Longitudinal motion within the guided packet inside the decelerator corresponds to a rotation in longitudinal phase space. A distribution of molecules which is coupled into the decelerator as a diagonal block in the (v_z, z) phase space will therefore start to rotate uniformly near the center. Molecules which are located in the large block near the center have completed about $1^1/_4$ revolutions by the time they leave the decelerator. Towards the outside, molecules rotate slower the further away they are from the center, such that they lag behind and form the distinct spiral arms seen in the upper left part of Fig. 6.9. After leaving the decelerator, molecules progress in free flight. In (v_z, z) space, this corresponds to a shear of the distribution, where faster molecules lagging behind (upper left quadrant of the diagram) catch up with molecules which are leading the pulse but are slower (lower right quadrant part of the diagram). As a consequence, the diagonal part in the center of the distribution shown in the upper left panel of Fig. 6.9 gives rise to the sharp main peak observed in the time-of-flight traces shown in the lower right. By the time the ionization laser intersects with the molecular beam, depicted in the middle section of the figure, the inner disk and the surrounding ring used in the modeling of the spatial profile of the laser in (z, x) space map onto diagonal stripes in (v_z, z) space. Because fast molecules are still lagging behind and slower ones lead the pulse, contributions of the molecules in the inner disk and the surrounding ring start to overlap, and occur at similar arrival times in the final time-of-flight trace as shown in the right part of Fig. 6.9. Note that the phase space plot on the upper right depicts *time* versus velocity for a fixed z position, while the diagrams on the left and in the upper center show the *position* along the beam axis, z, versus v_z for a fixed time. The time-of-flight traces in the lower left of Fig. 6.9, in contrast to Fig. 6.7, only show the contributions of molecules originating from the inner disk where depletion occurs and from the outer ring where enhancement takes place, respectively. Depletion within the outer ring is not accounted for.

Having disentangled which fraction of the difference depletion time-of-flight trace, $\mathcal{D}(t)$, is ascribed to depletion, it is straightforward to obtain its time-integrated value, $\bar{\mathcal{D}}$. Before computing the final value of γ_0, however, one has to take into account a scaling factor which arises from the particle detectors. In principle, the most direct way of obtaining a value for γ_0 is to operate the MCP's at high gain and reduce the signal until single events — i.e. single CO^+ ions and single electrons emitted from the surface — can be measured. This approach, however, is inconvenient for two reasons: First of all, stray light from the ionization laser overlaps the ion signal when MCP's are operated at high gain, which makes the evaluation of single events time-consuming. More important, one has to realize that the REMPI ionization produces CO^+ ions which arrive at the MCP detector within 100 ns. To avoid overlap of single event peaks, one has to operate in a regime where on average, only one ion is being counted per shot. The depletion difference signal, on the contrary, arrives spread out over almost 5 µs. For a value of γ_0 in the range of $10^{-1} - 10^{-3}$, the signal per molecule at the electron MCP is then one to three orders of magnitude lower. This means that averaging for $1 - 100$ seconds is necessary to detect one missing electron.

Since the ionization laser can deplete about 10 % of the CO* signal, it follows that per 1–100 s, a difference of 1 electron in 10 is expected, spread out over the 1000 bins of a 5 µs time gate. For reasonable statistics and comparison to simulated peak shapes, it is advisable to have a minimum signal of about 1 missing electron per bin, meaning that one measurement, involving time-of-flight traces with laser on and off, takes on the order of 30 minutes to 2 days. Instead, analogue signals are recorded with different gain of the MCP detectors, and the results are corrected by a measured calibration factor.

Absolute values for γ_0 were determined first in Berlin and, after moving the entire setup, in the new laboratory in Göttingen. Several small changes were incorporated prior to the Göttingen measurements. Most notably, the detection zone was modified such that instead of small rings, large charged plates are supporting the meshes in front of the MCP's, which makes the extraction fields more homogeneous and reduces the stray light on the MCP's. Due to the reduced stray light level, data can be acquired in a simpler way than described above. Only the signal with REMPI laser on and off is recorded repeatedly. The correction factor β is computed by scaling the outer parts of the two time-of-flight trace to each other which are not subject to depletion.

The values for the enhancement factor, ε_m, the REMPI laser FWHM, f, and the absolute electron emission yield, γ_0, that follow from the procedure explained above, are averaged, yielding values of $f = (410 \pm 50)$ µm and $\varepsilon_\mathrm{m} = 1.31 \pm 0.07$. For the electron emission yield of CO in the $a^3\Pi_1(v = 0, J = 1)$ state, the final result is

$$\gamma_0 = 0.13 \pm 0.05 \tag{6.15}$$

The measurements have been performed under slightly different conditions which are due to the changes that were made to the apparatus, regarding mainly the excitation laser system and the detection zone, as well as the re-alignment of the machine. The error bars given above already include the systematic uncertainty associated with these changes.

In order to elucidate the physical meaning of the model parameter ε_m, one has to consider that even when the one-photon $b^3\Sigma^+(v = 0) \leftarrow a^3\Pi_1(v = 0)$ transition is saturated, molecules are only excited to a point where the populations in the excited and the lower levels are equal. When only one transition is involved, 50 % of all molecules will be excited. Since in the present case, two upper levels are so close in energy that transitions to both of them are excited by the laser at the same time (see Fig. 6.12 in the following section), 2/3 of the molecules are excited to the upper level. The parameter ε_m, in contrast, is used to scale the signal of all the molecules in the laser intensity wings, not just a fraction. It is straightforward to calculate the enhancement, ε, of laser excited molecules only: since one third of the molecules that remain in the lower level have no contribution to enhancement, the relation $1/3 + 2/3 \times \varepsilon = \varepsilon_m$ holds, and the enhancement of laser-excited molecules is given by:

$$\varepsilon = \frac{3}{2}\left(\varepsilon_m - \frac{1}{3}\right) . \tag{6.16}$$

This yields a final value for the enhancement factor of

$$\varepsilon = 1.47 \pm 0.12 \,. \tag{6.17}$$

Moreover, some of the laser-excited molecules will relax not to vibrationally excited levels, but to the vibrational ground level of the $a^3\Pi$ state. To obtain the electron emission yield for the vibrationally excited states, one has to calculate the vibrational distribution after all molecules have relaxed to the $a^3\Pi$ state from the Franck-Condon factors (FCF) of the $b^3\Sigma^+ \rightarrow a^3\Pi$ transition. For this, the transition probability between upper and lower state is assumed to be proportional to $q(0, v'') \times \nu^3$, where ν is the transition frequency and $q(v', v'')$ denotes the FCF between upper vibrational level v' and lower vibrational level v''. This is an approximation, since it implies that the electronic transition dipole moment is assumed to be independent of the internuclear distance. Using FCF calculated by the program LEVEL [64] which match well with

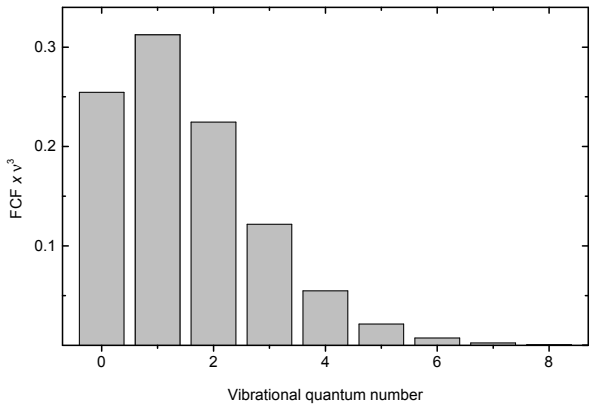

Figure 6.10: Vibrational distribution of molecules which are excited to the $b^3\Sigma^+(v = 0)$ state and subsequently relax to the $a^3\Pi$ state. See text for details.

experimental values [63], and transition frequencies calculated from molecular constants from reference [61], the vibrational distribution shown in Fig. 6.10 is obtained. Of those molecules excited but not ionized, 74.6 % end up in vibrationally excited states of $a^3\Pi$. The electron emission yield, γ_v, and relative population, p_v, of a vibrational level with quantum number v are related to the enhancement by $\sum p_v \gamma_v = \varepsilon\gamma_0$. This yields a final value of

$$\gamma_{v\geq 1} = (1.61 \pm 0.17) \times \gamma_0 \tag{6.18}$$

for the averaged electron emission yield of vibrationally excited CO ($a^3\Pi$).

Note that molecules excited to the $b^3\Sigma^+$ state will decay completely to the $a^3\Pi$ state. Transitions to the lower-lying singlet states are spin-forbidden, decay to the $e^3\Sigma^-$ state is parity-forbidden, and a transition to the $d^3\Delta$ state cannot take place due to angular

momentum selection rules. There appears to be no obvious selection rule which rules out a $b^3\Sigma^+ \rightarrow a'^3\Sigma^+$ decay. Such a transition, however, would require two electrons to change orbitals at once, since the outer electron configuration in an LCAO model is $(2p\pi)^3(2s\sigma)^2(2p\pi^*)^1$ for the $a'^3\Sigma^+$ state, but $(2p\pi)^4(2s\sigma)^1(3s\sigma)^1$ for the $b^3\Sigma^+$ state. For these reasons, all excited molecules relax to the $a^3\Pi$ state, but not necessarily into the $\Omega = 1$ manifold. Moreover, the relaxation takes place to different rotational levels (see Fig. 6.12). Since the energy difference between the different Ω manifolds is only about $40\,\mathrm{cm}^{-1}$ large, and thus small compared to the vibrational spacing of more than $1000\,\mathrm{cm}^{-1}$, this effect may be safely neglected. Since the rotational level energy difference is even smaller, the electron emission yield is assumed to depend only on the vibrational quantum number, v.

It is not only the magnitude of γ_0, but also the observation of signal enhancement for vibrationally excited CO* molecules which is unexpected. In order to find the origin of this vibrational dependence, a series of experiments was conducted which are described in detail in the next section.

6.2.2 The Role of Vibration in Quenching of Metastable Molecules at Metal Surfaces

The enhancement of electron emission yield, γ_v, for vibrationally excited molecules is an aspect of metastable quenching processes which has been hardly explored in experiments nor mentioned in the literature. Therefore, several experiments were carried out to shed light on the underlying mechanisms. Despite the fact that in the measurement of γ_0 presented in the previous section, strong evidence was found that vibrational excitation is causing the enhancement, further results are needed in order to confirm this hypothesis.

Vibrational dependence

To rule out stray light as a likely cause of errors, it is straightforward to monitor the electron depletion signal $\mathcal{D}_d(t)$ as a function of laser frequency as the REMPI laser is scanned over the ionizing resonance. While the influence of stray light on the overall enhancement was investigated before (see section 6.2.1), it lacked a systematic analysis of the central region where the direct laser beam overlaps the molecular beam. Prior to the frequency scan, the pulse energy of the REMPI laser is adjusted until only a small CO^+ signal is observed, such that only few molecules are ionized. In addition, the laser beam is widened to about 4 mm diameter using a telescope, such that a larger number of the molecules is directly exposed to the low intensity laser light. Results of the scan are shown in Fig. 6.11. The electron emission signal, time-integrated over a small region around the main peak, exhibits a significant increase whenever the frequency becomes resonant with the molecular transitions. For comparison, the (1+1) REMPI ionization signal is shown to identify the transition frequencies. A total of three transitions are observed within the scanning range of the laser: The $\Delta J_{F_f F_i}(J_i) = R_{32}(1)$ transition, and the $P_{32}(1)$ and $R_{12}(1)$ transitions which

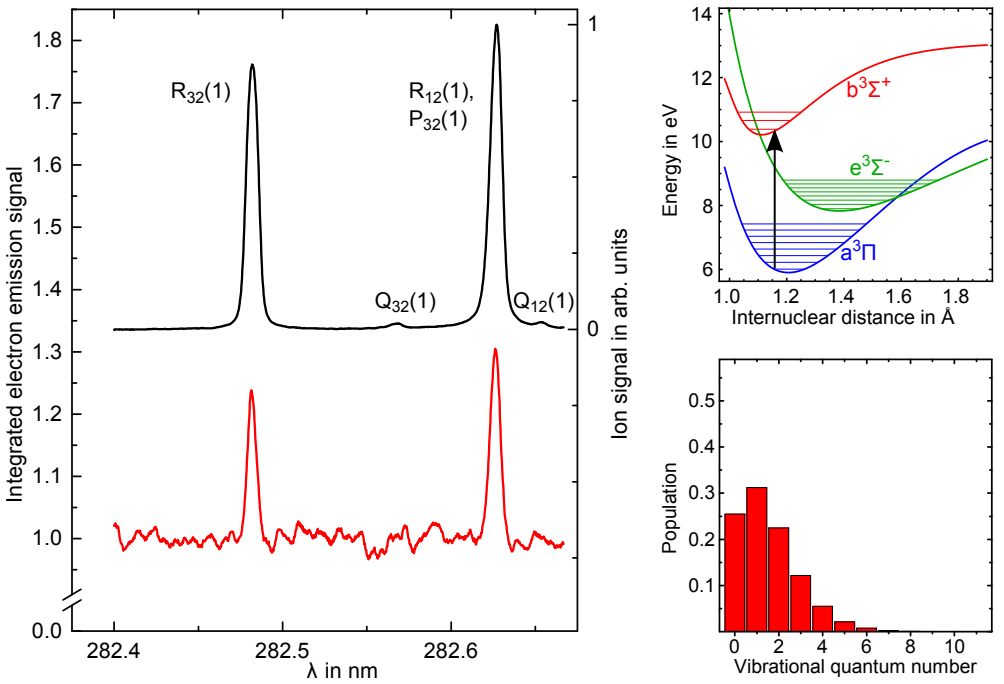

Figure 6.11: Enhancement of electron emission signal for Franck-Condon pumping via the $b^3\Sigma^+(v = 0)$ state. After relaxation to $a^3\Pi$, the vibrational distribution shown on the lower right side is obtained. The electron emission signal (solid red line) is enhanced whenever the excitation laser is on resonance with the $R_{32}(1)$ or the two overlapping $P_{32}(1)$ and $R_{12}(1)$ transitions, as is evident from the frequency scan on the left. The signal intensity is normalized to the averaged electron emission with the excitation laser off resonance, and its peak scaled to $\varepsilon_m = 1.31$ according to the value determined in section 6.2.1. The electron emission signal still contains the contributions of molecules not excited by the laser, such that the correct maximum signal of $\varepsilon = 1.47$ is obtained once the signal is corrected for the fraction of laser-excited molecules due to the contributions of two transitions. The ionization signal resulting from two-photon absorption is shown for comparison (solid black line). Figure adapted from reference [169].

overlap within the laser's linewidth. The ratio of both peaks can be explained in the following way: Assuming saturation, exciting one rotational transition will lead to a 50 : 50 distribution in the upper and lower levels. Driving two rotational transitions at once, in contrast, will drive one third of the molecules to each upper level, leaving only 1/3 of the molecules in the lower state. As a result, line intensities are expected

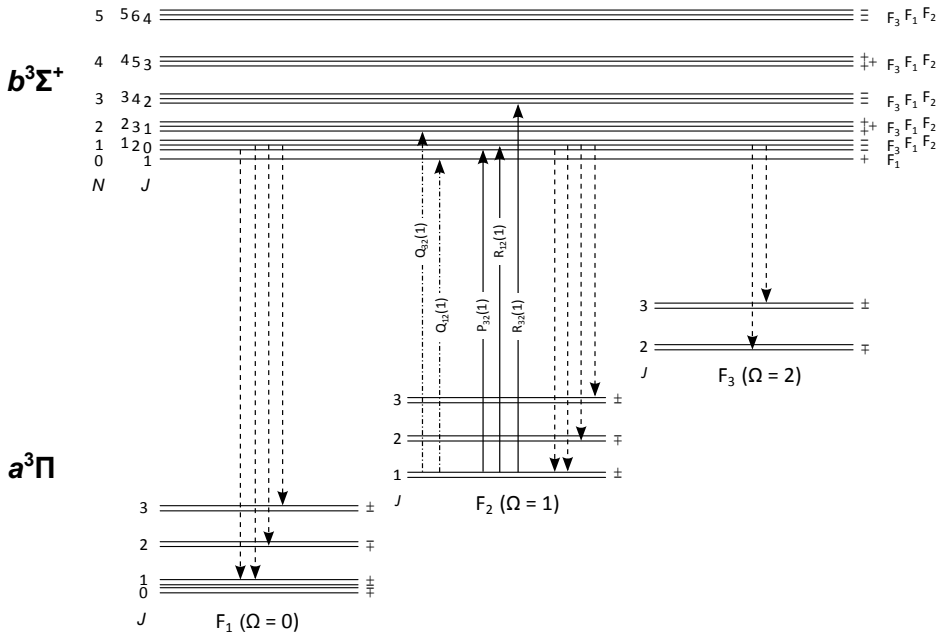

Figure 6.12: Excitation of the $b^3\Sigma^+(v = 0) \leftarrow a^3\Pi(v = 0)$ transition. Solid arrows indicate allowed transitions starting from the $a^3\Pi(v = 0, J = 1, +)$ state, dash-dotted lines the forbidden transitions which can be seen in the presence of a weak electric field. Relaxation accompanied by fluorescence to different Ω manifolds is depicted by dashed arrows. Note that there are no qualitative changes when higher vibrational levels are considered of either lower or higher state. Figure adapted from reference [202].

to have a ratio of $^2/_3 : {}^1/_2 \mathrel{\widehat{=}} 4 : 3$, which agrees well with experiment. Also note that two more lines with low intensity are observed at roughly 282.57 nm and 282.66 nm. These are the $Q_{12}(1)$ and $Q_{32}(1)$ transitions to the $N = 0$ and $N = 2$ state, which are parity-forbidden in the absence of external electric fields. In the extraction region, however, an electric field of approximately 140 V/cm weakly mixes levels of different parity in the $a^3\Pi_1$ manifold, such that these transitions become possible. It has been observed before that an electric field strength as low as 400 V/cm is sufficient to observe equal intensities for otherwise forbidden transitions [58]. For an overview of allowed ro-vibrational transitions between the $a^3\Pi$ and the $b^3\Sigma^+$ state and subsequent relaxation, see Fig. 6.12. Note that the time-integrated electron signal plotted in Fig. 6.11 is scaled such that the maximum enhancement, when it is corrected for the

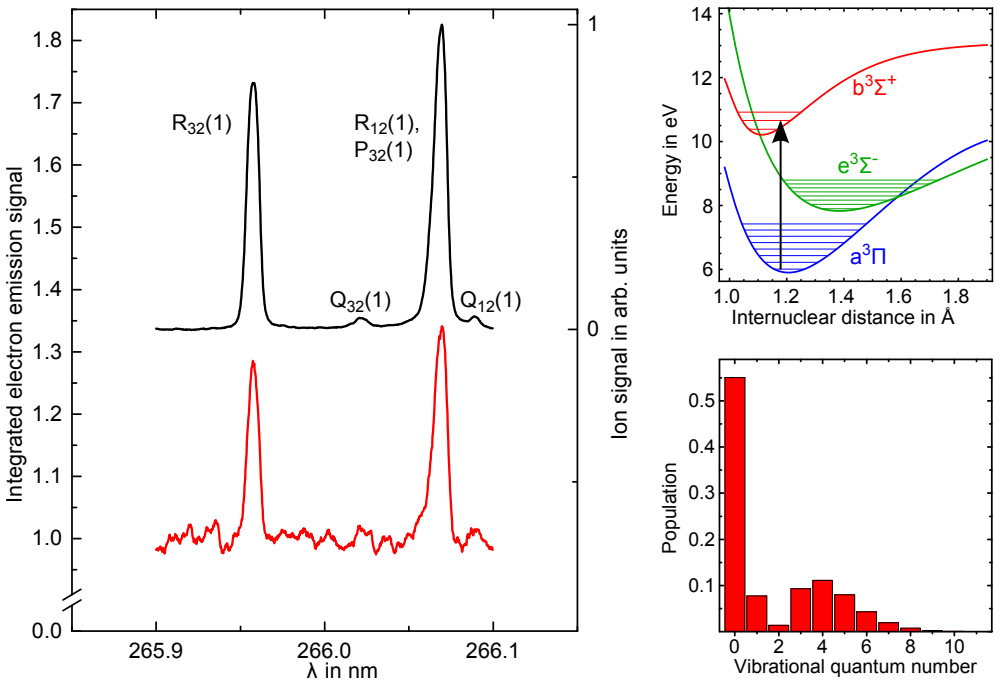

Figure 6.13: Enhancement of electron emission signal for Franck-Condon pumping via the $b^3\Sigma^+(v=1)$ state. The lower right side shows the final vibrational distribution after relaxation to $a^3\Pi$. See Fig. 6.11 and text for details. The electron emission signal is scaled by the same factor as in the case of pumping via the $b^3\Sigma^+(v=0)$ state. Figure adapted from reference [169].

fact that two upper rotational levels contribute using Eq. (6.16), will match the value of ε determined previously (see Eq. (6.17). The electron signal shown in the following Figs. 6.13 and 6.14 is scaled accordingly.

While this experiment proves that the stronger electron emission signal is indeed due to vibrationally excited states, it does not give any indication of which vibrational states actually contribute how much to the signal. A straightforward way to determine the electron emission yield for different vibrational levels, or at least average yields for groups of vibrational levels, is to create different vibrational distributions via Franck-Condon pumping (FCP). In this preparation method, molecules are laser-excited to one vibrational level of a higher-lying electronic state, and relax back to the original state with a vibrational distribution that is determined by the FCF between the two states. In Fig. 6.13 and Fig. 6.14, results are shown for FCP via the $b^3\Sigma^+(v=1)$ state and the lower-lying $e^3\Sigma^-(v=7)$ state, respectively. Note that the intensity ratio between the two observed lines is again roughly 4 : 3 when pumping via the $b^3\Sigma^+(v=1)$ state. This is because qualitatively, the level diagram shown in

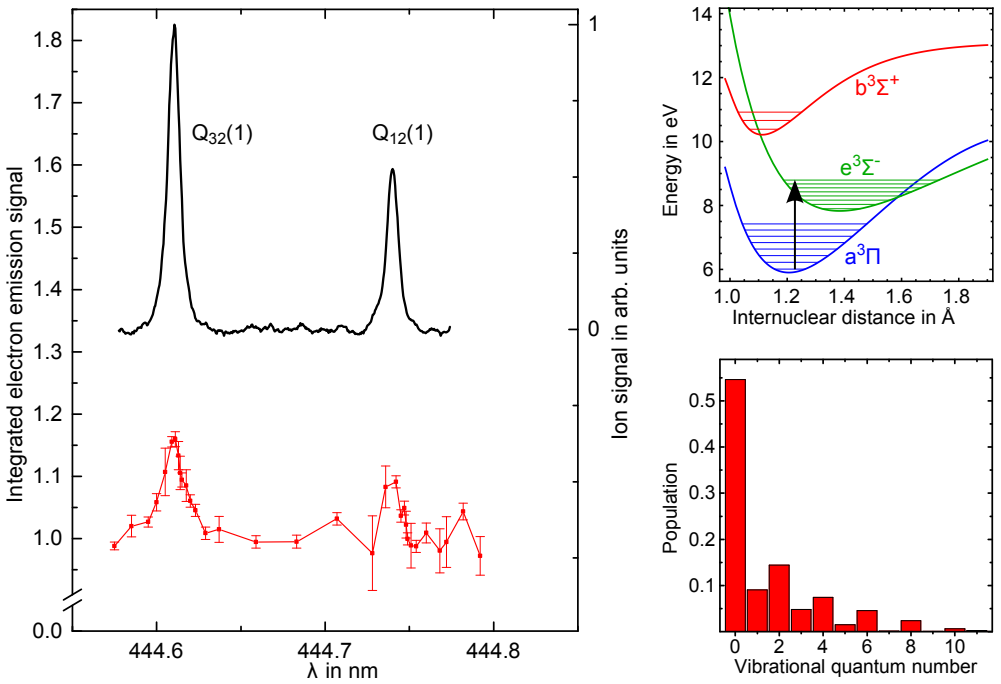

Figure 6.14: Enhancement of electron emission signal for Franck-Condon pumping via the $e^3\Sigma^-(v = 7)$ state. See Fig. 6.11, Fig. 6.13, and text for details. The reference signal (solid black line) is obtained by ionizing molecules in $a^3\Pi_1(v = 1)$ with a second laser tuned to resonance with the $b^3\Sigma^+(v = 0)$ state in a (1+1) REMPI process. The electron emission signal is obtained by toggling between two configurations with excitation laser switched on and excitation laser switched off at different fixed wavelengths. Figure adapted from reference [169].

Fig. 6.12 is still valid for higher vibrational levels. As a consequence, the higher peak in Fig. 6.13 contains two transitions and the smaller one only one. Unexpectedly, the two lines observed when pumping via the $e^3\Sigma^-(v = 7)$ state differ in intensity almost by a factor of 2, despite the fact that both represent only a single transition. Note that Fig. 6.12 still qualitatively holds true if the upper state is a Σ^- state if the parity of the upper levels is reversed (see also Fig. 2 of reference [203]).

In the case of pumping via the $b^3\Sigma^+(v = 1)$ state, it is possible to employ the same laser system as for pumping via the $b^3\Sigma^+(v = 0)$ state. Experimental conditions like pulse energy and beam size are comparable among these two measurements such that it is possible to compare them quantitatively. Data for pumping via the $e^3\Sigma^-(v = 7)$ state, however, is obtained using a different laser system, such that results should be compared cautiously. Because enhancement is barely observed in this case, a different

procedure is employed to measure the data shown in Fig. 6.14. For a range of fixed frequencies of the excitation laser, the setup is toggled between two configurations in which the excitation laser is either on or off. In the difference signal, enhancement is then clearly observed for sufficiently long averaging. In addition, monitoring of the ion signal is no longer possible because the photon energy at a wavelength of 445 nm is not sufficient for (1+1) REMPI, and laser pulse energies are too low for efficient (1+2) REMPI. Instead, the pumping efficiency and absolute frequency of the excitation laser is determined by shining in a second laser between excitation laser and surface. It is tuned to resonance with the $b^3\Sigma^+(v=0) \leftarrow a^3\Pi_1(v=1)$ transition at 297 nm, such that molecules produced in the $a^3\Pi_1(v=1)$ state by FCP are efficiently detected by (1+1) REMPI. The enhancement factor, ε, is obtained from these measurements by correcting for the fraction of laser excited molecules according to whether one or two transitions are involved (see Eq. (6.16)). This yields final values of:

$$\varepsilon(b^3\Sigma^+(v=1)) = 1.51\,, \quad \varepsilon(e^3\Sigma^-(v=7)) = 1.32\,. \tag{6.19}$$

The corresponding value for pumping via the $b^3\Sigma^+(v=0)$ state, as reported in Eq. (6.17), is 1.47 .

These values are surprising considering the corresponding vibrational populations created by FCP, which are depicted in the lower right of Figs. 6.11, 6.13, and 6.14 for each pumping scheme. The distribution arising from FCP via the $b^3\Sigma^+(v=1)$ state has more than twice as many molecules in the vibrational ground state than that arising from the $b^3\Sigma^+(v=0)$ pumping. Nonetheless, the total enhancement is weaker in the latter case. Since pumping via the $b^3\Sigma^+(v=0)$ state produces a large population in $v = 1, 2, 3$, whereas $b^3\Sigma^+(v=1)$ pumping populates the levels $v = 4, 5, 6$ more strongly, one can conclude that lower vibrational states exhibit far less enhancement than those which are more highly excited. To quantify this observation, one can solve the two coupled equations

$$\sum_v p_v(b^3\Sigma^+(v=0)) \times \gamma_v = \varepsilon(b^3\Sigma^+(v=0)) \times \gamma_0 \tag{6.20}$$

$$\sum_v p_v(b^3\Sigma^+(v=1)) \times \gamma_v = \varepsilon(b^3\Sigma^+(v=1)) \times \gamma_0 \tag{6.21}$$

for the vibrational level dependent electron emission yields γ_v. Here, p_v denotes the population in the vibrational level, v, resulting from the respective pumping scheme. For reasons discussed above, the $e^3\Sigma^-$ state measurements are for now not included in the quantitative evaluation of enhancement. Since there are obviously more variables γ_v than equations, it is necessary to average over groups of individual vibrational levels. A straightforward partition is into the groups of levels $v = 0$, $v = 1, 2, 3$, and $v \geq 4$, since this is where the population distributions resulting from $b^3\Sigma^+(v=0)$ and $b^3\Sigma^+(v=1)$ pumping differ most. Measurement uncertainties can be estimated from the known uncertainty of the electron emission yield averaged over all excited vibrational levels, $\gamma_{v\geq 1}$, determined in the previous section (see Eq. (6.17)). Since the measurement uncertainty of the single ε values obtained from statistical variation of

the scans is much smaller, it can be neglected. This yields a final result of

$$\bar{\gamma}_{v=1,2,3} = \gamma_0 \times (1.49 \pm 0.14) \tag{6.22}$$

$$\bar{\gamma}_{v\geq 4} = \gamma_0 \times (2.62 \pm 0.39) \tag{6.23}$$

for the electron emission yield averaged over groups of vibrational levels.

When a vibrational population distribution is created by FCP via the $e^3\Sigma^-(v = 7)$ state, the observed increase of electron emission compared to γ_0 is smaller than when the $b^3\Sigma^+(v = 0, 1)$ levels are used for FCP. From the averaged γ_v values above, a much higher enhancement by a factor of 1.42 is to be expected. In the case that these $e^3\Sigma^-(v = 7)$ state measurements are included into the calculation of γ_v for different groups of levels, the values $\bar{\gamma}_{v=1,2,3} = 1.44\gamma_0$, $\bar{\gamma}_{v=4,5} = 3.31\gamma_0$, and $\bar{\gamma}_{v\geq 6} = 0.96\gamma_0$ are obtained. As noted above, this discrepancy between FCP via the $e^3\Sigma^-(v = 7)$ state compared to the $b^3\Sigma^+(v = 0, 1)$ states may be due to different experimental conditions such as laser beam profile and size. Laser pulse energy, however, was much higher ($\approx$ 8 mJ) for the e state measurements than for the b state ($\approx$ 1.5 mJ), which makes the low enhancement even more remarkable.

A potential source of error which can be excluded is the finite lifetime of the $e^3\Sigma^-(v = 7)$ level. It is expected to be much larger than that of the b state, since other vibrational levels of the same electronic state have been shown to live on the order of 2.5 µs–7 µs (see, e.g., references [204–206]). In a coarse measurement, where the time between FCP laser and the REMPI laser probing $a^3\Pi_1(J = 1, v = 1)$ was varied and the position of the laser beam optimized, the lifetime of $e^3\Sigma^-$ was determined to be (12 ± 3) µs. Since the time-of-flight between excitation by the FCP laser and collision with the surface is about 53 µs, only 1 % of all molecules will hit the surface while still being in the excited state. It is possible that the calculated vibrational state distributions are not accurate enough for the e state pumping. The Franck-Condon factors for the $b^3\Sigma^+ \rightarrow a^3\Pi$ transition are well-known, and the calculations performed with the LEVEL [64] program agree well with experimental values. For the $e^3\Sigma^- \rightarrow a^3\Pi$ transition, however, no experimental data is available for higher vibrational quantum numbers of the $e^3\Sigma^-$ state. Since they play a crucial role in the analysis of the data, large inaccuracies in the FCF would lead to a spurious result.

Temperature effects

When scattering metastable species from atomically clean metal surfaces, the surface temperature, T_S, is usually of no practical relevance to experiment, since its effect on the population of electronic states is minute. Nonetheless, a thorough study on the surface temperature dependence of CO* in its vibrational ground level colliding with atomically clean Au(111) was conducted. Knowing the absolute electron emission yield at 350 K, collecting all data relative to one temperature is sufficient to determine the absolute electron emission yield for all temperatures. The T_S dependence of γ_0 is studied using two different approaches.

A laser tuned to resonance with the $b^3\Sigma^+(v = 0) \leftarrow a^3\Pi_1(v = 0)$ transition at 283 nm is overlapped with the molecular beam 20 mm upstream of the surface, where

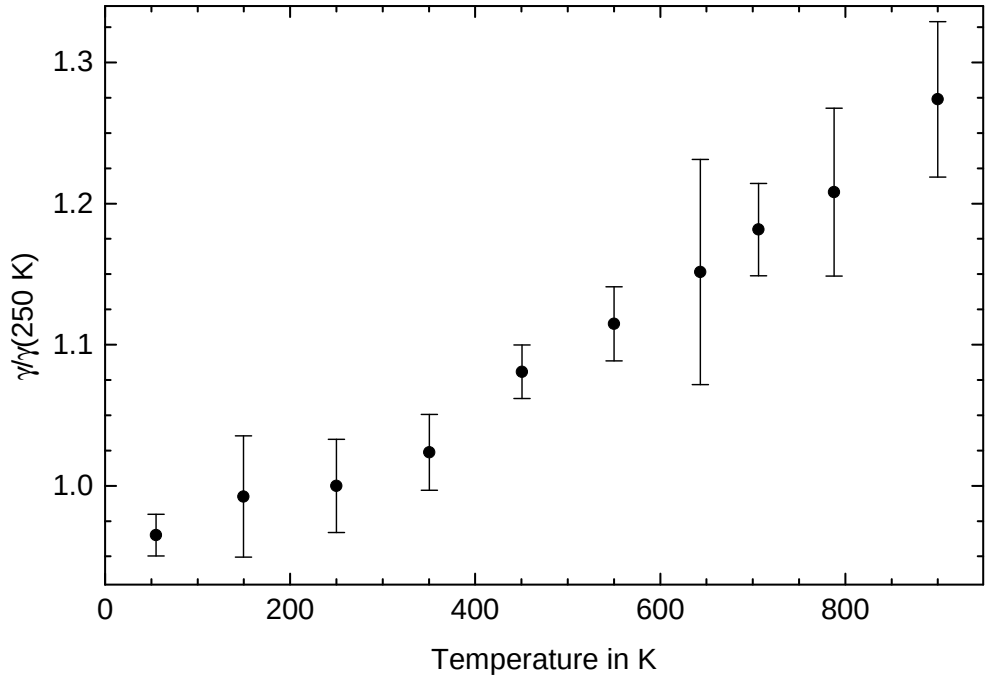

Figure 6.15: Surface temperature dependence of the electron emission yield. All γ_0 values are normalized to $\gamma_0(250\,\mathrm{K})$. The temperature uncertainty (no error bars shown) is $\pm 10\,\mathrm{K}$. Figure adapted from reference [169].

it ionizes a part of the molecules in a (1+1) REMPI process. The surface temperature is increased in discrete steps of about 100 K between 50 K and 900 K. For every temperature, two signals are recorded several times: The REMPI laser detection delay is scanned in time with respect to the molecular beam pulse, such that plotting the integrated ion signal versus detection laser delay yields a time-of-flight profile of the molecular beam. For the electrons emitted upon CO* impact on the surface, the time-of-flight profile is obtained directly. Both time-of-flight profiles are time-integrated and the electron signal is corrected for the decay of CO* on its way to the surface. The relative electron emission yield is then calculated by dividing the corrected, integrated electron signal by the total integrated ion signal. The surface is freshly prepared before each experimental cycle that comprises the full temperature range. Care must be taken not to contaminate the surface during the experiment: Different results are obtained depending on whether the cycle starts at low temperatures and proceeds to high temperatures or vice versa. The reason for that can be understood by repeating both temperature cycles in front of the Auger electron spectrometer, with no incident molecular beam. When going from high to low temperatures, carbon is observed to build up on the surface, most likely originating from the tungsten wires used for resis-

tive heating. When the procedure is performed going from low to high temperatures, no contamination is seen as long as the time when surface temperature is below 350 K is limited to less than 2 hours. In the actual experiments, this time is limited to 45 minutes or less.

After the move to Göttingen, computer controlled scanning of the heating power supply was implemented using `LabVIEW` [207]. This makes it possible to scan the surface temperature while the electron emission signal, time-integrated over a gate around the main peak of the time-of-flight profile, is recorded. Since the signal is sufficiently stable during one temperature scan to not exhibit a significant drift in magnitude, no reference REMPI signal is recorded. These temperature scans are limited to surface temperatures below 800 K to avoid thermionic emission of electrons from the heating filaments. In order to ease averaging with the data points taken in Berlin, these temperature scans are split into chunks and averaged over different temperature ranges, each one centered around one of the temperature values used before. A simple check proves that this procedure is feasible: If only a limited temperature range of ± 10 K is included in the average and all other data points discarded, the same result for γ_0 is obtained with negligible deviations. The resulting temperature uncertainty is therefore estimated to be ± 10 K, which is comparable to the accuracy achieved in Berlin. This uncertainty assumes that the contact between thermocouple junction and gold crystal is good enough to provide an accurate temperature reading. Data collected prior to and after the move shows reasonable agreement within the experimental uncertainty. The data points resulting from this temperature variation are shown in Fig. 6.15.

In contrast to predictions, γ_0 is not constant over the measured temperature range. Rather, an increase in electron emission of 27 % is observed between 250 K and 900 K. Only for $T_S \leq 250$ K is γ_0 observed to be constant. For higher temperatures, γ_0 rises nearly linearly with surface temperature. Since no temperature dependence has ever been observed for metastable atoms colliding with a clean metal surface, the explanation for this effect has to be sought in the fact that the metastable species is a molecule, and will be discussed in detail in the next section.

Velocity dependence

For gas-phase reactions involving the exchange of electronic excitation, several examples are known for which the reaction cross section exhibits an inverse velocity dependence, i.e. the reaction rate increases with decreasing velocity (see, e.g., reference [208] for a list of examples). In contrast, the Auger de-excitation mechanism leading to electron emission in collisions of CO* with Au(111) is predicted to be independent of velocity provided that the incident energy is low enough. Hardly any studies have been conducted, however, which attempt to verify this [170]; they involved a limited number of metastable atomic species with kinetic energies in the 10 meV–3 eV range [209–211]. The latter two references, in particular, only report few data points.

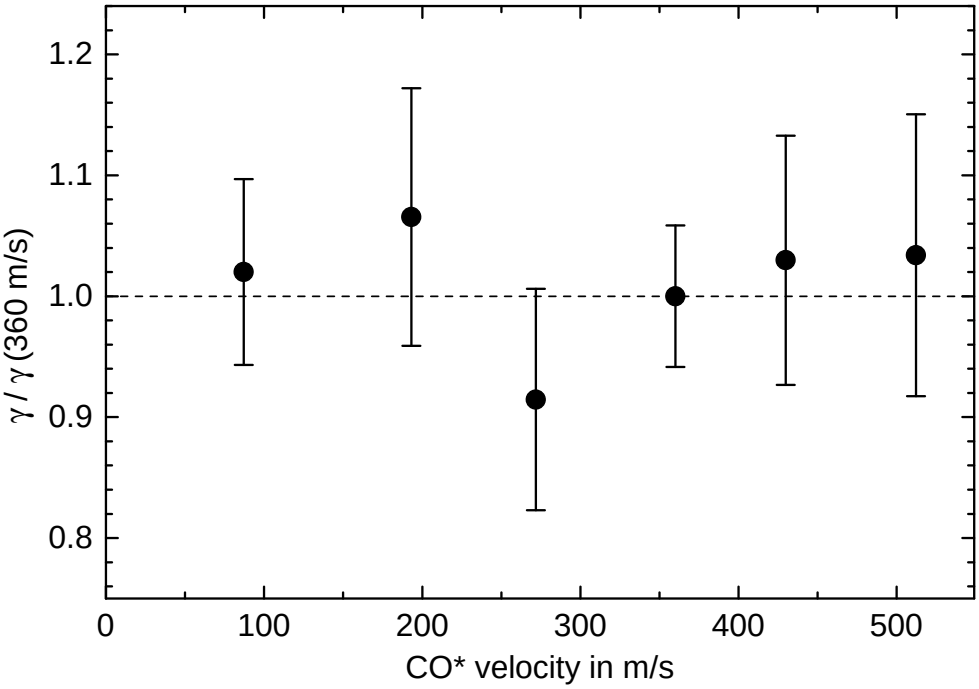

Figure 6.16: Velocity dependence of the electron emission yield. All γ_0 values are normalized to $\gamma_0(360\,\mathrm{m/s})$. Within the experimental uncertainty, γ_0 is independent on velocity between 87 m/s and 512 m/s. The horizontal line indicates a constant electron emission yield. Error bars represent the statistical error from the scatter of corresponding data, i.e the uncertainty of γ_0 from Eq. (6.15) is neglected. Figure adapted from reference [169].

Since there are some discrepancies between experimental observations and the Auger de-excitation mechanism both for the absolute magnitude of γ_0 and the unexpectedly strong temperature dependence, a study of the velocity dependence of γ_0 for the collision of CO* with Au(111) might also be expected to reveal a non-constant behavior. Measurements of γ_0 for different velocities are performed by two different methods. In the range of 193 m/s to 430 m/s, the procedure for determining the absolute electron emission yield as described in section 6.2.1 is repeated for different velocities. The values for the highest and lowest velocities are obtained in the same way as for the temperature curve: Time-of-flight traces obtained from electron emission and by scanning the delay of the REMPI laser are time-integrated and compared. Note that in this case, the time-integrated REMPI time-of-flight signal has to be multiplied by the beam velocity to obtain the correct result (see section 4.4.3). Results of this velocity scan are shown in Fig. 6.16. Electron emission relative to the value obtained for 360 m/s is constant within the experimental uncertainty, and data points agree

with a velocity independent yield within 10 %. This result agrees with the predictions of the Auger de-excitation model.

6.2.3 Discussion

Comparing the presented results with previous studies on metastable atoms and molecules reveals that the experimental observations for electron emission from the CO*-Au(111) system are unexpected in three main aspects. First of all, the absolute electron emission yield per incident CO molecule in the $a^3\Pi(v = 0)$ state, γ_0, is higher than expected. In addition, the increase of γ_0 with surface temperature is very pronounced, whereas in most studies of metastable de-excitation, it is so small that it is neglected. The third relevant observation is the variation of the electron emission yield with the vibrational level of CO*. Even though no yields for individual levels are determined, the experiment shows compelling evidence that some of the levels in the range of $v = 1 - 6$ must have an electron emission yield which is at least twice as large as γ_0.

The value of γ_0 has been determined to be 0.13 ± 0.05. In contrast, previous measurements by other groups report electron emission yields (averaged over the first eight vibrational levels) of CO* on chemically clean CuBeO of only 1.1×10^{-4} [182]. Rough estimates for γ_0 for CO* on heated chemically clean gold and γ_1 on heated atomically clean Ag(111) are reported to be 0.01 [57] and 0.2 [198], respectively. Considering that CO* has an internal energy of $E^\star = 6.01\,\text{eV}$, the excess energy over the work function, $\Phi(\text{Au}(111)) = 5.31\,\text{eV}$, is merely 0.70 eV. Cited results for Ag(111) are of the same order of magnitude, but the estimate by the authors is rather coarse. In addition, the work function of Ag(111), $\Phi(\text{Ag}(111)) = 4.74\,\text{eV}$ [212, 213], is considerably lower than in the case of Au(111). Among different systems, γ is known to strongly increases with $E^\star$ and decrease with Φ (see, e.g., [170, 200]), even though the assumption of a universal $\gamma(E^\star)$ curve valid for any metastable-surface combination as suggested by Borst [182] has been refuted [214]. The result for γ_0 for CO* on Au(111) is therefore expected to be less than similar values reported for metastable rare gases with higher electronic excitation energy impinging on a gold surface. However, γ values for Kr* in its $^3P_2(E^\star = 9.9\,\text{eV})$ and $^3D_3(E^\star = 11.4\,\text{eV})$ state are reported as much lower ($\gamma = 0.059$) and comparable ($\gamma = 0.162$) to CO*, respectively [214]. Note that the cited results were obtained from a chemically clean polycrystalline gold surface heated to 360 K. As no significant effect of cleaning the surface is seen for a surface heated to 373 K in the apparatus described here, these results are still assumed to be valid for comparison. Interestingly, the work function of polycrystalline gold ($\Phi = 5.1\,\text{eV}$ [212, 215]) is slightly lower than for Au(111), which makes the high value of CO* even more astonishing.

A coarse check was performed if any CO* survives the collision with the Au(111) without undergoing de-excitation. No surviving CO* could be detected by scanning the beam of the REMPI laser, tuned to ionize $\text{CO}(a^3\Pi_1(v = 0, J = 1))$, both in time and in space at a distance of 10 mm in front of the surface. This result is expected from past experiments where CO* scatters from a LiF(100) surface, where no efficient elec-

tronic de-excitation mechanism exists due to the large band gap of the insulator. Even in those experiments, only 1 % – 5 % of all molecules have been reported to survive in the metastable state [216, 217].

As the calculation of absolute electron emission yields for the case of molecules relies on knowledge of the interaction potential between metastable state and metal surface, it is beyond the scope of this work. The influence of vibrational quantum state and surface temperature, however, can be compared in detail to existing theories and extensions thereof.

Vibrational enhancement

Only a few studies have been undertaken so far which explore the electron emission for collisions of vibrationally excited molecules with clean metal surfaces. For both $CO^\star$ and $N_2{}^\star(A^3\Sigma_u^+, a^1\Pi_g)$, it has been observed before that γ depends on the vibrational state of the metastable molecule [182, 183, 218]. For $CO^\star$, only γ_1 was reported to be larger than γ_0 on an adsorbate covered surface, while higher vibrational excitation caused a decrease in the electron emission yield [183].

Within the simple model of Zubek and Borst (see Eqs. (6.10) and (6.12)), it is straightforward to obtain values for γ_v by use of Eq. (6.10), using values for the molecular constants and the Franck-Condon factors from references [61] and [219, 220], respectively. The latter is chosen because of its completeness and good agreement of FCF with more recent experimental data [221] for the $a^3\Pi_1(v' = 0) \rightarrow X^1\Sigma^+(v'')$ transition, where v' and v'' denote the vibrational level in the upper and lower electronic state, respectively. Upper levels up to $v' = 7$ and lower levels up to $v'' = 15$ are taken into account unless they contribute less than 1 % to the sum of FCF for any given v'. A surface temperature of 377 K is used, and the DOS of Au(111) is taken to be constant over the integration range, because it was reported to exhibit nearly no variation in the upper 2 eV of the conduction band [184]. The resulting dependence of $\gamma_{v'}$ with v' is shown in Fig. 6.17 as black circles. Only a small variation is seen in the value of $\gamma_{v'}$ in the range between $v' = 0$ and $v' = 7$. Extreme values of $\gamma_1 = 0.98\gamma_0$ and $\gamma_5 \approx \gamma_6 = 1.10\gamma_0$ are predicted. As should be obvious from the magnitude of single vibrational yields, averaged electron emission yields of $\bar{\gamma}_{v'=1,2,3} = 1.02\gamma_0$ and $\bar{\gamma}_{4,5,6} = 1.09\gamma_0$ are far from agreement with the experimental values reported in the previous section. Even though the values from Zubek's model are not consistent with experiment, they at least catch the overall trend of the curve: The enhancement rises slowly with the vibrational quantum number, peaks at around $v' = 6$, and starts to decrease for higher vibrational excitation. A decrease for $v \geq 7$ is consistent with values obtained when taking into account the results for FCP via the $e^3\Sigma^-$ state.

An important aspect which is not reflected by Zubek's model is the available final density of states, $\mathcal{D}_f(\epsilon)$, that an ejected electron can access. It is given by the square root of the final kinetic energy of a free electron that has been ejected. Thus, for an electron located at the Fermi level, one obtains $\mathcal{D}_f(\epsilon_F) = \sqrt{E_{\text{ex}}}$, while for an electron which is by E_{ex} lower in energy than the Fermi level, $\mathcal{D}_f(\epsilon_F - E_{\text{ex}}) = 0$. Here, $E_{\text{ex}} =$

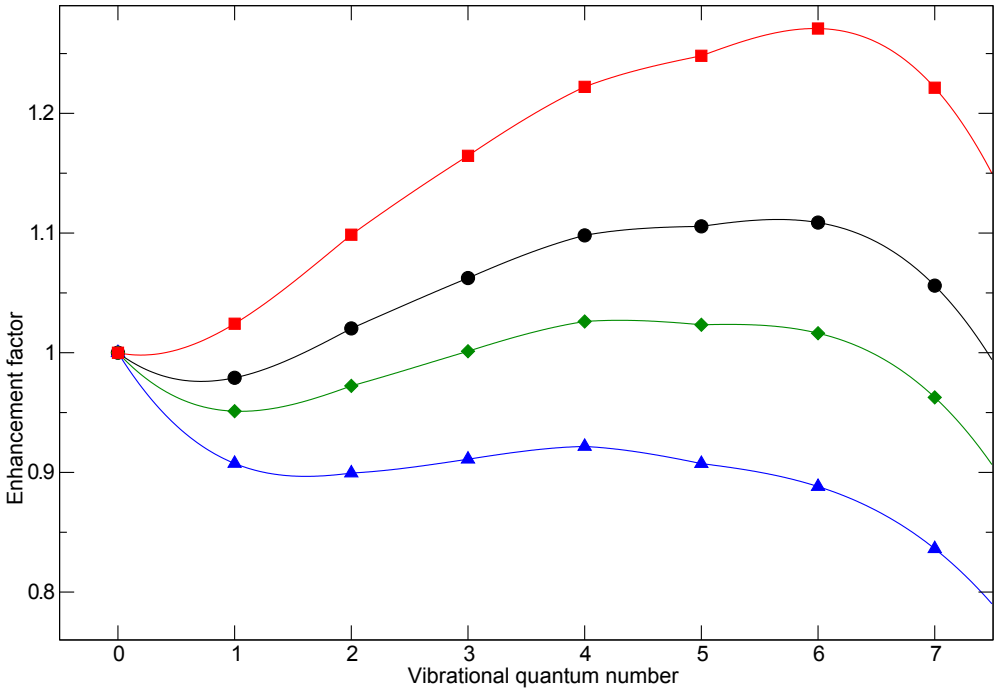

Figure 6.17: Theoretical prediction of $\gamma_{v'}$, for the lowest seven vibrational levels v'. Black circles depict results of applying Zubek's model to CO* on Au(111). Red squares show the result of modifying the model by including the final density of states into Eq. (6.10). Predictions of the tunneling model are shown as blue triangles for $d = 5$ Å and green diamonds for $d = 2$ Å. The solid lines are a guide to the eye.

$E^\star(v'', v') - \Phi$ is again the excess energy for electron emission. It is straightforward to include this term in the integral of Eq. (6.10), and obtain a modified formula for the electron emission yield:

$$\gamma_{v'} = \sum_{v''} \left(q(v'', v') \times \int_{\epsilon_F - E_{\mathrm{ex}}}^{\infty} f(\epsilon, T) \mathcal{D}(\epsilon) \sqrt{\epsilon - \epsilon_F + E_{\mathrm{ex}}} \, \mathrm{d}\epsilon \right) . \tag{6.24}$$

For the definition of the parameters, see Eq. (6.10). Relative electron emission yields obtained from this extended model, as depicted in Fig. 6.17, are in general higher than those predicted by the original model. In this extended model, $\gamma_{v'}$ increases with the upper vibrational quantum number for $v' \leq 6$, and then drops, as can be seen in Fig. 6.17. Averaged electron emission yields of $\bar{\gamma}_{v'=1,2,3} = 1.10\gamma_0$ and $\bar{\gamma}_{4,5,6} = 1.25\gamma_0$ are obtained, which are both too small compared to the experimental values. The experimentally observed dependence on v' can therefore be produced qualitatively, but not quantitatively.

The state-dependent electron emission yield, $\gamma_{v'}$, can be calculated in the tunneling model by including the transmission coefficient, $T(\epsilon, d)$, given in Eq. (6.9) into the integral of Eq. (6.10). In this case, $\gamma_{v'}$ is obtained for a fixed surface distance, d, from

$$\gamma_{v'} \propto \sum_{v''} \left(q(v'', v') \times \frac{1}{d} \int_{\epsilon_F - E_{\mathrm{ex}}}^{\infty} f(\epsilon, T) \mathcal{D}(\epsilon) T(\epsilon, d) \mathrm{d}\varepsilon \right) . \tag{6.25}$$

Refer to Eq. (6.10) for the definition of the variables. The dependence on v' and v'' arises from both the lower limit of integration and the FCF. In Fig. 6.17, results for this model are shown for surface distances of 5 Å and 2 Å. In addition, a comparison of the averaged values for all different models with theoretical predictions is shown in table 6.2. The tunneling model predicts values for $\bar{\gamma}_{1,2,3}$ and $\bar{\gamma}_{4,5,6}$ which are much too

averaged v'	Z	ZF	T(5 Å)	T(2 Å)	experimental
1, 2, 3	1.02	1.10	0.91	0.97	1.49
4, 5, 6	1.10	1.25	0.91	1.02	2.62

Table 6.2: Comparison of averaged values of $\gamma_{v'}/\gamma_0$ for different models with experimental values. Abbreviations are Z for Zubek's model, ZF for Zubek's model weighted by the final electron density of states, and T for tunneling model. See text for details of the models.

low. Its main effect of incorporating the tunneling mechanism is that the $\gamma_{v'}$ values for higher v' are shifted down. This is because electrons closer to the Fermi level will contribute much more strongly to the overall electron emission yield than those which are more strongly bound in the metal. Increasing the excess energy for electron emission by vibrational excitation has a weaker effect in this model, since additional electrons which become available will be lower in energy and are less likely to tunnel to the molecule. This effect increases as the tunneling probability is decreased by increasing d. One has to bear in mind that, in principle, the values obtained from the tunneling model need to be averaged over the whole range where AD takes place. Assuming the range of 3–5 Å determined by Woratschek *et al.* [175] to be approximately valid, effective values for $\gamma_{v'}$ will be closer to the values stated for 5 Å.

None of the discussed models is able to reproduce the increase of the electron emission yield, $\gamma_{v'}$, with the vibrational quantum number, v', of the metastable level. By extending Zubek's model to incorporate the final density of states for the free electron, qualitative agreement with experimental data can be obtained, but the predicted increase in electron emission is to low by a factor of about 5. All other models fail to predict the enhanced electron emission yield by at least one order of magnitude, if an increase is predicted at all.

Temperature dependence

For an atomically clean metal surface, i.e. a surface which is covered neither by impurities nor adsorbates, no big influence of surface temperature on the electron emission

yield γ is expected. This is because the only effect of temperature on electron density, which is important for Auger de-excitation, is to excite a small fraction of electrons to states above the Fermi level. Therefore, temperature is commonly neglected in studies dealing with clean surfaces (see, e.g. [49, p. 341]). Under non-UHV vacuum conditions or for chemically clean surfaces (i.e. surfaces that are only cleaned with solvents while they are still under atmosphere), in contrast, it plays an important role since adsorbates are removed from the surface [170]. A strong increase with temperature has been reported both for certain molecular [208, 222, 223] and for some atomic species [224]. For molecules, in principle the same arguments hold true as for atoms. Nonetheless, a somewhat larger effect of the temperature is expected because of two reasons. Usually, the excess energy, $E^\star - \Phi$, is smaller than for most metastable atoms or ions, therefore excited electrons constitute a larger fraction of the conduction band electrons which can energetically contribute to the signal. Moreover, exciting elec-

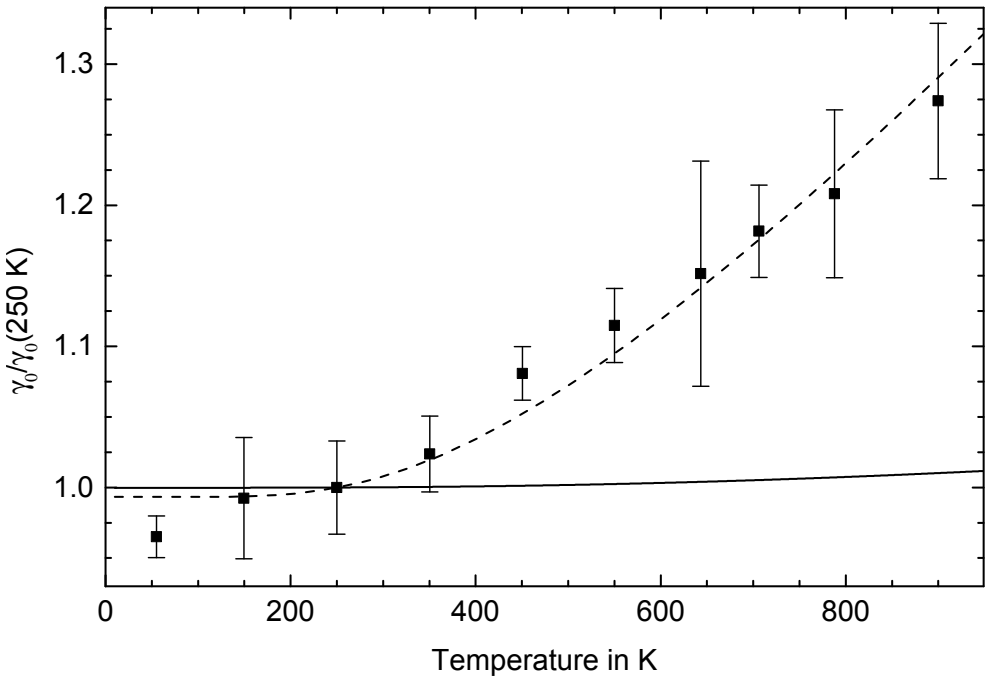

Figure 6.18: Theoretical prediction of the temperature dependence of γ_0. The solid black line is for Zubek's model using the known FCF for the $a^3\Pi \rightarrow X^1\Sigma^+$ transition and no free parameters. The dashed black line depicts the best fit in case that electron emission only occurs in a limited energy range, as will be described in the section discussing the anion resonance model. Both data and fit are scaled to $\gamma_0(250\,\mathrm{K})$. Figure adapted from reference [169].

trons to levels above the Fermi level has the added effect of making them available to de-excitation which proceeds via higher vibrational states of the electronic ground state that were formerly not energetically accessible.

The simplest way of modeling the experimental temperature dependence is to calculate the vibrational electron emission yield, γ_0, as a function of temperature according to Eq. (6.10):

$$\gamma_0(T_S) = \sum_{v''} \left(q(v'', 0) \times \int_{\epsilon_F - E_{ex}}^{\infty} f(\epsilon, T_S) \mathcal{D}(\epsilon) \mathrm{d}\epsilon \right) . \tag{6.26}$$

Note that the excess energy, E_{ex}, depends on v''. Using the same FCF for this model as before, one obtains an increase in γ_0 between 250 K and 900 K which is on the order of 1 %. This prediction is much less than the experimentally observed value, which is of course due to the fact that, in this model, excited electrons contribute little to the overall electron emission. When using more sophisticated models to calculate the temperature dependence, like weighting with the final density of states as in Eq. (6.24) or tunneling as is done Eq. (6.9), this value rises to about 3 %. This temperature increase still falls short of the experimental value of 27 % by one order of magnitude. In Fig. 6.18, experimental data is shown together with the temperature curve resulting from Eq.(6.26).

Note that, in principle, the experimentally observed surface temperature dependence can be reproduced if at least 85 % of all metastable molecules relax to excited vibrational levels of the electronic ground state with $v'' \geq 3$. This would, however, violate the Franck-Condon principle for the Auger de-excitation mechanism. The vibrational distribution of scattered electronic ground state CO can in principle be probed to verify that the de-excitation obeys the Franck-Condon principle. Unfortunately, the most efficient detection scheme for electronic ground state CO is only possible for lower vibrational levels $v'' \leq 2$ (see section 5.3.2). With the setup described here, no attempt has been made to measure the vibrational state distribution of scattered electronic ground state CO.

Enhancement and temperature effects in the anion model

In the model in which CO* de-excitation proceeds via a short-lived anionic state as described in section 6.1.2, it is not as straightforward to predict the effect of vibrational excitation and temperature as in the simple theories discussed above. Depending on which of the resonances introduced in section 6.2.3 is involved, the characteristics of the de-excitation change significantly.

Many properties of the anionic resonances that are relevant for the de-excitation of CO* on Au(111) can be obtained from the reverse process in which the $a^3\Pi$ state is excited by ineleastic electron scattering from the $X^1\Sigma^+$ electronic ground state. From the comparison of experiments with theoretical predictions, it can be concluded that the excitation of the $a^3\Pi$ state by electron scattering from the $X^1\Sigma^+$ state at an

electron kinetic energy of 10.04 eV can proceed by excitation of any of the four mentioned resonances[186, 187, 192]. This is because all of the shape resonances are broad enough in energy that they extend into this relevant energy range, despite their peak positions being very different in energy. An important consequence arises from the fact that the lifetime of the shape resonances is expected to be much shorter than the vibrational period of the corresponding state. The lifetime of the $^2\Pi$ resonance, for example, can be estimated from the equivalent $^2\Pi_g$ resonance of the isoelectronic N_2 molecule. For N_2, the lifetime of that resonance equals about half a vibrational period [185], while the lifetime of the $^2\Pi$ resonance is roughly one order of magnitude smaller. As a consequence, the position of the nuclei will not change significantly during the excitation and de-excitation of the $^2\Pi$ resonance. The same argument holds true for the $^2\Delta$ and $^2\Sigma^+$ shape resonances, which are also assumed to be broad in energy, based on the calculations for electron impact excitation of CO* [186]. The transition probability for the total excitation process therefore has to be weighted by the FCF between metastable $a^3\Pi$ state and the $X^1\Sigma^+$ electronic ground state. This argument is strongly supported by the fact that the FCF for the $a^3\Pi(v > 0) \rightarrow X^1\Sigma^+(v = 0)$ excitation determined from inelastic electron scattering experiments with electron energies just below 10 eV [187, 225] match well with the FCF determined from optically exciting the same state[85, 226].

In contrast, due to the much narrower width of the $^2\Sigma^+$ Feshbach resonance its lifetime is sufficiently long that the molecular anion can perform about six full periods of vibration. The transition probabilities for the excitation of that resonance from the electronic ground state to the resonance and for the de-excitation of the resonance to the $a^3\Pi$ state therefore have to be weighted by the corresponding FCF. Since the potential curve of the $^2\Sigma^+$ Feshbach resonance is unknown, only estimates for these FCF can be attained. As an approximation for the vibrational overlap between the Feshbach resonance and the $a^3\Pi$ state, the FCF can be assumed to be equal to the observed increase of vibrational line intensities in the excitation of the $a^3\Pi$ state from the $X^1\Sigma(v = 0)$ state by inelastic electron scattering at 10.04 eV. It has been found that excitation proceeds preferentially to vibrationally excited levels of the $a^3\Pi$ state [188, 189]. Following Swanson *et al.* [192], the final $v = 1$ vibrational level is preferred in the excitation via the Feshbach resonance, while according to Mazeau *et al.* [189], the contribution of the resonance is highest for the $v = 3$ vibrational level of the $a^3\Pi$ state. This behavior has been explained in terms of the equilibrium internuclear distance of the involved states [188, 189]. While the $a^3\Pi$ state has an equilibrium internuclear distance of 1.206 Å, the equilibrium internuclear distance in the $^2\Sigma^+$ Feshbach resonance is expected to be close to that of its parent state, $b^3\Sigma^+$, which is 1.113 Å. As a consequence, the $^2\Sigma^+$ Feshbach resonance has a higher overlap with vibrationally excited levels of the $a^3\Pi$ state. Following the same line of argumentation, estimates for the vibrational overlap of the $b^3\Sigma^+$ state with the electronic ground state of CO can be given. The resonance can be assigned a vibrational quantum number of zero, because it arises from the ground vibrational level of its $b^3\Sigma^+$ parent state. Assuming that the potential curve is similar to that of the parent state, the distance between the classical turning points will be significantly smaller than for

the $X^1\Sigma^+$ state. These considerations give rise to a vibrational wavefunction of the Feshbach resonance which is narrow and peaked at approximately the equilibrium internuclear distance of the electronic ground state, which is 1.128 Å. Obviously, this situation will strongly favor transitions to the vibrational ground level of the $X^1\Sigma^+$ state. Vibrational levels with odd v will have almost no contribution, and transitions to even-numbered vibrational states with $v > 0$ will be significantly weaker.

For CO* de-excitation to the electronic ground state, these findings imply that electron emission is possible by resonant tunneling from electrons near the Fermi level into the far wings of any of the shape resonances, independent of the surface distance. For all shape resonances, however, the overall de-excitation process is governed by the Franck-Condon factors between the $a^3\Pi$ state and the $X^1\Sigma^+$ state. Therefore, the predictions of a model involving any of the shape resonances will be very similar to the models for Auger de-excitation presented previously. Since those models cannot reproduce the vibrational enhancement of electron emission nor its increase with temperature, the shape resonances will not be discussed in detail.

The implication for the de-excitation of CO* on Au(111) via the $^2\Sigma^+$ Feshbach resonance is that higher vibrational states of the $a^3\Pi$ state are more likely to capture an electron to form the resonance, which then preferentially decays to the ground vibrational level of the electronic ground state. For the sake of simplicity, only the decay of the $^2\Sigma^+$ Feshbach resonance to the ground vibrational level of the $X^1\Sigma^+$ state will be considered in the following discussion. The electron emission yield under these assumptions becomes proportional to the Franck-Condon factors, $q(v'' = 0, v')$, between the vibrational level, v', of the $a^3\Pi$ state and the resonance. In addition, the density of final states, $\mathcal{D}_f \propto \sqrt{E_{\mathrm{ex}}(v'' = 0, v')}$, that is available to the emitted electron can be included again, like in the extension to Zubek's model presented previously. When taking into account only electrons near the Fermi level, the motivation for which will be given below, the electron emission yield is then given by:

$$\gamma_{v'} \propto q(v'' = 0, v') \times \sqrt{E_{\mathrm{ex}}(v'' = 0, v')} \,. \tag{6.27}$$

Using values of $q(0, v')$ from Mazeau *et al.* [189] yields $\bar{\gamma}_{1,2,3} = 2.7$ and $\bar{\gamma}_{4,5,6} = 2.5$. Based on measurements by Swanson *et al.* [192], values of $\bar{\gamma}_{1,2,3} = 1.3$ and $\bar{\gamma}_{4,5,6} = 0.7$ are obtained. The increase of electron emission yield with the vibrational quantum number predicted by this model is on the same order of magnitude as the experimental values, as can be seen from Fig. 6.19. In contrast to the experimental observations, however, the increase of $\gamma_{v'}$ is predicted to be higher for $v' = 1 - 3$ than for $v' = 4 - 6$.

The presented model predicts that CO* is de-excited preferentially to the $v'' = 0$ level of the electronic ground state. This implies that the experimentally observed temperature dependence cannot be explained by the de-excitation to higher final vibrational levels, which only leads to electron emission at elevated temperatures as mentioned previously in this section. A strong temperature dependence can arise nonetheless in the model where de-excitation takes place via the Feshbach resonance if the electron emission stops at a critical distance. This has the effect that only molecules from a narrow energy range below the Fermi level of the surface contribute

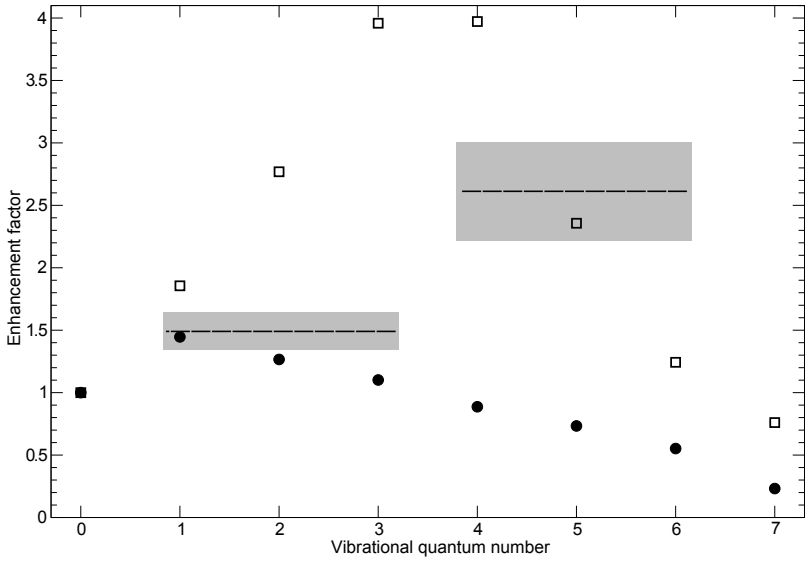

Figure 6.19: Vibrational enhancement in the model where de-excitation proceeds via the Feshbach resonance. Full circles denote electron emission yields calculated when using data from Swanson *et al.* [192], open squares are for data from Mazeau *et al.* [189]. Dashed lines and gray rectangles correspond to the experimentally determined values and their error bars, respectively.

to electron emission, because the energy of the resonance changes with the surface distance due to image charge stabilization. The electron emission yield is determined from Eq. (6.10) by setting $q(0,0) = 1$ and by cutting off the integral at the lower value $\epsilon_F - \Delta\epsilon$:

$$\gamma(T) \propto \int_{\epsilon_F - \Delta\epsilon}^{\infty} f(\epsilon, T)\mathcal{D}(\epsilon)\mathrm{d}\epsilon \tag{6.28}$$

The parameter $\Delta\epsilon$ can now be determined from a fit to the experimental data. Best agreement is obtained when $\Delta\epsilon = 0.08\,\mathrm{eV}$. The $^2\Sigma^+$ Feshbach resonance crosses this point in energy below the Fermi level at a surface distance of 3.13 Å, which is 0.15 Å after the resonance has crossed the Fermi level. The temperature dependence resulting from this model is depicted in Fig. 6.18 by the dashed blue line. Excellent agreement with experiment is achieved in this model.

A possible explanation why electron emission would stop at a distance of about 3 Å in front of the surface arises from the size of the highest occupied $3s\sigma$ Rydberg orbital of the anion. As suggested by Ermler and Mulliken [227], the size of a molecular Rydberg orbital may be estimated by correcting the formula for the mean radius of a Rydberg state of the hydrogen atom by the quantum defect, δ, of the orbital. The mean radius of an s orbital with principal quantum number, n, is then [176, 227] $r \approx \frac{3}{2}a_0(n -$

$\delta)^2$, where a_0 is Bohr's radius. For the $b^3\Sigma^+$ state, the parent state of the $^2\Sigma^+$ Feshbach resonance, the quantum effect is $\delta = 1.06$ [228], such that $r_{3s\sigma} \approx 3$ Å is obtained. Since the outer electrons in the anionic state experience a weaker attraction due to the additional electron, the size of the $3s\sigma$ orbital in the anion is expected to be bigger than in the neutral molecule. When the Feshbach resonance crosses the Fermi level of the metal at a surface distance of 3.28 Å, the $3s\sigma$ orbital in the anion will therefore be almost in contact with the surface. The overlap with the wavefunctions of electrons from the conduction band will be large at this point, leading to efficient ionization of CO*. At closer distances, however, there will be a repulsive force between the surface and the anionic state, because the $3s\sigma$ orbital cannot penetrate into the surface. As a consequence, the anionic state will be shifted upward in energy until it is above the Fermi level again, such that resonant capture of a surface electron into the $3s\sigma$ orbital is no longer possible.

The large size of the $3s\sigma$ orbital in the anion can also provide an explanation why de-excitation via the $^2\Sigma^+$ Feshbach resonance dominates over the other de-excitation channels, namely Auger de-excitation and de-excitation via one of the shape resonances. Auger de-excitation is very likely to occur before the molecule reaches a surface distance of 3.28 Å, but if the electron emission yield associated with it is only on the order of 1 % as expected, it will contribute only little to the observed signal. De-excitation via one of the shape resonances is believed to be less efficient in causing electron emission because the highest occupied 2π orbital is most likely less extended than the $3s\sigma$ orbital, and thus the overlap of molecular and surface electronic orbitals strongly favors de-excitation via the $^2\Sigma^+$ Feshbach resonance. Moreover, electrons which are too low in energy to cause electron emission can also tunnel into the broad shape resonances, such that the de-excitation occurs without electron emission.

Describing the de-excitation of CO* on Au(111) by means of the $^2\Sigma^+$ Feshbach resonance yields better agreement with experimental data than the other models discussed above. Since many approximations have been introduced in order to describe the de-excitation via his resonance, it is not surprising that the agreement with experiment is not perfect. Obviously, more thorough theoretical modeling of the $^2\Sigma^+$ Feshbach resonance at 10.04 eV and its interaction with the surface is needed to clarify whether it is indeed a possible mechanism for the de-excitation of CO* on Au(111). The discussed models disagree in their predictions of the final vibrational distributions in the electronic ground state: in the anion resonance model, most of the molecules will relax to the vibrational ground state, while in the other models, the vibrational levels are populated according to the Franck-Condon factors between the $a^3\Pi$ and the $X^1\Sigma$ state. In addition, only electrons close to the Fermi level of the surface are involved in the de-excitation in the anion resonance model, such that the kinetic energy distribution of emitted electrons will consist of a large narrow peak near 0.7 eV. In the other models, electrons from the entire accessible energy range take part, resulting in a kinetic energy distribution that reaches from 0 eV to 0.7 eV. These predictions can be probed experimentally by measuring the kinetic energy distribution of the emitted electrons, and by probing the population of different vibrational levels of the scattered electronic ground state CO.

6.2.4 Conclusion

The absolute electron emission yield for de-excitation of CO $(a^3\Pi_1, v = 0)$ has been determined to be $\gamma_0 = 0.13 \pm 0.05$. Variation of the final velocity of CO* between 87 m/s and 512 m/s showed no effect of the incident translational energy on γ_0 within 10 %. Experiments which probe the influence of vibrational excitation and surface temperature yield results which are unexpected in the context of previous work. The vibrational enhancement of electron emission, i.e. the increase of the electron emission yield of higher vibrational states, γ_v, relative to γ_0, has been determined by creating different vibrational distributions by means of Franck-Condon pumping. Final results for the enhancement averaged over groups of vibrational levels are $\bar{\gamma}_{v=1,2,3} = (1.49 \pm 0.14)\gamma_0$ and $\bar{\gamma}_{v\geq 4} = (2.62 \pm 0.39)\gamma_0$. When the surface temperature is varied, an increase of γ_0 by 27 % is observed between 250 K and 900 K.

A total of four different mechanisms, which have been shown to successfully reproduce experimental data in other cases, were employed to model the observations: A simple model by Zubek [183], which combines the vibrational structure with a well-established model for metastable and ionic atomic species, qualitatively predicts the observed vibrational enhancement, but falls short by an order of magnitude both for the enhancement and for the surface temperature dependence. Extending this model by weighting the electronic transitions from the conduction band of the metal not only by Franck-Condon factors, but also by the final density of states for the free electron, leads to better quantitative agreement, but still underestimates the vibrational enhancement of electron emission by a factor of 5 .

A different model, used by Woratschek *et al.* [175] to successfully reproduce electron energy spectra for metastable Helium atoms scattering off low work-function surfaces, treats the de-excitation as a tunneling process of an electron through an idealized rectangular potential barrier of height equal to the gap between the bottom of the conduction band and the vacuum level. For the relevant surface distances, this mechanism fails to correctly predict the magnitude of vibrational enhancement, but exhibits a similar overall trend as the model of Zubek. The temperature dependence falls short of experimental data points by one order of magnitude.

De-excitation via a short-lived anion resonance has been suggested to be involved in the de-excitation of metastable N_2 on metal surfaces [193, 194]. The anionic $^2\Sigma^+$ Feshbach resonance is possibly involved in the de-excitation of CO* on Au(111). It is located 10.04 eV in energy above the electronic ground state, and crosses the Fermi level of the surface at a surface distance of 3.28 Å due to image charge stabilization. Because of the large size of the highest occupied molecular orbital in this resonance, the overlap of molecular and surface electronic wavefunctions could provide a very effective de-excitation channel. The experimental surface temperature dependence can be reproduced if one assumes that this process will not be in action after the molecule approaches the surface closer than 3.13 Å. For the vibrational enhancement of electron emission this model predicts the correct order of magnitude. The averaged electron emission yield for the vibrational levels $v = 4, 5, 6$, however, is systematically smaller than that for the vibrational levels $v = 1, 2, 3$. Clearly, the anion reso-

nance model has to be considered as a possible pathway for the CO* de-excitation on Au(111), but it obviously needs more thorough analysis before it can be identified as the dominant mechanism. An important aspect is that the anion resonance de-excitation mechanism predicts both different final vibrational level distribution of ground state CO, and different final kinetic energy distributions of the emitted electrons. By measuring these two distributions, it should be possible to distinguish experimentally which de-excitation mechanism is in action.

The observed invariance of γ_0 with the velocity of the colliding CO* verifies for the first time that incident translational energy does not play an important role in the de-excitation of slow metastable molecules. The same result was obtained previously by other groups in a small number of experiments performed on metastable atoms [209–211]. From the measured velocity independence, it can be inferred that the process leading to electron emission must occur at a rate larger than $10^{12}\,\mathrm{s}^{-1}$. This is the inverse of the time which a molecule needs to traverse the distance of 3–5 Å in front of the surface, which has been shown to be critical for AD. Since all of the models are based on processes which happen fast compared to the time scale on which the molecule approaches the surfaces, the determined rate does not rule out any of the mechanisms discussed in this work.

Repeating the presented experiments with an apparatus suited for detecting the kinetic and angular distribution of emitted electrons would prove beneficial in understanding the processes involved, since kinetic energy spectra are known to exhibit signatures specific to certain mechanisms. Further evidence could be found by state-resolved detection of the scattered ground state molecules. A Franck-Condon distribution of the final vibrational state population would strongly support an Auger de-excitation mechanism, while preferential population of the lowest vibrational level of the electronic ground state would provide evidence for the $^2\Sigma^+$ Feshbach resonance being involved in the electron emission. For a quantitative analysis of electronic ground state vibrational levels beyond $v'' = 2$, however, a VUV (1+1) REMPI scheme should be used, the laser system for which is being developed in the Göttingen group. A VUV laser source could also be used to improve the accuracy of the measurement of the absolute electron emission yield. This is because by ionizing CO* molecules with a single photon, any ambiguity related to vibrational signal enhancement would be removed. In addition, vibrational enhancement could be measured for specific states using more sophisticated preparation schemes than Franck-Condon pumping. Stimulated emission pumping (SEP) [159], Stimulated Raman adiabatic passage (STIRAP) [229], or Pump-Dump-Sweep [230] are examples of methods which provide a much finer control of the final vibrational level populations. As an alternative, direct excitation of vibrational transitions is preferable to Franck-Condon pumping. This can be achieved either by overlapping an IR laser with the molecular beam between decelerator exit and the surface, or by exciting molecules to higher vibrational states of CO* in the first laser pumping step behind the skimmer.

Chapter 7

Summary and Outlook

This thesis describes the design and characterization of a novel apparatus for quantum-state resolved, velocity-controlled molecule-surface scattering. It presents the results of surface scattering experiments of metastable, electronically excited molecules with a clean metal surface. The collisions cause electron emission in a way which, as of now, cannot be explained by commonly used theories.

The new apparatus combines, for the first time, a Stark decelerator with a state-of-the-art surface scattering chamber. Its is designed to scatter high intensity pulses of molecules from a clean surface in a well-defined collision process and obtain information about the collisions by measuring all quantum states and lab-frame velocities. Molecules can be prepared in single quantum states with controlled, tunable velocities. The velocity can not only be controlled easily and changed rapidly during the experiment, but also has a small spread within the molecular beam pulse. The surface can be prepared either free of any contaminants or with a defined coverage of a chosen adsorbate. Its temperature is both controlled and measured accurately between cryogenic temperatures and the melting point of the metal. In addition, the angle of incidence is variable. Full information of the scattering process can be obtained by ionizing scattered particles with a laser which is scanned in frequency to probe the quantum state distribution of scattered molecules. The experimental geometry provides sufficient space for varying the position of laser beams, such that the scattering angle and the kinetic energy of scattered molecules can be determined from the experiment.

The design of the apparatus is laid out in chapters 3–5. It is optimized to produce molecular beams of CO, since it is prone to manipulation with high electric fields in its first electronically excited state, and at the same is important in the real world applications we seek to understand. Key components of the molecular beam setup are a switched electric hexapole focuser and a 131 stage Stark decelerator for velocity tuning. In order to manipulate CO with electric fields, it is first optically excited to the long-lived metastable $a^3\Pi_1(v = 0, J = 1)$ state, which has a large dipole moment as is described in chapter 2. The hexapole device not only focuses, but also deflects CO molecules in that quantum state by a small angle and separates them from the carrier gas and remaining CO in the electronic ground state. This step of background gas removal is crucial for performing experiments on a clean surface at low temperatures, since the remaining species of the molecular beam would otherwise hit the surface and, provided temperatures are low enough, stick to it. Removal of

the carrier gas has been demonstrated to be efficient enough that the pressure rise in the scattering chamber upon switching on the molecular beam cannot be measured, i.e. it is less than 10^{-10} mbar. The Stark decelerator uses rapidly switched electric fields to transport molecules within a narrow velocity and spatial range of the most intense part of the molecular beam from the exit of the hexapole to the surface. In this process, the selected molecules can be either accelerated or decelerated. In the standard setup, 1.1 cm^{-1}, equivalent to 1.4×10^{-4} eV, of translational energy can be added or removed in each of the 131 electric field stages of the decelerator. For an initial velocity of 360 m/s, molecular pulses of up to (512 ± 4) m/s and down to (50 ± 4) m/s can be generated, which corresponds to collision energies of (307 ± 5) cm^{-1} and (3.0 ± 0.5) cm^{-1}, respectively. With only small modifications to the setup, higher velocities of up to (1300 ± 25) m/s can be achieved, at the expense of the background gas not being removed. The surface is mounted such that laser access is possible in two dimensions. Molecules can be prepared in specific quantum states anywhere between a position six electric field stages before the end of the decelerator and directly in front of the surface. Using a pulsed detection laser makes it possible to vary the time-delay between scattering event and detection, and thus to determine the time-of-flight distribution of scattered particles. This allows the calculation of the kinetic energy of scattered molecules.

Scattering metastable CO in the $a^3\Pi$ state from Au(111) causes electron emission, because the excitation energy exceeds the work function. The absolute electron emission yield, defined as the number of electrons emitted per incident metastable particle, has been determined to be 0.13 ± 0.05 . This number is higher than expected when compared to the values reported by other groups for a variety of metastable species and surfaces. A study of the influence of vibrational excitation of metastable CO unambiguously reveals that higher vibrational levels are associated with more electron emission. The three lowest excited states contribute about $1^1/_2$ times as much to electron emission as the vibrational ground state, and the next three levels abound $2^1/_2$ times as much. When the temperature of the surface is increased, electron emission stays approximately constant between 50 K and 250 K, but rises steeply for higher temperatures. At 900 K, the electron emission yield is 27 % higher than at 250 K.

Theoretical models developed for metastable molecule-surface scattering are rather sparse and follow simple approaches. None of the models based on extensions of metastable atom-surface scattering predict the magnitude of the electron emission yield correctly, nor the changes observed with temperature or with vibrational excitation. General trends, however, match the experimentally observed behavior. A mechanism based on formation of a short-lived anion can, in principal, explain a strong increase of electron emission and reproduce the observed temperature dependence, but more detailed theoretical work is needed to obtain reliable predictions from the corresponding model. Because the anion model predicts a different kinetic energy distribution of the emitted electrons and a different vibrational state population of the de-excited CO, it should be possible to experimentally distinguish it from the Auger de-excitation models. Comparison of the discussed models with the experimental results obtained

with the new apparatus demonstrates the need to extend the existing models to fully account for the additional degrees of freedom of molecules, most importantly, their vibration.

In order to improve the understanding of electron emission caused by the impact of metastable molecules on metal surfaces, several experiments are planned for the new apparatus. At the present time, the influence of adsorbates on the de-excitation process is being investigated. For example, dosing the surface with one or more monolayers of rare gases is expected to have two competing effects: As the surface's work function is lowered by the adsorbate, electron emission is expected to increase, while the space introduced by the adsorbate decreases the likelihood of electron exchange between metastable and metal.

Several improvements are planned to extend existing measurements. With a recently implemented radiation shield for the surface, it should be possible to reach temperatures of about 20 K, which gives more flexibility in the adsorbates with which the surface can be dosed. More sophisticated pumping schemes than Franck-Condon pumping can be used to prepare single vibrationally excited states. This will make it possible to determine the electron emission yields for individual vibrational quantum states. The use of a VUV laser system capable of producing light of less than 155 nm wavelength, could provide a more accurate measurement of the electron emission yield, since no intermediate electronic states are involved in the ionization step. Detection of CO in the $a^3\Pi(v = 1)$ state with an F_2 excimer laser has already been demonstrated to be possible[58].

The knowledge obtained from the characterization of metastable molecule-surface scattering will serve as a valuable benchmark for subsequent scattering experiments with electronic ground state CO, since it allows the number of molecules impinging on the surface to be unambiguously determined. In this next stage of experiments, it will be possible to precisely monitor the energy transfer between individual degrees of freedom, thus providing a valuable steppingstone towards the goal of building an elementary model of molecule-surface interactions. CO exiting the decelerator will be prepared in different ro-vibrational levels of the electronic ground state. This is achieved either by pumping the corresponding $a^3\Pi_1 \rightarrow X^1\Sigma^+$ transition directly, as in the first excitation step, or by exploiting perturbations of the $A^1\Pi$ state[231]. When de-excitation takes place within the last few stages of the decelerator, remaining CO can be effectively de-focused or separated in time such that a pulse of pure electronic ground state CO is obtained. Since the apparatus is designed to allow maximum flexibility of laser access, scattering products can be detected with spatial and time resolution, such that the scattering angle and translational energy of the particles can be probed. Excitation and de-excitation of vibrational and rotational degrees of freedom of CO on Au(111) will be studied. No scattering studies exist for the range of incidence energies which is covered by the machine presented here. The low energy regime allows to study an important aspect, which is related not to the purely energetic, but primarily to a dynamic perspective of the scattering process. A slow molecule will spend much longer time near a surface than a fast one, which allows

processes to take place which occur only at low rates.

Extending the outlook further into the future, comparison of the results of scattering CO from Au(111) to scattering experiments on other surfaces will provide a more general insight in energy transfer mechanisms which are valid among different systems. Ag(111), e.g., is similar to Au(111), but has a slightly lower work function, which is expected to have a large effect for the electron emission yield of metastable CO. Also, comparing metals to insulator surfaces provides a means to study the effects of electronic excitation in the surface on the excitation and de-excitation of molecular degrees of freedom. Going even further, one can extend the use of the apparatus to other molecules to which Stark deceleration is applicable, like NO or NH_3.

In conclusion, a new apparatus for molecule-surface scattering has been designed and demonstrated to work which allows the full characterization of the surface scattering process with so far unprecedented incident energy resolution in the low energy regime. It incorporates the techniques of hexapole state selection and Stark deceleration into a state-of-the-art molecule-scattering setup, making it possible to perform scattering experiments in the so far unexplored low energy regime. A state-resolved study of de-excitation of metastable CO on Au(111) yields many unpredicted results and demonstrates the need to extend the models commonly used to describe this process. In the future, state-resolved scattering experiments of electronic ground state CO performed with the new setup will contribute to the understanding of energy transfer mechanisms.

Bibliography

[1] G. Scoles, ed., *Atomic and molecular beam methods*, vol. 1 & 2 (Oxford University Press, New York, NY, USA, 1988 & 1992), ISBN 0195042808.

[2] C. T. Rettner, J. Kimman, and D. J. Auerbach, J. Chem. Phys. **94**, 734 (1991).

[3] C. T. Rettner, C. B. Mullins, D. S. Bethune, D. J. Auerbach, E. K. Schweizer, and W. H. Weinberg, J. Vac. Sci. Technol. A **8**, 2699 (1990).

[4] M. Spruit, P. V. D. Hoek, E. Kuipers, F. Geuzebroek, and A. Kleyn, Surf. Sci. **214**, 591 (1989).

[5] J. Stark, Nature **92**, 401 (1913).

[6] J. Stark, Ann. Phys. **348**, 965 (1914).

[7] J. Stark and G. Wendt, Nachrichten von der Gesellschaft der Wissenschaften zu Göttingen, Mathematisch-Physikalische Klasse **1914**, 63 (1914).

[8] H. L. Bethlem, G. Berden, and G. Meijer, Phys. Rev. Lett. **83**, 1558 (1999).

[9] R. B. Neal, ed., *The Stanford two-mile accelerator* (W. A. Benjamin, New York, USA, 1968), http://www.slac.stanford.edu/library/2MileAccelerator/2mile.htm, retrieved on September 30, 2013.

[10] J. J. Gilijamse, S. Hoekstra, S. A. Meek, M. Metsälä, S. Y. T. van de Meerakker, G. Meijer, and G. C. Groenenboom, J. Chem. Phys. **127**, 221102 (2007).

[11] H. L. Bethlem, G. Berden, F. M. H. Crompvoets, R. T. Jongma, A. J. A. van Roij, and G. Meijer, Nature **406**, 491 (2000).

[12] H. L. Bethlem, F. M. H. Crompvoets, R. T. Jongma, S. Y. T. van de Meerakker, and G. Meijer, Phys. Rev. A **65**, 053416 (2002).

[13] S. D. Hogan, M. Motsch, and F. Merkt, Phys. Chem. Chem. Phys. **13**, 18705 (2011).

[14] A. I. Bishop, L. Wang, and P. F. Barker, New J. Phys. **12**, 073028 (2010).

[15] S. Merz, N. Vanhaecke, W. Jaeger, M. Schnell, and G. Meijer, Phys. Rev. A **85**, 063411 (2012).

[16] J. F. Barry, E. S. Shuman, E. B. Norrgard, and D. DeMille, Phys. Rev. Lett. **108**, 103002 (2012).

[17] J. M. Doyle, B. Friedrich, J. Kim, and D. Patterson, Phys. Rev. A **52**, R2515 (1995).

[18] M. Gupta and D. Herschbach, J. Phys. Chem. A **103**, 10670 (1999).

[19] M. Strebel, F. Stienkemeier, and M. Mudrich, Phys. Rev. A **81**, 033409 (2010).

[20] J. van Veldhoven, J. Küpper, H. L. Bethlem, B. Sartakov, A. J. van Roij, and G. Meijer, Eur. Phys. J. D **31**, 337 (2004).

[21] E. R. Hudson, H. J. Lewandowski, B. C. Sawyer, and J. Ye, Phys. Rev. Lett. **96**, 143004 (2006).

[22] H. L. Bethlem and W. Ubachs, Faraday Disc. **142**, 25 (2009).

[23] A. J. de Nijs, E. J. Salumbides, K. S. E. Eikema, W. Ubachs, and H. L. Bethlem, Phys. Rev. A **84**, 052509 (2011).

[24] V. V. Flambaum and M. G. Kozlov, Phys. Rev. Lett. **99**, 150801 (2007).

[25] M. R. Tarbutt, J. J. Hudson, B. E. Sauer, and E. A. Hinds, Faraday Disc. **142**, 37 (2009).

[26] M. R. Tarbutt, B. E. Sauer, J. J. Hudson, and E. A. Hinds, New J. Phys. **15**, 053034 (2013).

[27] R. V. Krems, Int. Rev. Phys. Chem. **24**, 99 (2005).

[28] J. J. Gilijamse, S. Hoekstra, S. Y. T. van de Meerakker, G. C. Groenenboom, and G. Meijer, Science **313**, 1617 (2006).

[29] L. Scharfenberg, K. Gubbels, M. Kirste, G. Groenenboom, A. van der Avoird, G. Meijer, and S. Meerakker, Eur. Phys. J. D **65**, 189 (2011).

[30] M. Kirste, L. Scharfenberg, J. Kłos, F. Lique, M. H. Alexander, G. Meijer, and S. Y. T. van de Meerakker, Phys. Rev. A **82**, 042717 (2010).

[31] M. Kirste, X. Wang, H. C. Schewe, G. Meijer, K. Liu, A. van der Avoird, L. M. C. Janssen, K. B. Gubbels, G. C. Groenenboom, and S. Y. T. van de Meerakker, Science **338**, 1060 (2012).

[32] M. Appl, *Ammonia* (John Wiley & Sons, 2006), ISBN 9783527306732.

[33] F. Haber, *Noble lecture* (1918), http://www.nobelprize.org/nobel_prizes/chemistry/laureates/1918/haber-lecture.pdf, retrieved on 27 Sep, 2013.

[34] C. Bosch, *Noble lecture* (1931), http://www.nobelprize.org/nobel_prizes/chemistry/laureates/1931/bosch-lecture.pdf, retrieved on 27 Sep, 2013.

[35] G. W. Huber, S. Iborra, and A. Corma, Chem. Rev. **106**, 4044 (2006).

[36] H. Schulz, Appl. Catal. A **186**, 3 (1999).

[37] G. Binnig and H. Rohrer, Angew. Chem. Int. Ed. **26**, 606 (1987).

[38] G. Binnig, C. Gerber, E. Stoll, T. Albrecht, and C. Quate, Surf. Sci. **189/190**, 1 (1987).

[39] W. Kohn, Rev. Mod. Phys. **71**, 1253 (1999).

[40] C. Rettner, D. Auerbach, J. Tully, and A. Kleyn, J. Chem. Phys. **100**, 13021 (1996).

[41] J. Barker and D. Auerbach, Surf. Sci. Rep. **4**, 1 (1984).

[42] I. Rahinov, R. Cooper, D. Matsiev, C. Bartels, D. J. Auerbach, and A. M. Wodtke, Phys. Chem. Chem. Phys. **13**, 12680 (2011).

[43] J. D. White, J. Chen, D. Matsiev, D. J. Auerbach, and A. M. Wodtke, Nature **433**, 503 (2005).

[44] J. D. White, J. Chen, D. Matsiev, D. J. Auerbach, and A. M. Wodtke, J. Chem. Phys. **124**, 064702 (2006).

[45] N. H. Nahler, J. D. White, J. LaRue, D. J. Auerbach, and A. M. Wodtke, Science **321**, 1191 (2008).

[46] Y. H. Huang, C. T. Rettner, D. J. Auerbach, and A. M. Wodtke, Science **290**, 111 (2000).

[47] N. Shenvi, S. Roy, and J. C. Tully, Science **326**, 829 (2009).

[48] H. W. Webb, Phys. Rev. **24**, 113 (1924).

[49] H. D. Hagstrum, Phys. Rev. **96**, 336 (1954).

[50] W. M. Haynes, ed., *CRC Handbook of Chemistry and Physics*, vol. 93 (CRC Press, Boca Raton, 2012), ISBN 978-1-439-88049-4.

[51] C. A. Burrus, J. Chem. Phys. **28**, 427 (1958).

[52] E. J. Salumbides, M. L. Niu, J. Bagdonaite, N. de Oliveira, D. Joyeux, L. Nahon, and W. Ubachs, Phys. Rev. A **86**, 022510 (2012).

[53] J. J. Gilijamse, S. Hoekstra, N. Vanhaecke, S. van de Meerakker, and G. Meijer, Eur. Phys. J. D **57**, 33 (2010).

[54] B. G. Wicke, R. W. Field, and W. Klemperer, J. Chem. Phys. **56**, 5758 (1972).

[55] H. Lefebvre-Brion and R. W. Field, *The Spectra and Dynamics of Diatomic Molecules* (Academic Press, San Diego, USA, 2004).

[56] G. Herzberg, *Molecular Spectra and Molecular Structure: Spectra of Diatomic Molecules*, vol. 1 (Krieger Publishing Company, Malabar, Fl, USA, 1989).

[57] S. A. Meek, Ph. D. thesis, Freie Universität Berlin (2010).

[58] R. T. Jongma, Ph.D. thesis, Katholieke Universiteit Nijmegen (1997).

[59] R. W. Fields, S. G. Tilford, and H. R. A., J. Mol. Spec. **44**, 347 (1972).

[60] J. J. Sakurai, *Modern Quantum Mechanics (Revised Edition)* (Addison-Wesley, Reading, MA, 1993), 1st ed., ISBN 9780201539295.

[61] K. P. Huber, G. Herzberg, J. W. Gallagher, and R. D. Johnson III, *"Constants of Diatomic Molecules" in NIST Chemistry WebBook, NIST Standard Reference Database Number 69 (http://webbook.nist.gov)* (National Institute of Standards and Technology, Gaithersburg MD, 20899, 2013), retrieved on May 1, 2013.

[62] F. Hund, Z. Phys. **36**, 657 (1926).

[63] C. Prasad, G. Bhale, and S. Reddy, **121**, 261 (1987).

[64] R. J. LeRoy, *LEVEL 8.0: A Computer Program for Solving the Radial Schrödinger Equation for Bound and Quasibound Levels*, Chemical Physics Research Report CP-663 (2007).

[65] S. Y. T. van de Meerakker, H. L. Bethlem, N. Vanhaecke, and G. Meijer, Chem. Rev. **112**, 4828 (2012).

[66] T. D. Hain, R. M. Moision, and T. J. Curtiss, J. Chem. Phys. **111**, 6797 (1999).

[67] G. Scoles, ed., *Atomic and molecular beam methods*, vol. 1 (Oxford University Press, New York, NY, USA, 1988).

[68] W. Gerlach and O. Stern, Z. Phys. **9**, 349 (1922).

[69] W. Gerlach and O. Stern, Z. Phys. **9**, 353 (1922).

[70] H. G. Bennewitz, W. Paul, and C. Schlier, Z. Phys. **141**, 6 (1955).

[71] J. P. Gordon, H. J. Zeiger, and C. H. Townes, Phys. Rev. **99**, 1264 (1955).

[72] J. P. Gordon, H. J. Zeiger, and C. H. Townes, Phys. Rev. **95**, 282 (1954).

[73] K. H. Kramer and R. B. Bernstein, J. Chem. Phys. **42**, 767 (1965).

[74] E. Kuipers, M. Tenner, A. Kleyn, and S. Stolte, Nature **334**, 420 (1988).

[75] D. Gerlich, Adv. Chem. Phys. **82**, 1 (1992).

[76] I. Szabo, Int. J. Mass Spectrom. Ion Phys. **73**, 197 (1986).

[77] R. W. Anderson, J. Phys. Chem. A **101**, 7664 (1997).

[78] Comsol, *Multiphysics 3.4* (2007), `http://www.comsol.com/products/news/3.4`.

[79] J. Küpper, F. Filsinger, F. Grätz, S. Putzke, and Y.-P. Chang, *`libcoldmol`: A particle trajectory calculation framework* (2003–2013), `http://desy.cfel.de/cid/cmi/software/libcoldmol/`.

[80] E. Wrede, Z. Phys. A **44**, 261 (1927).

[81] M. Broyer, R. Antoine, I. Compagnon, D. Rayane, and P. Dugourd, Physica Scripta **76**, C135 (2007).

[82] L. Holmegaard, J. H. Nielsen, I. Nevo, H. Stapelfeldt, F. Filsinger, J. Küpper, and G. Meijer, Phys. Rev. Lett. **102**, 023001 (2009).

[83] H. G. Bennewitz and W. Paul, Z. Phys. **139**, 489 (1954).

[84] M. Kirste, H. Haak, G. Meijer, and S. Y. T. van de Meerakker, Rev. Sci. Instrum. **84**, 073113 (2013).

[85] T. C. James, J. Chem. Phys. **55**, 4118 (1971).

[86] R. Golub, Ph.D. thesis, Massachusetts Institute of Technology, Cambridge (1967).

[87] E. E. A. Bromberg, Ph.D. thesis, University of Chicago (1972).

[88] D. Auerbach, E. E. A. Bromberg, and L. Wharton, J. Chem. Phys. **45**, 2160 (1966).

[89] J. R. Bochinski, E. R. Hudson, H. J. Lewandowski, G. Meijer, and J. Ye, Phys. Rev. Lett. **91**, 243001 (2003).

[90] E. R. Hudson, C. Ticknor, B. C. Sawyer, C. A. Taatjes, H. J. Lewandowski, J. R. Bochinski, J. L. Bohn, and J. Ye, Phys. Rev. A **73**, 063404 (2006).

[91] S. Jung, E. Tiemann, and C. Lisdat, Phys. Rev. A **74**, 040701 (2006).

[92] S. Y. T. van de Meerakker, I. Labazan, S. Hoekstra, J. Küpper, and G. Meijer, J. Phys. B **39**, S1077 (2006).

[93] S. Hoekstra, J. J. Gilijamse, B. Sartakov, N. Vanhaecke, L. Scharfenberg, S. Y. T. van de Meerakker, and G. Meijer, Phys. Rev. Lett. **98**, 133001 (2007).

[94] S. K. Tokunaga, J. M. Dyne, E. A. Hinds, and M. R. Tarbutt, New J. Phys. **11**, 055038 (2009).

[95] X. Wang, M. Kirste, G. Meijer, and S. Y. T. van de Meerakker, Z. Phys. Chem. (2013).

[96] T. E. Wall, J. F. Kanem, J. M. Dyne, J. J. Hudson, B. E. Sauer, E. A. Hinds, and M. R. Tarbutt, Phys. Chem. Chem. Phys. **13**, 18991 (2011).

[97] J. Riedel, S. Hoekstra, W. Jäger, J. J. Gilijamse, S. Y. T. van de Meerakker, and G. Meijer, Eur. Phys. J. D **65**, 161 (2011).

[98] S. A. Meek, H. Conrad, and G. Meijer, Science **324**, 1699 (2009).

[99] A. Osterwalder, S. A. Meek, G. Hammer, H. Haak, and G. Meijer, Phys. Rev. A **81**, 051401 (2010).

[100] N. E. Bulleid, R. J. Hendricks, E. A. Hinds, S. A. Meek, G. Meijer, A. Osterwalder, and M. R. Tarbutt, Phys. Rev. A **86**, 021404 (2012).

[101] M. Quintero-Pérez, P. Jansen, T. E. Wall, J. E. van den Berg, S. Hoekstra, and H. L. Bethlem, Phys. Rev. Lett. **110**, 133003 (2013).

[102] E. Vliegen, H. J. Wörner, T. P. Softley, and F. Merkt, Phys. Rev. Lett. **92**, 033005 (2004).

[103] E. Vliegen and F. Merkt, J. Phys. B **39**, L241 (2006).

[104] E. Vliegen, S. Hogan, H. Schmutz, and F. Merkt, Phys. Rev. A **76**, 023405 (2007).

[105] S. D. Hogan, C. Seiler, and F. Merkt, Phys. Rev. Lett. **103**, 123001 (2009).

[106] C. Seiler, S. D. Hogan, and F. Merkt, Phys. Chem. Chem. Phys. **13**, 19000 (2011).

[107] N. E. Shafer-Ray, K. A. Milton, B. R. Furneaux, E. R. I. Abraham, and G. R. Kalbfleisch, Phys. Rev. A **67**, 045401 (2003).

[108] K. Wohlfart, F. Filsinger, F. Grätz, J. Küpper, and G. Meijer, Phys. Rev. A **78**, 033421 (2008).

[109] K. Wohlfart, F. Grätz, F. Filsinger, H. Haak, G. Meijer, and J. Küpper, **77**, 031404 (2008).

[110] M. R. Tarbutt, H. L. Bethlem, J. J. Hudson, V. L. Ryabov, V. A. Ryzhov, B. E. Sauer, G. Meijer, and E. A. Hinds, Phys. Rev. Lett. **92**, 173002 (2004).

[111] J. A. Maddi, T. P. Dinneen, and H. Gould, Phys. Rev. A **60**, 3882 (1999).

[112] R. Fulton, A. I. Bishop, M. N. Shneider, and P. F. Barker, J. Phys. B **39**, S1097 (2006).

[113] T. Momose, Y. Liu, S. Zhou, P. Djuricanin, and D. Carty, Phys. Chem. Chem. Phys. **15**, 1772 (2013).

[114] S. Y. T. van de Meerakker, H. L. Bethlem, N. Vanhaecke, and G. Meijer, Chem. Rev. **112**, 4828 (2012).

[115] D. J. Griffiths, *Introduction to Electrodynamics (3rd Edition)* (Prentice Hall of India, 1998), 3rd ed., ISBN 9788120316010.

[116] D. J. Griffiths, *Introduction to electrodynamics. Instructor's Solution Manual* (Prentice Hall, 1999), ISBN 9780138598518.

[117] H. L. Bethlem, Ph.D. thesis, Katholieke Universiteit Nijmegen (2002).

[118] H. L. Bethlem and G. Meijer, Int. Rev. Phys. Chem. **22**, 73 (2003).

[119] S. Y. T. van de Meerakker, N. Vanhaecke, and G. Meijer, Ann. Rev. Phys. Chem. **57**, 159 (2006).

[120] S. Y. T. van de Meerakker, N. Vanhaecke, H. L. Bethlem, and G. Meijer, Phys. Rev. A **73**, 023401 (2006).

[121] K. Gubbels, G. Meijer, and B. Friedrich, Phys. Rev. A **73**, 063406 (2006).

[122] L. Scharfenberg, Ph. D. thesis, Technische Universität Berlin, Berlin, Germany (2012).

[123] H. L. Bethlem, G. Berden, A. J. A. van Roij, F. M. H. Crompvoets, and G. Meijer, Phys. Rev. Lett. **84**, 5744 (2000).

[124] M. S. Livingston and J. P. Blewett, *Particle accelerators*, International series in pure and applied physics (McGraw-Hill, New York, 1962).

[125] B. Friedrich, Eur. Phys. J. D **38**, 209 (2006).

[126] K. Gubbels, Master's thesis, Radboud University Nijmegen (2006).

[127] Bronstein, I. N. and Semendjajew, K. A. and Musiol, G. and Mühlig, H., *Taschenbuch der Mathematik* (Harri Deutsch Verlag, Thun, Frankfurt am Main, 2001), 5th ed., ISBN 3-8171-2005-2.

[128] S. Y. T. van de Meerakker, N. Vanhaecke, H. L. Bethlem, and G. Meijer, Phys. Rev. A **71**, 053409 (2005).

[129] L. Scharfenberg, H. Haak, G. Meijer, and S. Y. T. van de Meerakker, Phys. Rev. A **79**, 023410 (2009).

[130] G. Hill, Acta Mathematica **8**, 1 (1886).

[131] W. Paul, O. Osberghaus, and E. Fischer, Forschungsberichte des Wirtschafts- und Verkehrministeriums Nordrhein Westfalen (1958).

[132] W. Paul, Rev. Mod. Phys. **62**, 531 (1990).

[133] G. Teschl, *Ordinary differential equations and dynamical systems* (Am. Math. Soc., Providence, RI, 2012), ISBN 978-0-821-89105-6.

[134] M. Kirste, Diplomarbeit, Freie Universität Berlin, Berlin (2008).

[135] T. E. Wall, S. K. Tokunaga, E. A. Hinds, and M. R. Tarbutt, Phys. Rev. A **81**, 033414 (2010).

[136] M. Galassi, J. D. J. Theiler, B. Gough, G. Jungman, M. Booth, and F. Rossi, *GNU Scientific Library Reference Manual* (Network Theory Ltd., 2009), 3rd ed., ISBN 0954612078.

[137] W. Martienssen and H. Warlimont, eds., *Springer Handbook of Condensed Matter and Materials Data* (Springer, Berlin, Heidelberg, 2006), ISBN 978-3-540-30437-1.

[138] C. Wegst and M. Wengst, *Stahlschlüssel–Key to Steel* (Verlag Stahlschlüssel Wengst, Marbach, 2013), 23rd ed., ISBN 978-3-922599-29-6.

[139] A. Marian, H. Haak, and G. Meijer, unpublished (2011), A miniature Stark decelerator made from tantalum wires supported by molybdenum rods was constructed and proven to be working.

[140] Marian, A. and Haak, H. and Geng, P. and Meijer, G., Eur. Phys. J. D **59**, 179 (2010).

[141] M. Okawa, T. Shioiri, H. Okubo, and S. Yanabu, IEEE Trans. Electr. Insul. **23**, 77 (1988).

[142] T. Shioiri, T. Kamikawaji, E. Kaneko, M. Homma, H. Takahashi, and I. Ohshima, IEEE Trans. Dielectr. Electr. Insul. **2**, 317 (1995).

[143] J. Hudson, *Surface Science: An Introduction* (John Wiley & Sons, 1998).

[144] B. D. Kay, K. R. Lykke, J. R. Creighton, and S. J. Ward, J. Chem. Phys. **91**, 5120 (1989).

[145] Y. X. Zhang and Z. J. Xu, Am. Mineral. **80**, 670 (1995).

[146] D. M. Hoffman, B. Singh, J. H. Thomas III, and J. H. Thomas III, eds., *Handbook of Vacuum Science and Technology* (Academic Press, San Diego, 1998), ISBN 978-0-12-352065-4.

[147] A. T. Modak and P. J. Pagni, J. Chem. Phys. **59**, 2019 (1973).

[148] C. T. Rettner, J. Chem. Phys. **99**, 5481 (1993).

[149] I. Nakamura, A. Takahashi, and T. Fujitani, Catal. Lett. **129**, 400 (2009).

[150] N. Yoshimura, T. Sato, S. Adachi, and T. Kanazawa, J. Vac. Sci. Technol. A **8**, 924 (1990).

[151] D. G. Bills, J. Vac. Sci. Technol. **6**, 166 (1969).

[152] J. Bennett and R. Elsey, Vacuum **44**, 647 (1993).

[153] J. K. Fremerey, Vacuum **53**, 197 (1999).

[154] J. Bennett, S. Hughes, R. Elsey, and T. Parry, Vacuum **73**, 149 (2004).

[155] J. P. Looney, J. E. Harrington, K. C. Smyth, T. R. O'Brian, and T. B. Lucatorto, J. Vac. Sci. Technol. A **11**, 3111 (1993).

[156] R. Musket, W. McLean, C. Colmenares, D. Makowiecki, and W. Siekhaus, Applic. Surf. Sci. **10**, 143 (1982).

[157] J. V. Barth, H. Brune, G. Ertl, and R. J. Behm, Phys. Rev. B **42**, 9307 (1990).

[158] P. W. Palmberg, G. Riach, N. C. MacDonald, and R. E. Weber, *Handbook of Auger Electron Spectroscopy: A Reference Book of Standard Data for Identification and Interpretation of Auger Electron Spectroscopy Data* (Physical Electronics Industries, Inc., Edina, Minnesota, 1972), 1st ed.

[159] C. Kittrell, E. Abramson, J. L. Kinsey, S. A. McDonald, D. E. Reisner, R. W. Field, and D. H. Katayama, J. Chem. Phys. **75**, 2056 (1981).

[160] L. Velarde, D. P. Engelhart, D. Matsiev, J. LaRue, D. J. Auerbach, and A. M. Wodtke, Rev. Sci. Instrum. **81**, 063106 (2010).

[161] D. A. Dahl, *Simion 3D Version 6.0* (Idaho National Engineering Laboratory, Idaho Falls (USA), 1995).

[162] S. Wurm, P. Feulner, and D. Menzel, J. Chem. Phys. **105**, 6673 (1996).

[163] M. A. Hines, H. A. Michelsen, and R. N. Zare, J. Chem. Phys. **93**, 8557 (1990).

[164] H. Rottke and H. Zacharias, Opt. Comm. **55**, 87 (1985).

[165] F. Penning, Naturwissenschaften **15**, 818 (1927).

[166] H. D. Hagstrum, Phys. Rev. **150**, 495 (1966).

[167] H. Conrad, G. Ertl, J. Küppers, S. W. Wang, K. Gérard, and H. Haberland, Phys. Rev. Lett. **42**, 1082 (1979).

[168] F. Grätz, D. P. Engelhart, R. J. V. Wagner, H. Haak, G. Meijer, A. M. Wodtke, and T. Schäfer, Phys. Chem. Chem. Phys. **15**, 14951 (2013).

[169] F. Grätz, D. P. Engelhart, R. J. V. Wagner, G. Meijer, A. M. Wodtke, and T. Schäfer (2014), (in preparation).

[170] H. Hotop, in *Atomic, Molecular, and Optical Physics: Atoms and Molecules*, edited by F. Dunning and R. G. Hulet (Academic Press, 1996), vol. 29 B of *Experimental Methods in the Physical Sciences*, pp. 191–215.

[171] Y. Harada, S. Masuda, and H. Ozaki, Chem. Rev. **97**, 1897 (1997).

[172] H. D. Hagstrum, Phys. Rev. **96**, 325 (1954).

[173] H. D. Hagstrum, Phys. Rev. **104**, 672 (1956).

[174] J. A. Appelbaum and D. R. Hamann, Phys. Rev. B **6**, 1122 (1972).

[175] B. Woratschek, W. Sesselman, J. Küppers, G. Ertl, and H. Haberland, Surf. Sci. **180**, 187 (1987).

[176] A. Messiah, *Quantum Mechanics : Volume I* (North Holland, 1981), 12th ed., ISBN 9780720400441.

[177] W. Sesselmann, B. Woratschek, J. Küppers, G. Ertl, and H. Haberland, Phys. Rev. B **35**, 1547 (1987).

[178] R. Hemmen and H. Conrad, Phys. Rev. Lett. **67**, 1314 (1991).

[179] K. Makoshi, A. Yoshimori, and B. Lundqvist, Surf. Sci. **230**, 350 (1990).

[180] H. M. Rosenstock, K. Draxl, B. W. Steiner, and J. T. Herron, *"Ion Energetics Data" in NIST Chemistry WebBook, NIST Standard Reference Database Number 69 (http://webbook.nist.gov)* (National Institute of Standards and Technology, Gaithersburg MD, 20899, 2013), retrieved on September 10, 2013.

[181] E. Condon, Phys. Rev. **28**, 1182 (1926).

[182] W. L. Borst, Rev. Sci. Instrum. **42**, 1543 (1971).

[183] M. Zubek, **149**, 24 (1988).

[184] P. H. Citrin, G. K. Wertheim, and Y. Baer, Phys. Rev. Lett. **41**, 1425 (1978).

[185] G. J. Schulz, Rev. Mod. Phys. **45**, 423 (1973).

[186] L. A. Morgan and J. Tennyson, J. Phys. B **26**, 2429 (1993).

[187] J. Zobel, U. Mayer, K. Jung, and H. Ehrhardt, J. Phys. B **29**, 813 (1996).

[188] N. Swanson, C. E. Kuyatt, J. W. Cooper, and M. Krauss, Phys. Rev. Lett. **28**, 948 (1972).

[189] J. Mazeau, F. Gresteau, G. Joyez, J. Reinhardt, and R. I. Hall, J. Phys. B **5**, 1890 (1972).

[190] L. Sanche and G. J. Schulz, Phys. Rev. Lett. **26**, 943 (1971).

[191] J. Zobel, U. Mayer, K. Jung, H. Ehrhardt, H. Pritchard, C. Winstead, and V. McKoy, J. Phys. B **29**, 839 (1996).

[192] N. Swanson, R. J. Celotta, C. E. Kuyatt, and J. W. Cooper, J. Chem. Phys. **62**, 4880 (1975).

[193] P. Stracke, F. Wiegershaus, S. Krischok, and V. Kempter, Surf. Sci. **396**, 212 (1998).

[194] N. Lorente, D. Teillet-Billy, and J.-P. Gauyacq, Surf. Sci. **432**, 155 (1999).

[195] J. Marbach, F. X. Bronold, and H. Fehske, Phys. Rev. B **84**, 085443 (2011).

[196] H. Müller, D. Gador, and V. Kempter, Surf. Sci. **338**, 313 (1995).

[197] H. Müller, R. Hausmann, H. Brenten, and V. Kempter, Chem. Phys. **179**, 191 (1994).

[198] J. M. Price, A. Ludviksson, M. Nooney, M. Xu, R. M. Martin, and A. M. Wodtke, J. Chem. Phys. **96**, 1854 (1992).

[199] H. L. Bethlem, A. J. A. van Roij, R. T. Jongma, and G. Meijer, Phys. Rev. Lett. **88**, 133003 (2002).

[200] S. Schohl, D. Klar, T. Kraft, H. Meijer, M.-W. Ruf, U. Schmitz, S. Smith, and H. Hotop, Z. Phys. D **21**, 25 (1991).

[201] A. J. Smith, R. E. Imhof, and F. H. Read, J. Phys. B **6**, 1333 (1973).

[202] R. V. Wagner, Master's thesis, Georg-August-Universität Göttingen (2013).

[203] N. Bartels, T. Schafer, J. Huhnert, R. W. Field, and A. M. Wodtke, J. Chem. Phys. **136**, 214201 (2012).

[204] K. H. Strobl and C. R. Vidal, J. Chem. Phys. **86**, 62 (1987).

[205] W. C. Paske, A. W. Garrett, S. Shadfar, D. E. Golden, and J. R. Twist, J. Chem. Phys. **76**, 3002 (1982).

[206] A. L. Floch, J. Rostas, and F. Rostas, Chem. Phys. **142**, 261 (1990).

[207] LabVIEW (2000), http://www.ni.com/labview.

[208] W. Lee and R. M. Martin, J. Chem. Phys. **64**, 678 (1976).

[209] W. L. Borst, G. Nowak, and J. Fricke, Phys. Rev. A **17**, 838 (1978).

[210] B. Brutschy and H. Haberland, Phys. Rev. A **19**, 2232 (1979).

[211] M. R. Woodard, R. C. Sharp, M. Seely, and J. E. E. Muschlitz, J. Chem. Phys. **69**, 2978 (1978).

[212] H. B. Michaelson, J. Appl. Phys. **48**, 4729 (1977).

[213] A. W. Dweydari and C. H. B. Mee, Phys. Status Solidi A **17**, 247 (1973).

[214] S. Schohl, H. Meijer, M. Ruf, and H. Hotop, Meas. Sci. Technol. **3**, 544 (1992).

[215] D. E. Eastman, Phys. Rev. B **2**, 1 (1970).

[216] R. T. Jongma, G. Berden, D. van der Zande, T. Rasing, H. Zacharias, and G. Meijer, Phys. Rev. Lett. **78**, 1375 (1997).

[217] R. T. Jongma, G. Berden, T. Rasing, H. Zacharias, and G. Meijer, Chem. Phys. Lett. **273**, 147 (1997).

[218] J. Furlong and W. Newell, Meas. Sci. Technol. **7**, 641 (1996).

[219] P. H. Krupenie, NSDRS 5, Standard Reference Data, NIST (1966).

[220] R. Nicholls, J. Quant. Spectrosc. Radiat. Transf. **2**, 433 (1962).

[221] R. T. Jongma, G. Berden, and G. Meijer, J. Chem. Phys. **107**, 7034 (1997).

[222] C. E. Johnson and J. Robert S. Van Dyck, J. Chem. Phys. **56**, 1506 (1972).

[223] R. S. Freund, J. Chem. Phys. **55**, 3569 (1971).

[224] M. Zubek and G. C. King, J. Phys. E **15**, 511 (1982).

[225] M. M. Ristić, G. B. Poparić, and D. S. Belić, Phys. Rev. A **83**, 042714 (2011).

[226] R. T. Jongma, G. Berden, T. Rasing, H. Zacharias, and G. Meijer, J. Chem. Phys. **107**, 252 (1997).

[227] W. C. Ermler and R. S. Mulliken, J. Mol. Spec. **61**, 100 (1976).

[228] P. Hammond, G. C. King, J. Jureta, and F. H. Read, J. Phys. B **18**, 2057 (1985).

[229] U. Gaubatz, P. Rudecki, S. Schiemann, and K. Bergmann, J. Chem. Phys. **92**, 5363 (1990).

[230] N. Bartels, B. C. Krüger, S. Meyer, A. M. Wodtke, and T. Schäfer, J. Phys. Chem. Lett. **4**, 2367 (2013).

[231] J. H. Blokland, J. Riedel, S. Putzke, B. G. Sartakov, G. C. Groenenboom, and G. Meijer, J. Chem. Phys. **135**, 114201 (2011).

Danksagung

Als ich anfangs nach einem spannenden Projekt für meine Doktorarbeit suchte, wäre ich am liebsten am FHI geblieben. Dort hatte ich während meiner Diplomarbeit die Abteilung Molekülphysik bereits kennen gelernt, und die herausragenenden Forschungsbedingungen sowie die gute Atmosphäre unter den Mitabeitern sehr zu schätzen gelernt. Andererseits zog es mich ins Ausland, sowohl um neue Einblicke in ein anderes Forschungsfeld zu gewinnen, als auch um noch einmal ein anderes Land kennen zu lernen. Insofern passte es perfekt, als Gerard Meijer mir ein Projekt vorschlug, das eine Kooperation mit Alec Wodtke's Gruppe in Santa Barbara vorsah. Streuung von langsamen Molekülen an Oberflächen - das war in der Tat etwas Neues, und das dazu noch an einer renommierten Universität mit Blick auf den Pazifik und eigener Lagune auf dem Campus! Klar, dass ich nach kurzer Bedenkzeit zusagte. Am Ende kam es dann anders, und aus Santa Barbara wurde Göttingen. Was sich allerdings nicht änderte, war die vielfältige Unterstützung meiner Kollegen, die mir im Laufe meiner Doktorarbeit viel geholfen haben und dazu beigetragen haben, dass sie zu einer interessanten und angenehmen Zeit wurde.

An erster Stelle möchte ich meinem Doktorvater Gerard Meijer dafür danken, dass er mir die Gelegenheit gegeben hat, dieses spannende und anspruchsvolle Forschungsprojekt zu übernehmen. Insbesondere seine ständige Motivation und seine Begeisterung waren immer eine großer Ansporn und eine große Hilfe. Und das nicht nur im Labor! Ich erinnere mich noch gut daran, wie Du als Stürmer(!) im Viertelfinalspiel des Fußballturniers in Golm kurz vor Abpfiff im eigenen Strafraum dem Gegenspieler den Ball abgegrätscht und uns so ins Siebenmeterschießen gerettet hast.

Alec Wodtke hat unser gemeinsames Projekt von Anfang mit Begeisterung und großem Enthusiasmus vorangetrieben. Nicht nur die ins Detail gehenden wissenschaftlichen Diskussionen waren äußerst inspirierend - ich danke Dir auch für das warme Willkommen, das Du meinem Mitdoktoranden Dan Engelhart und mir in Göttingen bereitet hast. Für die Fertigstellung meiner Doktorabeit hatte ich stets Deine volle Unterstützung, obwohl die erste Veröffentlichung lange auf sich warten ließ.

Dan — Dir muss ich ganz besonders danken, für all die Zeit die wir es gut miteinander ausgehalten haben, erst im Labor, dann auch im Büro. Es hat immer wieder Spaß gemacht, die Tage zusammen im Labor zu verbringen und so manchen Abend beim Biertrinken. Zwar hatte ich was Liegestütze und Abnehmen betrifft nie eine ernsthafte Chance gegen Dich, aber am Kickertisch sind wir uns dafür immer auf Augenhöhe begegnet.

Tim Schäfer hat erst kurz vor unserem Umzug nach Göttingen als Gruppenleiter des Projekts angefangen. Tim, Du warst eine enorme Bereicherung, und zwar in jederlei Beziehung. Nicht nur was das Experiment angeht - Du hast auch allen Berlinern,

die auf Wohnungssuche in Göttingen verzweifelt sind, ein Exil bei Dir zu Hause geboten. Insbesondere das Korrekturlesen der Dissertation und die vielen Diskussionen während der Schlussphase der Doktorarbeit waren extrem hilfreich.

Luis, it was great working with you! From the very first time we met in Santa Barbara and later in Berlin, I learned to appreciate the way you would handle things. It has been more than once that Dan and I have missed you in the lab!

Roman Wagner ist in Göttingen im Rahmen seiner Masterarbeit zu uns gestoßen und war sofort einen wichtiger Teil unseres Teams. Einige Male, wenn Du zu uns gekommen bist und "nochmal so eine Frage" hattest, führte das dazu, dass wir unsere Ergebnisse besser verstanden haben! Es gibt kaum jemanden, der so detailiert Korrektur liest wie Du, unter anderem auch einen großen Teil dieser Doktorarbeit. Ich wünsche Dir alles Gute für Deine Doktorarbeit an unserer Apparatur!

Ohne die Hilfe von Henrik Haak sähe die Apparatur heute wohl ganz anders aus und würde bei weitem nicht so gut funktionieren. Henrik, Deine genialen Konstruktionen spiegeln nur einen kleinen Teil Deines Anteils am Experiments wider. Und wenn es einmal nicht so gut lief, bist Du immer eine große Motivation für mich gewesen ("Wie meinst Du das, die Abbremserstange ist beim Ausheizen runtergefallen? Ach, keine Panik, wir kriegen das hin!"). Egal, was für ein praktisches Problem ich während der Aufbauphase der Maschine hatte, Henrik wusste immer Rat.

Der Aufbau einer neuen Apparatur bringt es mit sich, dass man im intensiven Kontakt mit den Werkstätten steht. Besonders möchte ich mich beim damaligen Leiter der mechanischen Werkstätten, Horst Schwäricke, sowie Adrian Kluge und Peter Schmidt für die gute Zusammenarbeit bedanken. Außerordentlichen Einsatz haben Thorsten Nemes, Holger Giese und Christian Schmidt gezeigt, die sich bei der Politur der Hochspannungsteile auch von wunden Fingern nie abschrecken ließen. Wohl auch deswegen ist der Abbremser bis heute der hochspanunngsfesteste unter den Abbremsern.

Großer Dank geht auch an das gesamte Elektroniklabor unter Leitung von Georg Heyne. Gerade Victor Platschkowsky war stets ein hilfbereiter Ansprechpartner, genauso wie Patrick Schlecht. Und ohne die schnelle Hilfe von Wilko Genz und anderen hätte so manches Problem wohl erst nach vielen Tagen statt einigen Stunden gelöst werden können. Frank Hilgendorf hat unermüdlichen Einsatz in der Reparatur und dem Umbau der Hochspannugsschalter gezeigt, und mir bewusst gemacht, dass die Herstellerspezifikation "30 kV"nicht immer aussagekräftig ist, wenn man dann tatsächlich einen Abbremser schalten will. Übrigens würde dank des Elabs das komplette Experiment wohl auch problemlos bei 110 V und 60 Hz Netzspannung funktionieren — nur falls mal wieder ein Umzug anstehen sollte. Auch den Werkstätten der Uni und des MPI für Biophysikalische Chemie in Göttingen möchte ich für ihre Unterstützung danken.

Eine Große Hilfe beim Aufbau sind auch immer Georg Hammer, Rolf Meilicke, Manfred Erdmann und Andreas Liedke gewesen. Vielen Dank für die schnelle und unkomplizierte Hilfe bei vielen kleinen und großen Vorhaben. Die Starthilfe, die Reinhard Bürsing, Florian Lange und Milo in Göttingen geleistet haben, hat dafür gesorgt dass die Apparatur binnen kürzester Zeit wieder einsatzfähig war.

Petrik Bischoff hat aus mir zwar keinen Feinmechaniker gemacht, mir aber unzählige Tipps in der Bedienung von Drehbank und Fräsmaschine gegeben und auch Nachsicht gezeigt wenn doch einmal ein Stahl kaputt gegangen oder ein Bohrer abgebrochen ist. Petrik, Dein verschmitztes Grinsen, wenn Du ein Bauteil mal wieder nicht nur schnell, sondern auch viel genauer als gewünscht fertig hattest, ist einfach unschlagbar!

Ohne Uwe Hoppe hätte manch lange Nacht im Labor bereits am Nachmittag geendet, weil KouDA nicht so wollte wie ich es gerne wollte.

Sam Meek, Gabriele Santambrogio, and Mark Abel, it was great sharing a lab with you, even though it was only for a short time. Thanks for all the help with the excitation laser! Auch Sandy Gewinner hat so manchen dejustierten Laser schnell wieder auf Trab gebracht, gerne auch mal auf unkonventionelle Art und Weise.

Wann immer es um Organisation ging, konnte ich mich in Berlin auf Andrea Braaker, Inga von Dölln und Carmen Pilat, in Göttingen auf Inge Dreger, Jessica Paulsen, Liesel Roeder-Wodtke und Markus Hold verlassen. Andrea und Jessica, ihr seid einfach unersetzlich wenn es darum geht, an einem tiefgrauen Montag Morgen gute Stimmung zu verbreiten.

Dan Harding, Nicolas, Roman, und Tim haben durch ihre zahlreichen Korrekturen geholfen diese Dissertation leserlich zu gestalten, und haben dem Leser manch lustigen Rechtschreibfehler erspart. The difference between an "exhaustive" treatment and an "exhausting" treatment can be tremendous.

Viele Kollegen waren zwar nicht direkt am Projekt beteiligt, haben aber in vielerlei Hinsicht geholfen. Sie alle aufzuzählen würde diese Danksagung auf Buchdicke anschwellen lassen. Deswegen seien hier stellvertretend nur einige genannt, und ich bedanke mich hiermit bei allen, die an dieser Stelle fehlen. Peter, Frank, Christian Schewe und Dongdong, it was always pleasant to share an office with you! Unsere Labornachbarn aus der großen Halle waren immer zur Stelle, wenn Not am Mann war oder es alleine im Labor zu einsam wurde. In unserer FHI-Fußballgruppe hatten wir viele knappe und weniger knappe Spiele, aber alle haben sowohl als Mitspieler als auch als Gegner immer vollen Einsatz gezeigt. Ich hoffe, dass meine Nachfolger demnächst das Fußball-Turnier in Golm gewinnen werden!

Lautstark geäußerte Emotionen gab es für Außenstehende in der Göttinger Kaffeeküche zu bewundern, wo wir jeden Nachmittag große Fußballmomente in klein nachspielten. Für das herzliche Willkommen in Göttingen und für viele angenehme Stunden möchte ich allen meinen Kollegen herzlich danken.

Professor Troe hat durch viele aufmunternde Worte und angeregte Unterhaltung über Politik etwas Abwechslung in die langen Abende und Wochenenden im Büro gebracht.

Wenn man in einer neuen Stadt ankommt, kann der Start manchmal schwer fallen. Ich danke meinen Mitbewohnern dafür, dass dies in Göttingen nicht der Fall war und ich mich bereits am ersten Tag wie zu Hause gefühlt habe. Ihr seid großartig!

Meinen Kletterpartnern Franzi und Mike gebührt Dank für die Ablenkung in stres-

sigen Zeiten durch viel Adrenalin und gute Filme (ja Mike, auf deutsch!). Juliane, vielen Dank für Deine Unterstützung zu Berliner Zeiten. All meinen Moabiter und nicht-Moabiter Freunden danke ich dafür, dass sie das Leben außerhalb des Labors erst zu dem machen, was es ist.

Zum Schluss möchte ich ganz besonders meiner Familie danken, für den sicheren Rückhalt, dafür, dass ihr durch eure Unterstützung meiner Ausbildung diese Doktorarbeit erst möglich gemacht habt, und nicht zuletzt für die Engelsgeduld, wenn der nächste Anruf mal wieder allzu lange auf sich warten ließ.

Göttingen, Januar 2014

Fabian Grätz

List of Publications

- Kirstin Wohlfart, Fabian Grätz, Frank Filsinger, Henrik Haak, Gerard Meijer, and Jochen Küpper, *Alternating-gradient focusing and deceleration of large molecules*, Phys. Rev. A **77**, 031404 (2008).
- Kirstin Wohlfart, Frank Filsinger, Fabian Grätz, Henrik Haak, Jochen Küpper, and Gerard Meijer, *Stark deceleration of OH radicals in low-field-seeking and high-field-seeking quantum states*, Phys. Rev. A **78**, 033421 (2008).
- Fabian Grätz, Daniel P. Engelhart, Roman J. V. Wagner, Henrik Haak, Gerard Meijer, Alec M. Wodtke, and Tim Schäfer, *Vibrational enhancement of electron emission in* $CO(a^3\Pi)$ *quenching at a clean metal surface*, Phys. Chem. Chem. Phys. **15**, 14951 (2013).
- Fabian Grätz, Daniel P. Engelhart, Roman J. V. Wagner, Gerard Meijer, Alec M. Wodtke, and Tim Schäfer, *The role of vibration in de-excitation of metastable molecules on metal surfaces*, in preparation (2014).
- Fabian Grätz*, Daniel P. Engelhart*, Henrik Haak, Gerard Meijer, Alec M. Wodtke, and Tim Schäfer, *A novel setup for scattering velocity-controlled, state-selected molecules from clean and adsorbate-covered surfaces*, in preparation (2014).

*Both authors contributed equally to this work.

Curriculum Vitae

For reasons of data protection,
the curriculum vitae is not included in the online version.

Selbständigkeitserklärung

Hiermit erkläre ich, Fabian Grätz, die vorliegende Arbeit selbständig verfasst und keine anderen als die angegebenen Quellen und Hilfsmittel benutzt zu haben. Die vorliegende Arbeit ist zu keinem anderen Promotionsverfahren angenommen oder als ungenügend beurteilt worden.

Göttingen, 29. Oktober 2014 Fabian Grätz